



Iron fortification of foods

**Multi-mineral
pyrophosphate-
based salts**

Neshat Moslehi

Iron fortification of foods

Multi-mineral pyrophosphate-based salts

Neshat Moslehi

Iron fortification of foods

Multi-mineral pyrophosphate-based salts

PhD Thesis

Neshat Moslehi

ISBN: 978-94-6469-256-3

DOI: <https://doi.org/10.33540/1652>

Cover: Vivianite (a naturally-occurring iron phosphate mineral)

Photography by: Joren Vos | www.flickr.com/photos/154279732@N05

Cover Design by: Neshat Moslehi

Printed by: ProefschriftMaken | www.proefschriftmaken.nl

Iron fortification of foods

Multi-mineral pyrophosphate-based salts

IJzeren verrijking van voedingsmiddelen
Multiminerale zouten op basis van pyrofosfaat

(met een samenvatting in het Nederlands)

Proefschrift

ter verkrijging van de graad van doctor aan de
Universiteit Utrecht
op gezag van de
rector magnificus, prof.dr. H.R.B.M. Kummeling,
ingevolge het besluit van het college voor promoties
in het openbaar te verdedigen op

woensdag 15 maart 2023 des middags te 2.15 uur

door

Neshat Moslehi

geboren op 10 januari 1991
te Tehran, Iran

Promotoren:

Prof. dr. W.K. Kegel
Prof. dr. K.P. Velikov

Beoordelingscommissie:

Prof. dr. N.F. Shahidzadeh
Prof. dr. F.M.F de Groot
Prof. dr. A.P. Philipse
Prof. dr. M. Dijkstra
Prof. dr. R.H.H.G. van Roij

This research received funding from the Netherlands Organization for Scientific Research (NWO) in the framework of the Innovation Fund for Chemistry and from the Ministry of Economic Affairs in the framework of the “TKI/PPS-Toeslageregeling” (Grant 731017205).

For "Women, Life, Freedom"

Contents

1	Introduction	1
I Iron (III)-containing pyrophosphate salts		
2	Design and characterization of Ca-Fe(III) pyrophosphate salts	17
3	Dissolution behavior of Ca-Fe(III) pyrophosphate salts	37
4	Reactivity of Ca-Fe(III) pyrophosphate salts with phenolics	51
II Iron (II)-containing pyrophosphate salts		
5	Design and characterization of divalent metal pyrophosphate salts	85
6	Dissolution behavior of divalent metal pyrophosphate salts	113
7	Redox interactions of divalent metal pyrophosphate salts with vitamin C	131
III Cooperativity in binding of iron ions onto polymers		
8	Cooperative binding of iron ions onto terpyridine-functionalized polymers	151
	Summary	181
	Samenvatting in het Nederlands	185
	Acknowledgments	189
	List of publications	195
	About the author	197

Introduction

"Look within;
everything you want, you already are.

"As you start to walk on the way,
the way appears."

Rumi – Persian poet, 1207-1273

I**RON** deficiency in the human body is one of the most important nutrition problems to solve. Sufficient amount of iron in the human body is essential for proper respiration¹. While a normal healthy person takes roughly a thousand breaths per hour without even noticing, adequate amount of iron is required for production of hemoglobin molecules in red blood cells which are responsible for oxygen transport throughout the body. Therefore, it is urgently vital to contribute to solving the global issue of iron deficiency which has reached epidemic proportions in developing countries². This chapter is concerned with the importance, challenges, and strategies of overcoming iron deficiency.

General introduction on nutrients

Nutrients are chemical substances that are consumed by the human body to perform essential functions and maintain health. In general, the required nutrients for the human body are classified into two main categories; macronutrients and micronutrients. Macronutrients, which provide the human body with energy, are the nutrients needed in relatively larger amounts (gram quantities per day) such as proteins, carbohydrates, and fats³. In contrast, micronutrients like minerals and water- or oil-soluble vitamins⁴ are nutrients that are required in relatively smaller amounts, typically less than 100 mg per day⁵. The mentioned macronutrients and micronutrients plus water are the six essential dietary nutrients which must be obtained from the food since the human body cannot produce them.

The small amounts of micronutrients daily requirements for the human body is not a sign of their lack of significance. Micronutrients (i.e., vitamins and minerals)

play a vital role in optimal physiological functioning of the human body⁶. On the other hand, "*The more the merrier*." does not hold for micronutrients. While being crucial, exceeding the upper limit level of micronutrients intake can cause toxic effects leading to health problems depending on the dose and duration of intake⁷.

Micronutrients deficiencies

According to the World Health Organization (WHO), it is estimated that more than 2 billion people in the world suffer from key vitamins and minerals deficiencies, also known as 'hidden hunger'^{8–10}. Numerous investigations have indicated that iron, vitamin A, iodine, zinc, and calcium are the most deficient micronutrients that can cause nutritional problems with serious consequences^{9,11,12}. Micronutrients deficiencies can be caused by, among others, poor nutritional intake or uptake (absorption), health conditions, medications, gender, and age^{13,14}. Although over the past decade an increasing number of people, particularly in developing countries, have gained access to sufficient food¹⁵, having enough (or even a lot of) food does not guarantee nutritionally adequate food^{16,17}. Furthermore, keeping the price of micronutrient-rich food products to minimum has always been an issue to maintain a well-balanced diet that meets the estimated average requirements of the nutrients^{18,19}.

Iron deficiency

Iron is the fourth most abundant element in the Earth's crust and the most abundant element by mass²⁰. Moreover, iron is the most abundant transition metal in the human body as it is present in the metalloproteins such as hemoglobin²¹. On the other hand, it is the most deficient micronutrient in the human body²², and this deficiency can cause many diseases, leading to higher rates of morbidity and mortality²³.

Iron deficiency in the human body can be caused by the iron losses through menstrual blood losses, epithelial shedding of the intestine, urinary tract, and the skin²⁴. It has been reported that while the average daily iron intake by nutrition is 10 to 15 mg, the average iron uptake is only 1 to 2 mg²⁵. Therefore, the iron should be balanced by the diet^{24,26}. The recommended daily allowance (RDA) for iron which differs based on age, gender, and health condition is in the range of 7–27 mg^{2,25,27}. On the other hand, the tolerable upper intake level for adults is reported to be 45 mg/day.

Iron deficiency, receives significant attention due to the prevalence of iron deficiency anemia from which more than 25% of the world's population suffers^{23,28}. Iron deficiency anemia develops due to the insufficient iron to make hemoglobin in the red blood cells which affects the transportation of oxygen^{2,29}. According to WHO, around 0.8 million deaths are attributed to iron deficiency anemia each year³⁰.

Challenges upon addition of iron to foods

Iron is a challenging mineral to introduce to food products. Iron-containing compounds may trigger precipitation in food products, for instance when added to fish sauce³¹. Furthermore, iron compounds can cause organoleptic changes to food products due to the color of the compound, metallic off-flavor, and oxidation of lipids³². In addition, the off-color can be caused by complexation of iron with phenolic compounds that are abundant in plants and vegetables^{33–36}. This reactivity of iron with phenolics is responsible for a change in the organoleptic properties of the food and inhibits iron absorption^{37,38}.

Phenolic compounds consist of aromatic hydrocarbons with one or more hydroxyl groups directly on the aromatic ring³⁹. Provided that the structure of the phenolic contains two hydroxyl groups with adjacent positions on the aromatic ring (i.e., *ortho*-dihydroxyl groups), the reactivity with iron will result in off-color⁴⁰. It should be noted that deprotonation of these groups on the phenolic structure is a prerequisite for complexation with iron. The reaction of these compounds with iron (II) and iron (III) ions are shown in Figure 1.1.

It has previously been shown that the Fe(II)-phenolic is a colorless coordination complex⁴¹. However, this complex can undergo autoxidation in the presence of oxygen leading to a more stable and colored Fe(III)-phenolic complex^{41–43}. Because Fe(III) is a harder Lewis acid than Fe(II), the deprotonated phenolic (hard Lewis base) can be stabilized by binding to Fe(III)⁴¹. Fe(III) complexation with the *ortho*-diphenolic results in ligand-to-metal charge transfer (LMCT) phenomena. After complexation, a negative charge is transferred from π -orbital of the phenolic to the shell of d-orbital of the metal resulting in an energy gap which can be detected in the visible region of the absorbance wavelength spectrum.

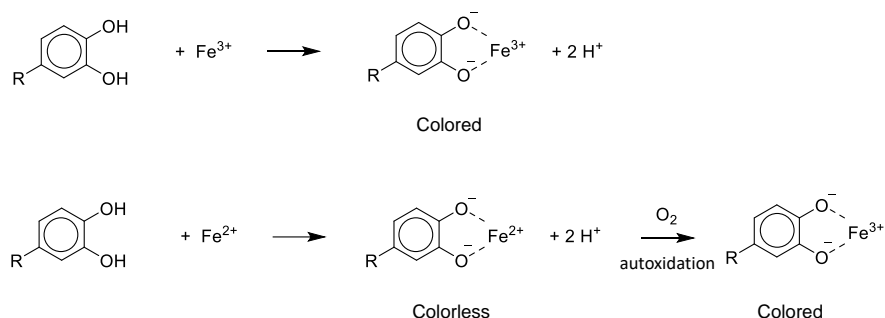


Figure 1.1 The reaction between Fe(III) (top) and Fe(II) (bottom) with the phenolic compounds containing *ortho*-dihydroxyl groups.

In the complexation process, up to three phenolic compounds can coordinate a single iron ion. The stoichiometry of the phenolic to iron depends on several factors, for instance the phenolic chemical structure, iron oxidation state, the equilibrium (stability) constants of the complex, and most importantly pH. Higher pH of the medium results in a higher degree of deprotonation of the phenolics and therefore formation of coordinate complexes with higher number of phenolics. It should be mentioned in this context that in the presence of iron, the pK_a values of phenolics tend to decrease and therefore deprotonation can occur at lower pH values⁴⁴. Table 1.1 summarizes the effect of pH on the stoichiometry and the color of the coordination complex of Fe(III) with phenolic (containing catecholate group)⁴¹.

In addition, the phenolics can undergo oxidation in the presence of iron (III) which upon dimerization or polymerization results in dark-colored products³⁸. It has been reported that phenolic oxidation in the presence of iron can occur at lower pH values (0–3) than the autoxidation of phenolic (6–10)⁴⁵.

Table 1.1 Observed colors, absorbance wavelength (λ_{max}), and stoichiometry of Fe(III)-phenolic (containing catecholate group) complexes at different pH values.

pH	Color	λ_{max} (nm)	Stoichiometry
< 4	Blue-Green	670-700	
5-6.5	Blue-Purple	540-590	
> 8	Red	490-520	

Strategies to overcome iron deficiency

Although there are several successful strategies that can contribute to combating iron deficiency such as dietary diversification and supplementation, studies have proven that fortification of food products with iron is the most efficient and cost-effective approach^{46,47}. In food fortification (i.e., the addition of essential nutrients to foods⁴⁸), factors such as selection of a functional food vehicle for the nutrient, the bio-availability of the added nutrient in the human body, and at the same time protecting sensory properties (e.g., flavor, color, and texture) of the fortified food, are of great importance^{23,48}.

The iron compounds which are used as food fortificants are divided into three main categories. These categories are: water-soluble, poorly water-soluble (but soluble in dilute acid), and water-insoluble (and poorly soluble in dilute acid), which all have their own pros and cons.

Among the mentioned iron compounds, the **water-soluble** iron sources are the preferred choice due to their high solubility in gastric juices and consequently the high bio-availability of iron from them. However, the water-soluble iron compounds of which ferrous sulfate is by far the cheapest and the most frequently used, are known to affect the organoleptic properties of foods the most.

Several physical and chemical approaches are currently being used to control the reactivity of iron ions by limiting their exposure to reactive phenolics³⁶. One strategy to limit the exposure of iron ions to reactive phenolics of the food is the micro-encapsulation of soluble iron-containing salts⁴⁹. However, encapsulated iron can lead to undesirable higher prices and therefore less acceptance by customers⁵⁰. Another approach to prevent the sensory changes is the use of strong molecular complexes such as FeEDTA (Ferrazone[®]) which reduces the reactivity of Fe ions while providing similar relative bioavailability as ferrous sulfate⁵². However, the relatively high costs and the concern that EDTA compounds may negatively influence the metabolism of other essential minerals, or increase absorption of potentially-toxic minerals limit consumer acceptance²³.

Using other iron compounds such as ferrous fumarate and ferric saccharate that falls under the category of **poorly water-soluble but soluble in dilute acid** is advantageous due to the fewer sensory and organoleptic problems in the chosen food vehicle. Furthermore, these poorly-soluble compounds have shown to be as bio-available as ferrous sulfate²³.

There is a considerable interest in using the third category of the iron compounds, **water-insoluble and poorly soluble in dilute acid**, as iron fortificants for foods owing to their minimized effects on the organoleptic properties of the foods (because insoluble compound is less reactive)²³. Within this category, ferric pyrophosphate

* Ferrous sulfate has been chosen as the reference and its bioavailability is 100 by definition⁵¹.

has attracted an extensive amount of attention because of its white/off-white appearance and its application in industrial scale to fortify rice, dairy products, cereal-based complementary food, and salt^{23,47,53}. In general, pyrophosphate salts are good candidates for food additives and mineral supplements because of formation of colorless and/or white and poorly water-soluble/water-insoluble compounds with most metals^{54–56} and therefore, they prevent introducing any undesired colors into food products. However, due to their low solubility, the water-insoluble iron compounds show relatively low bio-availability in the body which still remains a challenge.

Ferric pyrophosphate

Ferric pyrophosphate (Fe(III)PP), which is sometimes considered to be a poorly water-soluble iron compound as well, is of great interest in fortification of foods particularly because of its dissolution behavior. It has been previously shown that Fe(III)PP salt is very poorly soluble in the food relevant pH (3–7) which is the reason for the limited reactivity of this salt with the fortified food vehicle. In addition, Fe(III)PP has low solubility (< 5%) at pH 3 with enhanced dissolution to > 99% at pH 7–8⁵⁵ which is beneficial for ensuring the bio-accessibility of iron from this fortificant. However, a broad range of relative iron bio-availability values for Fe(III)PP have been reported in the literature that may change depending on the processing of the foods⁵¹. Effective strategies such as down-sizing the particle size to micron or even nanometer range have been proven to enhance the relative bio-availability of iron from Fe(III)PP to 82% in the case of an iron-fortified wheat-milk infant cereal^{51,57}. In addition, micronized Fe(III)PP is the suggested iron fortificant for fortification of other food vehicles such as fluid milk, juice, soft drinks, and bouillon cubes²³.

Despite the limited solubility of Fe(III)PP, it has previously been reported that addition of iron in the form of this salt cannot fully prevent discoloration in phenolic-rich foods^{58,59}. One commonly used approach to avoid the undesirable reactions between iron and phytochemicals present in the food is encapsulation⁵¹. However, it usually comes with a less customer acceptance due to the higher costs^{60,61}.

Even though both strategies of downsizing and encapsulation have been successful, finding a less complex and inexpensive approach to improve the function of Fe(III)PP as an iron fortificant still remains a challenge. Recently, colloidal systems such as colloidal Fe(III)PP salt have been studied with the purpose of being utilized as novel iron delivery system for functional foods⁶². It has previously been reported that coating colloidal Fe(III)PP with zein protein results in a decrease in the reactivity of iron with gallic acid, and an increase in the colloidal stability of the system for months, compared to pure Fe(III)PP⁶³. Furthermore, van Leeuwen and coworkers showed that in the case in which the majority of the iron in Fe(III)PP is substituted with a second (divalent) metal (mineral) such as Ca or Mg, a drastic decrease occurs

in its reactivity with gallic acid, with respect to the pure colloidal Fe(III)PP. In addition, at lower iron content (< 5%), no discoloration is observed in the mixed system after 5 h⁶³. Therefore, embedding iron in an inorganic (colloidal) matrix has proven to be a promising strategy to reduce the reactivity of iron.

Outline of this thesis

In this thesis, we focus on multi-mineral pyrophosphate-based iron-containing compounds with tunable design and properties for fortification of foods. Inspired by naturally occurring (but not necessarily edible) minerals such as anapaite (i.e., a calcium–iron phosphate mineral with the formula $\text{Ca}_2\text{Fe}^{\text{II}}(\text{PO}_4)_2 \cdot 4\text{H}_2\text{O}$)^{64–66}, we intend to integrate iron in a second mineral salt matrix for two main goals: (i) decreasing the iron-mediated solubility/reactivity in the food relevant conditions to preserve the organoleptic properties of the food vehicle, and (ii) increasing the iron dissolution from the designed multi-mineral pyrophosphate salts in the gastric and intestine-relevant conditions to ensure sufficient bio-accessibility of iron (and other minerals). Another benefit of these multi-mineral systems is the possibility of simultaneous delivery of at least two minerals by the fortified-food vehicle. To this aim, we use a second (divalent) mineral pyrophosphate salt with the following conditions: (i) low solubility in the food pH range and (ii) high and fast dissolution in the gastric and/or intestine pH ranges such as calcium pyrophosphate (CaPP). In contrast to Fe(III)PP, most divalent metal pyrophosphate salts such as CaPP dissolve well (> 99%) at pH 3 but are poorly soluble (< 5%) at pH 7–8⁶⁷. Consequently, due to the reversed dissolution behavior of Fe(III)PP and a second metal (mineral) pyrophosphate salt, we hypothesize that combination of calcium and iron in one matrix will result in a unique pH-dependent dissolution behavior of the resulting multi-mineral pyrophosphate salt.

Part I of the present thesis contributes to iron (III)-containing pyrophosphate salts. In **chapter 2**, we prepare pure as well as mixed Ca-Fe(III) pyrophosphate salts with the general formula $\text{Ca}_{2(1-x)}\text{Fe}_{4x}(\text{P}_2\text{O}_7)_{(1+2x)}$ ($0 \leq x \leq 1$) by a fast and facile coprecipitation method. The resulting mixed pyrophosphate salts are characterized and their reactivity is explored in a black tea solution. We find that the mixed salts with $0.14 \leq x \leq 0.35$ in the general formula, which yield homogeneous amorphous particles, can be potential dual-fortificants with tunable iron content.

In **chapter 3**, we explore the pH-dependent dissolution behavior of iron from the mixed $\text{Ca}_{2(1-x)}\text{Fe}_{4x}(\text{P}_2\text{O}_7)_{(1+2x)}$ with $0.14 \leq x \leq 0.35$. We find that besides the potential for simultaneous delivery of two minerals, the main advantage of these salts is that they show enhanced dissolution of iron at gastric pH up to a 4-fold increase, compared to Fe(III)PP, which is an early indication for bio-accessibility of iron in

them. Additionally, the salts with $x \leq 0.18$ show an 8-fold decrease in iron dissolution in the food-relevant pH range, with respect to Fe(III)PP.

The main goal of the **chapter 4** is to get more insight into the reactivity of the iron in the Fe(III)PP and the designed Ca-Fe(III) pyrophosphate salts ($0.14 \leq x \leq 0.35$) with the phenolic compounds present in the foods. To this aim, the complexation of a set of pure phenolics with different water-solubilities with the soluble iron from Fe(III)PP and the mixed Ca-Fe(III) pyrophosphate salts in the food relevant pH was explored. Furthermore, the oxidation of the selected phenolics in the presence of the salts is investigated. Our findings show that these mixed pyrophosphate salts with $x \leq 0.18$ can potentially be used as dual-fortificants with limited iron-mediated discoloration and oxidation in foods containing slightly water-soluble or water-insoluble phenolics.

In **Part II** of this thesis we explore the possibilities of fortification of foods with iron (II)-containing pyrophosphate salts with the key idea of diversity, meaning that inclusion of not only calcium but also other minerals such as zinc and manganese along iron is investigated. In **chapter 5**, similar to the first part, the pure and mixed salts $M_{2(1-x)}Fe_{2x}P_2O_7$ ($0 \leq x \leq 1$, where $M = Ca, Zn, \text{ or } Mn$) are prepared, characterized and tested for their potential as multi-mineral food fortificants in a black tea solution as a representative model system for phenolics in particular catechins. In this chapter we show that ferrous pyrophosphate (Fe(II)PP) can be used as an iron fortificant as it causes acceptable discoloration in a black tea solution, which is less than Fe(III)PP. Moreover, our results suggest that in the case of $M = Zn$, the salt with the measured $x = 0.470$ exhibited less color change and similar dissolved iron concentration in the black tea solution, compared to Fe(II)PP. Furthermore, we find that the mixed salts in which $M = Mn$ with $x \leq 0.220$ are the preferred salts for foods containing catechins due to reduced color change and decreased soluble iron concentration up to 2.3-fold in a black tea solution, with respect to Fe(II)PP.

In **chapter 6**, we demonstrate the pH-dependent dissolution profile of pure divalent metal pyrophosphate salts of iron (II), calcium, zinc, and manganese (i.e., Fe(II)PP, CaPP, ZnPP, and MnPP, respectively). We find that these salts are very poorly soluble in the pH 4-7, while they dissolve well in pH 1-3. In addition, the iron dissolution behavior from the mixed salts with the general formula: $M_{2(1-x)}Fe_{2x}P_2O_7$ ($0 < x < 1$, where $M = Ca, Zn, \text{ or } Mn$) showed that all the mixed salts ($M = Ca, Zn, \text{ and } Mn$) had very limited iron dissolution ($< 0.5 \text{ mM}$) in the moderate pH range (5-7) while showing enhanced dissolved iron concentration in the gastric- and intestine-relevant pH up to 5 and 1.3 mM, respectively. Furthermore, the dissolution of these salts in the physiologically relevant conditions was investigated. Additionally, our findings indicate that the pure Fe(II)PP and the mixed Fe(II)-containing pyrophosphate salts are expected to be biologically accessible and therefore, potential candidates for dual-fortification of foods with iron and calcium, zinc, or manganese.

The main goal of **chapter 7** is to investigate the possibility of applying the mixed $M_{2(1-x)}Fe_{2x}P_2O_7$ in combination with vitamin C for fortification of foods. We show in this chapter that the oxidation of vitamin C in the presence of Fe(II)PP and the mixed Fe(II)-containing pyrophosphate salts is very limited due to the oxidation state (+2) and the low/slow dissolution of iron from these salts. We show that although the presence of these salts enhances the oxidation of vitamin C, this is observed only up to 1.5 times (compared to autooxidation of vitamin C in pure water) over 48 h, which is equal to only $\approx 4\%$ loss of vitamin C. Our findings show that the mixed divalent metal Fe(II)-containing salts with the relatively lower iron contents ($x = 0.06, 0.086,$ and 0.053 where $M = Ca, Zn,$ and Mn respectively) are potential dual-fortificants that do not increase the oxidation of vitamin C over 48 h, compared to its autooxidation in water.

In **Part III** of this thesis, we challenge the notion that cooperative binding only happens in complicated biological systems like hemoglobin. To this aim, in **chapter 8** we choose a terpyridine-functionalized polymer as a model system to study the cooperative binding behavior of iron onto terpyridine functional groups on the polymer backbone and compare to terpyridine in its monomer form. We show for the first time that cooperativity occurs in such systems in a two-phase set-up of water and oil that are in contact with each other. At low iron concentrations, the polymer chains reside in the oil phase (their ground state) due to their hydrophobicity. However, increasing the iron concentration beyond a certain level in the water phase results in a sharp transition of the polymer chains from the oil to the water phase and a sudden increase in occupancy of the terpyridine functional groups on the polymer chains with iron. This dramatically steeper response, compared to terpyridine monomer, which is observed over a small range of free iron concentration is explained by the competition between the hydrophobic free energy of the polymer and binding of iron ions onto the terpyridine functional groups on the polymer chains in the water phase. The cooperative binding of iron onto terpyridine-functionalized polymers is explained and modeled by a modified formulation of MWC theory⁶⁸ which was originally introduced to describe the allosteric binding of oxygen on hemoglobin.

References

- 1 C. P. Gupta, IOSR Journal of Applied Chemistry (IOSR-JAC) 7, 38 (2014).
- 2 S. B. Kumar, S. R. Arnipalli, P. Mehta, S. Carrau, and O. Ziouzenkova, *Nutrients* 2022, Vol. 14, Page 2976 14, 2976 (2022).
- 3 J. E. Norton, Y. Gonzalez Espinosa, R. L. Watson, F. Spyropoulos, and I. T. Norton, *Food Function* 6, 663 (2015).
- 4 I. J. Joye, G. Davidov-Pardo, and D. J. McClements, *Trends in Food Science Technology* 40, 168 (2014).

- 5 S. M. T. Gharibzahedi and S. M. Jafari, Trends in Food Science Technology **62**, 119 (2017).
- 6 R. L. Bailey, K. P. West, and R. E. Black, Annals of Nutrition and Metabolism **66**, 22 (2015).
- 7 V. Pike and S. Zlotkin, Annals of the New York Academy of Sciences **1446**, 21 (2019).
- 8 “Worldwide prevalence of anaemia 1993-2005: WHO global database on anaemia. edited by bruno de benoist, erin mclean, ines egli and mary cogswell,” .
- 9 J. R. Díaz, A. De las Cagigas, and R. Rodríguez, European Journal of Clinical Nutrition **57**, S70 (2003).
- 10 S. Muthayya, J. H. Rah, J. D. Sugimoto, F. F. Roos, K. Kraemer, and R. E. Black, PLOS ONE **8**, e67860 (2013).
- 11 P. Mirmiran, M. Golzarand, L. Serra-Majem, and F. Azizi, Iranian Journal of Public Health **41**, 8 (2012).
- 12 R. Harika, M. Faber, F. Samuel, J. Kimiywe, A. Mulugeta, and A. Eilander, Nutrients **9**, 1096 (2017).
- 13 H. H. Chang, R. M. Nayga, and K. C. Chan, Journal of Family and Economic Issues **32**, 268 (2011).
- 14 S. Brownie, International Journal of Nursing Practice **12**, 110 (2006).
- 15 H. C. J. Godfray, J. R. Beddington, I. R. Crute, L. Haddad, D. Lawrence, J. F. Muir, J. Pretty, S. Robinson, S. M. Thomas, and C. Toulmin, Science **327**, 812 (2010).
- 16 C. Koliaki, T. Spinos, M. Spinou, M.-E. Brinia, D. Mitsopoulou, and N. Katsilambros, in *Healthcare*, Vol. 6 (Multidisciplinary Digital Publishing Institute, 2018) p. 73.
- 17 J. A. More and P. M. Emmett, Journal of Human Nutrition and Dietetics **28**, 135 (2015).
- 18 C. Termote, J. Raneri, A. Deptford, and B. Cogill, Food and Nutrition Bulletin **35**, 458 (2014).
- 19 M. Sohail, D. W. Sun, and Z. Zhu, Critical reviews in food science and nutrition **58**, 2650 (2018).
- 20 P. A. Frey and G. H. Reed, ACS Chemical Biology **7**, 1477 (2012).
- 21 M. A. Zoroddu, J. Aaseth, G. Crisponi, S. Medici, M. Peana, and V. M. Nurchi, Journal of Inorganic Biochemistry **195**, 120 (2019).
- 22 N. Moslehi, J. Bijlsma, W. J. de Bruijn, K. P. Velikov, J.-P. Vincken, and W. K. Kegel, Journal of Functional Foods **92**, 105066 (2022).
- 23 L. Allen, B. de Benoist, O. Dary, and R. Hurrell, World Health Organization , 341 (2006).
- 24 S. Dev and J. L. Babitt, Hemodialysis international. International Symposium on Home Hemodialysis **21 Suppl 1**, S6 (2017).
- 25 E. Piskin, D. Ciansiosi, S. Gulec, M. Tomas, and E. Capanoglu, ACS Omega **7**, 20441 (2022).
- 26 I. M. Zijp, O. Korver, and L. B. Tijburg, Critical reviews in food science and nutrition **40**, 371 (2000).
- 27 I. o. M. U. P. on Micronutrients, *Dietary Reference Intakes for Vitamin A, Vitamin K, Arsenic, Boron, Chromium, Copper, Iodine, Iron, Manganese, Molybdenum, Nickel, Silicon, Vanadium, and Zinc* (National Academies Press, 2001).
- 28 L. Pivina, Y. Semenova, M. D. Doşa, M. Dauletyarova, and G. Bjørklund, Journal of Molecular Neuroscience **68**, 1 (2019).

- 29 U. Ramakrishnan, *Nutrition Reviews* **60**, S46 (2002).
- 30 R. Olson, B. Gavin-Smith, C. Ferraboschi, K. Kraemer, and G. Davaasambuu, *Nutrients* **13**(4), 1118 (2021) 10.3390/nu13041118.
- 31 M. C. Fidler, L. Davidsson, T. Walczyk, and R. F. Hurrell, *The American journal of clinical nutrition* **78**, 274 (2003).
- 32 R. F. Hurrell, *Nutrition reviews* **55**, 210 (1997).
- 33 K. Ashwin, A. K. Pattanaik, and G. S. Howarth, *Food Bioscience* **44**, 101376 (2021).
- 34 J. Bijlsma, W. J. de Bruijn, K. P. Velikov, and J. P. Vincken, *Food Chemistry* **370**, 131292 (2022).
- 35 O. P. Bolade, A. B. Williams, and N. U. Benson, *Environmental Nanotechnology, Monitoring Management* **13**, 100279 (2020).
- 36 E. Habeych, V. van Kogelenberg, L. Sagalowicz, M. Michel, and N. Galaffu, *Food Research International* **88**, 122 (2016).
- 37 A. C. Bovell-Benjamin and J. X. Guinard, *Critical Reviews in Food Science and Nutrition* **43**, 379 (2003).
- 38 E. J. T. McGee and L. L. Diosady, *LWT - Food Science and Technology* **89**, 756 (2018).
- 39 G. Morabito, C. Miglio, I. Peluso, and M. Serafini, *Polyphenols in Human Health and Disease* **2**, 1107 (2014).
- 40 R. I. Mellican, J. Li, H. Mehansho, and S. S. Nielsen, *Journal of Agricultural and Food Chemistry* **51**, 2304 (2003).
- 41 N. R. Perron and J. L. Brumaghim, *Cell biochemistry and biophysics* **53**, 75 (2009).
- 42 N. R. Perron, H. C. Wang, S. N. Deguire, M. Jenkins, M. Lawson, and J. L. Brumaghim, *Dalton Transactions* **39**, 9982 (2010).
- 43 N. Petry, *Polyphenols in Human Health and Disease* **1**, 311 (2014).
- 44 R. C. Hider, Z. D. Liu, and H. H. Khodr, "Metal chelation of polyphenols," in *Methods in Enzymology*, Vol. 335 (Elsevier, 2001) pp. 190–203.
- 45 M. Mochizuki, S. I. Yamazaki, K. Kano, and T. Ikeda, *Biochimica et biophysica acta* **1569**, 35 (2002).
- 46 I. C. Ohanenye, C. U. Emenike, A. Mensi, S. Medina-Godoy, J. Jin, T. Ahmed, X. Sun, and C. C. Udenigwe, *Scientific African* **11**, e00667 (2021).
- 47 S. Saha and A. Roy, *Food Chemistry* **326**, 127049 (2020).
- 48 N. Huma, F. Muhammad Anjum, M. Anjum Murtaza, and M. A. Sheikh, *Critical Reviews in Food Science and Nutrition* **47**, 259 (2007).
- 49 M. B. Zimmermann, in *International Journal for Vitamin and Nutrition Research*, Vol. 74 (Verlag Hans Huber, 2004) pp. 453–461.
- 50 N. Zuidam, in *Encapsulation Technologies and Delivery Systems for Food Ingredients and Nutraceuticals* (Elsevier, 2012) pp. 505–540.
- 51 V. R. Preedy, R. Srirajaskanthan, V. B. Patel, *et al.*, *From Concepts to Public Health Applications* (2013).

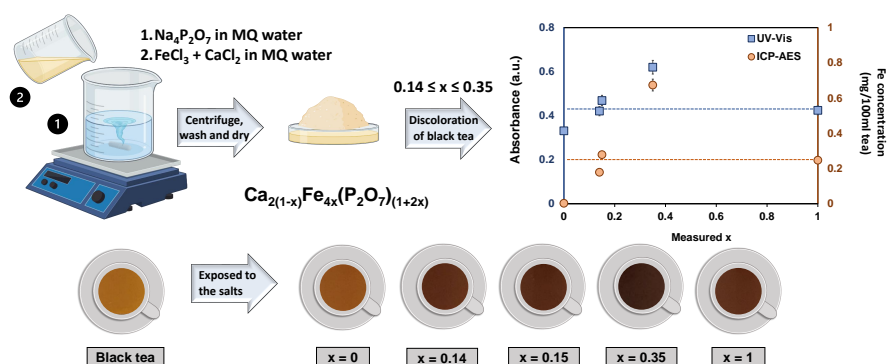
- 52 T. H. Bothwell and A. P. MacPhail, *International Journal for Vitamin and Nutrition Research* **74**, 421 (2004).
- 53 L. Davidsson, P. Kastenmayer, H. Szajewska, R. F. Hurrell, and D. Barclay, *American Journal of Clinical Nutrition* **71**, 1597 (2000).
- 54 L. Rossi, K. P. Velikov, and A. P. Philipse, *Food Chemistry* **151**, 243 (2014).
- 55 T. Tian, E. Blanco, S. K. Smoukov, O. D. Velev, and K. P. Velikov, *Food Chemistry* **208**, 97 (2016).
- 56 Y. M. van Leeuwen, K. P. Velikov, and W. K. Kegel, *RSC Advances* **2**, 2534 (2012).
- 57 M. C. Fidler, T. Walczyk, L. Davidsson, C. Zeder, N. Sakaguchi, L. R. Juneja, and R. F. Hurrell, *British Journal of Nutrition* **91**, 107 (2004).
- 58 V. Dueik, B. Chen, and L. Diosady, *Journal of Food Quality* **2017** (2017).
- 59 R. Hurrell, S. Lynch, T. Bothwell, H. Cori, R. Glahn, E. Hertrampf, Z. Kratky, D. Miller, M. Rodenstein, H. Streekstra, B. Teucher, E. Turner, C. Yeung, and M. Zimmermann, *International Journal for Vitamin and Nutrition Research* **74**, 387 (2004).
- 60 D. Moretti, M. B. Zimmermann, R. Wegmüller, T. Walczyk, C. Zeder, and R. F. Hurrell, *The American Journal of Clinical Nutrition* **83**, 632 (2006).
- 61 K. Shubham, T. Anukiruthika, S. Dutta, A. V. Kashyap, J. A. Moses, and C. Anandharamakrishnan, "Iron deficiency anemia: A comprehensive review on iron absorption, bioavailability and emerging food fortification approaches," (2020).
- 62 K. P. Velikov and E. Pelan, *Soft Matter* **4**, 1964 (2008).
- 63 Y. M. van Leeuwen, K. P. Velikov, and W. K. Kegel, *Food Chemistry* **155**, 161 (2014).
- 64 B. Lafuente, R. T. Downs, H. Yang, and R. A. Jenkins, *Acta Crystallographica Section E: Structure Reports Online* **70**, i16 (2014).
- 65 N. Ravet, Y. Chouinard, J. F. Magnan, S. Besner, M. Gauthier, and M. Armand, in *Journal of Power Sources*, Vol. 97-98 (Elsevier, 2001) pp. 503–507.
- 66 M. Catti, G. Ferraris, and G. Ivaldi, *Bulletin de Minéralogie* **102**, 314 (1979).
- 67 Y. M. van Leeuwen, *Colloidal Metal Pyrophosphates Salts Preparation, Properties and Applications*, Ph.D. thesis (2013).
- 68 J. Monod, J. Wyman, and J. P. Changeux, *Journal of Molecular Biology* **12**, 88 (1965).

Part I

Iron (III)-containing pyrophosphate salts

Mixed Fe(III)-containing pyrophosphate salts: Design and characterization for dual-fortification of foods

Abstract



Iron fortification of food products is challenging due to the interactions arising between iron and food phytochemicals which can result in drastic changes in the organoleptic properties of the food. Consequently, integration of iron in an edible carrier which reduces its reactivity is a promising approach. This study was conducted to design and characterize mixed Ca-Fe(III) pyrophosphate salts with the general formula $\text{Ca}_{2(1-x)}\text{Fe}_{4x}(\text{P}_2\text{O}_7)_{(1+2x)}$ as a potential simultaneous delivery system for iron and calcium. The salts were synthesized via a co-precipitation method and characterized by TEM-EDX, XRD, and FT-IR. All mixed salts with measured $0.14 \leq x \leq 0.35$ yielded homogeneous, amorphous particles. To assess the reactivity of the iron in these salts, the discoloration of a black tea model solution exposed to them was quantified by UV-Vis and ICP-AES. The results indicate that these mixed salts can be potential dual-fortificants with tunable iron content.

This chapter is based on N. Moslehi, J. Bijlsma, W. K. Kegel, and K. P. Velikov, "Iron-fortified food product", WO2022048952A1 (2022).

"If the eye of the heart is open, in each atom
there will be one hundred secrets."

Attar of Nishapur – Persian poet, 1146-1221

2.1 Introduction

As it was mentioned in chapter 1, a commonly used strategy to introduce iron to foods is the use of water-insoluble, or poorly water-soluble salts such as iron (III) pyrophosphate (Fe(III)PP)¹⁻³. In food research, Fe(III)PP receives an extensive amount of attention and it is often used in iron fortification of food products such as infant cereal and chocolate drink powders⁴⁻⁶. The low solubility of iron from Fe(III)PP reduces its impact on the organoleptic properties of the fortified food, but results in low iron bioavailability⁷. Micronization (i.e., downsizing the particle size to micron range, e.g. 0.3 to 0.5 μm) and emulsification techniques have been used to improve the bioavailability of Fe(III)PP. While the process of micronization has the advantage that it does not affect the organoleptic properties of the food, its high cost currently limits its use^{7,8}. Even though solubility of (micronized) Fe(III)PP is limited (in the pH range of 3-6), the addition of Fe(III)PP to phenolic-rich foods or model systems still results in discoloration^{9,10}. Fe(III)PP has also been incorporated with secondary minerals for higher efficiency and multipurpose applications^{11,12}. An example of this is the co-fortification of Fe(III)PP with zinc sulfate in extruded rice¹³. Furthermore, Fe(III)PP has been used in combination with citric acid or trisodium citrate in rice grains¹⁴ and with sodium pyrophosphate in bouillon cubes¹⁵ for relatively higher storage stability.

Inspired by nature, the main goal of the work presented in this chapter is to integrate iron ions in an inorganic poorly water-soluble matrix of another mineral as a carrier. Anastasenkoite ($\text{CaFe}^{\text{II}}\text{P}_2\text{O}_7$)¹⁶ and anapaite ($\text{Ca}_2\text{Fe}^{\text{II}}(\text{PO}_4)_2 \cdot 4\text{H}_2\text{O}$)^{17,18} are examples of naturally occurring but not necessarily edible mixed phosphates of multivalent metal salts^{18,19}. We particularly focus on pyrophosphate salts because pyrophosphate anions form colorless and/or white and water-insoluble compounds with most metals^{2,3,20}. This makes these salts good candidates for food additives and mineral supplements as they prevent introducing any undesired colors into food products. To maintain the organoleptic properties and (chemical) stability of the fortified food vehicle, iron dissolution from the iron-containing compound should ideally be limited in the pH range from 3-7, which is the pH range of most common food and beverages¹⁰. Due to the low water-solubility of both calcium pyrophosphate (CaPP) and Fe(III)PP salts, it is expected that the combination of Ca and Fe(III) in one (pyrophosphate) matrix will still result in low water-solubility. Although any

non-iron divalent metal (e.g. Zn, Ca, Mg, or Mn) could be used, Ca is selected due to its higher recommended nutrient intake and consequently less risk of overdosing compared to the other divalent metals²¹. Besides decreasing the reactivity of iron by embedding it in another less chemically reactive mineral carrier, the main advantage of these systems is that they can be used for simultaneous delivery of another essential mineral along with iron, in this case calcium. In this chapter, we explore the possibility to design mixed Ca-Fe(III) pyrophosphate salts with the general formula, $\text{Ca}_{2(1-x)}\text{Fe}_{4x}(\text{P}_2\text{O}_7)_{(1+2x)}$ ($0 \leq x \leq 1$), as a potential delivery system for two essential minerals. To this end, we develop a detailed synthesis for and perform in-depth characterization of such mixed salts. The range of the ratios of iron to calcium is guided by the Recommended Dietary Allowance (RDA)^{22,23}. Co-precipitation is used as a synthesis method in order to embed iron (III) ions homogeneously into the calcium pyrophosphate matrix. Finally, the designed salts are tested for their reactivity using a black tea model solution. The main aim of this study is to design mixed Ca-Fe(III) pyrophosphate salts with maximum iron content which shows no physical segregation as well as decreased reactivity compared to iron (III) pyrophosphate.

2.2 Materials and methods

2.2.1 Materials

Iron (III) chloride hexahydrate ($\text{FeCl}_3 \cdot 6\text{H}_2\text{O}$, > 99 wt.%), tetrasodium pyrophosphate decahydrate ($\text{Na}_4\text{P}_2\text{O}_7 \cdot 10\text{H}_2\text{O}$, > 99 wt.%), calcium dichloride (CaCl_2 , > 93 wt.%), and nitric acid (HNO_3 , 65 wt.%) were obtained from Sigma Aldrich (St. Louis, MO, USA). Ethanol absolute (≥ 99 wt.%) was obtained from VWR International (Radnor, PA, USA). The Milli-Q (MQ) water used was deionized by a Millipore Synergy water purification system (Merck Millipore, Billerica, MA, USA). The tea used for preparing the tea solutions was an Original English tea blend from Pickwick® (Amsterdam, The Netherlands).

2.2.2 Preparation of pure and mixed metal salts

Pure salts

Pure salts were synthesized as references for comparative purposes. The preparation method was a well-established co-precipitation procedure described elsewhere^{3,20}. Firstly, solutions of 0.857 mmol $\text{FeCl}_3 \cdot 6\text{H}_2\text{O}$ and 1.286 mmol CaCl_2 in 50 ml of MQ water were prepared independently. Following this, the solutions were added quickly (within 5 seconds) to a solution of 0.643 mmol $\text{Na}_4\text{P}_2\text{O}_7 \cdot 10\text{H}_2\text{O}$ (NaPP) in 100 ml of MQ water in order to prepare iron (III) pyrophosphate ($\text{Fe}_4(\text{P}_2\text{O}_7)_3$, Fe(III)PP) and calcium pyrophosphate ($\text{Ca}_2\text{P}_2\text{O}_7$, CaPP), respectively. This was done while the NaPP solution was stirring vigorously (~ 400 rpm) with a magnetic stir bar. In both cases,

a turbid white dispersion was formed a few seconds after the addition. The samples were then centrifuged at $3273 \times g$ for 15 minutes in 50 ml volume polypropylene conical centrifuge tubes using an Allegra X-12R Centrifuge (Beckman Coulter, Brea, CA, USA). This was followed by washing the precipitate with MQ water twice. The sediment was then post-treated by ultrasonication at 40 kHz for 10 minutes using a CPX8800H ultrasonic cleaning bath (Branson UltrasonicsTM, Brookfield, CT, USA), after which they were dried overnight in an oven at 45 °C (Fe(III)PP: 59% and CaPP: 74% yield).

Mixed salts

The mixed Ca-Fe(III) salts were prepared by the same procedure as the pure salts, by addition of 50 ml of a mixed solution of $\text{FeCl}_3 \cdot 6\text{H}_2\text{O}$ and CaCl_2 in MQ water to a solution of NaPP with a fixed concentration of pyrophosphate ions (6.43 mM, 100 ml). Eight salts containing various Ca to Fe(III) ratios were prepared, generally named as $\text{Ca}_{2(1-x)}\text{Fe}_{4x}(\text{P}_2\text{O}_7)_{(1+2x)}$ ($0 \leq x \leq 1$), for different theoretical x-values (i.e., 0.005, 0.006, 0.007, 0.011, 0.021, 0.051, 0.100 and 0.260, coded as Mix1 to Mix8). After adding the mixed solution to NaPP the eight solutions were stirred vigorously (~ 400 rpm) with a magnetic stir bar (final concentration of NaPP: 4.29 mM). In all ratios, a turbid white or off-white dispersion was formed a few seconds after the addition. The samples were then centrifuged, washed, post-treated in an ultrasonic bath, and dried in an oven following the same procedure explained for the pure salts. It is worth recalling here that the x-values in the general formula indicate the mineral composition of the salts. These values were chosen based on the average nutritional requirements for the human body (i.e., 1000 mg calcium and 15 mg iron intake per day²⁴). Consequently, the mole ratios were calculated based on which the x-value was found in the structural formula. The molar ratio of total metal ions (i.e., $[\text{Ca}] + [\text{Fe}]$, final concentration: 8.573 mM) to pyrophosphate ions was based on the stoichiometry of CaPP. The average yield of the prepared mixed salts was $67.3 \pm 4.2\%$. Standard deviation was calculated based on three independent syntheses of all the mixed salts.

2.2.3 Characterization methods

Transmission Electron Microscopy (TEM) and Energy-Dispersive X-ray spectroscopy (EDX)

Water dispersions of the salts were dried on a carbon-coated copper grid and analyzed by transmission electron microscopy (TEM) and energy-dispersive X-ray spectroscopy (EDX). This was performed on a TalosTM F200X (Thermo Fisher Scientific, San Jose, CA, USA) operated at 200 kV. The elemental composition of the mixed salts was obtained from EDX and used for finding the experimental (measured) x-value

based on the general formula of the mixed salts. The ratios of the atomic percentages (i.e., $\text{Ca/Fe} = 2(1-x)/4x$, $\text{Ca/P} = 2(1-x)/2(1+2x)$, and $\text{Fe/P} = 4x/2(1+2x)$) were used to find x in the structural formula $\text{Ca}_{2(1-x)}\text{Fe}_{4x}(\text{P}_2\text{O}_7)_{(1+2x)}$. The average x -value for each mixed salt was reported with a standard deviation based on 3 replicate preparations of the salts and 3 independent measurements. The average x -values were incorporated in the general formula of the mixed Ca-Fe(III) pyrophosphate salts to obtain the final chemical formula of the salts. For salts with heterogeneous morphology, this procedure was done separately on the different morphological phases.

High-Angle Annular Dark Field Scanning TEM (HAADF-STEM)

High-angle annular dark-field scanning TEM (HAADF-STEM) was performed on a TalosTM F200X (Thermo Fisher Scientific, San Jose, CA, USA) operated at 200 kV. The elemental mapping was recorded by assigning a color to each element. Color indications are as follows: calcium: green, iron: red, and phosphorus: blue.

X-Ray Diffraction (XRD)

The dried powders of the salts were analyzed at room temperature with an AXS D2 Phaser powder X-ray diffractometer (Bruker[®], Billerica, MA, USA), which was equipped with a LYNXEYE[®] detector in Bragg-Brentano mode. The radiation used was cobalt $K\alpha_{1,2}$, $\lambda = 1.79026 \text{ \AA}$, operated at 30 kV, 10 mA for $2\theta = 5$ to 70 degrees. A silicon holder was used and the measurements were repeated twice on the salts from independent synthesis batches.

Fourier Transform Infrared (FT-IR) Spectroscopy

FT-IR measurements were done on dried powders of the samples by an FT-IR spectrometer (PerkinElmer, Waltham, MA, USA), using the KBr pellet technique²⁵. 2.5 mg of each salt was mixed thoroughly with 250 mg of KBr (FT-IR grade) and dried in an oven at 60 °C overnight. Pellets were prepared using a press and the measurements were done in independent duplicate. The interferograms were accumulated over the spectral range of 1600 – 400 cm^{-1} using a resolution of 4 cm^{-1} , with a background spectrum recorded before each measurement.

2.2.4 Assessment of the reactivity of selected mixed salts in a black tea solution

To assess the reactivity of the iron in the mixed Ca-Fe(III) pyrophosphate salts, a black tea solution was used as a model system. Ground tea leaves of Original English blend (Pickwick[®]) were added to boiling MQ water (1 g of tea leaves in 100 ml of water). After stirring for 3 minutes, the tea leaves were filtered out using 1541-125 cellulose

filter papers (Whatman[®], Maidstone, UK). Selected mixed and pure Fe(III)PP salts with a normalized concentration of iron (i.e., 1.05 mg Fe in 100 ml tea) were added to the tea solution (pH $\sim 5.13 \pm 0.13$). For comparison, CaPP with a normalized concentration of 2.31 mg Ca in 100 ml tea (i.e., the concentration of Ca in the salt with the highest calcium content) was added as well. After stirring for 10 minutes using an RCT basic stirrer (IKA-Werke, Staufen, Germany), the tea solutions were filtered first over Whatman[®] cellulose filter papers and second over a 17845-ACK Minisart[®] NY polyamide (nylon) filter with 0.2 micron pore size, (Sartorius, Göttingen, Germany). During the procedure, the temperature was kept constant at approximately 90 °C. The residues on the filter papers were washed with ethanol to remove any unbound phenolics. The discoloration of the filtered tea solutions was quantified by ultraviolet-visible light (UV-Vis) spectroscopy at room temperature. UV-Vis spectra of the tea solutions were recorded on a Lambda-35 spectrophotometer (PerkinElmer, Waltham, MA, USA), using quartz cuvettes. The increase in absorbance at 550 nm compared to the blank black tea solution was used to quantify the iron-phenolic complexation¹. All the measurements were done in independent triplicate and the average values along with standard deviations were reported. The colors of the tea solutions were visualized by taking an image of all tea solutions standing next to each other illuminated with a uniform light source at room temperature. The images were evaluated using the online *ImageColorPicker* color conversion tool to the $L^*a^*b^*$ color space (i.e., L^* dark or light, a^* red vs. green, b^* yellow vs. blue) (Table 2.1 of Appendix 2.A). The concentration of the iron released from the salts in the tea solutions was measured by elemental analysis using ICP-AES. ICP-AES was performed on the tea solutions using an Optima 8300 instrument (PerkinElmer, Waltham, MA, USA). The samples were dissolved in 10 ml of a 2% HNO₃ solution to achieve optimal measurement concentration ranges. The measurements were performed in triplicate. Statistical analysis was carried out to evaluate the significance of differences in iron concentration (significant at $p < 0.05$).

2.3 Results and discussion

2.3.1 Characterization of the pure calcium and iron (III) pyrophosphate salts

The morphology of the pure CaPP and Fe(III)PP salts was analyzed by electron microscopy, Figure 2.1. The dried dispersions of CaPP and Fe(III)PP showed noticeably different morphologies. The TEM images for CaPP showed large micron-sized needle-shaped aggregates (Figure 2.1 A), which is in line with a previous study²⁶. However, the TEM image results for Fe(III)PP showed formation of large interconnected aggregates of irregularly shaped particles with an individual size of roughly 25 nm, see Figure 2.1 A.

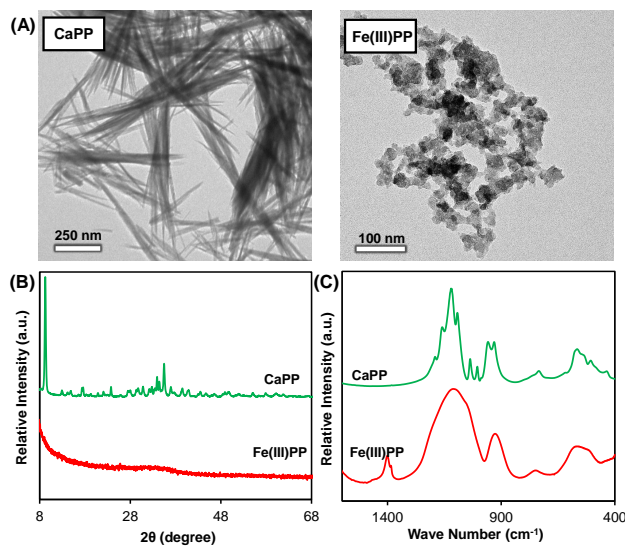


Figure 2.1 Characterization of the pure CaPP and Fe(III)PP salts. (A) TEM images of CaPP and Fe(III)PP, representing the difference between calcium and iron (III) pyrophosphate salts morphologies. CaPP forms large aggregates of micron-sized needles whereas Fe(III)PP yields large interconnected aggregates of irregularly shaped particles with an individual size of roughly 25 nm. (B) Comparison between XRD diffractograms of the two pure pyrophosphate salts shows that CaPP is crystalline, whereas Fe(III)PP is amorphous. (C) For the same reason, the FT-IR absorbance of the chemical bonds in the pyrophosphate ions appears sharp and strong for CaPP, and broad and smooth for Fe(III)PP.

It has been previously shown that the degree of crystallinity in metal pyrophosphate particles can strongly depend on the valence of the metal ion³. This has been confirmed by XRD diffractograms and FT-IR spectra of the pure CaPP and Fe(III)PP salts in this work as well. The X-ray diffraction pattern for CaPP indicated clear signals of crystallinity, while for Fe(III)PP it showed only noise and a broad peak indicating an amorphous structure for this salt (Figure 2.1 B). The XRD diffractograms of CaPP and Fe(III)PP are consistent with previous studies^{3,20}. However, we observed a strong, sharp signal at approximately $2\theta = 9.2$ degree for CaPP (Figure 2.1 B) that was not observed previously^{3,20}. This could be because of different crystalline structures from the fast co-precipitation method compared to the preparation of colloidal particles³ or solid-state preparation at high temperatures²⁷. Moreover, ultrasonication treatment on the salts could have led to induced crystallinity and heterogeneous nucleation²⁸. The observed amorphous structure of Fe(III)PP is suggested to be a result of the so-called valence mismatch of the metal (Fe^{3+}) and pyrophosphate ($\text{P}_2\text{O}_7^{4-}$) ions²⁰. Therefore, the complicated stoichiometry required to reach neutrality results

in an amorphous matrix for Fe(III)PP in a fast co-precipitation process, while calcium and pyrophosphate ions can form electroneutral crystalline unit cells more easily³.

The details of chemical bonding in both the CaPP and Fe(III)PP were investigated by FT-IR spectroscopy (Figure 2.1 C). The FT-IR spectrum for CaPP showed sharp and well-defined bands, whereas the peaks appeared broad and smooth for Fe(III)PP at the same wavenumbers. The sharper and well-defined bands were expected for crystalline materials. Spectral broadening in Fe(III)PP was a result of the pyrophosphates having to accommodate more types of bonding to reach neutrality²⁹, and indicates the amorphous nature of Fe(III)PP^{3,30}. Despite a difference in broadness, peak positions of the main peaks matched with each other because the pyrophosphate groups are the main vibrationally active species. The characteristic peaks attributed to bending of O-P-O bonds in the P_2O_7 groups appeared around 500-600 cm^{-1} . The signals observed at 745 and 945 cm^{-1} were assigned to symmetric and asymmetric vibrations in P-O-P, respectively, and the peaks in the range of 1000 to 1200 cm^{-1} corresponded to P-O stretching vibration frequencies. All the peaks observed for the $P_2O_7^{4-}$ anion are similar to previous reports³⁰⁻³².

2.3.2 Characterization of the mixed Ca-Fe(III) pyrophosphate salts

The morphology and chemical composition of the mixed metal salts, designed with $0.005 \leq x \leq 0.260$ in the general formula $Ca_{2(1-x)}Fe_{4x}(P_2O_7)_{(1+2x)}$, (coded as Mix1-Mix8) were characterized by electron microscopy (Figure 2.2). TEM images of the salt with the lowest iron content, Mix1, indicated a single phase of micron-sized needle-shaped aggregates (Figure 2.2 A). The measured x-value was 0.009, as determined from EDX measurements (Figure 2.2 B).

Detailed analysis of the TEM images and EDX results suggest that integrating Fe(III) as a second metal in the CaPP matrix can yield local segregation and coexistence of two morphological phases: a crystalline needle-shaped phase with relatively low Fe content, and amorphous irregularly shaped aggregates with higher Fe content (i.e., higher x-value). Samples Mix2 to Mix5 appeared to be a mixture of an iron-rich phase (mostly irregularly shaped particles) and a calcium-rich phase (needle-shaped particles) (Figure 2.2 A). EDX quantification indicated that the sample Mix2 is a mixture of micron-sized needles with $x = 0.012$ and irregularly shaped aggregates with $x = 0.455$ (Figure 2.2 B). Similarly, in both samples, Mix3 and Mix4, micron-sized needles and irregularly shaped aggregates were in coexistence, with the latter yielding higher x-values. In the case of the sample Mix5, the measured x-value was equal to 0.020 for the irregularly shaped aggregates, while the ellipse-shaped aggregates remained ill-defined in this salt. These ill-defined particles can be oxide or hydroxide sediments of iron (III) formed during the synthesis or drying procedures (Figure 2.2 A and Figure 2.6 of Appendix 2.A). The formation of the Ca-rich and Fe-rich phases of particles, resulting in different measured x-values (from EDX quantifica-

tion), might be explained by the possibility for phase separation in the resulting solid solutions^{33,34}.

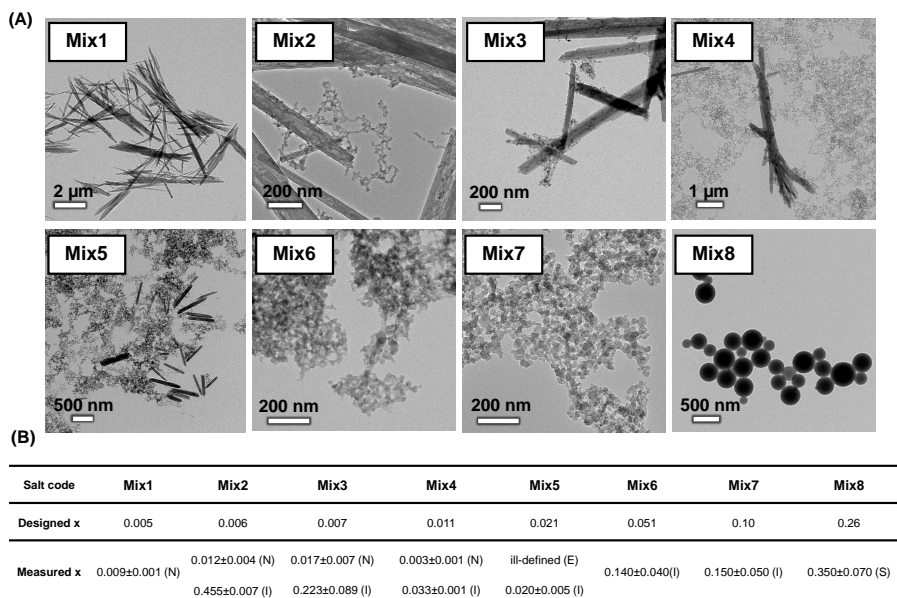


Figure 2.2 Morphology and chemical composition of the mixed Ca-Fe(III) pyrophosphate salts. (A) Morphology of the mixed Ca-Fe(III) pyrophosphate salts, coded as Mix1 to Mix8, obtained from TEM imaging. Comparison indicates that the Fe(III)-containing salts Mix1 and Mix6 to Mix8 are present in identical homogeneous morphologies, whereas the samples Mix2 to Mix5 show segregation into two coexisting structural phases. (B) The measured x-value for the mixed Ca-Fe(III) pyrophosphate salts obtained from EDX quantification. Salts Mix2 to Mix5 show different measured x-values for the coexisting morphologies, while the salts Mix1 and Mix6 to Mix8 have identical x-values. The morphology of the aggregates is indicated by (N) needle-shaped, (I) irregularly shaped, (E) ellipse-shaped, and (S) spherical.

The salts Mix6 to Mix8 showed uniform morphologies and chemical compositions. For Mix6 and Mix7, irregularly shaped aggregates of 50 to 80 nm in size were observed, (Figure 2.2 A). These morphologies were similar to the Fe(III)PP particles morphology and the x-values corresponding to these two salts were measured to be 0.140 and 0.150, respectively (Figure 2.2 B). Interestingly, TEM images of the mixed salt with the highest iron content, Mix8, showed almost perfect spherical particles (Figure 2.2 A), for which the x-value was measured to be 0.350 from EDX quantification (Figure 2.2 B). The formation of well-defined needle-shaped or spherical particles can be caused by the ultrasonication treatment in the preparation method. Ultrasound energy fields have been shown to aid shape changes in particles by lo-

cally overcoming energy barriers for specific structures³⁵ (Figure 2.7 of Appendix 2.A). The possible effects of ultrasonication treatment on the morphology of these particles are currently being studied separately.

The elemental distribution in the mixed Ca-Fe(III) pyrophosphate salts with uniform morphologies (i.e., measured $0.14 \leq x \leq 0.35$) was explored by HAADF-STEM. Homogeneous distribution of the elements Ca, Fe and P was observed by elemental mapping of the mixed salts Mix6 to Mix8 (Figure 2.3 A). The corresponding dark-field scanning TEM images of each elemental mapping are shown in Figure 2.3 B as well.

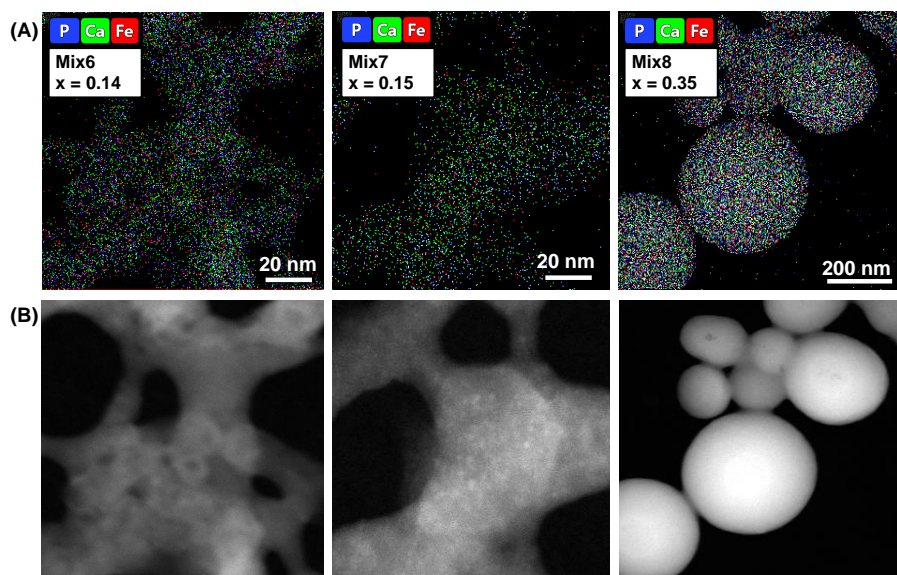


Figure 2.3 Elemental distribution in the selected mixed Ca-Fe(III) pyrophosphate salts. (A) Elemental mapping performed by HAADF-STEM on Mix6 ($x = 0.14$), Mix7 ($x = 0.15$) and Mix8 ($x = 0.35$). Color indications are as follows: calcium (Ca): green; iron (Fe): red; and phosphorous (P): blue. Elemental mapping clearly shows homogeneous distribution of the elements in these salts. (B) The corresponding dark-field images.

The crystallinity of the mixed Ca-Fe(III) pyrophosphate salts was investigated by X-ray powder diffraction analysis (Figure 2.4 A). The XRD diffractograms of the mixed salts were not in agreement with any existing XRD reference patterns in the international center for diffraction data (ICDD, <https://www.icdd.com>). In general, comparing the XRD patterns of the mixed salts to the diffraction peaks of the CaPP specified the gradual transformation of crystalline structures upon increasing iron content in these samples. Similar to the CaPP, the XRD patterns of the mixed Ca-Fe(III) pyrophosphate salts Mix1 to Mix5 (i.e., measured $0 \leq x < 0.14$), show consistent sharp peaks which were clear signs of crystalline structures in these salts³. The intensity of the diffraction peak at 9.2 degree (peak a), which appeared sharp and

strong for CaPP, decreased in the mixed Ca-Fe(III) pyrophosphate salts. Ultimately, this peak disappeared in the salt Mix4.

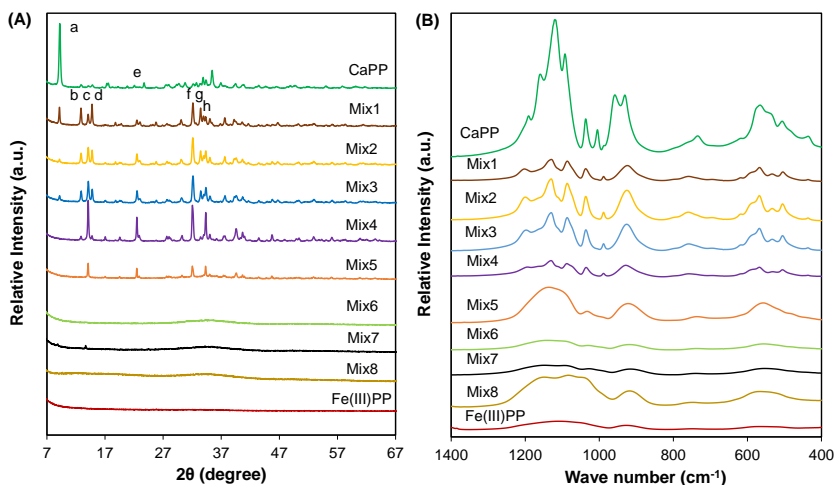


Figure 2.4 Crystallinity and the details of chemical bonds in the mixed Ca-Fe(III) pyrophosphate salts. (A) XRD diffractograms and (B) FT-IR spectra of the mixed Ca-Fe(III) pyrophosphate salts. The XRD diffractograms and FT-IR spectra of the pure CaPP ($x = 0$) and Fe(III)PP ($x = 1$) are shown for comparison. (A) For the salts Mix1-Mix5 and CaPP ($0 \leq x < 0.14$) samples show clear signals for crystalline structure. The diffractograms for the salts Mix6-Mix8 and Fe(III)PP ($0.14 \leq x \leq 1$) exhibit broad smooth peaks which indicate amorphous structures. (B) Positions of the peaks correspond to the chemical bonds in the pyrophosphate ions coincide between the mixed salts. Sharp and strong peaks are observed for the crystalline pyrophosphate salts Mix1-Mix5 and CaPP ($0 \leq x < 0.14$), whereas broad and smooth peaks are obtained for the amorphous salts Mix6-Mix8 and Fe(III)PP ($0.14 \leq x \leq 1$).

The diffraction patterns of the mixed salts in the range of 13-15 degrees (peaks b-d), 22.5 degree (peak e), and 32-34 degrees (peaks f-h) indicate the presence of distinct crystalline phases and polymorphs in their structures. Peaks b, d, and g appeared with maximum intensity in the salt Mix1. A gradual decrease was observed upon increasing iron content in the salts Mix2, Mix3, and Mix4, and eventually the peaks disappeared in the salt Mix5. Furthermore, the reflections c, e, f, and h slightly grew and reached a maximum at Mix4. However, the intensity of these peaks was drastically reduced in the salt Mix5 and reached zero in the samples Mix6-Mix8 ($0.14 \leq x \leq 0.35$).

Finally, the mixed Ca-Fe(III) pyrophosphate salts Mix6 to Mix8 ($0.14 \leq x \leq 0.35$) and Fe(III)PP ($x = 1$) showed no distinct diffraction peaks in their X-ray diffractograms which was a clear indication of an amorphous structure. The one exception to this

was in the sample Mix7 ($x = 0.15$) which showed two weak peaks at 10 and 14 degree. This could be related to ultrasonication-induced crystallization of the pyrophosphate salts^{3,28} which is out of the scope of the present study. Nonetheless, no sign of crystalline needle-shaped aggregates with iron or calcium dominant regions was observed in the TEM images of this sample (Figure 2.2 A).

The details of chemical bonds in the structure of the mixed Ca-Fe(III) pyrophosphate salts were explored by FT-IR spectroscopy (Figure 2.4 B). The analysis of the FT-IR spectra of the mixed salts showed that peak positions coincided between the salts because the vibrations only correspond to the chemical bonds present in the pyrophosphate ions. Pyrophosphate vibrations showed sharp and strong peaks for the crystalline salts with measured $0 \leq x < 0.14$, while the same peaks appeared broad and smooth for amorphous samples with measured $0.14 \leq x \leq 1$. The peak positions coincided with the values observed for pyrophosphate in the individual CaPP and Fe(III)PP salts as discussed in section 2.3.1.

2.3.3 Assessment of the reactivity of selected mixed salts by discoloration of a black tea solution

Black tea was chosen as a model system to investigate the reactivity of the mixed Ca-Fe(III) pyrophosphate salts in foods as, after water, it is the most widely consumed beverage in the world³⁶. Black tea contains a considerable amount of phenolic compounds that can trigger discoloration in the presence of iron ions, via iron-mediated complexation and oxidation³⁷⁻³⁹. According to what was discussed above, the mixed Ca-Fe(III) pyrophosphate salts Mix6-Mix8 are most desirable for the main application of this study as they present uniform morphologies and homogeneous distribution of the elements (i.e., Ca, Fe, P). On the contrary, the samples Mix2-Mix5 with two coexisting phases are not further investigated for their reactivity in a black tea solution. This is because of the presence of multiple structural phases and hence different chemical compositions that can result in unpredictable dissolution or reactivity behaviors of the salts. Furthermore, despite having a homogeneous morphology, the salt Mix1 is not particularly suitable for food application because of the specific shape and size of its aggregate, in addition to having a very low iron content^{3,40}.

The black tea model solution was exposed to the three selected mixed Ca-Fe(III) pyrophosphate salts (i.e., Mix6, Mix7, and Mix8), as well as the pure CaPP and Fe(III)PP salts (final pH of the solutions: 5.13 ± 0.13). The discoloration of the tea solution, caused by iron ions released from the salts after filtration is shown in Figure 2.5 A. Exposing the tea solutions to 1.05 mg Fe in the form of the pure Fe(III)PP and mixed Ca-Fe(III) pyrophosphate salts for 10 minutes, resulted in the darkening of the tea solutions compared to the reference, the pure black tea solution. The visual color comparison between tea solutions showed that surprisingly, the discoloration induced by these salts was a non-monotonic function of their iron content. The salts

Mix6 ($x = 0.14$), Mix7 ($x = 0.15$), and Fe(III)PP ($x = 1$) resulted in visually similar discolorations in the black tea solution. However, exposing the tea solution to Mix8 ($x = 0.35$) increased the discoloration and resulted in the darkest tea solution compared to all other salts.

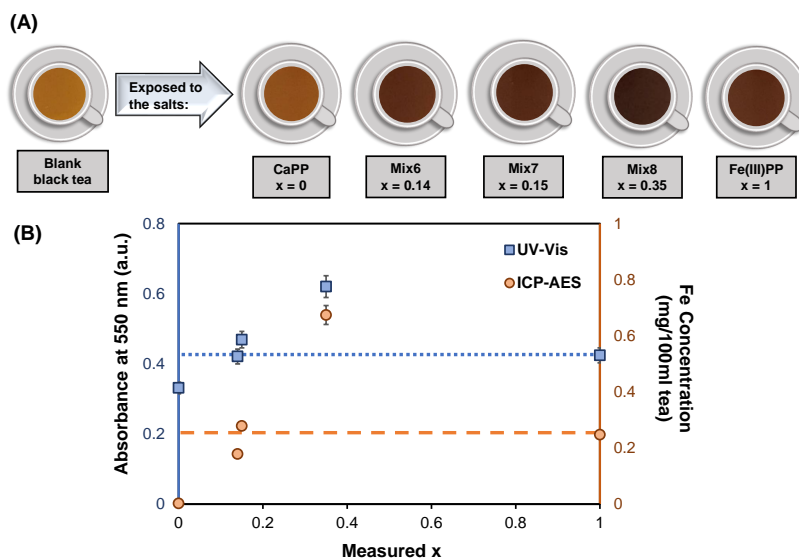


Figure 2.5 The reactivity assessment by exposure to a black tea solution. (A) Images show discoloration of the black tea solution after 10 minutes exposure to the pure salts CaPP ($x = 0$), Fe(III)PP ($x = 1$), and the mixed Ca-Fe(III) pyrophosphate salts with $x = 0.14$, 0.15 , and 0.35 compared to the blank tea solution ($\text{pH} \sim 5.13 \pm 0.13$). **(B)** Increase in absorbance of the tea solutions compared to the blank black tea solution measured at 550 nm by UV-Vis spectroscopy (blue squares, primary y-axis) and concentration of the dissolved Fe in the tea solution is determined by ICP-AES (orange circles, secondary y-axis). The horizontal lines correspond to the absorbance of the tea solution (blue, dotted) and the Fe concentration (orange, dashed) obtained for the tea solution exposed to Fe(III)PP.

The results obtained from the UV-Vis absorbance of the tea solutions are shown in Figure 2.5 B. The UV-Vis absorbance of the tea solutions was consistent with the discoloration (Figure 2.5 A) and showed the same non-monotonic relation between absorbance at 550 nm and iron content of the salts. Using the mixed salt Mix6 ($x = 0.14$) resulted in equal absorbance compared to Fe(III)PP, whereas for the salt Mix7 ($x = 0.15$) a slightly darker color and higher absorbance was observed (Table 2.1 of Appendix 2.A). After being exposed to Mix8 ($x = 0.35$), which had the highest iron content, the darkness of the tea solution increased significantly with an approximately 1.5-fold increase in the UV-Vis absorbance, compared to pure Fe(III)PP ($p <$

0.05). The discoloration induced by CaPP, shown for comparative purposes, caused slight darkening of the tea solution (lightness $L^* = 40$ for CaPP vs. $L^* = 49$ for blank). It was previously reported in the literature that complexation of calcium with phenolics does not lead to a change in color¹⁰. However, the slight discoloration observed in the tea solution in the presence of calcium is suggested to be due to interaction and oxidation of polyphenols with calcium at elevated temperatures, which is also responsible for tea stains on the surface of teacups⁴¹. The concentration of the dissolved iron from the salts in the tea solutions was measured by ICP-AES (Figure 2.5 B). ICP-AES analysis of the pure black tea solution before the addition of any salts showed that it contained on average $2.7 \pm 0.2 \mu\text{g}$ of iron per 100 ml of tea. Results showed that exposure to Fe(III)PP increased the iron concentration in the tea solution to 0.25 mg per 100 ml tea. Exposure to Mix6 ($x = 0.14$) resulted in a 28% lower iron concentration, compared to the Fe(III)PP. In the case of the salt Mix7 ($x = 0.15$), the amount of the iron released was slightly higher (i.e., 12%) than for pure Fe(III)PP. In line with the dissolution of the salts in water at pH ~ 5 (see chapter 3), the dissolved iron from Mix8 was higher compared to Fe(III)PP. In the tea solution tested with the salt Mix8 ($x = 0.35$), the dissolved iron concentration was almost 2.7 fold (0.67 mg per 100 ml tea) higher than in the tea exposed to Fe(III)PP. Consequently, exposure to Mix8 ($x = 0.35$) resulted in significantly higher discoloration compared to the other samples ($p < 0.05$). Despite the observed discoloration of tea upon exposure to the salts, the highest measured iron concentration was only 64% of the total amount of iron added. This indicates that a considerable amount of iron was retained in the salt matrix.

Interestingly, discoloration was also observed on the surface of the insoluble proportion of the salts that was recollected as a residue upon filtration of the black tea solutions (Figure 2.8 of Appendix 2.A). All salt powders were either white or off-white before performing the reactivity experiment. The color of the residues of all iron-containing pyrophosphate salts changed to dark brown or black after being in contact with the tea solution, whereas the residue of CaPP remained white. We suggest that the iron-containing salts show darkening due to the complexation of the iron ions on the surface of the salts with the phenolics present in the black tea solution.

Although the main intention of the performed black tea experiment in this work was not to fortify tea, we used the black tea solution as a representative example to investigate the reactivity of iron from the designed mixed salts with phenolic compounds (catechins), to show the novel salts' potential for food fortification. The mixed salts did not show noticeably less reactivity in black tea solution, compared to Fe(III)PP. However, in the next chapters, the dissolution behavior of iron from the Fe(III)-containing pyrophosphate salts in water, their reactivity, and surface interactions in the presence of phenolic compounds is further explored in model sys-

tems of selected pure phenolic compounds to get more insight into the mechanism for phenolic-mediated discoloration by complexation and oxidation, and stability of these mixed salts in foods and during storage.

2.4 Conclusions

In the present study, we report the design, synthesis, and characterization of the pure as well as the mixed calcium and iron (III) pyrophosphate salts with the general formula $\text{Ca}_{2(1-x)}\text{Fe}_{4x}(\text{P}_2\text{O}_7)_{(1+2x)}$ ($0 \leq x \leq 1$). Mixed salts with $0.14 \leq x \leq 0.35$ were amorphous and uniform in terms of their morphology. Assessment of the reactivity of the selected mixed Ca-Fe(III) pyrophosphate salts in a black tea solution showed that the concentration of the dissolved iron ions released from the salts was a non-monotonic function of the x-values and that none of the salts could reduce the development of discoloration, compared to Fe(III)PP. The present findings indicate that the mixed Ca-Fe(III) pyrophosphate salts with experimental $0.14 \leq x \leq 0.35$ can be potential food dual-fortificants with tunable iron composition. In future works, safety assessment of the designed mixed salts, their impact on sensorial attributes of foods, and bioavailability of the constituent iron should be further explored.

2.5 Acknowledgments

Hans Meeldijk from Materials Chemistry and Catalysis group of Utrecht University, is thanked for his help with the TEM-EDX and HAADF-STEM measurements. Coen Mulder from Geo-Science group of Utrecht University is thanked for ICP-AES measurements. K. P. V. acknowledges the stimulating discussion with Roumen Tsekov. The graphical abstract was made with content from BioRender.com.

2.A Appendix

Table 2.1 The details of color conversion of the black tea solutions obtained by an online color measurement tool. After exposing the tea solution to the pure CaPP and Fe(III)PP, and the selected mixed Ca-Fe(III) pyrophosphate salts, an image including all the solutions was taken while they were illuminated with a uniform light source. The image was then used to extract the colors. Using the mixed salt Mix6 ($x = 0.14$) results in equal darkness compared to Fe(III)PP (i.e., $L^* = 25$), whereas for the salt Mix7 ($x = 0.15$) a slightly darker color is observed (i.e., $L^* = 22$). Interestingly, exposing the tea solution to Mix8 ($x = 0.35$) increases the discoloration and results in the darkest tea solution compared to all other salts.

Color Conversion	Black tea	CaPP $x = 0$	Mix6 $x = 0.14$	Mix7 $x = 0.15$	Mix8 $x = 0.35$	Fe(III)PP $x = 1$
Shade						
NAME	Desert	Rope	Espresso	Brown Derby	Cedar	Espresso
HEX	#a5661c	#8f4d1b	#5d2e19	#542a17	#3d2217	#5c2f1b
$L^*a^*b^*$	49, 20, 49	40, 24, 40	25, 19, 23	22, 18, 21	16, 12, 13	25, 19, 22

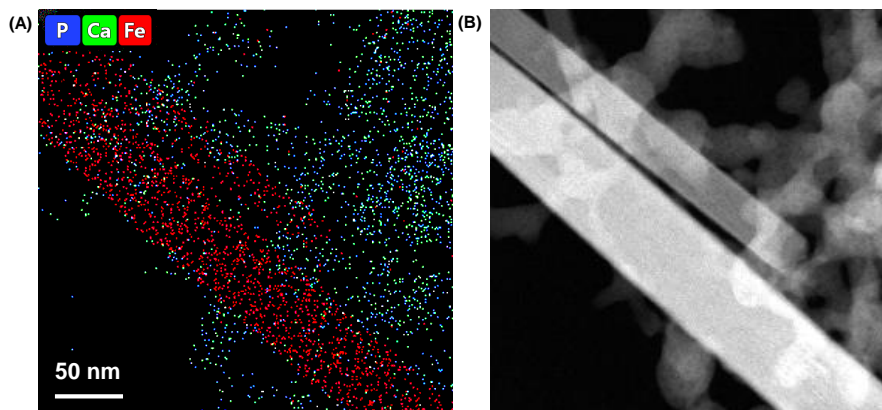


Figure 2.6 An example of heterogeneous elemental distribution in the mixed Ca-Fe(III) pyrophosphate salts. (A) Heterogeneous distribution of iron and calcium in the salt Mix5 obtained by elemental mapping using HAADF-STEM. Color indications are as follows: calcium (Ca): green; iron (Fe): red; and phosphorous (P): blue. The chemical composition of the needle-shaped particles in the salt Mix5 remains ill-defined (atomic percentages: O: 43.00%, P: 0.98%, Ca: 2.36%, Fe: 53.64%). (B) The corresponding-dark-field images.

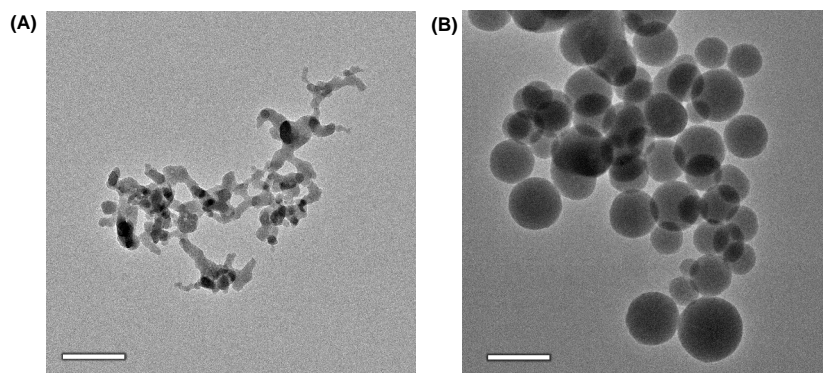


Figure 2.7 Ultrasonication-induced shape shifting. The mixed Ca-Fe(III) pyrophosphate salt Mix8 ($x = 0.35$), (A) before ultrasonication treatment and (B) after ultrasonication 10 minutes. The scale bar represents 200 nm. TEM images indicate the effect of ultrasonication treatment on the shape and size of the precipitates.

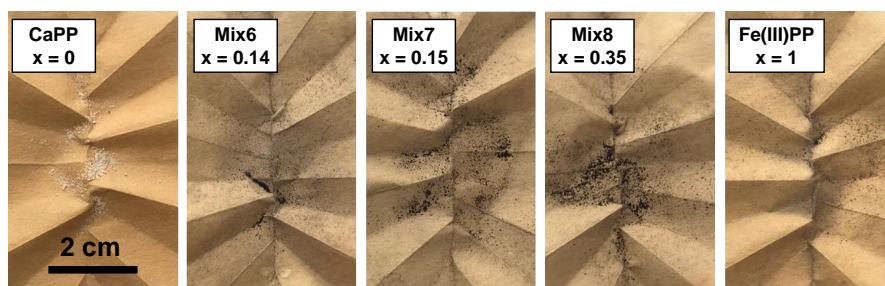


Figure 2.8 Discoloration of the surface of the insoluble proportion of the salts after exposure to a black tea solution. Images of residue of the black tea solution after being exposed to CaPP ($x = 0$), Fe(III)PP ($x = 1$), and the mixed Ca-Fe(III) pyrophosphate salts Mix6 ($x = 0.14$), Mix7 ($x = 0.15$), and Mix8 ($x = 0.35$) on filter papers (background). All filtrates were washed with ethanol and then dried. The CaPP powder remained white. Darkening at the surface of the iron-containing salts is observed after being exposed to the tea solution.

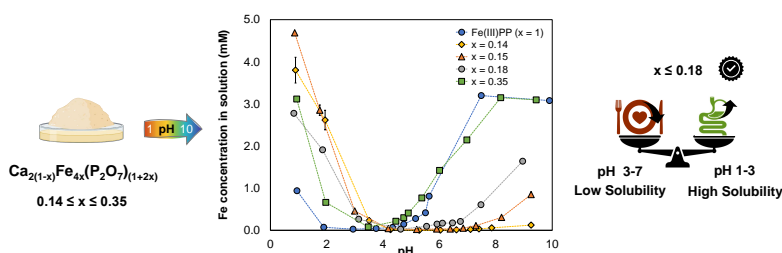
References

- 1 E. J. T. McGee and L. L. Diosady, *Food Analytical Methods* **11**, 1645 (2018).
- 2 T. Tian, E. Blanco, S. K. Smoukov, O. D. Velev, and K. P. Velikov, *Food Chemistry* **208**, 97 (2016).
- 3 Y. M. van Leeuwen, K. P. Velikov, and W. K. Kegel, *RSC Advances* **2**, 2534 (2012).
- 4 R. J. Baars, Y. M. van Leeuwen, Y. Hendrix, K. P. Velikov, W. K. Kegel, and A. P. Philipse, *Colloids and Surfaces A: Physicochemical and Engineering Aspects* **483**, 209 (2015).
- 5 M. J. Salgueiro and J. Boccio, in *Handbook of Food Fortification and Health: From Concepts to Public Health Applications*, Vol. 1 (Springer New York, 2013) pp. 91–97.
- 6 B. Y. Srinivasu, G. Mitra, M. Muralidharan, D. Srivastava, J. Pinto, P. Thankachan, S. Suresh, A. Shet, S. Rao, G. Ravikumar, T. S. Thomas, A. V. Kurpad, and A. K. Mandal, *RSC Advances* **5**, 61678 (2015).
- 7 D. Moretti, M. B. Zimmermann, R. Wegmüller, T. Walczyk, C. Zeder, and R. F. Hurrell, *The American Journal of Clinical Nutrition* **83**, 632 (2006).
- 8 K. Shubham, T. Anukiruthika, S. Dutta, A. V. Kashyap, J. A. Moses, and C. Anandharamakrishnan, “Iron deficiency anemia: A comprehensive review on iron absorption, bioavailability and emerging food fortification approaches,” (2020).
- 9 J. Bijlsma, W. J. de Bruijn, J. A. Hageman, P. Goos, K. P. Velikov, and J. P. Vincken, *Scientific Reports* **10**, 1 (2020).
- 10 E. Habeych, V. van Kogelenberg, L. Sagalowicz, M. Michel, and N. Galaffu, *Food Research International* **88**, 122 (2016).
- 11 Y. M. van Leeuwen, K. P. Velikov, and W. K. Kegel, *Food Chemistry* **155**, 161 (2014).
- 12 M. B. Zimmermann and F. M. Hilty, *Nanoscale* **3**, 2390 (2011).
- 13 L. Hackl, M. B. Zimmermann, C. Zeder, M. Parker, P. W. Johns, R. F. Hurrell, and D. Moretti, *The Journal of Nutrition* **147**, jn241778 (2017).
- 14 A. Gupta, R. Pratt, and B. Mishra, *BioMetals* **31**, 1091 (2018).
- 15 C. I. Cercamondi, G. S. Duchateau, R. K. Harika, R. Van Den Berg, P. Murray, W. P. Koppenol, C. Zeder, M. B. Zimmermann, and D. Moretti, *British Journal of Nutrition* **116**, 496 (2016).
- 16 R. Miyawaki, F. Hatert, M. Pasero, and S. J. Mills, *European Journal of Mineralogy* **32**, 443 (2020).
- 17 M. Catti, G. Ferraris, and G. Ivaldi, *Bulletin de Minéralogie* **102**, 314 (1979).
- 18 B. Lafuente, R. T. Downs, H. Yang, and R. A. Jenkins, *Acta Crystallographica Section E: Structure Reports Online* **70**, i16 (2014).
- 19 N. Ravet, Y. Chouinard, J. F. Magnan, S. Besner, M. Gauthier, and M. Armand, in *Journal of Power Sources*, Vol. 97-98 (Elsevier, 2001) pp. 503–507.
- 20 L. Rossi, K. P. Velikov, and A. P. Philipse, *Food Chemistry* **151**, 243 (2014).
- 21 L. Allen, B. de Benoist, O. Dary, and R. Hurrell, *World Health Organization*, 341 (2006).
- 22 S. B. Kumar, S. R. Arnipalli, P. Mehta, S. Carrau, and O. Ziouzenkova, *Nutrients* **2022**, Vol. 14, Page 2976 **14**, 2976 (2022).

- 23 E. Piskin, D. Cianciosi, S. Gulec, M. Tomas, and E. Capanoglu, *ACS Omega* **7**, 20441 (2022).
- 24 A. C. Ross, C. L. Taylor, A. L. Yaktine, and H. B. Del Valle, eds., *Dietary Reference Intakes for Calcium and Vitamin D* (National Academies Press, 2011).
- 25 N. L. Drenchev, K. K. Chakarova, O. V. Lagunov, M. Y. Mihaylov, E. Z. Ivanova, I. Strauss, and K. I. Hadjiivanov, *JoVE (Journal of Visualized Experiments)* **2020**, e60285 (2020).
- 26 P. Gras, C. Rey, O. Marsan, S. Sarda, and C. Combes, *European Journal of Inorganic Chemistry* **2013**, 5886 (2013).
- 27 A. M. El Kady, K. R. Mohamed, and G. T. El-Bassyouni, *Ceramics International* **35**, 2933 (2009).
- 28 M. D. Luque de Castro and F. Priego-Capote, *Ultrasonics Sonochemistry* **14**, 717 (2007).
- 29 Y. Lai, X. Liang, G. Yin, S. Yang, J. Wang, H. Zhu, and H. Yu, *Journal of Molecular Structure* **1004**, 188 (2011).
- 30 R. K. Singh, M. Srivastava, N. K. Prasad, S. Awasthi, A. Dhayalan, and S. Kannan, *Materials Science and Engineering C* **78**, 715 (2017).
- 31 N. V. Kosova, D. O. Rezepova, O. A. Podgornova, A. B. Slobodyuk, S. A. Petrov, and M. Avdeev, *Electrochimica Acta* **235**, 42 (2017).
- 32 J. C. Zheng, X. Ou, B. Zhang, C. Shen, J. F. Zhang, L. Ming, and Y. D. Han, *Journal of Power Sources* **268**, 96 (2014).
- 33 Y. Li, *Solid State Ionics* **323**, 142 (2018).
- 34 H. J. Tan, J. L. Dodd, and B. Fultz, *Journal of Physical Chemistry C* **113**, 20527 (2009).
- 35 K. S. Suslick, M. Fang, and T. Hyeon, *Journal of the American Chemical Society* **118**, 11960 (1996).
- 36 V. Dueik, B. Chen, and L. Diosady, *Journal of Food Quality* **2017** (2017).
- 37 J. Bijlsma, W. J. de Bruijn, K. P. Velikov, and J. P. Vincken, *Food Chemistry* **370**, 131292 (2022).
- 38 E. J. T. McGee and L. L. Diosady, *LWT - Food Science and Technology* **89**, 756 (2018).
- 39 Z. Wang, C. Fang, and M. Mallavarapu, *Environmental Technology and Innovation* **4**, 92 (2015).
- 40 N. M. Marian, G. Giorgetti, C. Magrini, G. C. Capitani, L. Galimberti, A. Cavallo, R. Salvini, C. Vanneschi, and C. Viti, *Journal of Hazardous Materials* **413**, 125419 (2021).
- 41 K. Yamada, T. Abe, and Y. Tanizawa, *Food Chemistry* **103**, 8 (2007).

Mixed Fe(III)-containing pyrophosphate salts: pH-dependent dissolution behavior

Abstract



Using poorly water-soluble mineral-containing compounds for fortification of foods is a common approach to deliver iron while maintaining the organoleptic properties and chemical stability of the food. The challenge in designing these systems is achieving pH-dependent dissolution behavior of the iron compound. To limit iron-mediated reactions while ensuring bio-accessibility, the iron dissolution should be limited at food pH (3-7) and fast at gastric pH (1-3) and/or intestinal pH (6-8). In the present study, we investigated the pH-dependent dissolution profile of iron from iron (III) pyrophosphate (Fe(III)PP) and four mixed Ca-Fe(III) pyrophosphate salts with the general formula $\text{Ca}_{2(1-x)}\text{Fe}_{4x}(\text{P}_2\text{O}_7)_{(1+2x)}$ with different x -values: 0.14, 0.15, 0.18, and 0.35. The soluble iron concentration from these mixed salts showed a four-fold increase at gastric pH compared to Fe(III)PP. In the food-relevant pH range, the salts with $x \leq 0.18$ showed up to an eight-fold decrease in soluble iron concentration. Our results indicate that mixed Ca-Fe(III) pyrophosphate salts are potential dual-mineral food fortificants with tunable pH-dependent dissolution that enable formulation of stable iron-fortified foods.

This chapter is based on N. Moslehi, J. Bijlsma, W. J.C. de Bruijn, K. P. Velikov, J-P. Vincken, and W. K. Kegel, "Design and characterization of Ca-Fe(III) pyrophosphate salts with tunable pH-dependent solubility for dual-fortification of foods", *Journal of Functional Foods* 92 (2022): 105066.

"What you seek is seeking you."

Rumi – Persian poet, 1207-1273

3.1 Introduction

As discussed in chapter 2, the organoleptic properties of the food and bio-availability of the micronutrients should be carefully balanced for successful food fortification^{1,2}. In order to maintain the organoleptic properties of the iron-fortified food, iron dissolution from the iron-containing compound should be limited in the food pH range 3-7³. Insolubility of the iron ions in the pH range of 3-7 will suppress iron-mediated reactivity in the food⁴. Additionally, to ensure bio-accessibility of iron, dissolution of iron from the iron-containing compound should be fast in gastric (i.e., pH 1-3) and/or intestinal (i.e., pH 6-8) conditions⁵⁻⁷. It should be noted that although bio-accessibility (i.e., the quantity of iron in solution and available for absorption in the gastrointestinal tract) is a prerequisite for bio-availability, it cannot directly be correlated to iron bio-availability, which also includes digestion, absorption, and metabolism⁷.

Fe(III)PP salt has low solubility (< 5%) at pH 3 with increased solubility to > 99% at pH 7-8⁸, whereas the pyrophosphate salts of divalent metals, such as calcium pyrophosphate (CaPP), dissolve well (> 99%) at pH 3 but are poorly soluble (< 5%) at pH 7-8⁹. Doping of iron (III) oxide with calcium has previously shown improved iron solubility in dilute acid and sensory characteristics in fortified foods^{10,11}. Due to the reversed solubility character of CaPP and Fe(III)PP salts, it is expected that the combination of Ca and Fe(III) in one matrix will result in a unique pH-dependent dissolution behavior. Furthermore, to use the Ca-Fe(III) pyrophosphate salts in fortified food products the pH-dependent dissolution behavior at pH 3-7 must be limited during storage (23 °C), consumption (37 °C), and cooking (90 °C). A previous study showed that the stability constants of Fe(III)PP complexes did not change upon an increase in temperature from 23 to 50 °C¹². However, thermodynamic modeling of the solubility of Fe(III) phosphate salts showed that the dissolution was enhanced upon heating from 0 to 35 °C at pH > 6 and that this dissolution behavior could be extrapolated to Fe(III) pyrophosphate¹³. Overall, no comprehensive information is available regarding the effect of elevated temperature on the pH-dependent dissolution of Fe(III) from pyrophosphate salts. We performed this study to investigate the pH and temperature dependence of the dissolution behavior of Ca-Fe(III) pyrophosphate salts with $x = 0.14, 0.15, 0.18, \text{ and } 0.35$ in the general formula $\text{Ca}_{2(1-x)}\text{Fe}_{4x}(\text{P}_2\text{O}_7)_{(1+2x)}$, to explore their potential as food fortificants. The pH dependence of the dissolution profile of the mixed Ca-Fe(III) pyrophosphate salts with various Ca:Fe(III) ratios are

explored and the effect of three food-relevant temperatures (23, 37, and 90 °C), as well as the dissolution time, are investigated. We hypothesize that incorporation of calcium and iron in a pyrophosphate salt matrix will improve the soluble iron from the salts at low pH (1-3), while it will decrease dissolved iron concentration at moderate pH (3-7) and high pH (7-10) compared to pure Fe(III)PP, and that the ratio of Ca:Fe(III) is an important determinant for the dissolution behavior of Fe(III) from the mixed Ca-Fe(III)pyrophosphate salts.

3.2 Materials and methods

3.2.1 Materials

Hydrochloric acid (37 wt.%), sodium hydroxide (≥ 98 wt.%), nitric acid (65 wt.%), iron (II) sulfate heptahydrate (≥ 99 wt.%), and 3-(2-pyridyl)-5,6-diphenyl-1,2,4-triazine-*p,p'*-disulfonic acid monosodium salt hydrate (i.e., ferrozine; ≥ 97 wt.%) were obtained from Sigma Aldrich (St. Louis, MO, USA). Ascorbic acid (≥ 99 wt.%) was obtained from VWR International (Radnor, PA, USA). All water used was prepared using a Milli-Q water purification system (Merck Millipore, Billerica, MA, USA).

3.2.2 Dissolution behavior of iron from Fe(III)PP and mixed Ca-Fe(III) pyrophosphate salts

To perform the iron dissolution measurements, the synthesis of the pure Fe(III)PP and CaPP as well as the mixed Ca-Fe(III) pyrophosphate salts with measured $x = 0.14, 0.15, 0.18, \text{ and } 0.35$ were up-scaled, see section 3.A.1 of Appendix 3.A. The dried powders of the salts were then re-dispersed by stirring (~ 250 rpm) with a magnetic stir bar in MQ water (final concentrations: 10 mg/ml). Next, the pH of the dispersions was adjusted using a pH-stat device (Metrohm, Herisau, Switzerland) by the addition of 0.1 M HCl or 0.1 M NaOH. Subsequently, all dispersions were incubated at 1000 rpm using an Eppendorf Thermomixer[®] F1.5 (Eppendorf, Hamburg, Germany) at pH values ranging from 1 to 11 (steps of one pH unit), over time (1, 2, and 48 h), and at three different temperatures (23, 37, and 90 °C). After incubation, the pH of each sample was measured again to determine the final pH. Finally, the samples were centrifuged at $15000 \times g$ for 10 min using an Eppendorf Centrifuge 5415R and the supernatants were separated to quantify the dissolved iron concentration.

Iron concentration measurement by ferrozine-based colorimetric assay

Total iron in solution was quantified using a ferrozine-based colorimetric assay¹⁴. Binding of Fe(II) to 3-(2-pyridyl)-5,6-diphenyl-1,2,4-triazine-*p,p'*-disulfonic acid (i.e., ferrozine) results in the formation of a complex with absorbance at 565 nm¹⁵. To ensure the reduction of Fe(III) to Fe(II), first an excess of ascorbic acid (50 μl , 100

mM) was added to 50 μl sample (supernatant). After 30 min incubation of the sample with ascorbic acid, ferrozine (50 μl , 10 mM) was added. Samples were transferred to 96-well microplates and the absorbance at 565 nm was measured at room temperature in a SpectraMax M2e (Molecular Devices, Sunnyvale, CA, USA). All measurements were performed in duplicate and quantification of total dissolved iron was performed based on intensity (absorbance at 565 nm) with a calibration curve of FeSO_4 (0.0078–1 mM, $R^2 > 0.99$). It was confirmed that the presence of the Ca ion did not interfere with the quantification of total iron (Figure 3.4 of Appendix 3.A). The pH of the samples was measured after the addition of ascorbic acid and ferrozine. Most samples had a pH of 2.7, except for the samples that were prepared at very acidic conditions (i.e., $\text{pH} < 2$). The pH of these samples after the addition of ascorbic acid and ferrozine was 1.7 ± 0.3 . At this pH, less Fe(II)-ferrozine complex is formed¹⁴. We corrected the absorbance of these acidic samples using the pH-dependent absorbance factors previously reported for the Fe(II)-ferrozine complex formation¹⁴. To test if the trend in iron dissolution was statistically significant, statistical analysis was carried out (significant at $p < 0.05$).

3.2.3 Inductively coupled plasma – atomic emission spectroscopy (ICP-AES)

Inductively coupled plasma–atomic emission spectroscopy (ICP-AES) was used for independent verification of the iron quantification by the ferrozine assay. For ICP-AES measurements, powders of pure Fe(III)PP and CaPP, as well as mixed Ca-Fe(III) pyrophosphate salts were dispersed in water to obtain final concentrations of 10 mg/ml. pH was set to reach a target pH 3, 6, or 8 after 2 hours of incubation at 23 °C while mixing at 1000 rpm using an Eppendorf Thermomixer[®] F1.5. Samples were five times diluted in 0.14 M HNO_3 , before injection in the ICP-AES system (Agilent 5110 VDV; Agilent Technologies, Tokyo, Japan). Independent duplicate samples were taken from the salt at each pH point by independent titrations. The concentration of iron, calcium, and phosphorus was determined using scandium as an internal standard. The limit of detection (LOD) values of iron, calcium, and phosphorus were respectively 0.05, 0.05, and 0.20 mg/l, the limit of quantification (LOQ) values were 0.15, 0.15, and 0.61 mg/l, respectively.

3.3 Results and discussion

3.3.1 Dissolution behavior of iron from Fe(III)PP and mixed Ca-Fe(III) pyrophosphate salts

As it was mentioned before, to limit iron-mediated reactions, while ensuring bio-accessibility, the iron dissolution should be limited at food pH (3–7) and fast at gastric pH (1–3) and/or intestinal pH (6–8). Therefore, we investigated the pH-dependent dissolution behavior of iron from Fe(III)PP and mixed Ca-Fe(III) pyrophosphate salts. The four mixed as well as pure pyrophosphate salts were prepared using the up-scaled synthesis method, see section 3.A.1 of Appendix 3.A. Up-scaling the synthesis did not affect the morphology or the elemental homogeneity in the salts (Figure 3.5 of Appendix 3.A). All salts with $0.14 \leq x \leq 0.35$ yielded homogeneous distribution of the elements (i.e., Ca, Fe, and P) in the salts matrices and uniformity in morphology and amorphous nature, as previously confirmed by TEM-EDX, HAADF-STEM, XRD, and FT-IR (see chapter 2). The dissolution behavior of iron from Fe(III)PP and mixed Ca-Fe(III) pyrophosphate salts was evaluated as a function of pH by UV-Vis spectroscopy using the ferrozine assay¹⁴. Quantification of the accuracy of total iron determination by the ferrozine assay was verified by comparison with the ICP-AES method (Figure 3.6 of Appendix 3.A). The iron concentrations measured by both methods were found to be in good agreement ($R^2 = 0.99$). Due to the affordability, availability, and high throughput of the ferrozine assay it was decided to use the ferrozine assay for further experiments. The aqueous dissolution behavior of iron from Fe(III)PP and the four mixed Ca-Fe(III) pyrophosphate salts was evaluated in the pH range from 1–10, Figure 3.1.

In the pH range 2–5.5, the soluble iron concentration from Fe(III)PP was below 0.50 mM, Figure 3.1 A. The limited solubility in this pH range is likely due to the presence of the solid species of $\text{Fe}_4(\text{P}_2\text{O}_7)_3$ ^{8,16}. Below pH 2, soluble iron concentration from Fe(III)PP increased to 1 mM due to the presence of ionic Fe(III) and the formation of soluble ferric pyrophosphate complexes (i.e., $\text{FeH}_3\text{P}_2\text{O}_7^{2+}$ and $\text{FeH}_2\text{P}_2\text{O}_7^+$)^{16,17}. Increased dissolution of iron from Fe(III)PP to 3.0 mM at pH > 5.5 could be explained by the formation of $\text{Fe}(\text{HP}_2\text{O}_7)_2^{3-}$, which is one of the soluble Fe(III)-pyrophosphate species^{16,18}. For three mixed salts with $x = 0.14, 0.15$, and 0.18 , lower dissolved iron concentration (< 0.25 mM) was observed at the food-relevant pH values (i.e., pH 3–7). This indicated that the ternary complex of $\text{Ca}_{2(1-x)}\text{Fe}_{4x}(\text{P}_2\text{O}_7)_{(1+2x)}$ with $x = 0.14, 0.15$, and 0.18 shows lower soluble iron concentration at pH 3–7, compared to Fe(III)PP. The lower amounts of dissolved iron at pH 3–7 for the mixed salts are desirable for application in food, as it could potentially lead to reduced iron-mediated reactivity of the food products upon iron fortification. For the salt with $x = 0.35$ similar or even higher dissolution of iron was observed in the food-relevant pH range, compared to

Fe(III)PP. These results indicate that in the mixed Ca-Fe(III) pyrophosphate salts the x-value should be ≤ 0.18 to reduce the iron dissolution at pH 3-7.

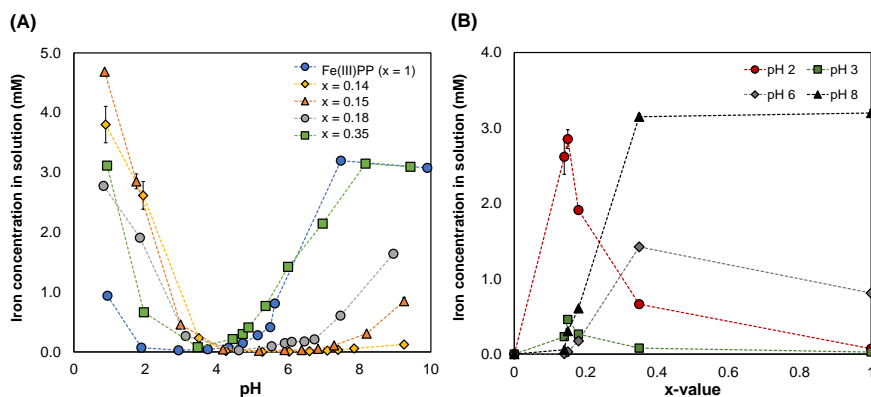


Figure 3.1 Dissolution behavior of iron from Fe(III)PP and the mixed Ca-Fe(III) pyrophosphate salts. **(A)** Concentration of soluble iron from Fe(III)PP and the mixed Ca-Fe(III) pyrophosphate salts with $x = 0.14, 0.15, 0.18$, and 0.35 as a function of pH. Compared to Fe(III)PP, the mixed salts with $x = 0.14, 0.15$, and 0.18 have a lower soluble iron concentration at food-relevant pH (3–7), whereas at gastric pH (1–3), the salts show enhanced iron dissolution up to a fourfold increase. **(B)** Dissolution behavior of iron from the salts as a function of x-value at pH 2, pH 3, pH 6, and pH 8. Lower x-values (i.e., ≤ 0.18) have higher iron dissolution at low pH (i.e., 2 and 3). However, the salts with higher x-values (i.e., 0.35 and 1) yielded the highest iron concentrations in solution at high pH (i.e., 6 and 8).

Interestingly, as the calcium content in the mixed salts increased, the salts showed enhanced dissolution of iron in the gastric pH range (1–3). For the mixed salt with $x = 0.14, 0.15$, and 0.18 an increase in the dissolved iron of at least a fourfold, compared to Fe(III)PP, was observed at pH 1. Higher quantities of total soluble iron at pH 1–3 and/or pH 6–9 are indicative of better bio-accessibility in the gastric and intestinal environment, respectively^{5–8,19}. At pH > 6, the opposite behavior was observed compared to acidic pH, with the highest dissolved iron concentration for Fe(III)PP and mixed salt with $x = 0.35$, and lowest for the salt with $x = 0.14$. Even though the dissolution of iron from the salts with $x = 0.14, 0.15$, and 0.18 was decreased compared to Fe(III)PP at intestinal pH, the poor iron solubility of these salts at pH 3–7 and increased dissolution at pH 1–3 (Figure 3.1) indicates that these salts likely cause less organoleptic changes in food and are expected to show adequate bio-accessibility in the stomach^{5,19}. It has previously been shown that *in vitro* solubility of Fe-containing salts at pH 1 is a good indicator for *in vivo* Fe uptake by rats⁶. Overall, these results indicate that increasing the proportion of calcium in the mixed Ca-Fe(III) pyrophosphate salts promotes the dissolution at low pH (1–3), whereas increasing the proportion of iron promotes dissolution at high pH (6–9). This is in line with previous results obtained

for pure pyrophosphate salts, in which pure CaPP and Fe(III)PP salts showed inverse pH-dependent solubility⁹. The dissolution behavior of iron from Fe(III)PP and the mixed Ca-Fe(III) pyrophosphate salts was evaluated as a function of the x-value in $\text{Ca}_{2(1-x)}\text{Fe}_{4x}(\text{P}_2\text{O}_7)_{(1+2x)}$. Figure 3.1 B shows the dissolution of iron from the salts as a function of x-value at four representative pH values (i.e., pH 2 for gastric conditions, pH 3 and 6 for food, and pH 8 for intestinal conditions). Lower x-values (i.e., ≤ 0.18) tend to have higher iron dissolution at low pH (i.e., 2 and 3). Furthermore, the salts with higher x-values (i.e., 0.35 and 1) yielded the highest iron concentrations in solution at high pH (i.e., 6 and 8). These findings show that the mixed Ca-Fe(III) pyrophosphate salts possess pH-dependent dissolution behavior which can be fine-tuned to the desired application by changing the x-value.

To get more insight into the dissolution of the pure and the mixed Ca-Fe(III) pyrophosphate salts the concentration of the three elements Ca, Fe, and P was determined in aqueous solution at the most relevant pH values (i.e., 3, 6, and 8) by ICP-AES, Figure 3.2.

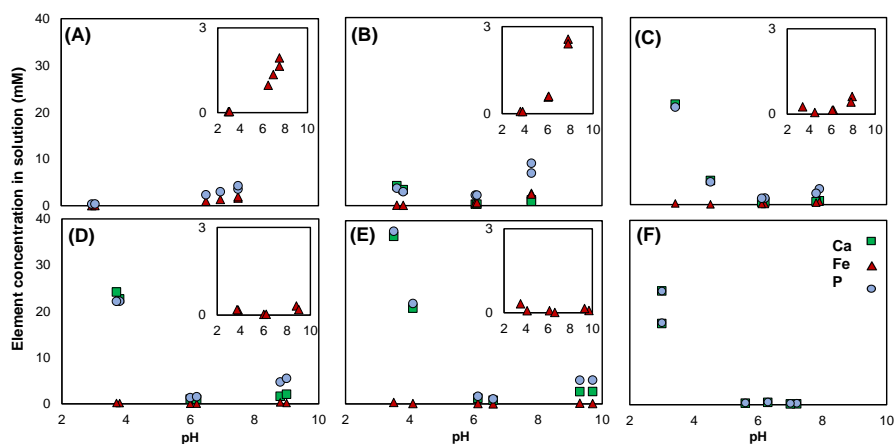


Figure 3.2 Concentration of dissolved iron, calcium, and phosphorus quantified by ICP-AES in aqueous supernatant. (A) Pure Fe(III)PP ($x = 1$) and the mixed Ca-Fe(III) pyrophosphate salts with (B) $x = 0.35$, (C) $x = 0.18$, (D) $x = 0.15$, (E) $x = 0.14$, and (F) CaPP ($x = 0$). The insets show the corresponding dissolved iron concentration in solution.

In the case of Fe(III)PP, the concentration of Fe and P was measured to be close to zero at pH 3, however increasing pH to 6 and further to 8 resulted in higher concentrations of Fe and P in solution, Figure 3.2 A. For CaPP the opposite behavior was observed compared to Fe(III)PP; measured concentrations of Ca and P were very low at moderate and high pH but yielded higher values at pH 3, Figure 3.2 F, in line with the inverse pH-dependent dissolution of pure CaPP and Fe(III)PP⁹. The dissolution

of these pure pyrophosphate salts is caused by the formation of various complexes of Ca or Fe(III) with pyrophosphate ions. These formed species depend on the stability constants and solubility limits at distinct pH^{16,18}. The main complexes of CaPP and Fe(III)PP and their states have not yet been studied in detail and inconsistent stability constants are reported in literature²⁰. This is because of the complex chemistry of metal pyrophosphate salts and the formation of insoluble and poorly soluble complexes and mixtures of species^{21,22}. Similar to the pure Fe(III)PP and CaPP salts, elemental analysis was performed for aqueous solutions of the mixed salts (Figure 3.2 B-E). Also here, the main elements in solution at acidic pH (< 3) were Ca and P, while at pH > 6 Fe became slightly soluble as well. The present results indicate that in addition to the cations ($\text{Ca}^{2+}(\text{aq})$ and $\text{Fe}^{3+}(\text{aq})$) and anion ($\text{P}_2\text{O}_7^{4-}(\text{aq})$), soluble and insoluble complexes of these ions can be formed in the aqueous medium. However, due to the complexity and lack of experimental data reported in literature, the nature and stability constants of these ternary complexes cannot be elucidated or modeled in more detail.

3.3.2 Effect of temperature and time on dissolution behavior of iron from Fe(III)PP and mixed Ca-Fe(III) pyrophosphate salts

To effectively apply the Ca-Fe(III) pyrophosphate salts in fortified food products the pH-dependent dissolution at pH 3–7 must be limited during storage (23 °C), consumption (37 °C), and cooking (90 °C). Therefore, the effect of temperature on iron dissolution from Fe(III)PP and the mixed Ca-Fe(III) pyrophosphate salts was investigated by incubating the samples at different temperatures (23, 37, and 90 °C), Figure 3.3 A.

Overall, no significant change ($p > 0.05$) in iron dissolution in the pH range 1–10 was observed upon elevating the temperature from 23 to 37 °C. This is in line with a previous study, that observed no change in the dissolution of Fe(III) from Fe(III)PP upon elevating the temperature from 23 to 50 °C¹². Increasing the incubation temperature to 90 °C resulted in a significant ($p < 0.05$) increase in dissolved iron from Fe(III)PP at pH 1 and 5.5, Figure 3.3 A. The iron dissolution for the mixed salt with $x = 0.35$ at pH ~ 7 also increased at 90 °C. The iron dissolution of the mixed salts with $x = 0.14, 0.15$, and 0.18 decreased at pH 1–2 after heating at 90 °C. Possibly the ionic Fe(III) that is present in solutions of these mixed salts at pH < 3 underwent hydrolysis to insoluble species, which has been well-documented for Fe(III) at elevated temperatures^{17,23}. For the mixed salts with $x \leq 0.18$, iron concentration in solution remained similar at elevated temperatures at pH 3–7. Therefore, these mixed salts could potentially be used for cooking without an increase in reactivity.

Monitoring time-dependent iron concentration in the solutions pointed to no remarkable difference between iron dissolution for one and two hours of incubation, Figure 3.3 B. Over the 48 h incubation, dissolution remained constant at all pH ranges

for all salts except for Fe(III)PP with a significant ($p < 0.05$) increase at pH < 2 and pH 5–6 (after 48 h).

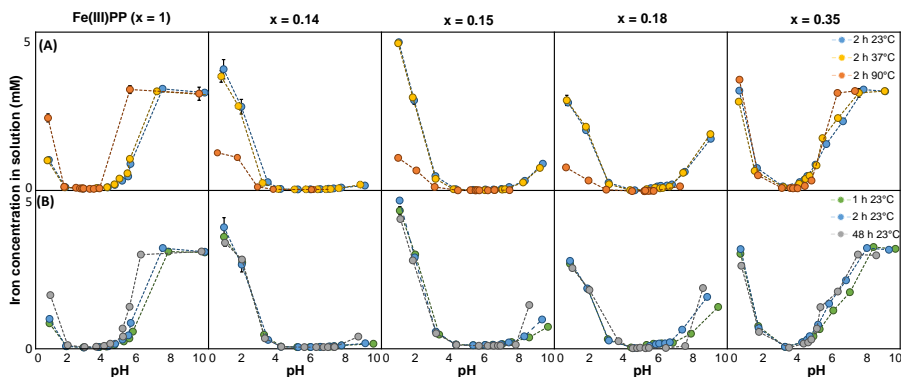


Figure 3.3 Effect of temperature (A) and time (B) on pH-dependent dissolution behavior of iron from Fe(III)PP and mixed Ca-Fe(III) pyrophosphate salts. (A) No significant change in iron dissolution ($p > 0.05$) was observed upon increasing the temperature from 23 to 37 °C over the studied pH range (1–10). Upon elevating the temperature to 90 °C, an increase in dissolved iron from Fe(III)PP at pH 1 and 5.5 and from the mixed salts with $x = 0.35$ at pH ~ 7 was observed. (B) Iron dissolution pointed to no remarkable difference between iron dissolution for one and two hours of incubation. After 48 h, dissolution remained constant at all pH ranges for all salts except for Fe(III)PP with a significant increase at pH < 2 and pH 5–6.

3.4 Conclusions

In this work, we demonstrate for the first time the tunable pH-dependent dissolution behavior of the mixed Ca-Fe(III) pyrophosphate salts with the general formula $\text{Ca}_{2(1-x)}\text{Fe}_{4x}(\text{P}_2\text{O}_7)_{(1+2x)}$. Our results indicate that the mixed salts with $x = 0.14$, 0.15 , and 0.18 have a lower soluble iron concentration at food-relevant pH (3–7), compared to Fe(III)PP. Furthermore, at gastric pH (1–3), the salts show enhanced dissolved iron concentration with up to a four-fold increase of soluble iron, compared to Fe(III)PP. The present findings suggest that mixed Ca-Fe(III) pyrophosphate salts with x -values ≤ 0.18 in the general formula $\text{Ca}_{2(1-x)}\text{Fe}_{4x}(\text{P}_2\text{O}_7)_{(1+2x)}$ can be potential food fortificants with reduced iron-mediated reactivity due to decreased iron dissolution at food pH (3–7) and improved bio-accessibility resulting from increased iron dissolution at gastric pH (1–3).

3.5 Acknowledgments

The author is grateful to Arjen Reichwein, Raymond Nijveld, and Teun de Bruin of Nouryon specialty chemicals B.V. for performing the ICP-AES measurements.

3.A Appendix

3.A.1 Up-scaled preparation of pure and mixed Ca-Fe(III) pyrophosphate salts

The synthesis of the pure and mixed pyrophosphate salts described in this study was up-scaled. Iron (III) pyrophosphate ($\text{Fe}_4(\text{P}_2\text{O}_7)_3$, Fe(III)PP) and calcium pyrophosphate ($\text{Ca}_2\text{P}_2\text{O}_7$, CaPP) were separately prepared using a fast co-precipitation method similar to the what described in the section 2.2.2). In short, 0.5 L solutions of 17.14 mM $\text{FeCl}_3 \cdot 6\text{H}_2\text{O}$ and 25.72 mM CaCl_2 in water were made. The solutions were quickly added to an aqueous solution of $\text{Na}_4\text{P}_2\text{O}_7 \cdot 10\text{H}_2\text{O}$ (6.43 mM, 1 L) while stirring vigorously (~ 500 rpm) by an IKA® RW16 basic electronic overhead stirrer (IKA-Werke, Staufen, Germany). A turbid white dispersion formed after a couple of seconds during addition. The samples were then centrifuged using an Avanti J-26 XP centrifuge (Beckman Coulter, Brea, CA, USA) using JLA-9.1000 rotor, at $6000 \times g$ and 25°C for 45 min in 1000 ml volume polycarbonate centrifuge bottles (95×191 mm-2Pk) with caps followed by washing the precipitates twice with water. The sediments were dried in an oven at 45°C overnight. The mixed Ca-Fe(III) pyrophosphate salts were prepared by the same procedure as the pure salts, at a fixed concentration of $\text{Na}_4\text{P}_2\text{O}_7 \cdot 10\text{H}_2\text{O}$ (6.43 mM, 1 L) and by addition of a mixed solution of $\text{FeCl}_3 \cdot 6\text{H}_2\text{O}$ and CaCl_2 in 0.5 L of water. Three different mixed salts were synthesized with the general formula $\text{Ca}_{2(1-x)}\text{Fe}_{4x}(\text{P}_2\text{O}_7)_{(1+2x)}$ ($0 \leq x \leq 1$), containing low to high Fe(III) content corresponding to three different theoretical x-values (i.e., 0.05, 0.10, 0.26). The x-values were chosen based on the recommended nutrient intake of iron and calcium (respectively 20 and 833 mg for adult females, assuming 15 % bio-availability of Fe and 30 % of Ca in the salt)²⁴. The molar ratio of total metal to pyrophosphate ion was based on the stoichiometry of calcium pyrophosphate (final concentration of $[\text{Ca}] + [\text{Fe}] = 8.57$ mM). The average yield of the prepared salts was $73.3 \pm 5.5\%$.

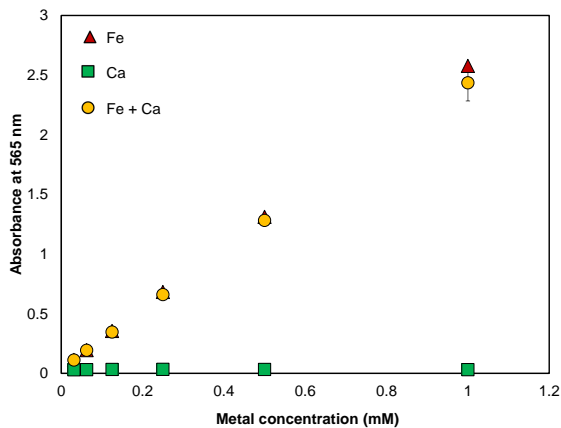


Figure 3.4 Interference of presence of Ca ion with the quantification of total iron in the ferrozine-based colorimetric assay. Absorbance of the ferrozine complex at 565 nm in the presence of increasing concentrations of iron, calcium, or a mixture containing equimolar concentrations of iron and calcium.

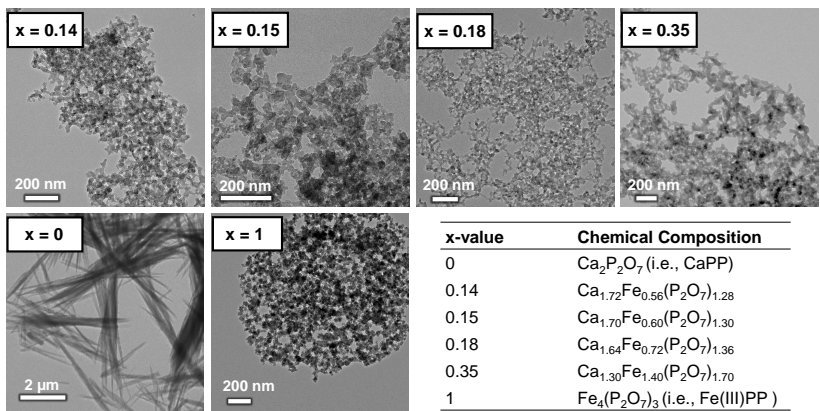


Figure 3.5 Characterization of the pure and mixed Ca-Fe(III) pyrophosphate salts synthesized with the up-scaled method. TEM images of CaPP ($x = 0$), Fe(III)PP ($x = 1$), and the mixed Ca-Fe(III) pyrophosphate salts prepared by co-precipitation. The x-values and chemical formula of the pure and mixed salts were obtained from the elemental composition determined by EDX.

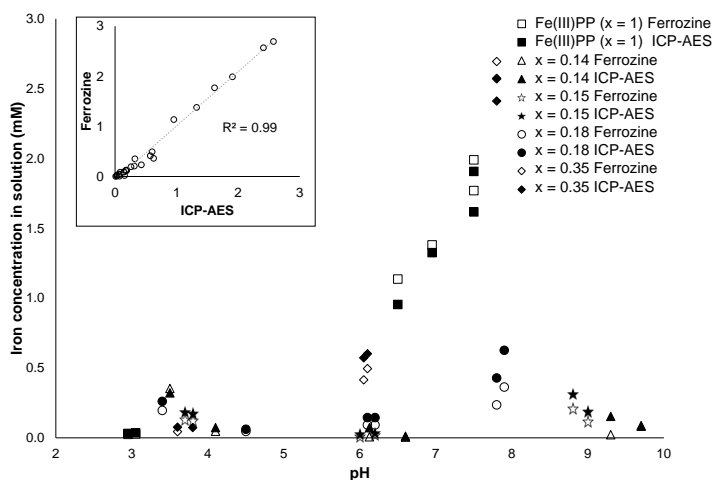


Figure 3.6 Independent verification of ferrozine assay with ICP-AES method. Dissolution of iron from Fe(III)PP and the mixed Ca-Fe(III) pyrophosphate salts as a function of pH determined by ICP-AES (filled markers) and by the ferrozine (open markers) methods.

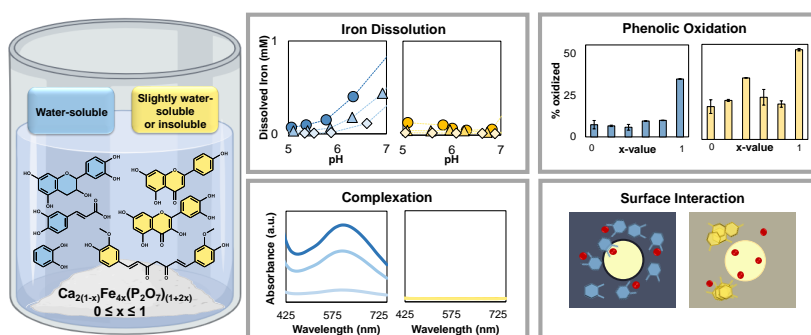
References

- 1 A. C. Bovell-Benjamin and J. X. Guinard, *Critical Reviews in Food Science and Nutrition* **43**, 379 (2003).
- 2 N. Zuidam, in *Encapsulation Technologies and Delivery Systems for Food Ingredients and Nutraceuticals* (Elsevier, 2012) pp. 505–540.
- 3 E. Habeych, V. van Kogelenberg, L. Sagalowicz, M. Michel, and N. Galaffu, *Food Research International* **88**, 122 (2016).
- 4 J. Bijlsma, W. J. de Bruijn, J. A. Hageman, P. Goos, K. P. Velikov, and J. P. Vincken, *Scientific Reports* **10**, 1 (2020).
- 5 R. Hurrell, Nestel, Beard, and Freire, *Nutrition reviews* **60**, S7 (2002).
- 6 F. Rohner, F. O. Ernst, M. Arnold, M. Hilbe, R. Biebinger, F. Ehrensperger, S. E. Pratsinis, W. Langhans, R. F. Hurrell, and M. B. Zimmermann, *The Journal of Nutrition* **137**, 614 (2007).
- 7 K. J. Wienk, J. J. Marx, and A. C. Beynen, *European Journal of Nutrition* 1999 **38**:2 **38**, 51 (1999).
- 8 T. Tian, E. Blanco, S. K. Smoukov, O. D. Velez, and K. P. Velikov, *Food Chemistry* **208**, 97 (2016).
- 9 Y. M. van Leeuwen, *Colloidal Metal Pyrophosphates Salts Preparation, Properties and Applications*, Ph.D. thesis (2013).

- 10 F. M. Hilty, J. T. Knijnenburg, A. Teleki, F. Krumeich, R. F. Hurrell, S. E. Pratsinis, and M. B. Zimmermann, *Journal of Food Science* **76**, N2 (2011).
- 11 M. B. Zimmermann and F. M. Hilty, *Nanoscale* **3**, 2390 (2011).
- 12 R. B. Wilhelmy, R. C. Patel, and E. Matijević, *Inorganic Chemistry* **24**, 3290 (1985).
- 13 T. Zhang, L. Ding, H. Ren, Z. Guo, and J. Tan, *Journal of Hazardous Materials* **176**, 444 (2010).
- 14 L. L. Stookey, *Analytical chemistry* **42**, 779 (1970).
- 15 J. Bijlsma, W. J. de Bruijn, K. P. Velikov, and J. P. Vincken, *Food Chemistry* **370**, 131292 (2022).
- 16 C. L. Jiang, X. H. Wang, B. K. Parekh, and J. W. Leonard, *Mining, Metallurgy Exploration* **15**, 1 (1998).
- 17 C. M. Flynn Jr., *Chemical Reviews* **84**, 31 (2002).
- 18 Y. Sun, L. Zhao, and Y. Teng, *Chemical Engineering Journal* **390**, 124574 (2020).
- 19 J. H. Swain, S. M. Newman, and J. R. Hunt, *The Journal of nutrition* **133**, 3546 (2003).
- 20 R. Lemire, P. Taylor, H. Schlenz, and D. Palmer, "Chemical Thermodynamics of Iron, Part 2," (2020).
- 21 O. Masala, E. J. McInnes, and P. O'Brien, *Inorganica Chimica Acta* **339**, 366 (2002).
- 22 A. M. Brown, *Computer Methods and Programs in Biomedicine* **79**, 89 (2005).
- 23 J. Dousma and P. L. De Bruyn, *Journal of Colloid and Interface Science* **56**, 527 (1976).
- 24 L. Allen, B. de Benoist, O. Dary, and R. Hurrell, *World Health Organization* , 341 (2006).

Mixed Fe(III)-containing pyrophosphate salts: Reactivity with Phenolics

Abstract



Mixed pyrophosphate salts, $\text{Ca}_{2(1-x)}\text{Fe}_{4x}(\text{P}_2\text{O}_7)_{(1+2x)}$, are dual-fortificants with potentially less iron-phenolic reactivity, compared to ferric pyrophosphate (Fe(III)PP), due to decreased soluble Fe in the food-relevant pH range 3-7. We investigated reactivity (i.e., complexation, oxidation, and surface interaction) of the Fe(III)PP and mixed salts (with $x = 0.14, 0.15, 0.18$, and 0.35) in the presence of diverse phenolics. At pH 5-7, increased soluble iron from all salts was observed in the presence of water-soluble phenolics. XPS confirmed that these phenolics solubilize iron after coordination at the salt surface, resulting in increased discoloration. However, color changes for the mixed salts with $x \leq 0.18$ remained acceptable for slightly water-soluble and insoluble phenolics. Furthermore, phenolic oxidation in the presence of the mixed salts was significantly reduced, compared to Fe(III)PP, at pH 6. In conclusion, these mixed Ca-Fe(III) pyrophosphate salts with $x \leq 0.18$ are potential iron fortificants suitable for foods containing slightly water-soluble and/or insoluble phenolics.

This chapter is based on N. Moslehi, J. Bijlsma, K. P. Velikov, W. K. Kegel, J-P. Vincken, and W. J.C. de Bruijn, "Reactivity of Fe(III)-containing pyrophosphate salts with phenolics: complexation, oxidation, and surface interaction", *Journal of Food Chemistry* 407 (2023): 135156.

"A hair divides what is false and true."

Omar Khayyam – Persian polymath, 1048-1131

4.1 Introduction

Fortification of food with iron is an effective approach to overcome the global iron deficiency¹. However, the addition of iron to foods is problematic due to its high reactivity with phenolic compounds present in the food. Complexation and oxidation of phenolics in the presence of iron ions cause an undesirable change in the organoleptic properties of the food products such as discoloration, or changes in taste and texture²⁻⁴. Moreover, the reactivity of iron with phenolic compounds can hinder iron bio-availability and can consequently reduce iron uptake in the human body⁵. One strategy to counter the iron-mediated reactivity problem is to use a poorly water-soluble/water-insoluble iron-containing salt such as iron (III) pyrophosphate (Fe(III)PP)^{3,6}. However, even addition of iron as Fe(III)PP cannot fully prevent discoloration in phenolic-rich foods^{7,8}. Moreover, the poor solubility of Fe(III)PP in the gastrointestinal tract results in limited iron bio-availability^{7,8}. Our previous study indicated that including calcium as a divalent metal, alongside iron, in the pyrophosphate salt matrix can be utilized to design potential dual-fortificants. The soluble iron concentration from these mixed salts, with the general formula of $\text{Ca}_{2(1-x)}\text{Fe}_{4x}(\text{P}_2\text{O}_7)_{(1+2x)}$, was reduced by up to eight-fold at food-relevant pH ranges, whereas it was enhanced up to four-fold in gastric relevant pH ranges, compared to Fe(III)PP (see chapter 3)⁹. Additionally, the inclusion of calcium as the second metal in the mixed Ca-Fe(III) pyrophosphate salt is expected to lower the iron content at the surface of these salts and therefore lead to a decrease in reactivity, with respect to Fe(III)PP. Despite a much lower soluble iron concentration and the expected lower iron content at the surface, the mixed Ca-Fe(III) pyrophosphate salts previously did not show noticeably lower reactivity compared to Fe(III)PP in a black tea solution, as discussed in chapter 2⁹. To create a clear link between the dissolution behavior of iron from these mixed salts and the observed reactivity of the salts, the current work aims to investigate the soluble iron from the Ca-Fe(III) pyrophosphate salts in the presence of phenolics as representative food matrix compounds that can react with iron.

We previously observed that the solubility of flavonoids* affects the soluble iron concentration². Therefore, a set of six model phenolic compounds with different chemical properties, most notably different water solubilities, were selected to investigate their interaction behavior with the mixed Ca-Fe(III) pyrophosphate salts,

*Dietary flavonoids (e.g. polyphenolic compounds) are an important class of phytochemicals and ubiquitous in vegetables, herbs, and fruits²

Figure 4.1. The chosen phenolic compounds also differ in the most likely Fe(III)-complexation sites, as are highlighted in Figure 4.1^{2,10–12}. The solubility values are calculated and shown as LogS (i.e., the logarithm of water-solubility in molar) in Figure 4.1. Catechol, caffeic acid, and epicatechin show LogS values ranging from 0 to -2 , which was previously classified as water-soluble by Sorkun and co-authors¹³. Accordingly, quercetin and apigenin ($-4 < \text{LogS} < -2$) are slightly soluble, and curcumin ($\text{LogS} < -4$) is insoluble. These phenolics were chosen because they are common in food products^{3,14}, except for catechol which was selected as a model for o-dihydroxybenzenes.

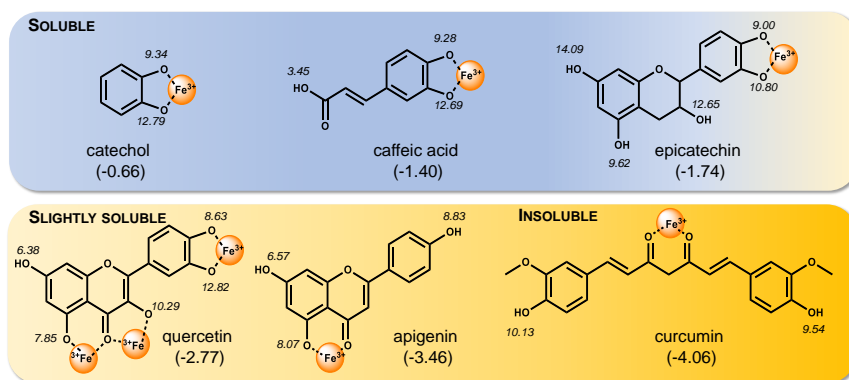


Figure 4.1 Structure of phenolic compounds used in this study, and the most likely Fe(III)-complexation sites. The pK_a values for hydroxyl groups of the phenolics are shown in italic, and LogS values of the phenolic compounds are given in brackets. LogS values were calculated using MarvinSketch 22.3 (ChemAxon). Based on the LogS values, the water-solubility of the phenolics was classified as soluble, slightly soluble, and insoluble.

Deprotonation of the hydroxyl substituents is a prerequisite for iron coordination¹². The pK_a values of the hydroxyl groups are indicated in Figure 4.1. It should be noted that in the presence of iron ions the deprotonated state is stabilized and that the apparent pK_a values will therefore be lowered to values in the range of pH 5–8 for the phenol moiety¹⁵.

We hypothesize that mixed Ca-Fe(III) pyrophosphate salts will show decreased reactivity towards phenolic compounds at food-relevant pH values compared to pure Fe(III)PP due to (i) decreased soluble iron concentration from the salts at pH 3–7, and (ii) decreased iron content at the surface of these salts. To this end, we evaluate

iron dissolution behavior, spectral changes indicating iron-mediated complexation, oxidation of the phenolic compounds, and reactions at the surface of these salts.

4.2 Materials and methods

4.2.1 Chemicals

Hydrochloric acid (37 wt.%), sodium hydroxide (≥ 98 wt.%), nitric acid (65 wt.%), iron(II) sulfate heptahydrate (≥ 99 wt.%), 3-(2-pyridyl)-5,6-diphenyl-1,2,4-triazine-*p,p'*-disulfonic acid monosodium salt hydrate (≥ 97 wt.%; ferrozine), ferric chloride hexahydrate ($\text{FeCl}_3 \cdot 6\text{H}_2\text{O}$, ≥ 99 wt.%), tetrasodium pyrophosphate decahydrate ($\text{Na}_4\text{P}_2\text{O}_7 \cdot 10\text{H}_2\text{O}$, ≥ 99 wt.%, NaPP), calcium dichloride (CaCl_2 , ≥ 93 wt.%), quercetin hydrate (≥ 95 wt.%), 1,2-dihydroxybenzene (≥ 99 wt.%; catechol), caffeic acid (≥ 98 wt.%), and curcumin (≥ 94 wt.%), were obtained from Merck Life Science (Darmstadt, Germany). (-)-Epicatechin (≥ 97 wt.%) was purchased from TCI Europe NV (Zwijndrecht, Belgium), apigenin (≥ 98 wt.%) from Indofine Chemical Company (Hillsborough, NJ, USA), and ascorbic acid (≥ 99 wt.%) was obtained from VWR International (Radnor, PA, USA). ULC-MS grade acetonitrile (ACN) and water, both containing 0.1 vol.% formic acid (FA) were purchased from Biosolve (Valkenswaard, The Netherlands). Water for other purposes than UHPLC was prepared using a Milli-Q (MQ) water purification system (Merck Millipore, Billerica, MA, USA).

4.2.2 Preparation of the CaPP, Fe(III)PP, and mixed Ca-Fe(III) pyrophosphate salts

Iron (III) pyrophosphate ($\text{Fe}_4(\text{P}_2\text{O}_7)_3$, Fe(III)PP), calcium pyrophosphate ($\text{Ca}_2\text{P}_2\text{O}_7$, CaPP), and mixed Ca-Fe(III) pyrophosphate salts with different iron to calcium ratios according to the general formula $\text{Ca}_{2(1-x)}\text{Fe}_{4x}(\text{P}_2\text{O}_7)_{(1+2x)}$ with (measured) $x = 0.14$, 0.15, 0.18, and 0.35 were prepared using a co-precipitation method as described in chapter 3, section 3.A.1. Uniformity in morphology was confirmed by transmission electron microscopy (TEM).

4.2.3 Reactivity of the CaPP, Fe(III)PP, and mixed Ca-Fe(III) pyrophosphate salts with phenolics

The CaPP, Fe(III)PP, and the mixed Ca-Fe(III) pyrophosphate salts were re-dispersed in water by stirring (~ 250 rpm) with a magnetic stir bar (final concentration of salt: 10 mg/ml) followed by the addition of aqueous solutions (catechol, caffeic acid, and epicatechin) or dispersions (quercetin, apigenin, and curcumin) of the phenolics to reach a final concentration of 5 mM phenolic. Next, the pH of the dispersions was adjusted using a pH-stat device (Metrohm, Herisau, Switzerland) by automatic titration using 0.1 M HCl or 0.1 M NaOH. Subsequently, the dispersions with pH

values ranging from one to eleven (steps of one) were incubated for 2 h at 23 °C under continuous stirring at 1000 rpm. After incubation, the pH of each sample was measured again to determine the final pH. Finally, the samples were centrifuged at $15000 \times g$ for 10 min, and the supernatants were separated to quantify the dissolved iron concentration and obtain the absorbance spectra.

Iron concentration measurement by ferrozine-based colorimetric assay

The total iron in the solution was quantified using a ferrozine-based colorimetric assay¹⁶ with slight adaptations, as described in chapter 3⁹. In short, the absorbance of the iron(II)-ferrozine complex at 565 nm was measured at room temperature in a SpectraMax M2e (Molecular Devices, Sunnyvale, CA, USA). All measurements were performed in duplicate and quantification of the total dissolved iron was performed with a calibration curve of FeSO_4 ($0.0078 - 1 \text{ mM}$, $R^2 > 0.99$). The relative change in soluble iron concentration after addition of phenolics was defined according to Equation 4.1.

$$\text{Relative change} = \frac{[\text{Fe}]_{\text{phenolics}} - [\text{Fe}]_{\text{blank}}}{[\text{Fe}]_{\text{blank}}} \quad (4.1)$$

In which $[\text{Fe}]_{\text{phenolics}}$ and $[\text{Fe}]_{\text{blank}}$ are the total dissolved iron concentration in the presence and absence of the phenolics, respectively.

The iron quantification in presence of phenolics by the ferrozine assay was verified independently using inductively coupled plasma–atomic emission spectroscopy (ICP-AES), see section 4.A.1 in Appendix 4.A.

4.2.4 Monitoring reactivity and discoloration by UV-Vis spectroscopy

The reactivity of the pure Fe(III)PP and CaPP , as well as the mixed Ca-Fe(III) pyrophosphate salts in the presence of the different phenolic compounds, was monitored using ultraviolet-visible light (UV-Vis) spectroscopy. After centrifugation, 200 μl sample was transferred to a Corning[®] UV-transparent flat-bottom polystyrene 96-well plate (Sigma Aldrich, St. Louis, MO, USA). Spectra were recorded in the range from 250 – 750 nm in a SpectraMax M2e (Molecular Devices, Sunnyvale, CA, USA), at room temperature. The color of the samples was visualized by taking an image (One-Plus 7T, Beijing, China) of the Eppendorf tubes with a uniform light source against a white background. The images were evaluated using the $L^*a^*b^*$ color space (i.e., L^* dark or light, a^* red vs. green, b^* yellow vs. blue). The values were extracted using the standard image analysis software (Photoshop CC 2021, Adobe). In this procedure, the $L^*a^*b^*$ value was taken at five different spots in the supernatant and five spots in the precipitate (Appendix, Figure 4.8). The degree of difference between the blank phenolic and the samples of phenolics in presence of the iron-containing salts,

ΔEab , corresponds to the distance between two points within the $L^*a^*b^*$ color space. E stands for 'Empfindung' which is the German for sensation (after the extensive research of Hermann von Helmholtz and Ewald Hering in the field of color vision). The ΔEab value (i.e., the absolute value of the color difference, not the direction) was calculated according to Equation 4.2^{17,18}.

$$\Delta Eab = [(L_0^* - L_x^*)^2 + (a_0^* - a_x^*)^2 + (b_0^* - b_x^*)^2]^{1/2} \quad (4.2)$$

in which L_0^* , a_0^* , b_0^* and L_x^* , a_x^* , b_x^* are the color space values for the blank phenolic and the phenolic exposed to the iron-containing salts, respectively.

4.2.5 Monitoring phenolics solubility and oxidation by RP-UHPLC-PDA-ESI-IT-MSⁿ

The water-solubility of the blank phenolics at pH 3, 6, and 8, and oxidation of epicatechin and quercetin at pH 3, 6, and 8 after incubation with the iron-containing salts, were analyzed by reversed-phase ultra-high performance liquid chromatography coupled to electrospray ionization ion trap mass spectrometry (RP-UHPLC-PDA-ESI-IT-MSⁿ). Here, pH 3, 6, and 8 were chosen as they respectively represent gastric, food, and intestinal conditions^{3,19}.

To test the oxidation of epicatechin and quercetin after incubation with the iron-containing salts, the supernatants from section 4.2.3 were separated from the precipitate to obtain the water-soluble fractions. The precipitates were then solubilized in DMSO (100 vol.%), which is known to be a suitable solvent for metal:ligand systems^{2,20}. The resulting suspensions were centrifuged once more (at $15000 \times g$ for 5 min) and the supernatants were separated to obtain the DMSO-soluble fractions. The phenolics' recovery and their oxidation products in the water-soluble and DMSO-soluble fractions were separated on a Thermo Vanquish UHPLC system (Thermo Scientific, San Jose, CA, USA) equipped with an autosampler, a pump, and a photodiode array (PDA) detector. A sample (1 μ l) was injected on an Acquity UPLC BEH C18 column (150 mm \times 2.1 mm i.d., 1.7 μ m) with a VanGuard (5 mm \times 2.1 mm i.d., 1.7 μ m) guard column of the same material (Waters, Milford, MA). Water (A) and acetonitrile (B), both acidified with 0.1 vol.% formic acid, were used as eluents. The flow rate was 400 μ l min⁻¹, and the temperature of the column oven was 45 °C with the post-column cooler set to 40 °C. The elution profiles can be found in section 4.A.2 of Appendix 4.A. The PDA detector was set to measure the wavelength range of 190 – 680 nm. Mass spectrometric data were acquired using a Velos Pro ion trap mass spectrometer (Thermo Scientific) equipped with a heated electrospray ionization probe (ESI-IT-MSⁿ) coupled in-line to the Vanquish UHPLC system. Nitrogen was used as a sheath gas (50 arbitrary units) and auxiliary gas (13 arbitrary units). Data were

collected over the m/z range of 100 – 1500 in negative and positive ionization mode by using source voltages of 2.5 and 3.5 kV, respectively. For both modes, the S-lens RF level was set at 67 %, the ion transfer tube and the source heater temperatures were 263 and 425 °C, respectively. Data-dependent MS² analysis was performed on the most intense ion by collision-induced dissociation (CID) with a normalized collision energy of 35 %. A dynamic mass exclusion approach was used, in which the most intense ion was fragmented 3 times and was subsequently excluded from fragmentation for the following 5 seconds, allowing data-dependent MS² of less intense co-eluting compounds. Data acquisition and processing were performed using Xcalibur (version 4.1, Thermo Scientific). Quantification of phenolic was performed based on PDA peak area (280 nm) and an external calibration curve of the corresponding authentic standard (0.003 – 0.5 mM, in duplicate, $R^2 = 1.00$). To assess whether the change in phenolic recovery was statistically significant, ANOVA analysis was performed using IBM SPSS Statistic v23 software (SPSS Inc., Chicago, IL, USA). Tukey's *post hoc* comparisons (significant at $p < 0.05$) were carried out to evaluate the total concentration of the phenolics at different pH values in presence of the different salts.

4.2.6 Surface composition of the CaPP, Fe(III)PP, and mixed Ca-Fe(III) pyrophosphate salts by X-ray photoelectron spectroscopy

The surface composition of CaPP, Fe(III)PP, and the mixed Ca-Fe(III) pyrophosphate particles was determined by X-ray photoelectron spectroscopy (XPS), the sampling depth of XPS is 3-10 nm²¹. The salts were also analyzed after incubation with epicatechin (pH 6) using the same incubation set-up as in section 4.2.3. After incubation, the samples were centrifuged at 5000 × g for 10 min and the precipitate was washed twice with water. Complete removal of water from the samples was ensured by overnight drying in a vacuum oven at 50 °C. Samples were prepared on indium foil. XPS measurements were performed using a JPS-9200 photoelectron spectrometer (JEOL Ltd., Japan). All samples were analyzed using a focused monochromated Al K α X-ray source (spot size of 300 μ m), wide scans were recorded at a constant dwelling time of 50 ms and pass energies of 50 eV. The power of the X-ray source was 240 W (20 mA and 12 kV). The charge compensation was used during the XPS scans with an accelerating voltage of 2.8 eV and a filament current of 4.8 A. XPS wide-scan were obtained under ultrahigh-vacuum conditions (base pressure, 3×10^{-7} Pa). The spectra were fitted with symmetrical Gaussian/Lorentzian (GL(30)) line shapes using CasaXPS (version 2.3.22PR1.0). All spectra were referenced to the C 1s peak attributed to C-C and C-H atoms at 285.0 eV.

4.3 Results and discussion

4.3.1 Dissolution behavior of iron from Fe(III)PP and mixed Ca-Fe(III) pyrophosphate salts in the presence of phenolics

The dissolution of total iron from Fe(III)PP and the mixed Ca-Fe(III) pyrophosphate salts in the presence of phenolic compounds was studied as a function of pH, using the ferrozine assay¹⁶. This assay was verified for the combination of epicatechin and all salts by comparison with the ICP-AES method, Figure 4.9 of Appendix 4.A. The soluble iron concentration from 10 mg/ml dispersions of Fe(III)PP and the four mixed salts in the presence of the six different phenolics was evaluated in water in the food-relevant pH range 3-7, Figure 4.2 A. The dispersions were prepared based on an equal amount of the salts (10 mg/ml), no direct relationship was observed between the theoretical maximum iron concentration of the dispersion and the measured iron concentration in solution, see Table 4.1 of Appendix 4.A. The soluble iron concentrations presented here were determined after two hours incubation of the salt dispersions, and are therefore not necessarily equal to the solubilities (i.e., the equilibrium saturation concentrations). Based on the results of chapter 3, we assume that the iron dissolution from the mixed salt was complete at that time point⁹. Moreover, we confirmed experimentally that at pH 3, 6, and 8 epicatechin, caffeic acid, and catechol showed good water-solubility and that quercetin, apigenin, and curcumin were slightly soluble or insoluble in water in the absence of iron, Figure 4.10 of Appendix 4.A.

At food-relevant pH values (3-7), the mixed salts with $x \leq 0.18$ exhibit a lower soluble iron concentration than Fe(III)PP, Figure 4.2 A (blank). Additionally, the soluble iron concentration from the mixed salts with $x \leq 0.18$ depended on the pH and water-solubility of the phenolic compound as well.

In the range from pH 3 to 5, iron from the mixed Ca-Fe(III) pyrophosphate salts with $x \leq 0.18$ was (practically) insoluble regardless of the presence of the phenolics, i.e., iron concentration in solution was < 0.18 mM which equals < 0.1 g/l²². The theoretical maximum concentrations of the dissolved iron from the salts, based on the initial amount of 10 mg/ml salt, are listed in Table 4.1 of Appendix 4.A. In the pH range from 3 to 5, the phenolics did not affect the iron dissolution because all hydroxyl groups are protonated (the apparent pK_a range of phenolate is expected to be 5-8) and therefore do not coordinate iron¹⁵. Upon increasing the pH from 5 to 7 the hydroxyl groups of the phenolics are deprotonated, leading to differential iron dissolution from the pyrophosphate salts for the different categories of phenolics, see Figure 4.2 A. For the water-soluble phenolics (i.e., catechol, caffeic acid, and epicatechin), an up to 11-fold increase in soluble iron concentration from the mixed Ca-Fe(III) pyrophosphate salts with $x \leq 0.18$ was observed at pH 6-6.5 compared to the iron salt in the absence of the phenolics, Figure 4.2 B. However, in the presence of

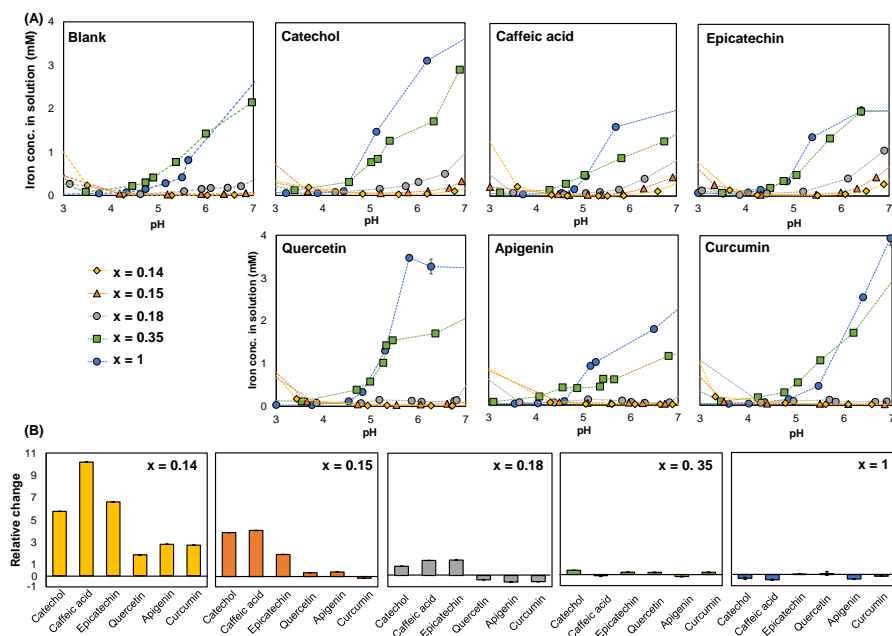


Figure 4.2 Dissolution behavior of iron from Fe(III)PP and the mixed Ca-Fe(III) pyrophosphate salts in the absence and presence of the phenolics. **(A)** Concentration of the dissolved iron at pH 3–7 from Fe(III)PP ($x = 1$) and mixed Ca-Fe(III) pyrophosphate salts with $x = 0.14$, $x = 0.15$, $x = 0.18$, and $x = 0.35$, in the absence of phenolics (blank), and in presence of catechol, caffeic acid, epicatechin, quercetin, apigenin, and curcumin after 2 h incubation at 23 °C. **(B)** Relative change (defined in Equation 4.1) in the soluble iron concentration from the salts in the presence of the phenolic compounds compared to the salts in absence of phenolic compounds at pH 6–6.5.

the slightly water-soluble (i.e., quercetin and apigenin) and insoluble (i.e., curcumin) phenolics, the relative change in soluble iron concentration was lower compared to water-soluble phenolics and the iron remained practically insoluble. Furthermore, the salt with $x = 0.35$ showed the highest absolute soluble iron concentration among the mixed salts and was similar to Fe(III)PP ($x = 1$) in the presence of all phenolics over the food-relevant pH range (3–7), Figure 4.2 A. At pH 6–6.5 the soluble iron concentration from the salts with $x = 0.35$ and $x = 1$ was not affected by the solubility of the phenolic, Figure 4.2 B.

At pH < 3, in the blank and in presence of all phenolics, an increase in soluble iron concentration was observed from all mixed Ca-Fe(III) pyrophosphate salts compared to pure Fe(III)PP, Figure 4.11 of Appendix 4.A. No clear trend was observed below pH 3 between the category of the phenolic and the soluble iron concentration. At pH > 7, which includes the intestinal pH range, irrespective of the phenolic compound, lower

iron concentrations in solution were measured for all the mixed Ca-Fe(III) pyrophosphate salts, compared to Fe(III)PP. There was only one exception to this observation; for the salt with $x = 0.35$, at $\text{pH} > 8$ in the presence of epicatechin and caffeic acid, the soluble iron concentration was measured to be equal to and higher than that of Fe(III)PP, respectively, Figure 4.11 of Appendix 4.A. Finally, the soluble iron from the mixed salts with $x = 0.14$ and 0.15 remained low (i.e., $< 0.15 \text{ mM}$) and in line with the blank (no phenolics) in the presence of apigenin and curcumin at $\text{pH} > 8$.

The effect of temperature on the dissolution behavior of iron from the pyrophosphate salts in the presence of epicatechin was also investigated. The soluble iron concentration from the salts with $x \leq 0.18$ was observed to be similar at 23, 37, and 90°C in the gastric and food-relevant pH ranges, Figure 4.12 of Appendix 4.A. These results suggest that the soluble iron concentration does not change in gastric conditions (37°C), and after cooking (90°C)²³.

4.3.2 Discoloration of CaPP, Fe(III)PP, and mixed Ca-Fe(III) pyrophosphate salts with phenolics

The total absorbance and discoloration of the CaPP, Fe(III)PP, and the mixed Ca-Fe(III) pyrophosphate salts in the presence of all phenolics was assessed at $\text{pH} 6\text{--}6.5$, Figure 4.3 A. This pH range was explored as it is in the range of most food products, and more particularly savory concentrates, which is one of the preferred foods for iron fortification²⁴. The pH of three commercial savory concentrates was measured to be 6.27 ± 0.59 . The color of the supernatants and the precipitates were evaluated visually, Figure 4.3 B, and according to the *CIELab*^{*} color space. The $L^*a^*b^*$ values were used to calculate the ΔE_{ab} as a qualitative tool for the color difference between the supernatant and precipitate after exposing the phenolics to the iron-containing salts, Figure 4.3 C. It was assumed that when the ΔE_{ab} value is 3–5, the color difference can be observed by an average consumer²⁵. A ΔE_{ab} value of up to 10 is considered to indicate an acceptable color change for iron-fortified salts²⁶. For all samples the ΔE_{ab} value was > 5 , indicating that a color difference could be observed, Figure 4.3 C.

For the samples in the presence of the water-soluble phenolics (i.e., epicatechin, caffeic acid, and catechol), an absorbance band was observed with $\lambda_{\text{max}} \sim 580 \text{ nm}$, Figure 4.3 A. This broad absorbance band is due to the ligand-to-metal charge transfer (LMCT) phenomenon. This absorbance band with $\lambda_{\text{max}} \sim 580 \text{ nm}$ is typically observed for Fe(III)-catechol complexes with a stoichiometry of 1:2 at pH ranging from 5–7^{27,28} and causes the bluish to purplish appearance of the supernatants, Figure 4.3 B. Moreover, in the presence of the water-soluble phenolics, the precipitate changed from white to a greyish/bluish color. We hypothesized previously that the discoloration of the precipitates at $\text{pH} 6.5$ can be due to the formation of Fe(III)-phenolic complexes at the surface of the salts⁹, which is further discussed in section 4.3.4.

In line with these color changes in the supernatant and precipitate, the ΔE_{ab} differences for water-soluble phenolics in presence of the Fe(III)-containing salts were unacceptable and much larger than for the slightly water-soluble and insoluble phenolics (quercetin, apigenin, and curcumin), Figure 4.3 C.

In the case of quercetin, increased absorbance in the visual spectra was observed in the presence of Fe(III)PP and the mixed salt with $x = 0.35$, Figure 4.3 A. The absorbance band with $\lambda_{max} \sim 570$ nm is due to the LMCT phenomenon and the increase in the intensity of absorbance at 450 nm is due to the bathochromic shift (red shift i.e., shift to longer wavelengths) of the cinnamoyl band of quercetin². In the absence of any of the iron-containing salts or in the presence of the mixed salts with $x \leq 0.18$, the supernatant of the quercetin sample did not show any absorbance due to the poor solubility of quercetin in water. The increased absorbance observed in the supernatant in the presence of the salts with $x = 0.35$ and $x = 1$ is suggested to be a result of the formation of a charged Fe(III)-quercetin complex that improves the solubility of quercetin²⁹. A charged, and therefore soluble, iron-phenolic complex is more likely for quercetin compared to apigenin and curcumin because quercetin has multiple possible iron-binding sites³⁰ and iron-quercetin complexes have higher reported stability constants due to the presence of a catechol moiety, Table 4.2 of Appendix 4.A. For apigenin and curcumin, no increase in absorbance was observed in the presence of iron-containing salts, Figure 4.3 A, in line with the transparent supernatants of these samples, Figure 4.3 B. For the supernatants of quercetin in the presence of CaPP and the mixed salts (with $x \leq 0.18$) and for apigenin and curcumin in the presence of all salts the ΔE_{ab} value was at maximum around 10. The images of apigenin indicate that the precipitates in the presence of Fe(III)PP and the mixed salt with $x = 0.35$ turned dark brown. Additionally, for curcumin a slightly darker layer was observed on the precipitate in the presence of Fe(III)PP, Figure 4.3 B. This indicates that complexation reactions between iron and apigenin or curcumin occurred, but the formed products remained insoluble. This is most likely for one or a combination of the following three reasons: (i) Fe(III)-phenolic complexation at the surface of the undissolved salt particles, (ii) the formation of neutral and/or insoluble complexes of iron with these phenolics²⁹, or (iii) the inherently poor solubility of these phenolics, see Figure 4.10 of Appendix 4.A. In line with the observed discoloration in the precipitate, Figure 4.3 B, the ΔE_{ab} value of quercetin and apigenin in the presence of Fe(III)PP or the salt with $x = 0.35$ was unacceptable (> 10). The ΔE_{ab} value for the precipitate of curcumin in the presence of the salts with $x \leq 0.15$ was also > 10 . This apparent color change to lighter shades of orange (lightness $L^* = 48$ for blank versus $L^* = 64$ for CaPP) is resulting from the presence of white or off-white insoluble pyrophosphate salts in these precipitates that mix with curcumin, compared to the orange color of pure curcumin (blank), rather than from dark-color formation.

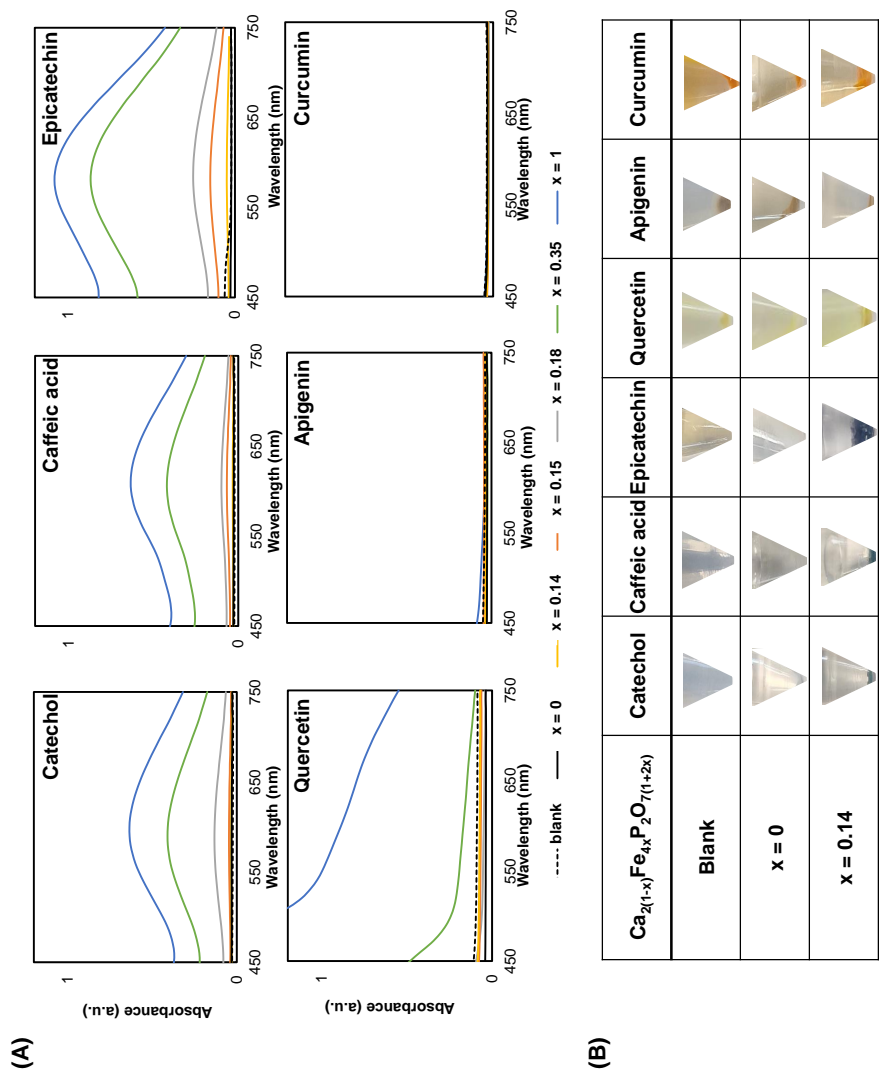


Figure 4.3 Discoloration of CaPP, Fe(III)PP, and mixed Ca-Fe(III) pyrophosphate salts with phenolics. (A) Absorbance spectra of the supernatants of CaPP ($x=0$), Fe(III)PP ($x=1$), and mixed Ca-Fe(III) pyrophosphate salts with 0.14, 0.15, 0.18, and 0.35 in the presence of the different phenolics at pH 6. The dashed lines indicate the absorbance of the pure phenolics (in the absence of any salts). (B) Pictures of the supernatants and precipitates in the Eppendorf tubes.

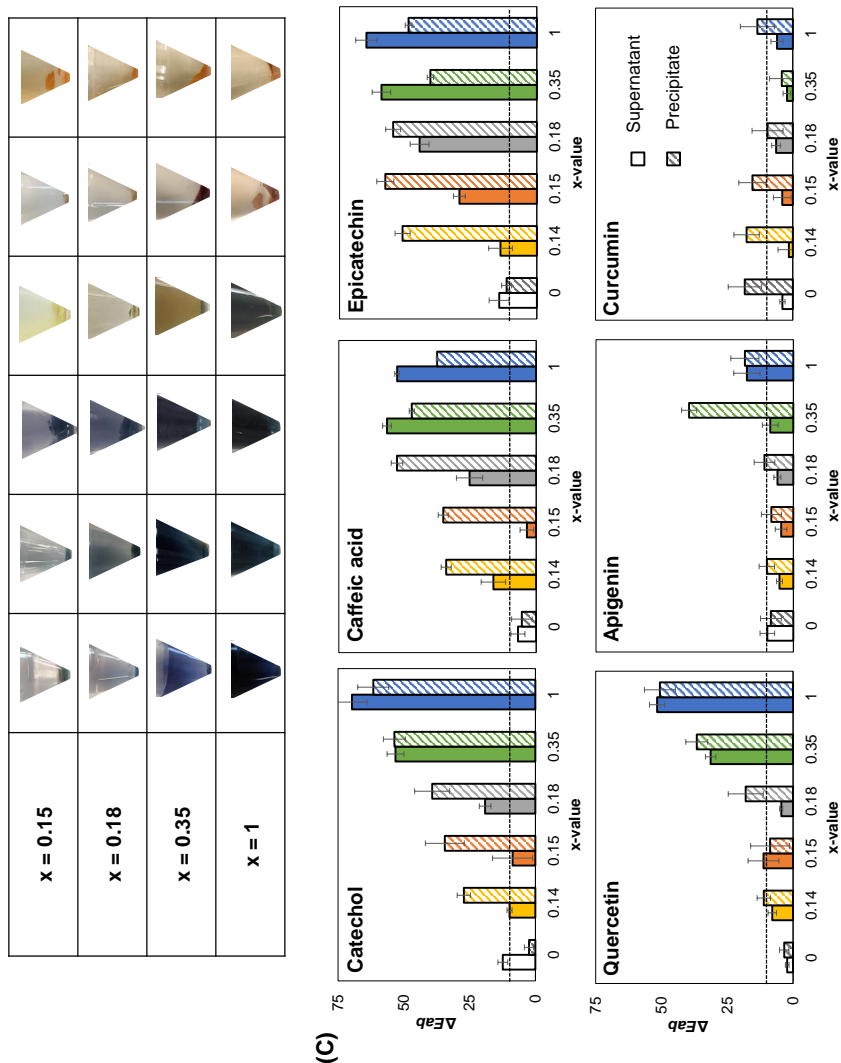


Figure 4.3 (continued): (C) The values of ΔE_{ab} correspond to the color changes in the supernatant (filled bar) and precipitate (striped bar) after being exposed to CaPP, Fe(III)PP, and the mixed Ca-Fe(III) pyrophosphate salts, compared to no salts (i.e. blank phenolics). The dashed line indicates the maximum acceptable color change (i.e., $\Delta E_{ab} = 10$).

We observed that the intensity of the LMCT absorbance band, Figure 4.3 A, increased monotonically with the x -value of the mixed Ca-Fe(III) pyrophosphate salts. For the mixed salts with $0 \leq x \leq 0.35$ in the presence of catechol, caffeic acid, epicatechin, and quercetin, the area under the curve in the visible range ($AUC_{380-750}$) showed a linear relationship with the iron concentration in solution ($R^2 > 0.97$), Figure 4.13 of Appendix 4.A. For epicatechin and quercetin the R^2 value decreased from 0.995 to 0.970 and from 0.990 to 0.872, respectively, if the point corresponding to Fe(III)PP ($x = 1$) was included, because the slope of $AUC_{380-750}$ suddenly increased from $x = 0.35$ to $x = 1$. It has previously been shown that the inclusion of the divalent metals (i.e., M(II)), such as calcium, can change the dark-colored iron-phenolic complexation product towards a colorless M(II)-phenolic reaction product via metal competition for complexation with phenolics³¹. If this competition would occur in these samples, then we would expect this relation between $AUC_{380-750}$ and iron concentration to be non-linear, because the samples at lower x -value contain relatively more Ca compared to higher x -values (i.e., for $x = 0.14$: Ca/Fe = 3.1 and for $x = 0.35$: Ca/Fe = 0.93). However, our findings show a direct linear relationship between the iron concentration and color. Thus, we conclude that the effect of metal competition on color was likely very limited in these samples. We suggest that competition is limited because Fe(III) is a harder Lewis acid compared to Ca, and therefore a much larger excess of Ca (i.e. Ca/Fe ≥ 10) should be present to effectively limit color change via metal competition³.

Overall, for water-soluble phenolics, the use of the mixed Ca-Fe(III) pyrophosphate salts did not protect against adverse color changes that are caused by iron-phenolic complexation, as is indicated by the observed color change and presence of the LMCT band in the absorbance spectra. For quercetin, apigenin, and curcumin, the color change was limited to acceptable values ($\Delta E_{ab} \approx 10$) in the presence of the salts with $x \leq 0.18$. These outcomes show that the mixed Ca-Fe(III) pyrophosphate salts are more suitable for fortification of food products that contain slightly water-soluble and/or water-insoluble phenolic compounds. Moreover, these findings explain why the mixed salts show comparable reactivity to Fe(III)PP in a model black tea solution, which mainly contains water-soluble phenolics, see chapter 2⁹.

4.3.3 Oxidation rate of phenolics in the presence of CaPP, Fe(III)PP, and mixed Ca-Fe(III) pyrophosphate salts

Complexation reactions can be followed by oxidation reactions of phenolics because the complexation can be followed by an electron transfer from the ligand to Fe(III)³². Subsequent reactions of the oxidized phenolics yield a plethora of products that can arise from phenolic degradation and oxidative coupling. Because of the extended conjugated system of phenolics after oxidative coupling, these products may also contribute to discoloration³³. To date, the effect of Fe(III)PP and the mixed Ca-Fe(III)

pyrophosphate salts on phenolic oxidation is unknown. Therefore, we quantified the recovery of phenolics after incubation in the presence of the studied pyrophosphate salts at selected pH values (i.e., 3, 6, and 8) by RP-UHPLC-PDA-MSⁿ, Figure 7.5. In other words, the fraction of the phenolics which doesn't remain intact is considered as oxidized. Epicatechin and quercetin were chosen as representatives for water-soluble and slightly soluble/insoluble categories of the studied phenolics, respectively.

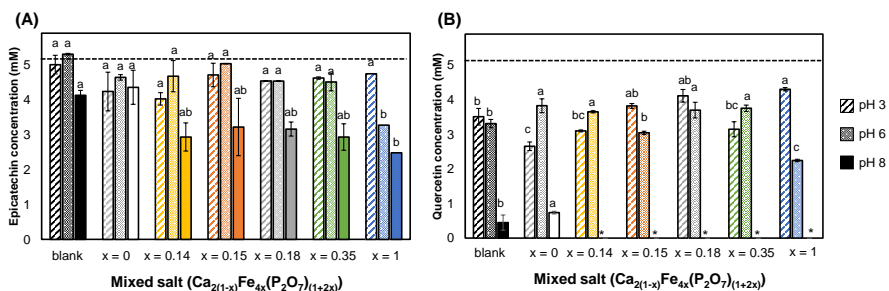


Figure 4.5 Oxidation rate of selected phenolics in the presence of the CaPP, Fe(III)PP, and mixed Ca-Fe(III) pyrophosphate salts. Recovery of (A) epicatechin and (B) quercetin in the absence and presence of CaPP ($x = 0$), Fe(III)PP ($x = 1$), and mixed Ca-Fe(III) pyrophosphate salts with $x = 0.14, 0.15, 0.18$, and 0.35 at pH 3 (striped bar), 6 (dotted bar), and 8 (filled bar) after incubation for 2 h at 23 °C. The error bars indicate the standard deviation of independent duplicates. The dashed line indicates the initial concentration of the phenolics (5 mM). Different letters indicate a significant difference in the concentration compared to the other x -values for the same pH value (Tukey's test, $p < 0.05$). * indicates that the concentration was below the limit of quantification.

At pH 3, no significant difference ($p > 0.05$) was observed in the recovery of epicatechin in the presence of the different pyrophosphate salts, Figure 7.5 A. Because the hydroxyl groups are protonated at pH 3 (see Figure 4.1), no complexation or subsequent oxidation reactions occurred at pH 3. In the case of quercetin at pH 3, a significant decrease in recovery was observed for the blank and in presence of the different salts, Figure 7.5 B. These differences could not be linked to the x -value of the salts, and because no oxidation products were detected in these samples (results not shown) it remains unclear why significantly different recoveries were observed at pH 3. Possibly some quercetin was lost due to the poor solubility and adsorption on the electrode during pH adjustment. At pH 6, a significant decrease ($p < 0.05$) in the recovery of epicatechin and quercetin in the presence of Fe(III)PP ($x = 1$) was observed compared to the blank, CaPP, and all mixed Ca-Fe(III) pyrophosphate salts. The significant decrease in intact epicatechin and quercetin by 35% and 55% of their initial amount, respectively, after 2 hours of exposure to the Fe(III)PP is suggested to

be due to oxidation of the phenolic compounds. This was supported by an increase in peak areas of the main oxidation products from epicatechin (δ -type dehydrocatechin) and quercetin (2,4,6-trihydroxyphenyl glyoxylic acid and 3,4-dihydroxybenzoic acid) upon increasing x-value (Figures 4.14, and 4.15 of Appendix 4.A)^{2,33}. For quercetin, more oxidative degradation products rather than oxidative coupling products were observed compared to epicatechin due to the presence of the 3-OH group in conjugation with the C₂-C₃ double bond, which enables formation of the highly reactive quinone methides as intermediates in the degradation of quercetin³⁴.

Faster oxidation of the phenolics in the presence of Fe(III)PP at pH 6 can be linked to a higher degree of complexation as shown in section 4.3.2. Exposure to Fe(III)PP resulted in the most intense discoloration caused by more complex formation of quercetin and epicatechin with iron ions. After 2 h incubation of epicatechin at pH 8 in the presence of Fe(III)PP, the epicatechin concentration significantly decreased compared to incubation of the blank or in the presence of CaPP ($p < 0.05$), Figure 7.5 A. The concentration of recovered epicatechin was not significantly different in the presence of the various mixed Ca-Fe(III) pyrophosphate salts. Similarly, no significant difference between the salts could be found for quercetin because its fast oxidation in the presence of the Fe(III)-containing pyrophosphate salts at pH 8 resulted in concentrations being below the limit of quantification. However, in the blank or in presence of CaPP, a significantly higher amount of quercetin was recovered compared to all iron-containing salts.

At food-relevant pH (i.e., 6), the inclusion of calcium in the Fe(III)-containing pyrophosphate salts resulted in less oxidation of the phenolic compound compared to pure Fe(III)PP. This is the first indication that fortification of foods with mixed Ca-Fe(III) pyrophosphate salts instead of pure Fe(III)PP can potentially limit the extent of iron-mediated food oxidation. Even though oxidation is already limited to a certain extent in the presence of Fe(III)PP compared to FeSO₄, because of the decreased soluble iron concentration^{26,35}, inclusion of calcium in the Ca-Fe(III) pyrophosphate salts further lowers the soluble iron concentration, thereby further limiting phenolic oxidation. This is in line with our hypotheses. Besides oxidation of phenolics, oxidation of fatty acids, amino acids, and other micronutrients may also occur in presence of Fe(III)³⁵. It should be further investigated whether these iron-mediated oxidation reactions are also limited in the presence of the mixed Ca-Fe(III) pyrophosphate, compared to Fe(III)PP.

4.3.4 Surface composition of CaPP, Fe(III)PP, and mixed Ca-Fe(III) pyrophosphate salts in the absence and presence of phenolics

The original reason for designing mixed Ca-Fe(III) pyrophosphate salts is reducing the reactivity of iron (particularly from the surface of these salts) with phenolics present in the food. These salts, based on the general formula $\text{Ca}_{2(1-x)}\text{Fe}_{4x}(\text{P}_2\text{O}_7)_{(1+2x)}$,

with a theoretical x -value < 0.33 , contain a lower percentage of Fe compared to Ca in bulk. This $\text{Ca/Fe} > 1$ has previously been confirmed for the salts with $x \leq 0.18$ by TEM-EDX, see chapter 2⁹, and is indicated by the ratios of Fe/P and Ca/P for the salts as shown in Figure 4.6 A. We hypothesized that the incorporation of calcium as a second mineral along iron in the pyrophosphate matrix would reduce the iron content at the surface of the mixed Ca-Fe(III) pyrophosphate salts and thereby lower the soluble iron concentration and iron-mediated reactivity. XPS measurements were employed to find the elemental composition at the surface of these salts, Figure 4.6 B (for wide scan XPS spectra see Figure 4.16 of Appendix 4.A). To interpret the data, the elemental percentages of the salts obtained from XPS were normalized with respect to phosphorus. It was confirmed that Fe(III)PP and all the mixed salts contained a lower iron to phosphorus ratio (Fe/P) at the surface than in the bulk, with up to a 5.5-fold decrease in the case of the mixed salt with $x = 0.14$. This variation in distribution of iron elements in the salt matrix (i.e., surface vs. bulk) can be caused by the higher dissolution of Fe ions than Ca ions from the surface of the pyrophosphate salts in water at the pH of the reaction mixture which results in higher Fe solubilization from the salts during the washing steps for purification^{9,36}. This solubilization of Fe from the surface of the salts can be experimentally linked to the negative surface charge of the salts particles in their colloidal state (before drying to powder) at this pH range as well, see Figure 4.18 of Appendix 4.A. However, comparing the calcium to phosphorus ratio (Ca/P) in the bulk and at the surface of the salts showed that this ratio was the same or slightly lower (on average 1.18 ± 0.18 fold). These results suggest that the mixed pyrophosphate salts have a lower iron to calcium ratio at their surface compared to their bulk composition, despite having homogeneous elemental distribution throughout their aggregates⁹.

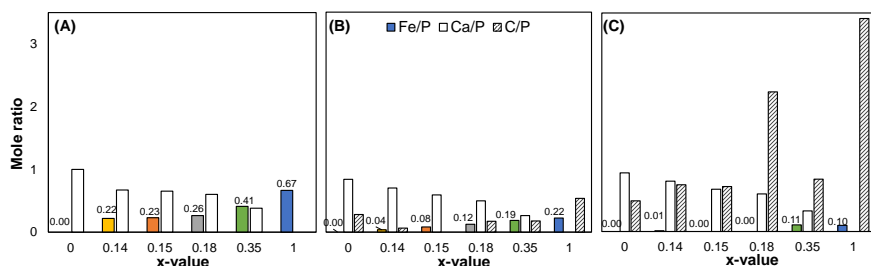


Figure 4.6 Analysis of the elemental ratios of the CaPP ($x = 0$), Fe(III)PP ($x = 1$), and mixed Ca-Fe(III) pyrophosphate salts with $x = 0.14$, 0.15 , 0.18 , and 0.35 . (A) in the bulk by TEM-EDX obtained from⁹ (chapter 2), (B) at the surface by XPS, and (C) at the surface after reactivity with epicatechin at pH 6. The data labels on the bars indicate the Fe/P ratios.

The XPS measurements were also utilized to obtain the carbon to phosphorus ratio (C/P) as an indication of the presence of phenolics on the surface of the salts. Accurate determination of elemental ratios of carbon in the bulk using TEM-EDX was not possible due to the carbon film on the TEM grids. The XPS measurements indicated that after exposing the salts to epicatechin and removal of the free epicatechin by washing with water, C/P at the surface of the salts increased noticeably, by up to 13-fold, Figure 4.6 C (for wide scan XPS spectra see Figure 4.17 of Appendix 4.A). Although the minor amounts of carbon present in XPS spectra are inevitable (e.g., due to the presence of atmospheric carbon dioxide impurities), this considerable increase in the carbon content at the surface of the Fe(III)-containing iron salts is additional confirmation, besides the color of the precipitates, for the presence of epicatechin at the surface of the insoluble pyrophosphate salts. In addition, Fe/P at the surface of the iron-containing salts decreased substantially, up to a 3.2-fold, after incubation with epicatechin, whereas the Ca/P ratio remained similar, Figure 4.6 C. This indicates that besides binding of Fe at the surface of the salt by epicatechin, a significant proportion of Fe was released into the solution after complexation with epicatechin, which is in line with the increased soluble iron concentration in the presence of epicatechin, Figure 4.2, and Figure 4.19 of Appendix 4.A. Furthermore, it is possible that a fraction of Fe at the surface of these salts is covered by the bound epicatechin and therefore the detection intensity of iron can be decreased in XPS measurements due to this spatial hindrance.

4.3.5 Possible mechanism for reactivity of iron from Fe(III)PP and mixed Ca-Fe(III) pyrophosphate salts

This study demonstrates that the dissolution behavior of iron from Fe(III)PP and the mixed Ca-Fe(III) pyrophosphate salts depends on the x -value of the salt, the pH, the solubility of the phenolic compound, and the Fe(III)-coordinating group(s) of the phenolic compound. Figure 4.7 schematically summarizes the fate of the Fe(III)-containing pyrophosphate salts with different x -values in the absence and presence of the phenolics at pH 6-6.5 (representative pH for food products).

In the absence of phenolics, the salts with $x \leq 0.18$ show up to an eight-fold decrease in soluble iron concentration compared to Fe(III)PP. In the presence of water-soluble phenolics, the color of both the supernatant and the precipitate is negatively affected. Firstly, the precipitate turns dark due to interactions of the water-soluble phenolic with the iron present at the surface of the salts. Secondly, after binding the water-soluble phenolic to the iron at the surface, the iron-phenolic complex releases into solution and becomes soluble, causing discoloration of the supernatant. For slightly water-soluble and insoluble phenolics with an *ortho*-diphenolic group, we suggest that the soluble iron can form stable charged complexes that are solubilized in water, leading to discoloration in both the supernatant and precipitate. For

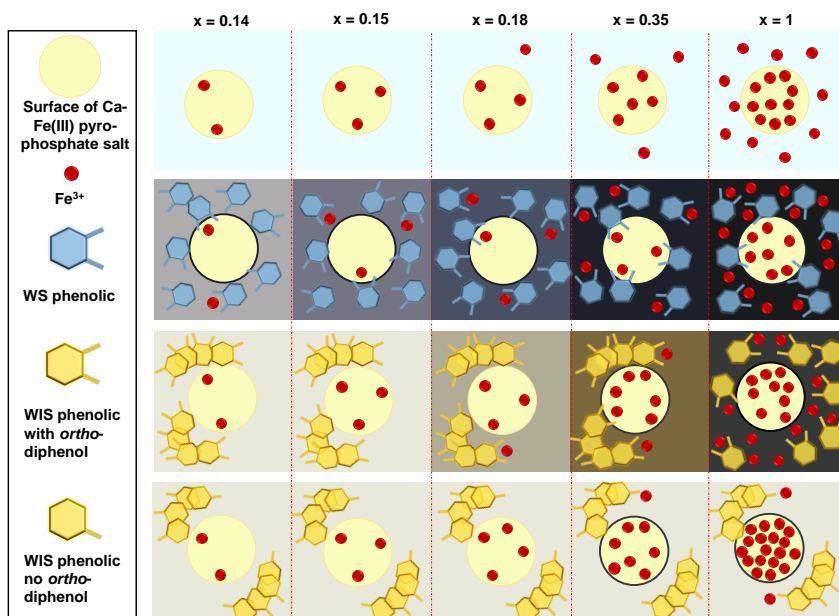


Figure 4.7 Schematic overview of possible mechanism for reactivity of iron from Fe(III)PP and mixed Ca-Fe(III) pyrophosphate salts. The proposed mechanism underlies the observed dissolution behavior of iron at the surface of the Fe(III)PP ($x = 1$) and mixed Ca-Fe(III) pyrophosphate salts with $x = 0.14, 0.15, 0.18$, and 0.35 , and the reactivity of iron from these salts in the presence of phenolics at pH 6. The colors in the squares are in line with the experimentally observed color of the supernatant, a dark outline on the salt surface indicates the discoloration observed in the precipitate. WS = water-soluble, WIS = slightly water-soluble or water-insoluble.

slightly water-soluble and insoluble phenolics without the *ortho*-diphenolic group, there is no interaction between the iron and the phenolic for the mixed salts with $x \leq 0.18$. If iron is already present in the solution (i.e., $x = 0.35$ and 1), it can coordinate with the insoluble phenolic and cause discoloration in the precipitate but these Fe(III)-phenolic coordinates remain insoluble. The schematic overview in Figure 4.7 only applies when the pH is above the apparent pK_a of the phenolic compounds, as deprotonation of the phenolic hydroxyl groups is a prerequisite for these interactions.

This is the first study to report that the reactivity of Fe(III)-containing pyrophosphate salts in the presence of phenolic compounds is dependent on the solubility and iron-coordinating groups of the phenolic. Understanding the reactivity of the mixed pyrophosphate salts with phenolics is helpful for the application of these salts in the

design of iron-fortified food products. The present findings show that these salts are potential iron fortificants for application in food products that mainly contain slightly water-soluble phenolic compounds, such as savory concentrates. In future studies, the reactivity of the mixed salts can be assessed in real food products and in the presence of product-specific mixtures of phenolic compounds.

4.4 Conclusions

In this study, we investigate the reactivity of Fe(III)PP and the mixed Ca-Fe(III) pyrophosphate salts (based on the general formula $\text{Ca}_{2(1-x)}\text{Fe}_{4x}(\text{P}_2\text{O}_7)_{(1+2x)}$ with $0 \leq x \leq 1$) in the presence of six different phenolic compounds. Besides iron-phenolic reactivity, which results in complexation and oxidation, the effect of the presence of phenolic compounds on iron solubility from the salts is also assessed. At pH 5-7, the water-soluble phenolics (i.e., catechol, caffeic acid, and epicatechin) increased iron solubility from the mixed pyrophosphate salts up to 11 times, by solubilization of iron from the surface of the salts. This led to unacceptable discoloration as a result of Fe(III)-phenolic complexation. In the presence of the slightly water-soluble (i.e., quercetin and apigenin) and insoluble phenolics (i.e., curcumin), iron from the salts remained practically insoluble. Furthermore, for the salts with $x \leq 0.18$, the color change after exposure to these slightly water-soluble phenolics remained acceptable for application. In addition, all mixed Ca-Fe(III) pyrophosphate salts resulted in significantly less oxidation of epicatechin and quercetin at pH 6 compared to Fe(III)PP. In conclusion, the mixed Ca-Fe(III) pyrophosphate salts with $x \leq 0.18$ can potentially be used as dual-fortificants with limited iron-mediated discoloration and oxidation in foods containing slightly water-soluble or water-insoluble phenolics. In future studies, the reactivity of these salts in the real food products, along with associated changes in other organoleptic properties and *in vitro* iron bio-availability should be addressed.

4.5 Acknowledgments

We are grateful to Barend van Lagen (Organic Chemistry, Wageningen University & Research) and Judith Bijlsma (Food Chemistry, Wageningen University & Research) for performing the XPS, and RP-UHPLC-PDA-ESI-IT-MSⁿ measurements, respectively. Arjen Reichwein, Raymond Nijveld, and Teun de Bruin of Nouryon Chemicals B.V. are thanked for performing the ICP-AES measurements. The graphical abstract was made with content from BioRender.com.

4.A Appendix

4.A.1 Dissolution of CaPP, Fe(III)PP, and mixed Ca-Fe(III) pyrophosphate salts in the presence of the phenolics by inductively coupled plasma – atomic emission spectroscopy (ICP-AES)

Inductively coupled plasma–atomic emission spectroscopy (ICP-AES) was used for independent verification of the iron quantification by the ferrozine assay. For ICP-AES measurements, CaPP, Fe(III)PP, and the mixed Ca-Fe(III) pyrophosphate salts were re-dispersed in water by stirring (~ 250 rpm) with a magnetic stir bar (final amount of salt 10 mg/ml) followed by the addition of aqueous solutions (i.e., catechol, caffeic acid, and epicatechin) or dispersions (i.e., quercetin, apigenin, and curcumin) of the phenolics at a final concentration of 5 mM. pH was set to reach a target pH 3, 6, or 8 after 2 h of incubation at 23 °C while mixing at 1000 rpm. Samples were five times diluted in 0.14 M HNO₃, before injection in the ICP-AES system (Agilent 5110 VDV; Agilent Technologies, Tokyo, Japan). Independent duplicate samples were taken from the salts at each pH point by independent titrations. The concentration of iron, calcium, and phosphorus was determined using scandium as an internal standard. The limit of detection values of iron, calcium, and phosphorus were respectively 0.05, 0.05, and 0.20 mg/l, the limit of quantification values were 0.15, 0.15, and 0.61 mg/l, respectively.

4.A.2 Elution profiles reversed-phase chromatography

Elution profiles reversed-phase chromatography The following elution profile was used to measure the solubility of the phenolics at pH 3, 6, and 8: 0.00 – 1.09 min, isocratic on 1 vol.% B; 1.09 – 20.72 min, linear gradient from 1 – 55 vol.% B; 20.72 – 21.81 min linear gradient from 55 – 100 vol.% B; 21.81 – 27.26 min isocratic on 100 vol.% B; 27.26 – 28.35 min linear gradient from 100 – 1 vol.% B; 28.35 – 33.81 min isocratic on 1 vol.% B. The following elution profile was used to monitor the oxidation of epicatechin and quercetin: 0.00 – 1.09 min, isocratic on 1 vol.% B; 1.09 – 13.45 min, linear gradient from 1 – 35 vol.% B; 13.45 – 14.54 min linear gradient from 35 – 100 vol.% B; 14.54 – 19.99 min isocratic on 100 vol.% B; 19.99 – 21.08 min linear gradient from 100 – 1 vol.% B; 21.08 – 26.54 min isocratic on 1 vol.% B.

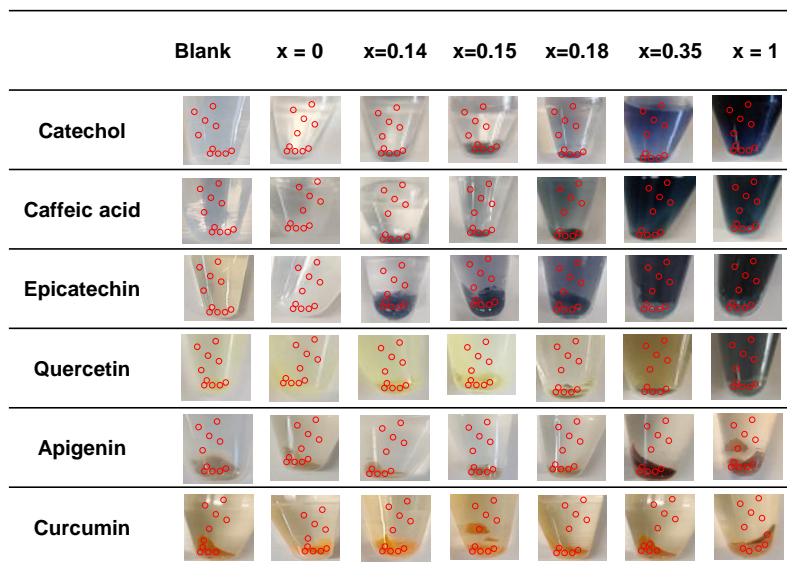


Figure 4.8 Images of Eppendorf tubes containing the studied phenolics in combination with CaPP ($x = 0$), Fe(III)PP ($x = 1$), and the mixed Ca-Fe(III) pyrophosphate salts with $x = 0.14, 0.15, 0.18$, and 0.35 at pH 6. The red spots indicate the positions where the $L^*a^*b^*$ values were extracted using a standard image analysis software (Photoshop CC2021, Adobe).

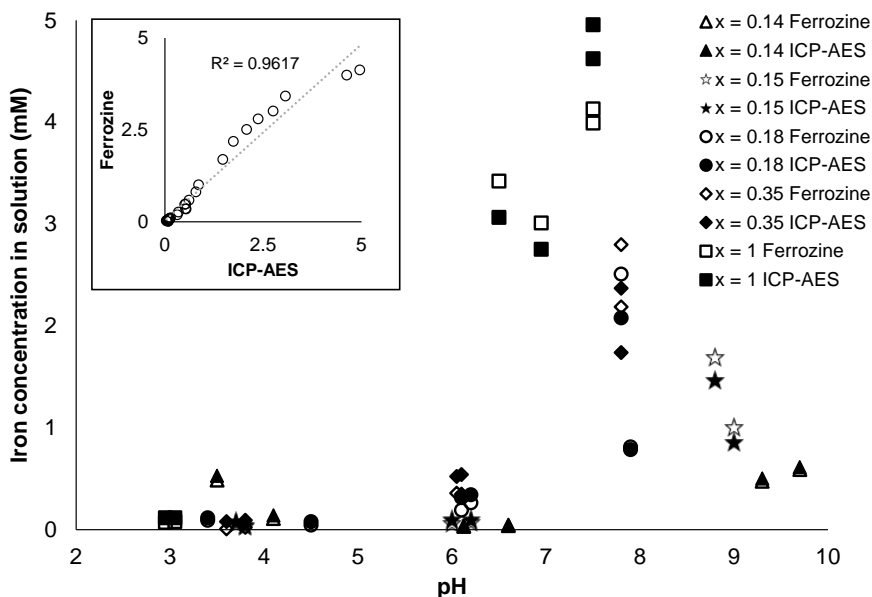


Figure 4.9 Independent verification of ferrozine assay with ICP-AES method. Soluble iron concentration from Fe(III)PP ($x = 1$) and mixed Ca-Fe(III) pyrophosphate salts with $x = 0.14, 0.15, 0.18$, and 0.35 in the presence of epicatechin as a function of pH determined by ICP-AES (filled markers) and by the ferrozine (open markers) methods. The inset depicts the correlation between the iron concentration measured using both methods. The iron concentrations in solution measured by the two different methods were found to be in good agreement ($R^2 = 0.96$).

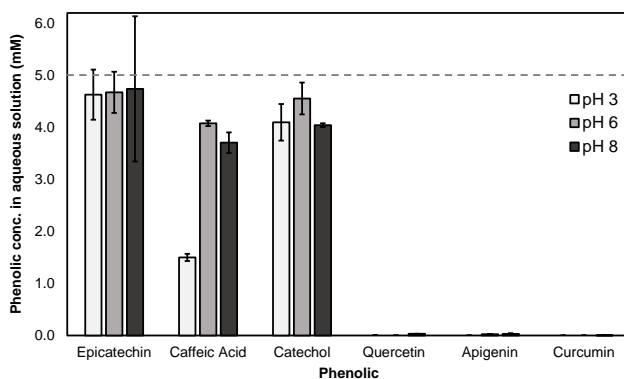


Figure 4.10 Water solubility of the phenolics in the absence of any iron- or calcium-containing salts at pH 3, 6, and 8 as quantified by RP-UHPLC-PDA-MS. The dashed line indicates the prepared concentration of the phenolic solution.

Table 4.1 Iron content (mole percentage), theoretical maximum concentration (mM), and the measured iron concentration (mM) from Fe(III)PP ($x = 1$) and the mixed Ca-Fe(III) pyrophosphate salts with $x = 0.14, 0.15, 0.18$, and 0.35 , based on the iron content of the salt and the amount of salt in the starting dispersion (10 mg/ml for all salts).

x-value	Iron content (Mole %)	Theoretical maximum iron concentration (mM)	Measured iron concentration (mM)		
			pH 3	pH 6	pH 8
0.14	4.06	17.35	0.232±0.000 ^a	0.006±0.000	0.059±0.001
0.15	4.29	17.75	0.365±0.017	0.032±0.003	0.307±0.014
0.18	4.93	21.03	0.265±0.005	0.147±0.002	0.608±0.009
0.35	7.78	32.87	0.080±0.004	1.422±0.037	3.148±0.037
1	12.90	53.69	0.028±0.001	0.810±0.029	3.198±0.016

^a standard deviation of independent duplicates

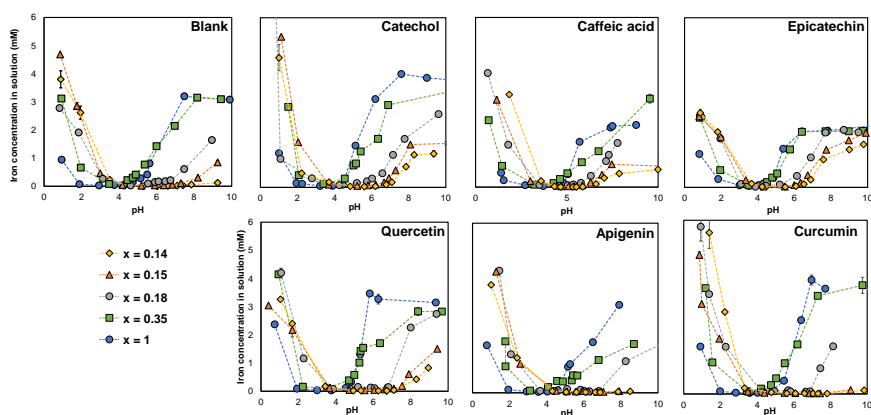


Figure 4.11 Dissolution behavior of iron from Fe(III)PP ($x = 1$) and the mixed Ca-Fe(III) pyrophosphate salts with $x = 0.14$, $x = 0.15$, $x = 0.18$, and $x = 0.35$ at pH 1-10; in the absence of phenolics (blank), and in presence of catechol, caffeic acid, epicatechin, quercetin, apigenin, and curcumin at 23 °C.

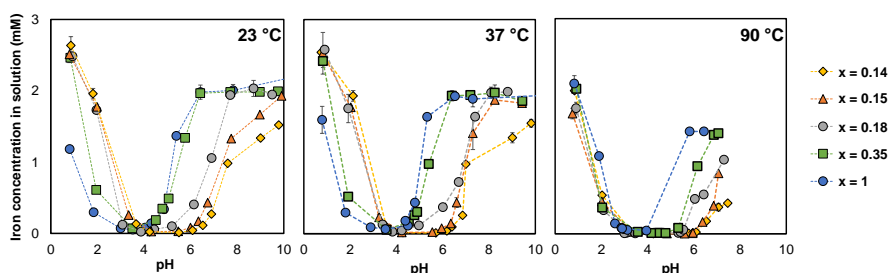


Figure 4.12 Effect of temperature on dissolution behavior of iron. Dissolution behavior of iron from Fe(III)PP ($x = 1$) and the mixed Ca-Fe(III) pyrophosphate salts with $x = 0.14$, $x = 0.15$, $x = 0.18$, and $x = 0.35$ at pH 1-10 in the presence of epicatechin at 23, 37, and 90 °C.

Table 4.2 Reported stability constants of Fe(III) with the phenolic compounds tested in this study.

Phenolic	Log β	Reference
Catechol	43.8	³⁷
Caffeic acid	18.9	³⁸
Catechin	47.4	IUPAC. (1979). IUPAC stability constants of metal-ion complexes, part B, organic ligands. Oxford, UK: Pergamon Press. ¹²
Quercetin	44.2	³⁹
Apigenin	Not reported	-
Curcumin	22.1	⁴⁰

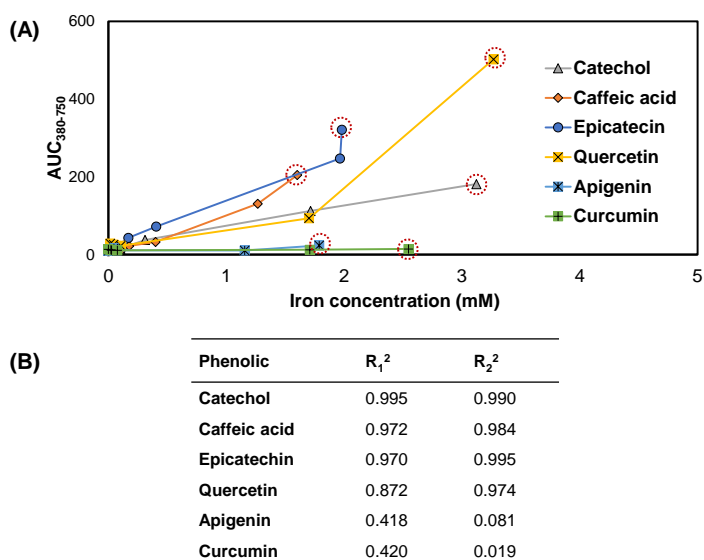


Figure 4.13 The area under curve in the range of 380-750 nm ($AUC_{380-750}$) vs. the soluble iron concentration. (A) Relationship between the area under the curve in the visible light spectra ($AUC_{380-750}$) versus the iron concentration in solution and (B) R_1^2 the regression value from the mixed salts and Fe(III)PP (including the red dashed point from A), and R_2^2 the regression value of the mixed salts only (excluding the red dashed point from A).

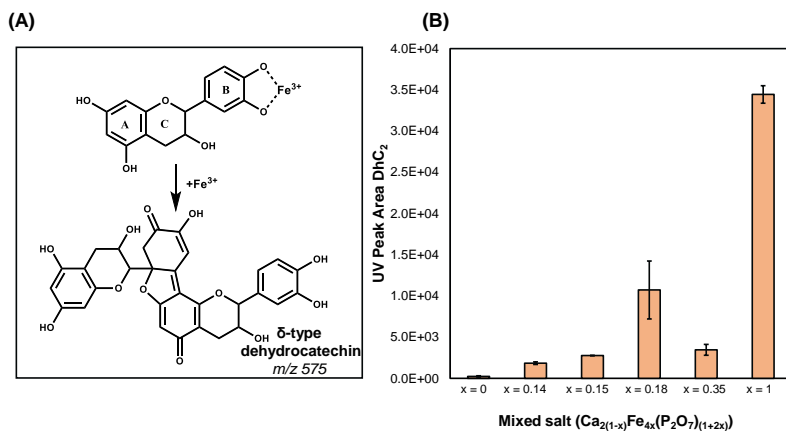


Figure 4.14 Details of oxidation of epicatechin. **(A)** Proposed main oxidation compound (δ -type dehydrocatechin; δ -type DhC₂) of Fe(III)-mediated oxidation of epicatechin^{2,33}. **(B)** Bar graph indicating the peak area of δ -type DhC₂ after incubation of CaPP ($x = 0$), Fe(III)PP ($x = 1$), and the mixed Ca-Fe(III) pyrophosphate salts with epicatechin at pH 6.

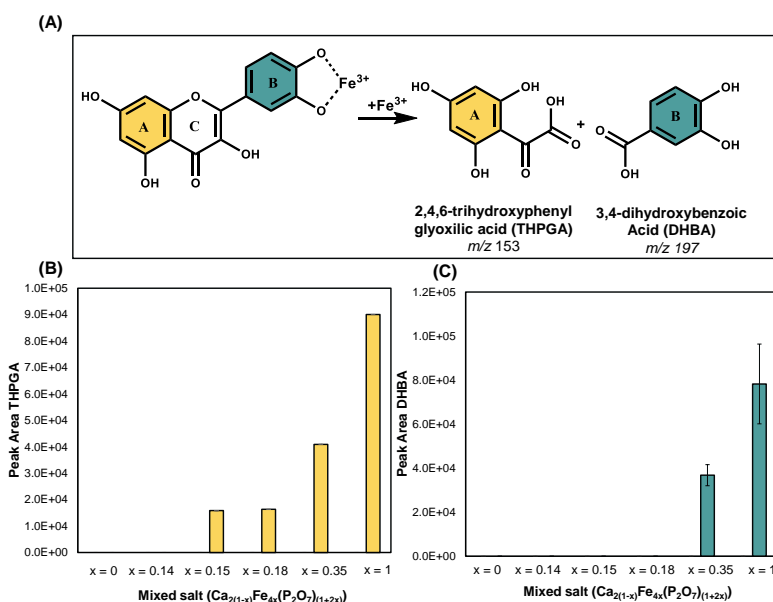


Figure 4.15 Details of oxidation of quercetin. **(A)** Main oxidation compounds of Fe(III)-mediated oxidation of quercetin². Bar graphs indicating the peak area of **(B)** THPGA and **(C)** DHBA after incubation of CaPP ($x = 0$), Fe(III)PP ($x = 1$), and the mixed Ca-Fe(III) pyrophosphate salts with $x = 0.14, 0.15, 0.18$, and 0.35 , with quercetin at pH 6.

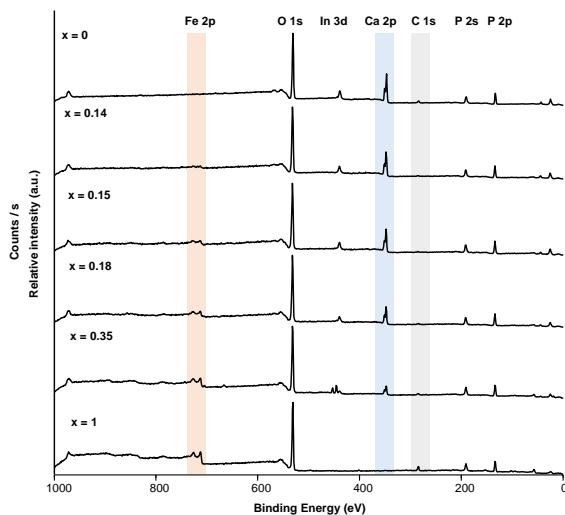


Figure 4.16 Surface composition of the salts. XPS Wide scan spectrum of CaPP ($x = 0$), Fe(III)PP ($x = 1$), and the mixed Ca-Fe(III) pyrophosphate salts with $x = 0.14, 0.15, 0.18$, and 0.35 . The salts were measured on an indium (In) surface.

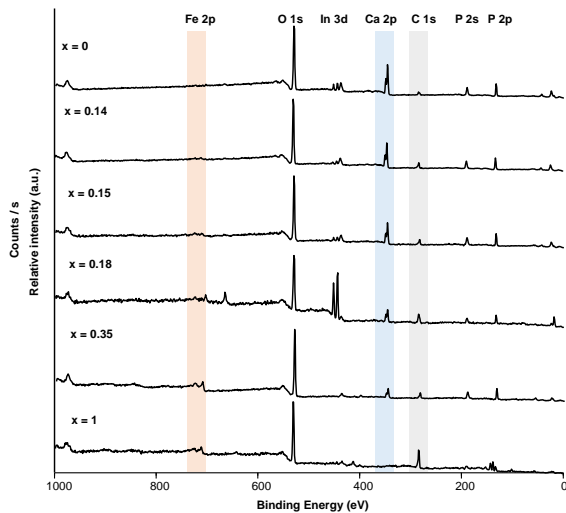


Figure 4.17 Surface composition of the salts after exposure to epicatechin. XPS Wide scan spectrum of CaPP ($x = 0$), Fe(III)PP ($x = 1$), and the mixed Ca-Fe(III) pyrophosphate salts with $x = 0.14, 0.15, 0.18$, and 0.35 after incubation with epicatechin (pH 6). The salts were measured on an indium (In) surface.

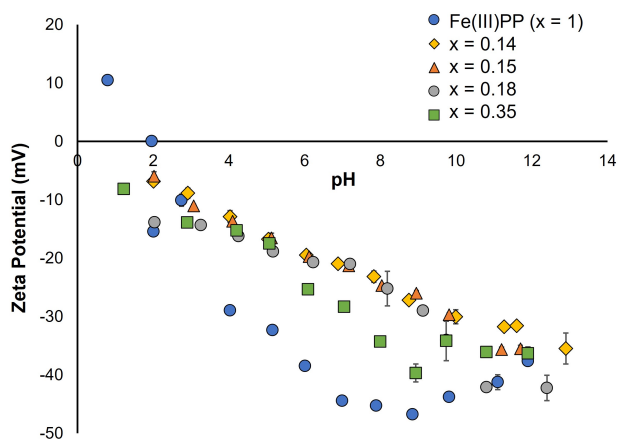


Figure 4.18 Zeta potential of the salts as a function of pH. The zeta potential of the Fe(III)PP ($x = 1$) and the mixed Ca-Fe(III) pyrophosphate salts with $x = 0.14, 0.15, 0.18$, and 0.35 as a function of the pH of their dispersions.

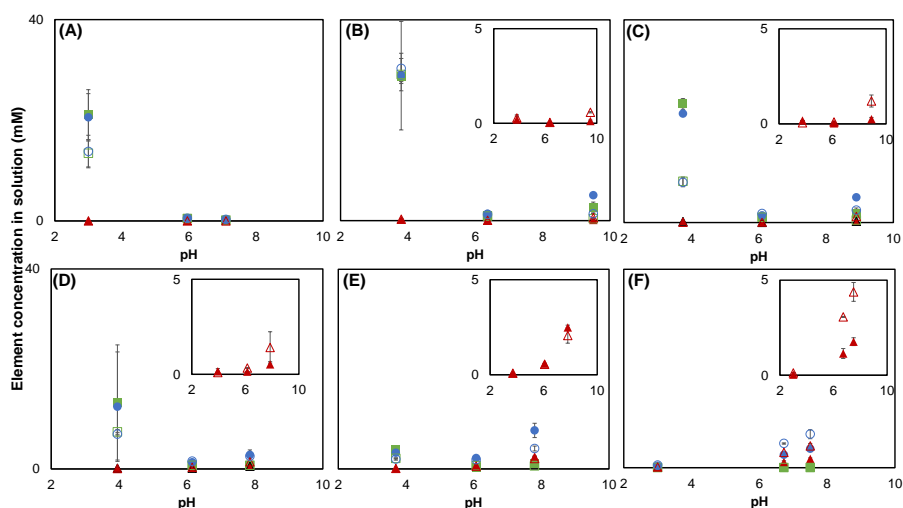


Figure 4.19 Comparison between the elements concentrations in the solution in the absence and presence of epicatechin. Concentration of iron (red triangle), calcium (green square), and phosphorus (blue circle) quantified by ICP-AES in aqueous supernatant for (A) CaPP ($x = 0$) and the mixed Ca-Fe(III) pyrophosphate salts with (B) $x = 0.14$, (C) $x = 0.15$, (D) $x = 0.18$, (E) $x = 0.35$, and (F) Fe(III)PP ($x = 1$) in the absence (filled markers) and presence (open markers) of epicatechin. The insets show the corresponding iron concentration in solution.

References

- 1 L. Allen, B. de Benoist, O. Dary, and R. Hurrell, World Health Organization , 341 (2006).
- 2 J. Bijlsma, W. J. de Bruijn, K. P. Velikov, and J. P. Vincken, Food Chemistry **370**, 131292 (2022).
- 3 E. Habeych, V. van Kogelenberg, L. Sagalowicz, M. Michel, and N. Galaffu, Food Research International **88**, 122 (2016).
- 4 R. H. Janssen, G. Canelli, M. G. Sanders, E. J. Bakx, C. M. Lakemond, V. Fogliano, and J. P. Vincken, Scientific Reports **9**, 1 (2019).
- 5 C. M. Andre, D. Evers, J. Ziebel, C. Guignard, J.-F. Hausman, M. Bonierbale, T. zum Felde, and G. Burgos, Journal of Agricultural and Food Chemistry **63**, 9012 (2015).
- 6 R. Hurrell, Nestel, Beard, and Freire, Nutrition reviews **60**, S7 (2002).
- 7 V. Dueik, B. Chen, and L. Diosady, Journal of Food Quality **2017** (2017).
- 8 R. Hurrell, S. Lynch, T. Bothwell, H. Cori, R. Glahn, E. Hertrampf, Z. Kratky, D. Miller, M. Rodenstein, H. Streekstra, B. Teucher, E. Turner, C. Yeung, and M. Zimmermann, International Journal for Vitamin and Nutrition Research **74**, 387 (2004).
- 9 N. Moslehi, J. Bijlsma, W. J. de Bruijn, K. P. Velikov, J.-P. Vincken, and W. K. Kegel, Journal of Functional Foods **92**, 105066 (2022).
- 10 F. Mohammed, F. Rashid-Doubell, S. Cassidy, and F. Henari, Spectrochimica Acta Part A: Molecular and Biomolecular Spectroscopy **183**, 439 (2017).
- 11 E. Nkhili, M. Loonis, S. Mihai, H. El Hajji, and O. Dangles, Food function **5**, 1186 (2014).
- 12 N. R. Perron and J. L. Brumaghim, Cell biochemistry and biophysics **53**, 75 (2009).
- 13 M. C. Sorkun, A. Khetan, and S. Er, Scientific Data **6**, 143 (2019).
- 14 A. M. Delgado, M. Issaoui, and N. Chammem, Journal of AOAC International **102**, 1356 (2019).
- 15 R. C. Hider, Z. D. Liu, and H. H. Khodr, "Metal chelation of polyphenols," in *Methods in Enzymology*, Vol. 335 (Elsevier, 2001) pp. 190–203.
- 16 L. L. Stookey, Analytical chemistry **42**, 779 (1970).
- 17 H. Araki, J. Kim, S. Zhang, A. Banks, K. E. Crawford, X. Sheng, P. Gutruf, Y. Shi, R. M. Pielak, and J. A. Rogers, Advanced Functional Materials **27**, 1604465 (2017).
- 18 C. Poynton, *Digital video and HD: Algorithms and Interfaces* (Elsevier, Waltham, MA, USA, 2012).
- 19 T. Tian, E. Blanco, S. K. Smoukov, O. D. Velev, and K. P. Velikov, Food Chemistry **208**, 97 (2016).
- 20 A. A. El-Sherif, M. M. Shoukry, and M. M. A. Abd-Elgawad, Journal of Solution Chemistry **42**, 412 (2013).
- 21 M. Giesbers, A. T. M. Marcelis, and H. Zuilhof, Langmuir **29**, 4782 (2013).
- 22 A. Liangou, K. Florou, M. Psychoudaki, E. Kostenidou, E. Tsiligiannis, and S. N. Pandis, Environmental Science Technology **56**, 3952 (2022).
- 23 J. H. Swain, S. M. Newman, and J. R. Hunt, The Journal of nutrition **133**, 3546 (2003).

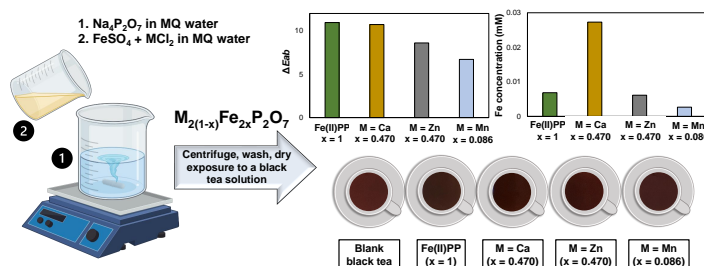
- 24 D. Moretti, R. F. Hurrell, and C. I. Cercamondi, "Bouillon cubes," in *Food Fortification in a Globalized World* (Elsevier, 2018) pp. 159–165.
- 25 S. Ghidouche, B. Rey, M. Michel, and N. Galaffu, *Food Chemistry* **139**, 978 (2013).
- 26 R. Wegmüller, M. B. Zimmermann, and R. F. Hurrell, *Journal of Food Science* **68**, 2129 (2003).
- 27 J. Bijlsma, W. J. de Bruijn, J. A. Hageman, P. Goos, K. P. Velikov, and J. P. Vincken, *Scientific Reports* **10**, 1 (2020).
- 28 M. Elhabiri, C. Carrër, F. Marmolle, and H. Traboulsi, *Inorganica Chimica Acta* **360**, 353 (2007).
- 29 L. Malacaria, C. La Torre, E. Furia, A. Fazio, M. C. Caroleo, E. Cione, L. Gallelli, T. Marino, and P. Plastina, *Journal of Molecular Liquids* **345**, 117895 (2022).
- 30 L. Malacaria, G. A. Corrente, A. Beneduci, E. Furia, T. Marino, and G. Mazzone, *Molecules* **26**, 2603 (2021).
- 31 J. Guo, Y. Ping, H. Ejima, K. Alt, M. Meissner, J. J. Richardson, Y. Yan, K. Peter, D. Von Elverfeldt, and C. E. Hagemeyer, *Angewandte Chemie International Edition* **53**, 5546 (2014).
- 32 P. Ryan and M. J. Hynes, *Journal of Inorganic Biochemistry* **102**, 127 (2008).
- 33 J. Tan, W. J. C. de Bruijn, A. van Zadelhoff, Z. Lin, and J.-P. Vincken, *Journal of Agricultural and Food Chemistry* **68**, 13879 (2020).
- 34 V. Stepanic, A. C. Gasparovic, K. G. Troselj, D. Amic, and N. Zarkovic, *Current Topics in Medicinal Chemistry* **15**, 496 (2015).
- 35 N. Zuidam, in *Encapsulation Technologies and Delivery Systems for Food Ingredients and Nutraceuticals* (Elsevier, 2012) pp. 505–540.
- 36 Y. M. van Leeuwen, *Colloidal Metal Pyrophosphates Salts Preparation, Properties and Applications*, Ph.D. thesis (2013).
- 37 A. Avdeef, S. R. Sofen, T. L. Bregante, and K. N. Raymond, *Journal of the American Chemical Society* **100**, 5362 (1978).
- 38 M. J. Hynes and M. O’Coinceanainn, *Journal of Inorganic Biochemistry* **98**, 1457 (2004).
- 39 G. M. Escandar and L. F. Sala, *Canadian journal of chemistry* **69**, 1994 (2011).
- 40 M. Borsari, E. Ferrari, R. Grandi, and M. Saladini, *Inorganica Chimica Acta* **328**, 61 (2002).

Part II

Iron (II)-containing pyrophosphate salts

Mixed Fe(II)-containing pyrophosphate salts: Design and characterization for dual-fortification of foods

Abstract



Even though iron (II) has been proven to be more bio-accessible than iron (III), to date the possibilities of using ferrous pyrophosphate (Fe(II)PP) for food applications have not been explored, compared to the widely-applied ferric pyrophosphate (Fe(III)PP). In the current work, Fe(II)PP as well as the mixed Fe(II)-containing pyrophosphate salts with the general formula $\text{M}_{2(1-x)}\text{Fe}_{2x}\text{P}_2\text{O}_7$ ($0 \leq x \leq 1$, where $\text{M} = \text{Ca}, \text{Zn}, \text{or Mn}$) were synthesized as simultaneous delivery systems for iron and a second mineral (M). The salts were prepared via a fast and facile co-precipitation method and characterized by TEM-EDX, ICP-AES, XRD, and FT-IR. Furthermore, the iron-mediated reactivity of these salts was assessed using a black tea solution. Results showed that the Fe(II)PP caused 1.5 times less discoloration of the black tea solution, compared to Fe(III)PP. Moreover, exposure of the black tea solution to the mixed salts with $x = 0.470$ and 0.086 in which $\text{M} = \text{Zn}$ and Mn , respectively, resulted in reduced discoloration, with respect to Fe(II)PP. Our results indicate that the pure Fe(II)PP and mixed Fe(II)-containing pyrophosphate salts are potential candidates for dual-fortification of foods.

This chapter is based on N. Moslehi, J. Bijlsma, W. K. Kegel, and K. P. Velikov, "Iron-fortified food product", WO2022048952A1 (2022).

"Yesterday I was clever so I wanted to change the world. Today I am wise so I am changing myself."

Rumi – Persian poet, 1207-1273

5.1 Introduction

As it was mentioned before, iron is a problematic mineral as a food additive due to its high reactivity with phenolic compounds that are plentiful in plants and vegetables^{1,2}. In order to address the issue of high reactivity of iron with the chemicals present in foods, fortification of food products with poorly water-soluble or water-insoluble iron sources such as iron (III) pyrophosphate (Fe(III)PP) has been proven to be a beneficial and cost-effective approach³⁻⁵. Formerly, it was shown that Fe(III)PP has low water solubility (< 5%) at pH 2-5.5, yet dissolves well below pH 2^{6,7}. Even though poorly soluble Fe(III)PP can cause fewer changes in the organoleptic properties, it has been shown before that it cannot fully suppress the iron-mediated reactions with phenolic compounds upon addition to foods in the pH range relevant to human diet^{8,9}. Furthermore, poorly soluble Fe(III)PP has the drawback of low iron bio-availability and consequently inadequate iron update in the human body^{10,11}. In contrast, it has been shown that Fe(II) is better absorbed than Fe(III),¹² and iron (II) sources such as ferrous sulfate and ferrous fumarate, exhibit high iron bio-availability⁴. Nevertheless, due to their high solubility and therefore high iron-mediated reactivity with foods, they are not preferred for foods that are highly sensitive to color and flavor changes¹³, and are often encapsulated which is less desirable due to the higher costs of preparation¹⁴⁻¹⁶.

Among iron (II) sources, there is a lack of published literature on iron (II) pyrophosphate (Fe₂P₂O₇, Fe(II)PP) salt. Fe(II)PP is widely studied as anode material with relatively higher specific capacity and better cyclic performance for lithium-ion batteries¹⁷⁻¹⁹. However, it has not been investigated for its potential in food applications to our knowledge. Although Fe(III)PP is more preferred to be introduced to foods because of its off-white color, compared to the green Fe(II)PP, the advantage of using the latter is delivering iron in ferrous form which has been previously shown to have a significantly higher absorption, compared to ferric form^{12,20}.

It was previously demonstrated that inclusion of a divalent metal such as Ca alongside iron (III) in pyrophosphate matrix enhanced the iron solubility from the mixed Ca-Fe(III) pyrophosphate salts in gastric condition (pH 1-3) up to fourfold, while showing decreased iron solubility up to eight-fold in food pH range (3-7), compared to Fe(III)PP, see chapter 3⁶. Additionally, it was shown by van Leeuwen and

co-authors that incorporation of an excess amount of a divalent metal (M) such as Mg in ferric pyrophosphate (i.e., Mg:Fe(III) ratio 50:1), hindered its reactivity towards phenolics²¹. Therefore, we hypothesize that the combination of a second divalent metal and Fe(II) in one pyrophosphate matrix will result in reduced iron-mediated reactivity of the Fe(II)-containing salts. Besides decreasing the reactivity of iron by embedding it in another less chemically reactive mineral carrier, the main advantage of these compounds is that they can be potential dual-fortificants with tunable composition of a second essential mineral, in this case calcium, zinc, or manganese, along with iron.

In this research study, we establish the potential of pure Fe(II)PP and mixed Fe(II)-containing pyrophosphate salts in the field of food fortification. To do so, we investigate the possibility of mixing Fe(II) with a second divalent metal in the pyrophosphate matrix, based on the general formula, $M_{2(1-x)}Fe_{2x}P_2O_7$, ($0 < x < 1$, where M = Ca, Zn, or Mn), as simultaneous delivery systems for two essential minerals (i.e., Fe and M). Conventional co-precipitation is used as the synthesis method to integrate iron (II) and the second divalent metal homogeneously into one pyrophosphate salt matrix. Moreover, the chemical compositions of the salts are explored by TEM-EDX and ICP-AES, and their crystallinity is investigated by XRD and FT-IR. Finally, the designed salts are tested for their Fe-mediated discoloration of a black tea solution as a representative model for phenolics (in particular catechins).

5.2 Materials and methods

5.2.1 Materials

Iron (III) chloride hexahydrate ($FeCl_3 \cdot 6H_2O$, ≥ 99 wt.%), Iron (II) chloride tetrahydrate ($FeCl_2 \cdot 4H_2O$, ≥ 99 wt.%), manganese (II) chloride ($MnCl_2$, ≥ 96 wt.%), tetrasodium pyrophosphate decahydrate ($Na_4P_2O_7 \cdot 10H_2O$, > 99 wt.%), calcium dichloride ($CaCl_2$, > 93 wt.%), nitric acid (HNO_3 , 65 wt.%), and 3-(2-pyridyl)-5,6-diphenyl-1,2,4-triazine-*p,p'*-disulfonic acid monosodium salt hydrate (i.e., ferrozine; ≥ 97 wt.%), were obtained from Sigma Aldrich (St. Louis, MO, USA). Iron (II) sulfate heptahydrate ($FeSO_4 \cdot 7H_2O$, ≥ 99 wt.%) and anhydrous zinc chloride ($ZnCl_2$, ≥ 98 wt.%) were obtained from Alfa Aesar (Haverhill, MA, USA). Ethanol absolute (≥ 99 wt.%) and ascorbic acid (≥ 99 wt.%) were obtained from VWR International (Radnor, PA, USA). The Milli-Q (MQ) water used was deionized by a Millipore Synergy water purification system (Merck Millipore, Billerica, MA, USA). The tea used for preparing the tea solutions was an Original English tea blend from Pickwick[®] (Amsterdam, The Netherlands).

5.2.2 Preparation of pure and mixed divalent metal salts

Pure divalent metal pyrophosphate salts

Pure salts were synthesized as references for comparative purposes. The preparation was done via a co-precipitation method similar to the methods described in chapter 2^{6,22,23}. Firstly, solutions of 1.286 mmol $\text{FeSO}_4 \cdot 7\text{H}_2\text{O}$, CaCl_2 , ZnCl_2 , and MnCl_2 in 50 ml of MQ water were prepared independently. Following this, the solutions were added quickly (within 5 seconds) to a solution of 0.643 mmol $\text{Na}_4\text{P}_2\text{O}_7 \cdot 10\text{H}_2\text{O}$ (NaPP) in 100 ml of MQ water in order to prepare iron (II) pyrophosphate ($\text{Fe}_2\text{P}_2\text{O}_7$, Fe(II)PP), calcium pyrophosphate ($\text{Ca}_2\text{P}_2\text{O}_7$, CaPP), zinc pyrophosphate ($\text{Zn}_2\text{P}_2\text{O}_7$, ZnPP), and manganese (II) pyrophosphate ($\text{Mn}_2\text{P}_2\text{O}_7$, MnPP), respectively. This was done while the NaPP solution was stirring vigorously (~ 400 rpm) with a magnetic stir bar. In the case of the Fe(II)PP a turbid green, and in other cases turbid white/off-white dispersions were formed a few seconds after the addition. The samples were then centrifuged at $3273 \times g$ for 30 minutes in 50 ml volume polypropylene conical centrifuge tubes using an Allegra X-12R Centrifuge (Beckman Coulter, Brea, CA, USA). This was followed by washing the precipitate with MQ water twice. Finally, the salts were dried overnight in an oven at 45°C (Fe(II)PP: 88%, CaPP: 74%, ZnPP: 80%, and MnPP: 72% yield).

Mixed divalent metal Fe(II)-containing pyrophosphate salts

The mixed divalent metal salts were prepared by the same procedure as the pure salts, by addition of 50 ml of a mixed solution of $\text{FeSO}_4 \cdot 7\text{H}_2\text{O}$ and CaCl_2 , ZnCl_2 , or MnCl_2 in MQ water to a solution of NaPP with a fixed concentration of pyrophosphate ions (6.43 mM, 100 ml). Three different series of mixed Fe(II)-containing pyrophosphate salts each with a second divalent metal M, and different M to Fe(II) ratios were prepared, based on the general formula $\text{M}_{2(1-x)}\text{Fe}_{2x}\text{P}_2\text{O}_7$ ($0 < x < 1$), for different theoretical x-values (i.e., 0.05, 0.10, 0.25, and 0.50, coded as MMix1 to MMix4, respectively, where M = Ca, Zn, or Mn). After adding the mixed solutions to NaPP, the solutions were stirred vigorously (~ 400 rpm) with a magnetic stir bar (final concentration of NaPP: 4.29 mM). The molar ratio of total metal ions (i.e., $[\text{M}] + [\text{Fe}]$, final concentration: 8.573 mM) to pyrophosphate ions was 2:1. In all ratios, a turbid dispersion was formed a few seconds after the addition. The samples were then centrifuged, washed, and dried in an oven following the same procedures as explained for the pure divalent metal salts, see section 5.2.2. The colors of the dried powders of all the mixed as well as the pure salts were visualized by taking an image of them illuminated with a uniform light source using identical camera settings. The images were evaluated using an online color conversion tool (<https://imagecolorpicker.com/>) and converted to the $L^*a^*b^*$ color space (i.e., L^* dark or light, a^* red vs. green, b^* yellow vs. blue), see Figure 5.7 of Appendix 5.A. It is worth recalling here that the x-values in

the general formula indicate the minerals (i.e., M and Fe(II)) composition of the salts. Consequently, the mole ratios were calculated based on which the x-value was found in the structural formula. The average yields of the prepared mixed salts with M = Ca, Zn, and Mn were $33 \pm 3\%$, $69 \pm 10\%$, and $82 \pm 7\%$, respectively. Standard deviation was calculated based on three independent syntheses of all the mixed salts.

5.2.3 Characterization

Transmission Electron Microscopy (TEM) and energy-dispersive X-ray spectroscopy (EDX)

Water dispersions of the salts were dried on carbon-coated copper and nickel grids for M = Ca and Zn, respectively, and analyzed by transmission electron microscopy (TEM) and energy-dispersive X-ray spectroscopy (EDX). This was performed on a TalosTM F200X (Thermo Fisher Scientific, San Jose, CA, USA) operated at 200 kV. The elemental composition of the mixed salts was obtained by EDX and used for finding the experimental (measured) x-value based on the general formula of the mixed salts. The ratios of the atomic percentages (i.e., $M/Fe = 2(1-x)/2x$, $M/P = 2(1-x)/2$, $Fe/P = 2x/2$) were used to find x in the structural formula $M_{2(1-x)}Fe_{2x}P_2O_7$. The average x-value for each mixed salt was reported with a standard deviation based on 3 replicate preparations of the salts and 3 independent measurements. The average x-values were incorporated in the general formula of the mixed divalent metal pyrophosphate salts to obtain the actual chemical formula of the salts. Elemental composition of the mixed salts in which M = Mn could not be obtained accurately by this technique (TEM-EDX) due to the overlapping Mn and Fe lines in the energy spectrum.

Inductively Coupled Plasma Atomic Emission Spectroscopy (ICP-AES)

For the salts with M = Mn, the chemical composition was obtained by elemental analysis using ICP-AES. After ensuring the identical morphology and homogeneous distribution of Fe and Mn in the salts (i.e., MnMix₁ to MnMix₃), their samples were dissolved in 10 ml of a 2% HNO₃ solution to achieve optimal measurement concentration ranges. ICP-AES measurements were performed using an Optima 8300 instrument (PerkinElmer, Waltham, MA, USA) and in triplicate. Finally, the ratios of Mn/Fe and P/Fe were used to obtain the average x-value for each salt based on the general formula. For the salt with heterogeneous morphology (i.e., MnMix₄), the approximate x-values were estimated using EDX analysis on the different morphological phases separately, as described in the previous section.

High-Angle Annular Dark Field Scanning TEM (HAADF-STEM)

High-angle annular dark-field scanning TEM (HAADF-STEM) was performed on a TalosTM F200X (Thermo Fisher Scientific, San Jose, CA, USA) operated at 200 kV. The elemental mapping was recorded by assigning a color to each element. Color indications are as follows: second divalent metal (i.e., M = Ca, Zn, or Mn): green, iron: red, and phosphorus: blue.

X-Ray Diffraction (XRD)

The dried powders of the salts were analyzed at room temperature with an AXS D2 Phaser powder X-ray diffractometer (Bruker®, Billerica, MA, USA), which was equipped with a LYNXEYE® detector in Bragg-Brentano mode. The radiation used was cobalt $K\alpha_{1,2}$, $\lambda = 1.79026 \text{ \AA}$, operated at 30 kV, 10 mA for $2\theta = 5$ to 70 degrees. A silicon holder was used, and the measurements were repeated twice on the salts from independent synthesis batches.

Fourier Transform Infrared (FT-IR) Spectroscopy

FT-IR measurements were done on dried powders of the samples by an FT-IR spectrometer (PerkinElmer, Waltham, MA, USA), using the KBr pellet technique²⁴. 2.5 mg of each salt was mixed thoroughly with 250 mg of KBr (FT-IR grade) and dried in an oven at 60 °C overnight. Pellets were prepared using a press and the measurements were done in independent duplicate. The interferograms were accumulated over the spectral range of 1600–400 cm^{-1} using a resolution of 4 cm^{-1} , with a background scan recorded before each measurement.

5.2.4 Assessment of the reactivity of iron from the pure and mixed pyrophosphate salts in a black tea solution

To have an early indication of iron-mediated reactivity of the mixed divalent metal pyrophosphate salts, a black tea solution was used as a representing model system for phenolic compounds (catechins). The iron-mediated reactivity of the salts was evaluated by discoloration of the black tea solution caused by the dissolved iron from the salts in the tea solution.

The procedure was similar to what was described in chapter 2. Ground tea leaves of Original English blend (Pickwick®) were added to boiling MQ water (1 g of tea leaves in 100 ml of water). After stirring for 3 minutes, the tea leaves were filtered out using 1541-125 cellulose filter papers (Whatman®, Maidstone, UK). The Fe(II)-containing salts with a normalized concentration of iron (i.e., 1.05 mg Fe in 100 ml tea) were added to the tea solution ($\text{pH} \approx 5.13 \pm 0.13$). For comparison, CaPP, ZnPP, or MnPP with a normalized concentration of 1.05 mg Ca, Zn, or Mn in 100

ml tea were added to the tea solution as well. After stirring for 10 minutes using an RCT basic stirrer (IKA-Werke, Staufen, Germany), the tea solutions were filtered first over Whatman® cellulose filter papers and second over a 17845-ACK Minisart® NY polyamide (nylon) filter with 0.2-micron pore size, (Sartorius, Göttingen, Germany). During the procedure, the temperature was constant at approximately 90 °C. The discoloration of the filtered tea solutions was quantified by ultraviolet-visible light (UV-Vis) spectroscopy at room temperature. The visible spectra of the tea solutions were recorded on a Lambda-35 spectrophotometer (PerkinElmer, Waltham, MA, USA). The increase in absorbance at wavelength range of 500-600 nm was compared to the blank black tea solution and used at the wavelength of 550 nm to quantify the iron-phenolic complexation²⁵. The colors of the tea solutions were visualized by taking an image of all tea solutions standing next to each other illuminated with a uniform light source at room temperature. The images were evaluated using the on-line color conversion tool (mentioned in section 5.2.2). For better elaboration of the discoloration of the black tea solution, the color difference between the tea solutions before and after exposure to the salts, ΔE_{ab} , was used as a numerical tool, as described in chapter 4. In this procedure, the $L^*a^*b^*$ value was taken at three different spots on the images. The absolute value of color difference, ΔE_{ab} , corresponds to the distance between two points within the $L^*a^*b^*$ color space (not only the darkness i.e., L^* value) and is calculated according to Equation 5.1^{26,27}.

$$\Delta E_{ab} = [(L_0^* - L_x^*)^2 + (a_0^* - a_x^*)^2 + (b_0^* - b_x^*)^2]^{1/2} \quad (5.1)$$

Where L_0^* , a_0^* , b_0^* and L_x^* , a_x^* , b_x^* are the color space values for the blank black tea and the black tea after exposure to the salts, respectively.

The concentration of the iron released from the salts in the tea solutions was measured using a ferrozine-based colorimetric assay, as described in chapter 3. The absorbance of total Fe at 565 nm was measured at room temperature by a Lambda-35 spectrophotometer (PerkinElmer, Waltham, MA, USA). It was confirmed that the presence of Ca, Zn, or Mn ions did not interfere with the quantification of total iron, Figure 5.8 of Appendix 5.A. All measurements were performed in independent duplicates and quantification of the dissolved iron was performed based on intensity and with a calibration curve of FeSO_4 (0.0078 – 1 mM, $R^2 > 0.99$). Statistical analysis was carried out to evaluate the significance of differences in iron concentration (significant at $p < 0.05$).

5.3 Results and discussion

5.3.1 Characterization of the pure divalent metal pyrophosphate salts

The morphology of the pure divalent metal pyrophosphate salts (i.e., Fe(II)PP, CaPP, ZnPP, and MnPP) was explored by electron microscopy, Figure 5.1 A. The dried dispersions of these salts showed diverse morphologies. The TEM images of Fe(II)PP showed large aggregates of 50-100 nm thin irregularly-shaped particles, while CaPP yielded interconnected aggregates of noticeably smaller (10-20 nm) spherical particles, which was in line with a previous study²³. Moreover, the TEM image results showed that ZnPP formed relatively larger (roughly 200 nm) platelets of 10-25 nm thick, whereas MnPP was a mixture of round and rod-shaped platelets of maximum 100 nm long, see Figure 5.1 A.

As mentioned in chapter 2, it has previously been shown that the crystallinity of metal pyrophosphate particles can depend on the valence match/mismatch of the metal and pyrophosphate ions²³. In general, divalent metals are expected to form crystalline compounds with pyrophosphate ions due to the less complicated stoichiometric ratio to reach neutrality²³. This was confirmed for CaPP and ZnPP by XRD diffractograms and FT-IR spectra. The X-ray diffraction pattern for CaPP and ZnPP indicated clear signals of highly crystalline structures which are similar to the previously reported diffractograms for monoclinic calcium pyrophosphate tetrahydrate β (m-CPPT β)²⁸ and polymorphs of zinc pyrophosphate^{29,30}, respectively, Figure 5.1 B. In the XRD diffractogram of MnPP, we observed only one signal of crystallinity at approximately $2\theta = 8$ degrees which has not been reported before³¹⁻³³. This could be due to the formation of different polymorphs of pyrophosphate anions during the co-precipitation in water compared to the solid-state preparation. In addition the synthesis method proposed in the current work is similar to synthesis of amorphous MnPP which has been reported before³³. Nevertheless, the pyrophosphate anion is known to possess multiple conformations in the solid state such as staggered and eclipsed the terminal PO_3 groups with a linear or bent P-O-P bridge³³ which can result in appearance or interference of various peaks in the XRD diffractograms. Furthermore, it was expected for Fe(II)PP to show crystalline structure as well based on the stoichiometry of Fe^{2+} and $\text{P}_2\text{O}_7^{4-}$ ions for formation of unit cells^{22,34}. However, the spectrum for Fe(II)PP showed only noise and a broad peak being indicative of amorphous structure for this salt, Figure 5.1 B.

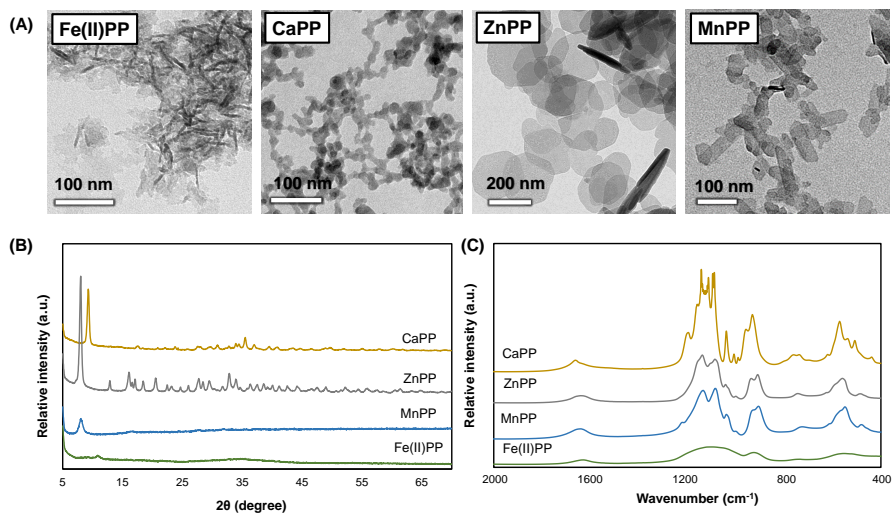


Figure 5.1 Characterization of the pure divalent metal pyrophosphate salts. **(A)** TEM images of Fe(II)PP, CaPP, ZnPP, and MnPP shows formation of 50–100 nm irregularly shaped, 10–20 nm spherical (and aggregated), roughly 200 nm platelets, and 100 nm round and rod-shaped platelets for these salts, respectively. **(B)** Comparison between XRD diffractograms of the pure pyrophosphate salts shows that while CaPP, ZnPP, and MnPP are crystalline, Fe(II)PP is amorphous. **(C)** For the same reason, the FT-IR absorbance of the chemical bonds in the pyrophosphate ions appear sharp and strong for CaPP, ZnPP, and MnPP, and broad and smooth for Fe(II)PP.

The details of chemical bonding in the Fe(II)PP, CaPP, ZnPP, and MnPP were investigated by FT-IR spectrometry, Figure 5.1 C. The FT-IR spectrum for CaPP, ZnPP, and MnPP showed well-defined bands, whereas these peaks appeared broad and smooth for Fe(II)PP at the same wavenumbers. The sharper and well-defined bands were expected for crystalline materials. Spectral broadening in Fe(II)PP was a sign and a result of its amorphous nature. Despite different broadness, peak positions of the main characteristic peaks matched with each other because the pyrophosphate groups are the main vibrationally active species. The characteristic peaks attributed to bending for O-P-O bonds in the P_2O_7 groups appeared around 500–600 cm^{-1} . The signals observed at 745 and 945 cm^{-1} were assigned to symmetric and asymmetric vibrations in P-O-P, respectively, and the peaks in the range of 1000 to 1200 cm^{-1} corresponded to P-O stretching vibration frequencies. All the peaks observed for the $P_2O_7^{4-}$ anion are similar to what was described in chapter 2 as well as previous reports^{6,30,32,35–37}.

5.3.2 Characterization of the mixed divalent metal Fe(II)-containing pyrophosphate salts

The morphology and chemical composition of the mixed divalent metal pyrophosphate salts, designed with $x = 0.05, 0.10, 0.25,$ and 0.50 in $M_{2(1-x)}Fe_{2x}P_2O_7$, (coded as MMix1 to MMix4, where $M = Ca, Zn,$ or Mn) were characterized by electron microscopy, Figure 5.2. TEM images showed that inclusion of Ca as the second divalent metal (i.e., $M = Ca$) in the Fe(II)-containing pyrophosphate salts resulted in homogeneous and similar morphologies to CaPP for all the designed x -values, indicating aggregates of small (10-20 nm) spherical particles for the salts CaMix1-CaMix4, Figure 5.2 A. Moreover, the x -values for the salts CaMix1-CaMix4 were measured (by EDX) to be 0.060, 0.130, 0.240, and 0.470, respectively, which were rather close to the designed x -values, Figure 5.2 D.

In the case of $M = Zn$, the mixed salts yielded aggregates of thin platelets of approximately 100-200 nm large which were homogeneous in terms of their morphology, Figure 5.2 B. The EDX measurements indicated that for these salts the measured x -values were relatively close to but slightly lower than the expected x -values in all the mixed salts; 0.047, 0.074, 0.202, and 0.47 for the salts ZnMix1 to ZnMix4, respectively, Figure 5.2 D.

Detailed analysis of the TEM images and ICP-AES results of the mixed pyrophosphate salts in which $M = Mn$ suggested that incorporating Mn as the second divalent metal alongside Fe(II) in the pyrophosphate matrix yields formation of a uniform morphology which was observed to be irregularly-shaped particles of 100-200 nm in all the mixed salts, except for the salt MnMix4 (i.e., the mixed salt with the highest iron content). Moreover, the average x -values for the salts MnMix1-MnMix3 were measured (by ICP-AES) to be approximately 0.053, 0.086, and 0.220, respectively. The salt MnMix4 yielded local segregation and coexistence of two morphological phases: a rod-shaped phase with relatively higher Fe content (i.e., higher x -value), and irregularly shaped aggregates with lower Fe content (i.e., lower x -value), R: rod shape and I: irregular shape in Figure 5.2 D, respectively. The salt MnMix4 appeared to be a mixture of an iron-rich phase with $x \approx 0.520$, and a manganese-rich phase with $x \approx 0.350$, Figure 5.2 C. The formation of the Fe-rich and Mn-rich phases of particles, resulting in different measured x -values (approximation from EDX quantification), might be explained by the possibility of phase separation in the resulting solid solutions^{7,38}.

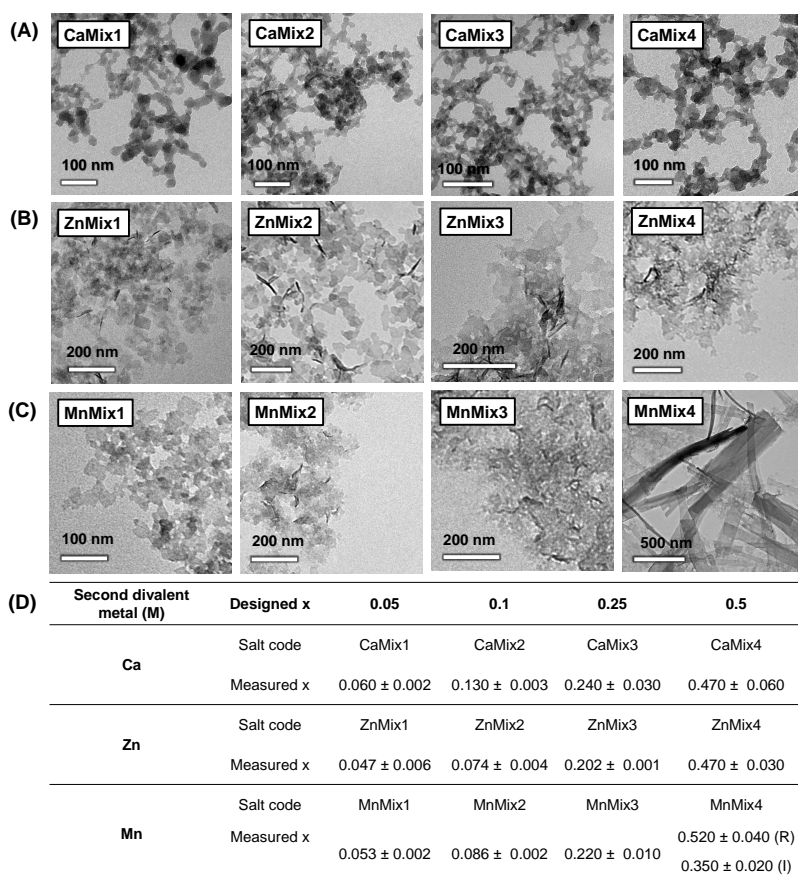


Figure 5.2 Morphology of the mixed divalent metal Fe(II)-containing pyrophosphate salts with the general formula $M_{2(1-x)}Fe_{2x}P_2O_7$, coded as MMix1 to MMix4 where (A) M = Ca, (B) M = Zn, and (C) M = Mn obtained from TEM imaging. Comparison indicates that all the mixed Fe(II)-containing salts yield uniform morphology and homogeneous particles, except for the salt MnMix4 which shows segregation into two coexisting structural phases. **(D)** The measured x-value for the mixed Fe(II)-containing pyrophosphate salts obtained from EDX (for M = Ca and Zn) and ICP-AES (for M = Mn) quantification. The measured x-values for all the mixed salts were close to the designed values, except for in the case of MnMix4. This salt shows different measured x-values for the coexisting morphologies, (R) rod shape and (I) irregular shape.

The elemental distribution in the mixed Fe(II)-containing pyrophosphate salts was visualized by HAADF-STEM. Homogeneous distribution of the elements M (= Ca, Zn, or Mn), Fe, and P was observed by elemental mapping of the mixed salts CaMix1-CaMix4, (Figure 5.3 A), ZnMix1-ZnMix4 (Figure 5.3 B), and MnMix1-MnMix3 (Figure 5.3 C). In line with the results of TEM-EDX, the elemental mapping of the salt MnMix4 showed different distribution of Fe for Fe-rich and Mn-rich (or Fe-poor) coexisting morphologies.

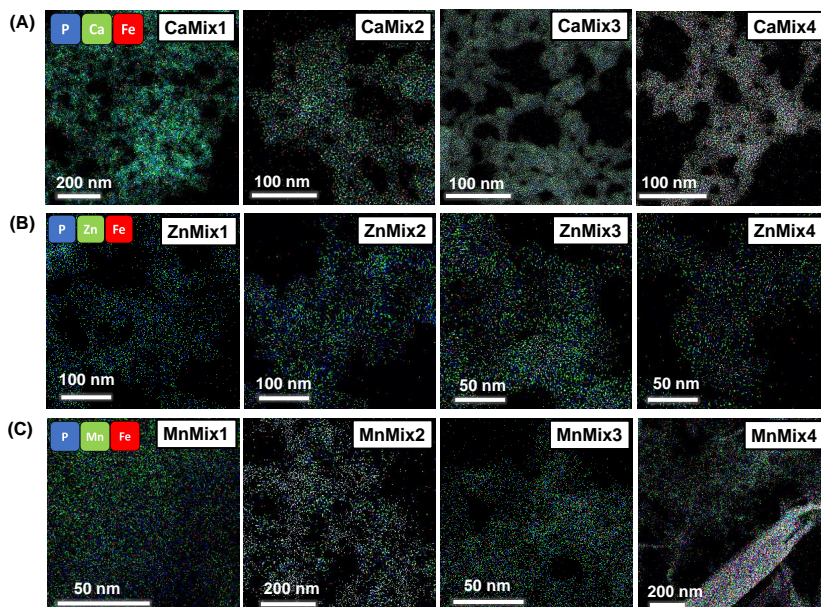


Figure 5.3 Elemental mapping performed by HAADF-STEM on the mixed Fe(II)-containing pyrophosphate salts with the general formula $M_{2(1-x)}Fe_{2x}P_2O_7$, coded as MMix1 to MMix4 where (A) M = Ca, (B) M = Zn, and (C) M = Mn. Color indications are as follows: second divalent metal (M = Ca, Zn, or Mn): green; iron (Fe): red; and phosphorous (P): blue. Elemental mapping clearly shows homogeneous distribution of the elements in all the mixed salts except for the salt MnMix4.

The crystallinity of the mixed divalent metal Fe(II)-containing pyrophosphate salts was investigated by X-ray powder diffraction analysis, Figure 5.4 (left). The XRD diffractograms of the mixed salts were not similar to any of the existing XRD reference patterns in the international center for diffraction data (ICDD, <https://www.icdd.com>). Comparing the XRD patterns of the pure CaPP and Fe(II)PP to their mixed salts (i.e., CaMix1-CaMix4) showed that inclusion of Ca alongside Fe(II) in the pyrophosphate matrix results in amorphous structures of these mixed salts and

therefore appearing noise and broad peaks in their XRD diffractograms, Figure 5.4 A (left).

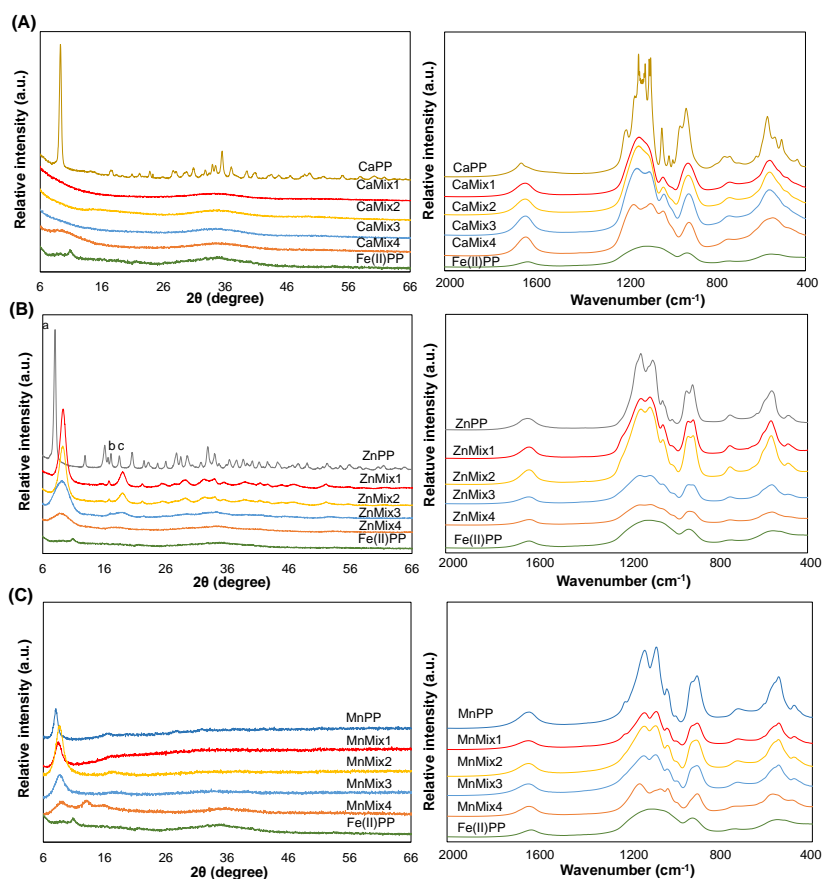


Figure 5.4 XRD diffractograms (left) and FT-IR spectra (right) of the mixed Fe(II)-containing pyrophosphate salts with the general formula $M_{2(1-x)}Fe_{2x}P_2O_7$ ($0 < x < 1$) where (A) $M = Ca$, (B) $M = Zn$, and (C) $M = Mn$. The spectra of the pure CaPP, ZnPP or MnPP and Fe(II)PP are shown for comparison. (A) The salts CaMix1–CaMix4 show broad peaks in their XRD diffractograms and FT-IR spectra which is a sign of their amorphous structures. (B) A gradual transformation in the crystalline structure was observed in the XRD diffractograms and FTIR spectra of the salts ZnMix1–ZnMix4 upon increasing Fe content. Eventually the characteristic peak at 9.5 degree for crystalline structure and the chemical bond vibration peaks in the FT-IR spectra of the mixed salts ZnMix3 and ZnMix4 appeared broad and smooth. (C) The characteristic peak in the XRD diffractogram of MnPP appeared broader upon increasing Fe content in the salts MnMix1–MnMix4. For the same reason, the peaks corresponding to their chemical bonds in the pyrophosphate ions appeared broad and smooth.

However, in the case of Zn as the second divalent metal (M) comparison between the XRD diffractograms of the mixed salts (i.e., ZnMix₁-ZnMix₄) and the pure ZnPP and Fe(II)PP specified a gradual transformation of crystalline structure upon increasing iron content in these samples, Figure 5.4 B (left). The characteristic peak at $2\theta = 8$ degree (a), which appeared sharp and strong for ZnPP, shifted to approximately 9.5 degree in the mixed salts. Moreover, the intensity and sharpness of this peak decreased noticeably upon increasing iron content in these mixed salts. Additionally, the peaks at 17 degree (b), 19 degree (c), and in the range of 25-35 degree appeared broader with a decreased intensity in the salts ZnMix₁-ZnMix₃, compared to ZnPP. Ultimately, these peaks disappeared in the diffractogram of the salt ZnMix₄.

The XRD patterns of the mixed Fe(II)-containing pyrophosphate salts with M = Mn (i.e., MnMix₁-MnMix₄) were consistent with the pattern of MnPP, Figure 5.4 C (left). The characteristic peak at approximately $2\theta = 8$ degree appeared in all the mixed salts and broadened upon increasing iron content in these salts. Eventually, the multiple peaks appearing for the salt MnMix₄ can be likely due to the multiple conformational phases resulting from the physical segregation observed in the morphology of this salt, see Figure 5.4 C.

The details of chemical bonds in the structure of the mixed Fe(II)-containing pyrophosphate salts were explored by FT-IR spectroscopy, Figure 5.4 (right). The analysis of the FT-IR spectra of the mixed salts showed that peak positions coincided between the salts because the vibrations only correlate with the chemical bonds in the pyrophosphate ions. Pyrophosphate vibrations showed sharp and well-defined peaks for the crystalline salts, whereas the same peaks appeared broad and smooth for the amorphous salts. The peak positions matched with the wavenumbers observed for pyrophosphate group in the pure Fe(II)PP, CaPP, ZnPP, and MnPP salts as discussed in section 5.3.1.

5.3.3 Assessment of the reactivity of the pure and mixed divalent metal Fe(II)-containing pyrophosphate salts by discoloration of a black tea solution

Even though the main intention of the present work is not to fortify tea, we used a black tea solution as a representative model solution to investigate the reactivity of iron in the designed mixed salts with phenolics (catechins), to show the prospects of fortification of foods with the Fe(II)-containing pyrophosphate salts. The substantial amount of phenolic compounds in black tea can provoke discoloration in the presence of iron-containing salts by iron-mediated complexation and/or oxidation³⁹⁻⁴¹. Ferrous ion is known to make colorless complex with phenolics (catechol moiety)⁴². However, autooxidation of Fe(II) in this complex to Fe(III) (in the presence of oxygen) results in more stable yet colored Fe(III)-phenolic complex which eventually leads to discoloration of the food, in this case the black tea solution^{43,44}.

The black tea model solution was exposed to the pure Fe(II)PP, CaPP, ZnPP, and MnPP as well as the mixed Fe(II)-containing pyrophosphate salts (the final pH of the solutions was approximately 5-6.5). Because these pure pyrophosphate salts are poorly water-soluble⁴⁵, it was expected that their mixed salts would also show less reactivity and therefore, less discoloration upon food fortification. The results of discoloration of the tea solution, caused by iron ions released from the salts are shown in Figure 5.5. The discoloration of the black tea solution after exposure to FeSO₄ and Fe(III)PP was investigated for comparison as well. FeSO₄ is known to be an iron (II) source with high solubility and therefore high discoloration upon addition to the foods^{13,39}. In contrast, Fe(III)PP receives a great deal of attention for its application in food fortification due to its poor solubility and therefore less reactivity with the phenolics present in the foods^{6,7,25}.

Exposing the tea solution to iron in the form of the pure Fe(II)PP salt for 10 minutes, resulted in the darkening of the tea solution compared to the reference i.e., the pure black tea solution, Figure 5.5 A. However, Fe(II)PP caused significantly ($p < 0.05$) less discoloration in the black tea solution in comparison with FeSO₄ and Fe(III)PP, in line with the total absorbance spectra of the tea solutions at 550 nm, see Figure 5.5 A. The color difference in the tea solution before and after being exposed to the iron-containing salts was evaluated by calculating the ΔE_{ab} value. It is assumed that when the ΔE_{ab} is in the range of 3-5, the color difference can be observed by an average consumer⁴⁶, and when $\Delta E_{ab} \approx 10$, the color difference is acceptable in the presence of the iron-fortified salt⁴⁷. The results showed that the ΔE_{ab} of the black tea solution after being exposed to Fe(II)PP was approximately 10.9, which was a nearly acceptable color change, yet about 1.5 times less than Fe(III)PP (i.e., $\Delta E_{ab} \approx 16$). The darker color of the black tea solution after exposure to Fe(III)PP, compared to Fe(II)PP, is expected to be related to faster dissolution of Fe(III)PP in the tea, see chapter 6. Furthermore, the concentration of the dissolved iron from the salts in the tea solutions indicated that Fe(II)PP resulted in approximately 3-fold less dissolved iron in the tea solution, compared to Fe(III)PP, Figure 5.5 A. Nevertheless, the measured soluble iron from the Fe(II)PP and Fe(III)PP were only 3.7% and 11.7%, respectively, of the total amount of added iron (in the form of these salts). This indicates that a remarkable amount of iron was retained in these salts' matrices. It should also be noted that the final pH of the tea solution after exposure to both Fe(III)PP and Fe(II)PP was measured to be approximately 4.8. These results suggest that Fe(II)PP is an iron source with potentially lower iron-mediated reactivity and practically acceptable color change upon addition to model catechin-containing solutions such as black tea, compared to Fe(III)PP.

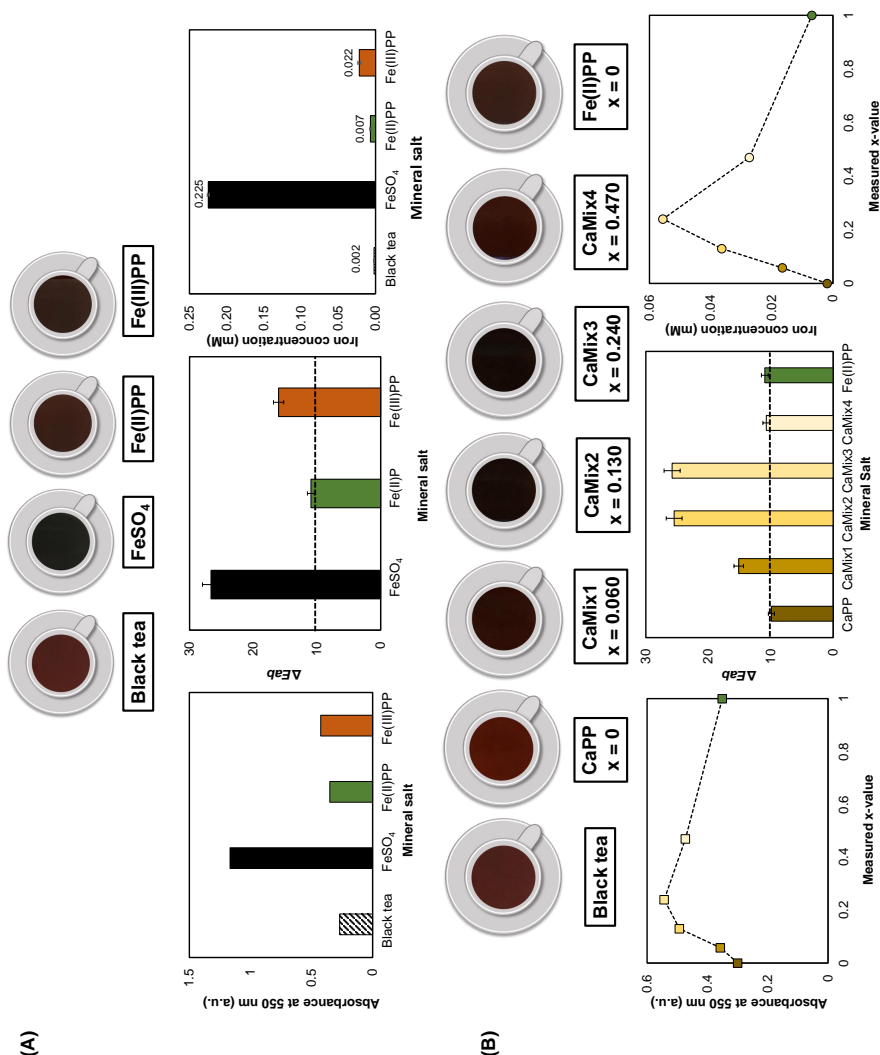


Figure 5.5 The results of the reactivity assessment in a black tea solution exposed to (A) Fe(II)PP, compared to FeSO₄ and Fe(III)PP, and the mixed $M_{2(1-x)}Fe_{2x}P_2O_7$ salts where (B) M = Ca, (C) M = Zn, and (D) M = Mn. In each section of the figure, the visual comparison of the colors of the tea solutions (tea cups), the absorbance of the tea solutions at 550 nm (left), the quantitative color difference (i.e., ΔEab) with respect to the blank tea (middle), and the dissolved iron concentration from the salts in the tea solutions (right) after exposure to the salts are shown. (A) In the case of Fe(II)PP, the color change, ΔEab , is approximately 1.5 times less than Fe(III)PP. Moreover, in the case of Fe(II)PP the dissolved iron concentration in the tea solution is approximately 3-fold lower, compared to Fe(III)PP.

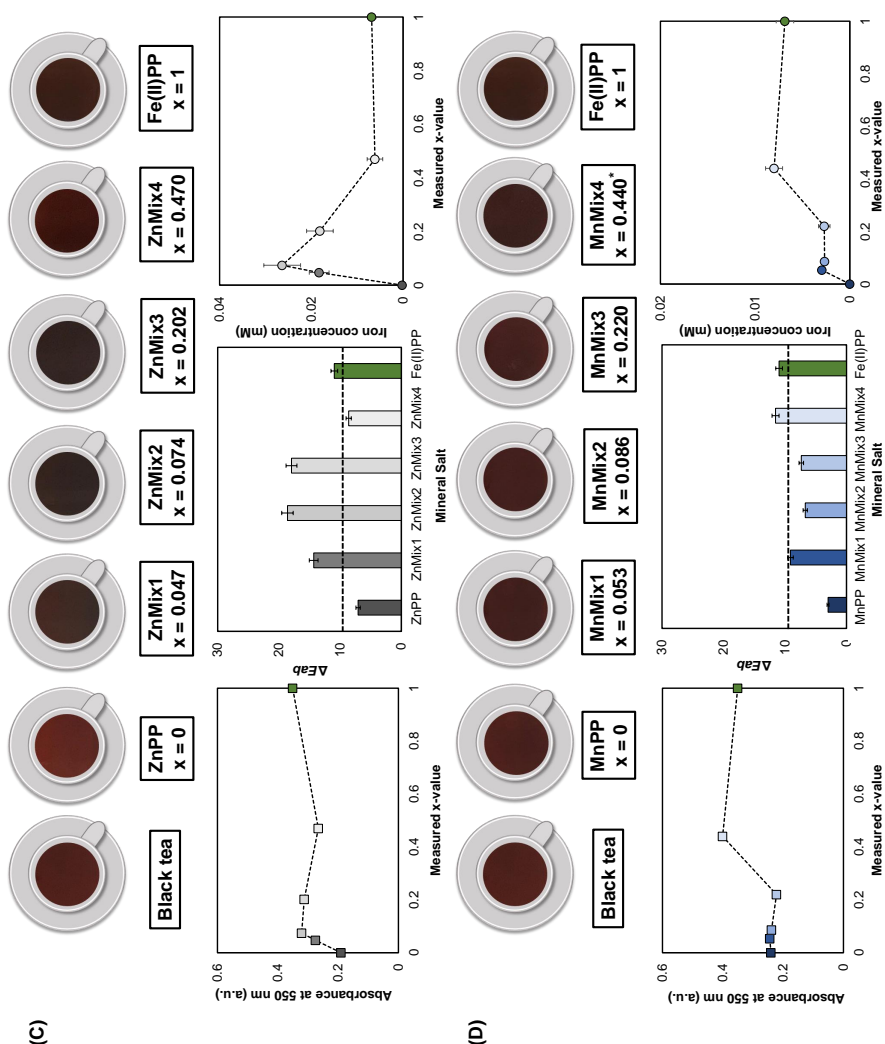


Figure 5.5 (continued): With respect to Fe(II)PP, among the mixed divalent metal Fe(II)-containing pyrophosphate salts, **(B)** CaMix4 ($x = 0.470$) with similar color difference ($\Delta E_{ab} = 10.7$), **(C)** ZnMix4 ($x = 0.470$) with less color difference ($\Delta E_{ab} = 8.6$) and similar concentration of the dissolved iron, and **(D)** MnMix2 ($x = 0.086$) with much less color change ($\Delta E_{ab} = 6.7$) and lower iron dissolution (2.3-fold) exhibit less iron-mediated reactivity and discoloration in the black tea solution.

* The average of the two x -values corresponding to the two morphological phases of the salt MnMix4 is used here (0.440).

The visual color comparison between tea solutions exposed to the mixed salts $M_{2(1-x)}Fe_{2x}P_2O_7$, where $M = Ca$ (i.e., CaMix1 to CaMix4 with measured $x = 0.060$, 0.130 , 0.240 , and 0.470 , respectively), showed that the discoloration induced by these salts in the tea solution was a non-monotonic function of their iron content, Figure 5.5 B. The color difference, ΔEab , was the highest for the mixed salt CaMix3 ($x = 0.240$), which was approximately 2.4-fold higher than Fe(II)PP ($x = 1$). This was in line with the fact that this salt had the highest absorbance among all other salts at 550 nm and the highest area under the curve in the whole range of 500-600 nm (data not shown). It's important to mention in this context that the color change illustrated by ΔEab value can partly be due to the discoloration caused by the oxidation of the phenolics present in the black tea solution. Moreover, conditions such as pH and temperature can affect the oxidation of the phenolic compounds⁴⁸. Therefore, the instability of color of the tea solution after exposure to the mixed salt can also be due to the differences in their pH values and the oxidation of phenolics at high temperature. Moreover, the mixed salt with the highest Fe(II) content (i.e., CaMix4 with $x = 0.470$) exhibited similar discoloration of the tea solution to Fe(II)PP ($\Delta Eab = 10.7$). The illustration of the dissolved iron concentration from these salts versus their measured x -values showed enhanced dissolved iron concentration in the tea solution for all the mixed salts up to an 8-fold increase for the salt CaMix3 ($x = 0.240$), compared to Fe(II)PP ($x = 1$), Figure 5.5 B. Additionally, the salt CaMix4 ($x = 0.470$) with similar discoloration to Fe(II)PP showed approximately 4 times higher soluble iron concentration, compared to Fe(II)PP. It was previously reported that the presence of the water-soluble phenolics (such as catechins present in tea) can promote the soluble iron from the mixed Ca-Fe(III) salts, see chapter 4. This non-monotonic behavior of discoloration of black tea solution with respect to the iron content was previously observed for the mixed Ca and Fe(III) pyrophosphate salts as well⁶, see chapter 2. Furthermore, discoloration of the tea solution in this case (with Ca as the second (divalent) metal) is suggested to be due to the interaction and oxidation of polyphenols in the presence of calcium at elevated temperatures as well⁴⁹, since the complexation of calcium with phenolics is not reported to lead to a change in color⁹.

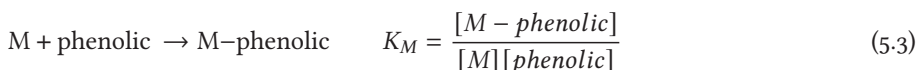
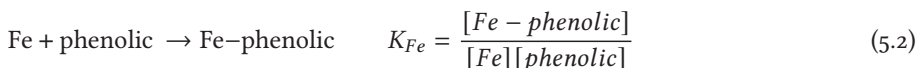
Exposing the black tea solution to the mixed salts $M_{2(1-x)}Fe_{2x}P_2O_7$, where $M = Zn$ (i.e., ZnMix1 to ZnMix4 with measured $x = 0.047$, 0.074 , 0.202 , and 0.470 , respectively), resulted in enhanced discoloration with a maximum 1.7-fold increase in the case of the salt ZnMix2 ($x = 0.074$), compared to Fe(II)PP ($x = 1$), Figure 5.5 C. Similar to the case of $M = Ca$, the color difference ΔEab was the lowest and even lower than 10 (≈ 8.6) for the mixed salt with the highest iron content, ZnMix4 ($x = 0.470$). In line with the results obtained from the color difference, the dissolved iron in the tea solution was maximum for the salt ZnMix2 ($x = 0.074$), which was approximately 3.8-fold higher than the concentration of the dissolved iron from the pure Fe(II)PP ($x = 1$). The dissolved iron concentration in the tea solution was measured to be mini-

mum for the salt ZnMix₄ ($x = 0.470$) among all other salts, and similar to Fe(II)PP (0.0061 vs. 0.0068 mM, respectively), see Figure 5.5 C. These results suggest that the designed mixed salt ZnMix₄ ($x = 0.470$) is a potential candidate for delivery of Fe(II) and Zn, which shows less discoloration in a black tea solution, compared to Fe(II)PP. Interestingly, exposing the black tea to the pure ZnPP ($x = 0$) caused a slight lightening in the black tea solution (lightness $L^* = 24$ for ZnPP vs. $L^* = 20$ for pure black tea). This could be explained by the fact that zinc is known to undergo complexation with tea catechins (with absorbance characteristic peak < 350 nm)^{50,51} and form light yellow-colored complexes with phenolics⁵². Moreover, it has previously been reported that zinc has antioxidant activity^{53,54}. Therefore, it is expected that the discoloration of the black tea solution resulted from the oxidation of its phenolics is limited after exposure to ZnPP.

The results obtained from discoloration of the black tea solution after being exposed to the mixed $M_{2(1-x)}Fe_{2x}P_2O_7$, where $M = Mn$ (i.e., MnMix₁ to MnMix₄ with measured $x = 0.053, 0.086, 0.220$, and 0.440 , respectively) are shown in Figure 5.5 D. It's worth mentioning here that even though the salt MnMix₄ is not considered as a suitable candidate for the purpose of this work because of its non-homogeneous morphology, it was still assessed for its iron-mediated reactivity in the tea experiment. To show the results, the average of the two x -values corresponding to the two morphological phases of this salts was chosen as the x -value for this salt (i.e., average of $x = 0.35$ and 0.52 , which equals 0.44), see Figure 5.2 D.

Overall, results showed that inclusion of Mn as the second divalent metal in the pyrophosphate salt matrix successfully limited the iron-mediated reactivity in these salts and consequently caused less discoloration of the black tea solution compared to Fe(II)PP. All these mixed salts exhibited lower absorbance at 550 nm, less color change (i.e., lower ΔE_{ab} value), and lower dissolved iron concentration in solution, compared to Fe(II)PP, except for the salt MnMix₄ ($x = 0.440$), Figure 5.5 D. It was expected from the results obtained from EDX and elemental mapping for this salt not to show less reactivity and therefore discoloration in the black tea solution, compared to Fe(II)PP, due to the heterogeneity in morphology and iron distribution in its matrix. The reason is that coexisting salt composition which possess higher iron content will have more available iron to be exposed to the phenolics present in the tea solution, compared to the irregular homogeneous aggregates. Furthermore, the mixed salt MnMix₂ ($x = 0.087$) with $\Delta E_{ab} = 6.7$ exhibited the least discoloration among all other mixed salts with $M = Mn$ in the general formula. In addition, the dissolved iron concentration from these mixed salts in the tea solution decreased up to a 2.3-fold for the mixed salt MnMix₂ ($x = 0.087$), compared to Fe(II)PP ($x = 1$). Therefore, the mixed salts with Mn as the second divalent metal with $x \leq 0.220$ are the preferred candidates in terms of their iron-mediated reactivity with catechins present in black tea solution.

Additionally, it has previously been shown that inclusion of a competitive divalent metal (M) with respect to the complexation with phenolics can limit the complexation of Fe-phenolic via shifting the equilibrium towards formation of colorless/less dark-colored M-phenolic complexes⁵⁵. Two competitive reactions in this case will be:



In order to limit the formation of Fe-phenolic, M-phenolic complex should be favored, therefore $[\text{M-phenolic}] \gg [\text{Fe-phenolic}]$, and as a result $K_M[\text{M}] \gg K_{Fe}[\text{Fe}]$ should hold⁹. Unfortunately, the information regarding the stability constants of complexes of the metals studied in this work with tea catechins are not known to our knowledge. However, we surveyed the existing data on complexes of these metals with catechol due to the similar metal chelating groups of catechins and catechol (i.e., catechol moiety), see Figure 4.1 in chapter 4. The existing data on stability constant of metal-catechol complexes indicates that first Fe(II)-catechol complex has a lower stability constant, compared to Fe(III)-catechol ($K \approx 14$ vs. 20, respectively)⁵⁶, which is the explanation for autoxidation of Fe(II) to Fe(III) after complexation to phenolics⁵⁷. Furthermore, the stability constant of the complex of the (second) divalent metals (M) investigated in this work with catechol have been reported to be approximately 2.5, 8.3, and 7.5 for M = Ca, Zn, and Mn, respectively^{56,58,59}. This indicates that in the ratio of M/Fe(II), M = Zn and Mn are stronger competitive metals than Ca. It has been reported that the metal competition can effectively limit the color change when a large excess of M is present⁹. In the current work the ratio of M/Fe(II) in the mixed salts (based on their x-values) is in the range of 1.1 to 15.7, 1.1 to 20.3, or 1.3 to 17.9 for the salts in which M = Ca, Zn, or Mn, respectively.

On the condition that the second divalent metal (M) competes with Fe(II) to bind to the catechins present in the black tea solution, a non-linear relation is required between the area under the absorbance curve of the tea solutions in the visible range ($\text{AUC}_{380-700}$) with increasing the concentration of the dissolved iron from the salts (in the same concentration of the phenolics). We observed that for none of the sets of the mixed salts, the above-mentioned correlation is perfectly linear, see Figure 5.9 A-C of Appendix 5.A for the mixed salts in which M = Ca, Zn, and Mn, respectively. The insets in Figure 5.9 shows that the correlation between the $\text{AUC}_{380-700}$ is non-linear for the salts in which the second metal is in excess as well, with respect to Fe(II) (M/Fe(II) is in the range of 6.7-15.7, 12.5-20.3, and 10.6-17.9 for M = Ca, Zn, and Mn,

respectively). However, as shown in Figure 5.5 D, the measured iron concentration in the solution was a monotonic function of the iron only in the case of the mixed salts when $M = \text{Mn}$, and not for $M = \text{Ca}$ or Zn . Monitoring the area under the curve in the visible range versus dissolved Fe concentration in the tea solution suggests that by adding the same amount of iron (1.05 mg Fe/100 ml tea) in the form of Fe(II)PP, the slope of $\text{AUC}_{380-700}$ showed a sudden increase with respect to the mixed Mn-Fe(II) salts with homogeneous morphology (i.e., $x = 0.053$, 0.086 , and 0.220), Figure 5.9 D of Appendix 5.A. This suggests that in these mixed salts with $x \leq 0.220$, Mn can compete with Fe(II) toward formation of less dark complexes with catechins present in the tea. It has also been shown before that the Mn-phenolic complex has a much lighter brown color, compared to Fe-phenolic complex⁵⁵. Nonetheless, the competition between the metals for complexation with the phenolics (present in tea) should be further investigated in the future works.

To summarize, our results suggest that mixed Fe(II)-containing pyrophosphate salts are potential candidates for dual-fortification of foods with tunable minerals compositions. The results of the current work shows that the mixed salts CaMix₄ ($x = 0.470$), ZnMix₄ ($x = 0.470$), and MnMix₂ ($x = 0.086$) with similar or less iron-mediated discoloration of a black tea solution, compared to Fe(II)PP, are the preferred candidates for simultaneous fortification of foods with F(II) and Ca, Zn, or Mn, respectively. Thus, these salts are preferred candidates with the main benefit of minimized dissolved iron concentration and therefore reduced iron-mediated discoloration to be applied for dual-fortification of foods containing catechins.

5.4 Conclusions

In the current work, we report the design, synthesis, and characterization of ferrous pyrophosphate (Fe(II)PP) as well as the mixed divalent metal Fe(II)-containing pyrophosphate salts with the general formula $\text{M}_{2(1-x)}\text{Fe}_{2x}\text{P}_2\text{O}_7$ ($0 \leq x \leq 1$, where $M = \text{Ca}$, Zn , or Mn). All the mixed salts showed uniform morphology, except for the mixed salt where $M = \text{Mn}$ with designed $x = 0.5$. We demonstrate for the first time the reactivity of the pure and mixed Fe(II)-containing salts in a black tea solution as a representative model system for phenolics in particular catechins. Results indicated that the Fe(II)PP caused acceptable color change in the black tea solution which was 1.5 times less than the conventional ferric pyrophosphate (Fe(III)PP). In addition, our results suggest that the concentration of the dissolved iron ions released from the mixed salts was a non-monotonic function of the x -values where $M = \text{Ca}$ and Zn . In the case of $M = \text{Ca}$, none of the salt compositions we studied were able to reduce discoloration as compared to Fe(II)PP. For the case of $M = \text{Zn}$, the salt with the measured $x = 0.470$ exhibited less color change ($\Delta E_{ab} = 8.6$) and similar dissolved iron concentration, compared to Fe(II)PP ($\Delta E_{ab} = 10.9$). Furthermore, the present

findings suggest that the mixed salts in which $M = \text{Mn}$ with $x = 0.086$ are the preferred salts for foods containing catechins due to reduced color change (minimum $\Delta E_{ab} = 6.7$) and decreased soluble iron concentration up to 2.3-fold, with respect to Fe(II)PP . In the next chapter, the dissolution behavior of the pure and mixed divalent metal Fe(II) -containing pyrophosphate salts, as well as their dissolution behavior in gastric-mimicked conditions will be explored.

5.5 Acknowledgments

Hans Meeldijk from Materials Chemistry and Catalysis group of Utrecht University, is thanked for TEM-EDX and HAADF-STEM measurements. Coen Mulder and Helen de Waard from the Geo-Science group of Utrecht University are thanked for ICP-AES measurements. The author is thankful to Wouter J.C. de Bruijn from the Laboratory of Food Chemistry, Wageningen University and Research for fruitful discussions. The graphical abstract was made with content from BioRender.com.

5.A Appendix

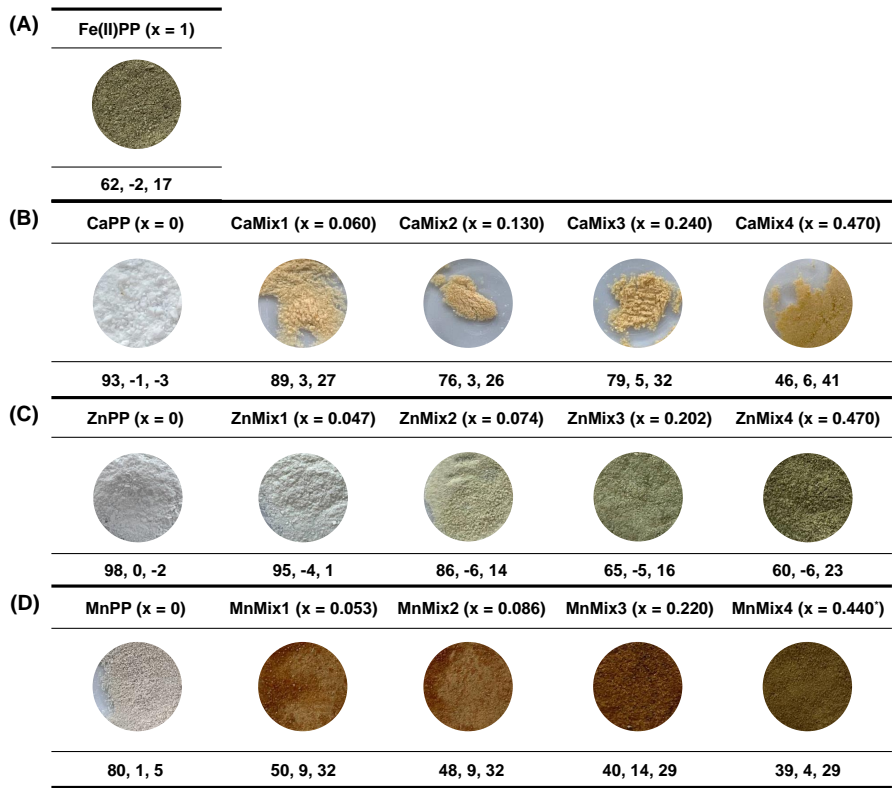


Figure 5.7 The images and details of color conversion (i.e., $L^*a^*b^*$ values) of (A) pure Fe(II)PP, the mixed pyrophosphate salts with the general formula $M_{2(1-x)}Fe_{2x}P_2O_7$ where (B) M = Ca, (C) M = Zn, and (D) M = Mn. The pure CaPP, ZnPP, and MnPP are shown for comparison as well. The details of color conversions of the salts are obtained by an online color measurement tool <https://imagecolorpicker.com/> and reported by L^* , a^* , b^* values, respectively.

* The average of the two x-values corresponding to the two morphological phases of the salt MnMix4 is used here (0.440).

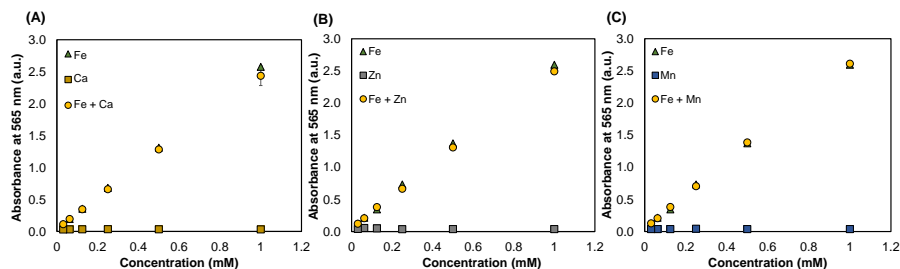


Figure 5.8 Interference of presence of Ca, Zn, or Mn ion with the quantification of total iron in the ferrozine-based colorimetric assay. Absorbance of the ferrozine complex at 565 nm in the presence of increasing concentration of iron, second divalent metal (M), and a mixture containing their equimolar concentrations where (A) M = Ca, (B) M = Zn, and (C) M = Mn. Presence of none of the studied divalent metals (i.e., Ca, Zn, and Mn) resulted in absorbance or interference with the absorbance of the Fe-ferrozine complex at 565 nm.

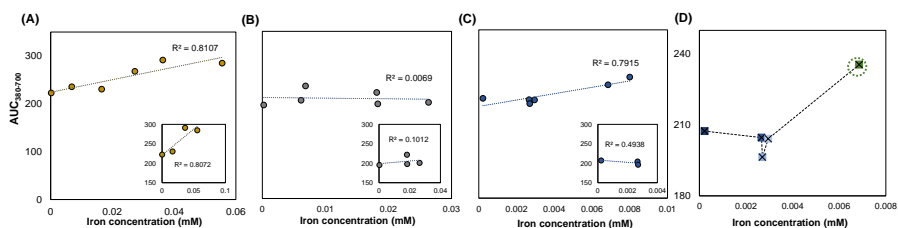


Figure 5.9 The correlation between the area under the absorbance curve in the visible light range ($AUC_{380-700}$) versus the dissolved iron concentration from the mixed Fe(II)-containing pyrophosphate salts where (A) M = Ca, (B) M = Zn, and (C) M = Mn in the black tea solutions. The insets show the same correlation for the salts where M is in excess with respect to iron. The regression values (R^2) of each correlation are shown as well. (D) The slope of the area under the absorbance curve versus the dissolved iron concentration increased in the mixed salts where M = Mn. The circled point shows the corresponding values for Fe(II)PP.

References

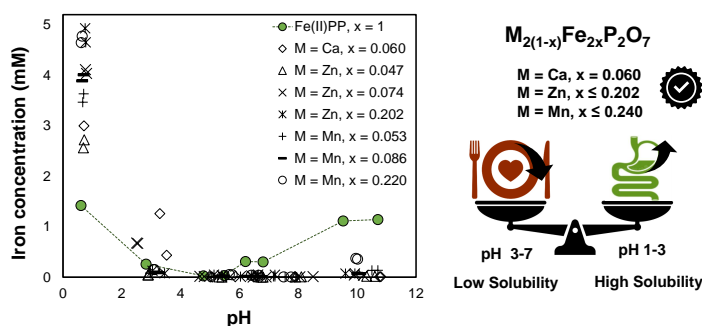
- 1 K. Ashwin, A. K. Pattanaik, and G. S. Howarth, *Food Bioscience* **44**, 101376 (2021).
- 2 O. P. Bolade, A. B. Williams, and N. U. Benson, *Environmental Nanotechnology, Monitoring Management* **13**, 100279 (2020).
- 3 M. J. Salgueiro and J. Boccio, in *Handbook of Food Fortification and Health: From Concepts to Public Health Applications*, Vol. 1 (Springer New York, 2013) pp. 91–97.
- 4 A. Vatandoust and L. Diosady, *Current Opinion in Food Science* **43**, 232 (2022).
- 5 N. Zuidam, in *Encapsulation Technologies and Delivery Systems for Food Ingredients and Nutraceuticals* (Elsevier, 2012) pp. 505–540.
- 6 N. Moslehi, J. Bijlsma, W. J. de Bruijn, K. P. Velikov, J.-P. Vincken, and W. K. Kegel, *Journal of Functional Foods* **92**, 105066 (2022).
- 7 T. Tian, E. Blanco, S. K. Smoukov, O. D. Velev, and K. P. Velikov, *Food Chemistry* **208**, 97 (2016).
- 8 J. Bijlsma, W. J. de Bruijn, J. A. Hageman, P. Goos, K. P. Velikov, and J. P. Vincken, *Scientific Reports* **10**, 1 (2020).
- 9 E. Habeych, V. van Kogelenberg, L. Sagalowicz, M. Michel, and N. Galaffu, *Food Research International* **88**, 122 (2016).
- 10 C. M. Andre, D. Evers, J. Ziebel, C. Guignard, J. F. Hausman, M. Bonierbale, T. Zum Felde, and G. Burgos, *Journal of Agricultural and Food Chemistry* **63**, 9012 (2015).
- 11 D. Moretti, M. B. Zimmermann, R. Wegmüller, T. Walczyk, C. Zeder, and R. F. Hurrell, *The American Journal of Clinical Nutrition* **83**, 632 (2006).
- 12 S. K. Bardal, J. E. Waechter, and D. S. Martin, *Applied pharmacology* (Elsevier Health Sciences, 2011).
- 13 R. F. Hurrell, *The Journal of Nutrition* **151**, 3S (2021).
- 14 M. Abbasi, F. Mazhari, M. R. Jaafari, E. Afshari, H. Bagheri, and I. Parisay, *Pediatric Dental Journal* **31**, 256 (2021).
- 15 O. Modupe, Yao, O. Li, Levente, and L. Diosady, *Journal of Food Science and Technology* **2022**, 1 (2022).
- 16 Y. Wang, A. Ye, Y. Hou, Y. Jin, X. Xu, J. Han, and W. Liu, *Trends in Food Science Technology* **119**, 36 (2022).
- 17 G. Ji, X. Ou, R. Zhao, J. Zhang, J. Zou, P. Li, D. Peng, L. Ye, B. Zhang, and D. He, *Resources, Conservation and Recycling* **174**, 105802 (2021).
- 18 G. H. Lee, S. D. Seo, H. W. Shim, K. S. Park, and D. W. Kim, *Ceramics International* **38**, 6927 (2012).
- 19 S. Liu, C. Gu, H. Wang, R. Liu, H. Wang, and J. He, *Journal of Alloys and Compounds* **646**, 233 (2015).
- 20 W. L. He, Y. Feng, X. L. Li, Y. Y. Wei, and X. E. Yang, *Journal of Zhejiang University. Science. B* **9**, 707 (2008).
- 21 Y. M. van Leeuwen, K. P. Velikov, and W. K. Kegel, *Food Chemistry* **155**, 161 (2014).

- 22 L. Rossi, K. P. Velikov, and A. P. Philipse, *Food Chemistry* **151**, 243 (2014).
- 23 Y. M. van Leeuwen, K. P. Velikov, and W. K. Kegel, *RSC Advances* **2**, 2534 (2012).
- 24 N. L. Drenchev, K. K. Chakarova, O. V. Lagunov, M. Y. Mihaylov, E. Z. Ivanova, I. Strauss, and K. I. Hadjiivanov, *JoVE (Journal of Visualized Experiments)* **2020**, e60285 (2020).
- 25 E. J. T. McGee and L. L. Diosady, *Food Analytical Methods* **11**, 1645 (2018).
- 26 H. Araki, J. Kim, S. Zhang, A. Banks, K. E. Crawford, X. Sheng, P. Gutruf, Y. Shi, R. M. Pielak, and J. A. Rogers, *Advanced Functional Materials* **27**, 1604465 (2017).
- 27 C. Poynton, *Digital video and HD: Algorithms and Interfaces* (Elsevier, Waltham, MA, USA, 2012).
- 28 P. Gras, C. Rey, O. Marsan, S. Sarda, and C. Combes, *European Journal of Inorganic Chemistry* **2013**, 5886 (2013).
- 29 A. Karaphun, S. Sawadsitang, T. Duangchuen, P. Chirawatkul, T. Putjuso, P. Kumnorkaew, S. Maensiri, and E. Swatsitang, *Surfaces and Interfaces* **23**, 100961 (2021).
- 30 M. A. Petrova, V. I. Shitova, G. A. Mikirticheva, V. F. Popova, and A. E. Malshikov, *Journal of Solid State Chemistry* **119**, 219 (1995).
- 31 B. Boonchom and R. Baitahe, *Materials Letters* **63**, 2218 (2009).
- 32 K. Brouzi, A. Ennaciri, and M. Harcharras, *Phosphorus, Sulfur, and Silicon* **179**, 1329 (2010).
- 33 S. Schneider and R. L. Collin, *Inorganic Chemistry* **12**, 2136 (1973).
- 34 Y. Lai, X. Liang, G. Yin, S. Yang, J. Wang, H. Zhu, and H. Yu, *Journal of Molecular Structure* **1004**, 188 (2011).
- 35 N. V. Kosova, D. O. Rezepova, O. A. Podgornova, A. B. Slobodyuk, S. A. Petrov, and M. Avdeev, *Electrochimica Acta* **235**, 42 (2017).
- 36 R. K. Singh, M. Srivastava, N. K. Prasad, S. Awasthi, A. Dhayalan, and S. Kannan, *Materials Science and Engineering C* **78**, 715 (2017).
- 37 J. C. Zheng, X. Ou, B. Zhang, C. Shen, J. F. Zhang, L. Ming, and Y. D. Han, *Journal of Power Sources* **268**, 96 (2014).
- 38 Y. Li, *Solid State Ionics* **323**, 142 (2018).
- 39 J. Bijlsma, W. J. de Bruijn, K. P. Velikov, and J. P. Vincken, *Food Chemistry* **370**, 131292 (2022).
- 40 E. J. T. McGee and L. L. Diosady, *LWT - Food Science and Technology* **89**, 756 (2018).
- 41 Z. Wang, C. Fang, and M. Mallavarapu, *Environmental Technology and Innovation* **4**, 92 (2015).
- 42 N. R. Perron and J. L. Brumaghim, *Cell Biochemistry and Biophysics* **53**, 75 (2009).
- 43 N. R. Perron, H. C. Wang, S. N. Deguire, M. Jenkins, M. Lawson, and J. L. Brumaghim, *Dalton Transactions* **39**, 9982 (2010).
- 44 N. Petry, *Polyphenols in Human Health and Disease* **1**, 311 (2014).
- 45 D. L. Perry, *Handbook of inorganic compounds* (CRC press, 2016).
- 46 S. Ghidouche, B. Rey, M. Michel, and N. Galaffu, *Food Chemistry* **139**, 978 (2013).
- 47 R. Wegmüller, M. B. Zimmermann, and R. F. Hurrell, *Journal of Food Science* **68**, 2129 (2003).

- 48 M. Mochizuki, S. I. Yamazaki, K. Kano, and T. Ikeda, *Biochimica et biophysica acta* **1569**, 35 (2002).
- 49 K. Yamada, T. Abe, and Y. Tanizawa, *Food Chemistry* **103**, 8 (2007).
- 50 X. Wang, Y. Feng, C. Chen, H. Yang, and X. Yang, *LWT* **131**, 109810 (2020).
- 51 Z. Zheng, M. Mounsamy, N. Lauth-De Viguerie, Y. Coppel, S. Harrisson, M. Destarac, C. Mingotaud, M. L. Kahn, and J. D. Marty, *Polymer Chemistry* **10**, 145 (2018).
- 52 J. Guo, Y. Ping, H. Ejima, K. Alt, M. Meissner, J. J. Richardson, Y. Yan, K. Peter, D. Von Elverfeldt, C. E. Hagemeyer, *et al.*, *Angewandte Chemie International Edition* **53**, 5546 (2014).
- 53 A. Primikyri, G. Mazzone, C. Lekka, A. G. Tzakos, N. Russo, and I. P. Gerothanassis, *Journal of Physical Chemistry B* **119**, 83 (2015).
- 54 Y. Song, S. W. Leonard, M. G. Traber, and E. Ho, *The Journal of Nutrition* **139**, 1626 (2009).
- 55 J. Guo, Y. Ping, H. Ejima, K. Alt, M. Meissner, J. J. Richardson, Y. Yan, K. Peter, D. Von Elverfeldt, and C. E. Hagemeyer, *Angewandte Chemie International Edition* **53**, 5546 (2014).
- 56 L. D. Pettit, *Chemistry International – Newsmagazine for IUPAC* **28**, 14 (2006).
- 57 G. N. Jameson and W. Linert, *Journal of the Chemical Society, Perkin Transactions 2* **0**, 569 (2001).
- 58 E. Amble and E. Amble, *Polyhedron* **2**, 1063 (1983).
- 59 A. K. Rao, P. Venkataiah, and M. srinivas Mohan, *Journal of coordination chemistry* **20**, 69 (2009).

Mixed Fe(II)-containing pyrophosphate salts: pH-dependent dissolution behavior

Abstract



The challenge in designing micronutrient-fortified foods is ensuring the balance between the organoleptic properties of the food and bio-availability of the micronutrients. In this work, the pH-dependent dissolution behavior of the pure as well as the mixed salts $M_{2(1-x)}Fe_{2x}P_2O_7$ ($0 \leq x \leq 1$, where M = Ca, Zn, or Mn) after 2 h incubation at 23 °C was studied for their application as dual-fortificants for iron and a second mineral (M). Results showed that the pure salts were very poorly soluble at pH 4-7, while they dissolved well at pH 1-3. In addition, dissolution behavior of iron from the mixed salts showed that all the salts with M = Ca, Zn, and Mn, had very limited iron dissolution (< 0.5 mM) in the moderate pH range (5-7) while showing enhanced dissolved iron concentration up to 5 mM in the gastric and 1.3 mM in intestine pH range. Furthermore, investigating the dissolution of these salts in physiologically relevant conditions indicated that the pure ferrous pyrophosphate (Fe(II)PP) and the mixed pyrophosphate salts are expected to be biologically accessible and suitable for dual-fortification of foods with Fe and Ca, Zn, or Mn.

This chapter is based on N. Moslehi, M. van Eekelen, K. P. Velikov, and W. K. Kegel, "Mixed divalent pyrophosphate salts for simultaneous delivery of iron and calcium, zinc, or manganese in foods", *To be submitted*.

"Have patience,
all things are difficult before they become
easy."

Saadi Shirazi – Persian poet, 1210-1291

6.1 Introduction

The main benefit of using poorly water-soluble or water-insoluble iron-containing compounds for food fortification is their reduced impact on the organoleptic properties of the food due to their low solubilities¹⁻³. However, the poor solubility in gastrointestinal tract can also result in limited iron bio-availability and consequently reduced iron (and other micronutrients) uptake in the human body^{4,5}. Therefore, the challenge relies on the fact that the dissolution of iron from the iron-containing compound should strongly depend on pH, meaning that the solubility needs to be limited in the food pH range², while being high and/or fast in gastrointestinal conditions⁶⁻⁸.

It has previously been shown that iron (II) is absorbed better than iron (III)⁹. For instance, sources such as ferrous sulfate (water-soluble) and ferrous fumarate (poorly water-soluble), exhibit high iron bio-availability¹⁰. Nevertheless, among iron (II) sources, there is a lack of published work on iron (II) pyrophosphate ($\text{Fe}_2\text{P}_2\text{O}_7$, Fe(II)PP) salt and its potential as an iron fortificant. In addition, it was previously demonstrated that inclusion of a second divalent metal such as Ca, Zn, or Mn alongside iron (II) in pyrophosphate matrix with the general formula $\text{M}_{2(1-x)}\text{Fe}_{2x}(\text{P}_2\text{O}_7)$ ($0 \leq x \leq 1$, where M = Ca, Zn, or Mn, respectively) can reduce discoloration of a black tea solution, compared to Fe(II)PP, see chapter 5. On the other hand, calcium pyrophosphate (CaPP), zinc pyrophosphate (ZnPP), and manganese (II) pyrophosphate (MnPP) are reported to be poorly water-soluble or water-insoluble, but dissolve well in inorganic mineral acids^{11,12}. Therefore, we hypothesize that the combination of a second divalent metal alongside Fe(II) in pyrophosphate matrix will result in poor water-solubility of the resulting mixed mineral salt as well, while showing relatively higher iron solubility in gastric pH range (1-3).

In this study, we explore the dissolution behavior of pure as well as the mixed divalent metal pyrophosphate salts with the general formula $\text{M}_{2(1-x)}\text{Fe}_{2x}(\text{P}_2\text{O}_7)$ ($0 \leq x \leq 1$, where M = Ca, Zn, or Mn). Furthermore, in order to provide an indication of bio-accessibility of iron and the second metal from the pure and mixed salts, their dissolution behavior in the physiologically relevant conditions is investigated.

6.2 Materials and methods

6.2.1 Materials

Nitric acid (HNO_3 , 65 wt.%), 3-(2-pyridyl)-5,6-diphenyl-1,2,4-triazine-*p,p'*-disulfonic acid monosodium salt hydrate (i.e., ferrozine; ≥ 97 wt.%), hydrochloric acid (HCl , 37 wt.%), and sodium hydroxide (NaOH , ≥ 98 wt.%) were obtained from Sigma Aldrich (St. Louis, MO, USA). Iron (II) sulfate heptahydrate ($\text{FeSO}_4 \cdot 7\text{H}_2\text{O}$, ≥ 99 wt.%) was obtained from Alfa Aesar (Haverhill, MA, USA). Ethanol absolute (≥ 99 wt.%) and ascorbic acid (≥ 99 wt.%) were obtained from VWR International (Radnor, PA, USA). The Milli-Q (MQ) water used was deionized by a Millipore Synergy water purification system (Merck Millipore, Billerica, MA, USA).

6.2.2 Dissolution behavior of the pure and the mixed divalent metal Fe(II)-containing pyrophosphate salts

The dried powders of the pure or mixed salts were re-dispersed in MQ water by stirring (~ 250 rpm) with a magnetic stir bar (final concentration: 10 mg/ml). Then, the pH of the dispersion was adjusted using a pH-stat device (Metrohm, Herisau, Switzerland) by the addition of 0.1 M HCl or 0.1 M NaOH . Subsequently, all dispersions were incubated at 1000 rpm using an Eppendorf Thermomixer[®] F1.5 (Eppendorf, Hamburg, Germany) at pH values ranging from one to eleven (steps of two pH units), for 2 h at 23 °C. After incubation, the pH of each sample was measured to indicate the final pH. Finally, the samples were centrifuged at $15000 \times g$ for 10 min using an Eppendorf Centrifuge 5415R and the supernatants were separated to quantify the dissolved elements concentrations.

Iron concentration measurement by a ferrozine-based colorimetric assay

The concentration of the dissolved iron from Fe(II)PP and the mixed Fe(II)-containing pyrophosphate salts was monitored by a ferrozine-based colorimetric assay¹³, as described previously. An excess of ascorbic acid (50 μl , 100 mM) was added to 50 μl sample (supernatant). After 30 minutes incubation of the sample with ascorbic acid, ferrozine (50 μl , 10 mM) was added. The absorbance at 565 nm was measured at room temperature by a SpectraMax M2e (Molecular Devices, Sunnyvale, CA, USA). Quantification of dissolved iron was performed based on intensity and with a calibration curve of FeSO_4 (0.0078 – 1 mM, $R^2 > 0.99$). It was confirmed that the presence of the Ca, Zn, or Mn ions did not interfere with the quantification of total iron (Figure 5.8 of Appendix 5.A). Statistical analysis was carried out to evaluate the significance of differences in iron concentration (significant at $p < 0.05$).

Elements concentration measurement by inductively coupled plasma – atomic emission spectroscopy (ICP-AES)

Inductively coupled plasma–atomic emission spectroscopy (ICP-AES) was used for independent determination of iron concentration, to be compared to the ferrozine assay. After incubation, the samples (i.e., supernatants) were 10 times diluted in 0.14 M HNO_3 , before injection in the ICP-AES system (Agilent 5110 VDV; Agilent Technologies, Tokyo, Japan). All measurements were done in duplicate. The concentrations of iron, calcium, zinc, manganese, and phosphorus from Fe(II)PP, CaPP, ZnPP, and MnPP salts were determined using scandium as an internal standard. The limit of detection (LOD) values of iron, calcium, zinc, manganese and phosphorus were 5, 20, 5, 1, and 50 $\mu\text{g/l}$, respectively.

6.2.3 Dissolution behavior the pure and the mixed Fe(II)-containing pyrophosphate salts in gastric-mimicked conditions

In order to get an early indication of the bio-accessibility of iron the minerals in the designed salts, dissolution of the salts in gastric-mimicked conditions was studied. The dried powders of the pure and mixed pyrophosphate salts were re-dispersed in MQ water (final concentration: 10 mg/ml), followed by adjusting the pH of the dispersions to pH 2 using a SevenExcellence Multiparameter pH meter (Mettler Toledo, Columbus, OH, USA) by the addition of 0.5 M HCl. Subsequently, all dispersions were incubated at 1000 rpm using an Eppendorf Thermomixer® F1.5 (Eppendorf, Hamburg, Germany) at 37 °C for 75 min. After the incubation, the pH of each sample was measured again to determine the final pH. Finally, the samples were centrifuged at $15000 \times g$ for 10 minutes using an Eppendorf Centrifuge 5415R and the supernatants were isolated to quantify the dissolved Fe and the other elements (i.e., Ca, Zn, or Mn and P) concentrations by the ferrozine-based colorimetric assay and ICP-AES, respectively (see section 6.2.2). All measurements were performed in duplicate, and quantification of dissolved iron was performed based on intensity and with a calibration curve of FeSO_4 (0.0078 – 1 mM, $R^2 > 0.99$). To quantify both Fe(II) and Fe(III) concentrations, the ferrozine-based colorimetric assay was done both with and without addition of excess amount of ascorbic acid. Presence of ascorbic acid results in reduction of Fe(III) to Fe(II) and consequently total Fe in solution can be measured. In the case of addition of no ascorbic acid, the concentration of Fe(II) can be quantified. Accordingly, Fe(III) concentration can be calculated by the difference between total Fe and Fe(II) concentrations.

6.3 Results and discussion

6.3.1 Dissolution behavior of the pure divalent metal pyrophosphate salts; Fe(II)PP, CaPP, ZnPP, and MnPP

As mentioned previously (in chapter 3), one of the main challenges in designing iron-containing compounds for food fortification is tuning their pH-dependent dissolution behavior. To prevent additional reactions between the iron source and the phytochemicals present in the fortified food vehicle while ensuring bio-accessibility of the iron, it is necessary for the compound to have limited dissolution in the food pH range (3-7), and good and fast dissolution in the gastrointestinal pH (1-3 and 6-8). In the case of mixing two or several minerals, the forementioned conditions should in principle hold for at least one of the pure components as well. Therefore, the dissolution behavior of the pure divalent metal pyrophosphate salts; Fe(II)PP, CaPP, ZnPP, and MnPP was evaluated as a function of pH by ICP-AES method, Figure 6.1. Quantification of the metals (i.e., Fe, Ca, Zn, and Mn) and phosphorus (P) concentrations from the pure pyrophosphate salts showed that interestingly all the salts have limited solubilities in the pH range 4-7, and fast dissolution in the low pH (1-3), Figure 6.1 (top).

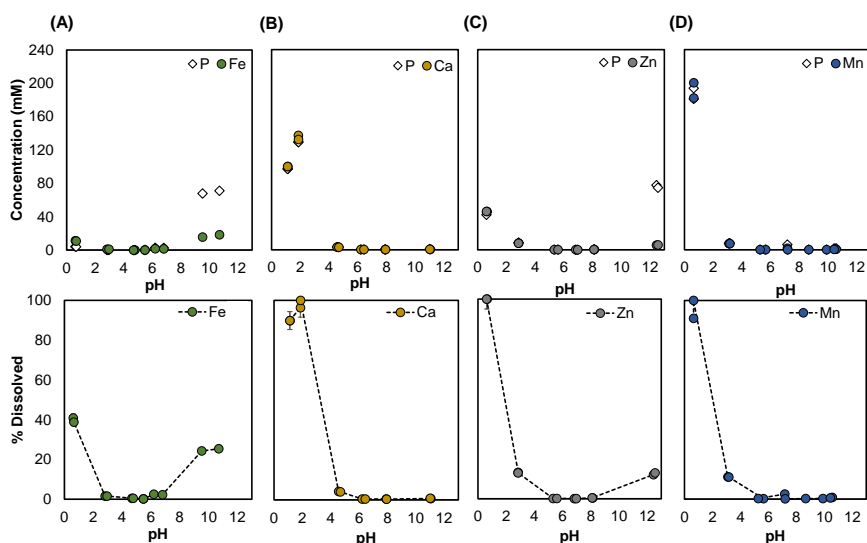


Figure 6.1 pH-dependent dissolution behavior of the pure divalent metal pyrophosphate salts obtained by ICP-AES. Concentrations of the elements (top) and percentage of the dissolve metal (bottom) for (A) Fe(II)PP, (B) CaPP, (C) ZnPP, and (D) MnPP.

Results showed that Fe(II)PP remained (practically) insoluble (i.e., $< 0.1 \text{ g/l}^{14}$) in the pH range 3-7. The soluble iron concentrations from this salt were below 1.7 mM, Figure 6.1 A (top) at pH 5-7, which was calculated to be maximum 0.5% of the total iron present in the solid, Figure 6.1 A (bottom). It was previously shown that the soluble iron concentration from Fe(III)PP in the same pH range (5-7) can reach up to 2.5 mM, see chapter 3¹⁵. This finding can explain why Fe(II)PP caused less discoloration of a black tea solution (pH ≈ 5.2), compared to Fe(III)PP, see section 5.3.3 of chapter 5. Below pH 3, the soluble iron concentration from Fe(II)PP increased up to approximately 11 mM around pH 1 which is equivalent to approximately 40% dissolved iron, Figure 6.1 A. The dissolution of iron from Fe(II)PP at pH < 3 can be due to the formation of soluble ferrous pyrophosphate complexes such as $\text{Fe}(\text{H}_3\text{P}_2\text{O}_7)_2$ and $\text{Fe}(\text{H}_2\text{P}_2\text{O}_7)_2^{2-16}$, ferric pyrophosphate complexes such as $\text{FeH}_3\text{P}_2\text{O}_7^{2+}$ and $\text{FeH}_2\text{P}_2\text{O}_7^{+17,18}$, free iron ions at low pH, and/or possible Fe(II)/Fe(III) chloride complexes with pyrophosphate species (pyrophosphoric acid has $\text{pK}_{\text{a}1}$ and $\text{pK}_{\text{a}2}$ values of 0.92 and 2.1, respectively¹⁹).

At pH > 7 , the soluble iron concentration increased up to 18 mM at pH 10. Interpolation of the soluble iron concentration data between pH 7 and 9 indicated that the iron concentration from this salt at pH 8 was approximately 7.8 mM, Figure 6.1 A (top). Furthermore, the lower measured Fe concentration, compared to P, at pH 10-11 was suggested to be due to the formation and sedimentation of the iron oxides and hydroxides at high pH values which was visually observed as dark orange/brown sediments in the titrated sample. Comparison between dissolution behavior of Fe(II)PP and Fe(III)PP (see chapter 3) at gastrointestinal pH range (i.e., 1-3 and 6-8) indicates that the soluble iron concentration from Fe(II)PP was higher than Fe(III)PP up to 11 times at pH 1 and 2.6 times at pH 8. These findings suggest that Fe(II)PP is a potential candidate for iron fortification of foods particularly at the pH range 5-7. Moreover, Fe(II)PP is expected to exhibit higher bio-accessibility of iron in the gastrointestinal tract due to its faster dissolution at biologically-relevant conditions, compared to Fe(III)PP^{6-8,20,21}.

Quantification of soluble calcium concentration from CaPP indicated limited solubility of this salt at pH ≥ 5 with maximum 3.2 mM Ca concentration at roughly pH 5, Figure 6.1 B (top), which corresponds to dissolution of 4.2% of the total initial Ca present in the solid salt Figure 6.1 B (bottom). At pH < 5 , the soluble Ca concentration was observed to increase up to approximately 130 mM at pH ≈ 2 which was $> 96\%$ dissolution. It has previously been shown that due to the limited solubilities of CaPP and Fe(III)PP, inclusion of Ca and Fe(III) in one pyrophosphate matrix can limit the soluble iron concentration from the mixed salts up to 8-fold in the pH range 3-7¹⁵ (see chapter 3). According to the results obtained from dissolution of the pure CaPP, which were in agreement with a previous work¹², it is hypothesized that inclusion of Ca alongside Fe(II) in the pyrophosphate matrix also results in limited dissolution of

the mixed compound (salt) at least at pH range 5-7, while showing relatively higher soluble iron (and calcium) concentrations at $\text{pH} < 3$.

ZnPP showed poor solubility at pH range 5-8 with a maximum concentration of 0.3 mM for Zn at $\text{pH} \approx 8$, Figure 6.1 C (top), which was roughly 0.5% of the total Zn present in the solid salt, Figure 6.1 C (bottom). At $\text{pH} \leq 5$, ZnPP is relatively soluble with $> 99\%$ Zn dissolution around pH 1. Moreover, at $\text{pH} > 8$, the solubility of the ZnPP was enhanced up to 6 mM at $\text{pH} \approx 12$ which was approximately 13% of the total zinc present in the solid salt. The lower Zn concentration measured with respect to P was again suggested to be due to the insoluble zinc oxide and hydroxide which was detected by the color of the remained sediment (dull white).

pH-dependent dissolution behavior of MnPP indicated that at $\text{pH} > 5$ the dissolved manganese concentration was below 2 mM, Figure 6.1 D (top) which corresponds to roughly 2.5% of the total Mn present in the solid salt. Moreover, at $\text{pH} < 5$ the measured soluble Mn concentration from MnPP increased up to $> 99\%$ (≈ 193 mM) at pH 2, see Figure 6.1 D (bottom).

The findings on the dissolution behavior of ZnPP and MnPP as a function of pH indicate that integration of Zn or Mn along Fe(II) in a pyrophosphate matrix is expected to result in poor solubility of iron from the matrices of the resulting mixed pyrophosphate salts with $M = \text{Zn}$ or Mn in the general formula at pH 5-7, while exhibiting higher soluble iron concentrations at $\text{pH} < 4$.

6.3.2 Dissolution behavior of iron from the mixed divalent metal Fe(II)-containing pyrophosphate salts

The dissolution of iron from the iron-containing salt should be limited at food pH (3-7) and high and fast at gastric pH (1-3) and/or intestinal pH (6-8). Therefore, the dissolution behavior of iron from Fe(II)PP and mixed divalent metal Fe(II)-containing pyrophosphate salts was evaluated as a function of pH by UV-Vis spectroscopy using the ferrozine assay¹³. It was confirmed that the presence of the Ca, Zn, or Mn ions did not interfere with the quantification of total iron in this assay, (see Figure 5.8 of Appendix 5.A). The dissolution behavior of iron from Fe(II)PP and the twelve mixed divalent Fe(II)-containing pyrophosphate salts in aqueous solution was evaluated in the pH range from 1-11, Figure 6.2. Quantification of the dissolution total iron from the mixed $M_{2(1-x)}\text{Fe}_{2x}\text{P}_2\text{O}_7$ salts indicated that overall all the mixed salts (i.e., $M = \text{Ca}$, Zn , and Mn) showed very limited dissolution of iron (< 0.5 mM) in the moderate pH range (4-7) while showing enhanced dissolved iron concentration in the gastric- and intestine-relevant pH (up to 5 and 1.3 mM, respectively), see Figure 6.2 A, B, and C for the mixed salts with $M = \text{Ca}$, Zn , and Mn , respectively. Therefore, as it was hypothesized, inclusion of the divalent metals studied in this work (i.e., Ca , Zn , or Mn) alongside Fe(II) in the pyrophosphate matrix resulted in a unique dissolution behavior of the mixed salts.

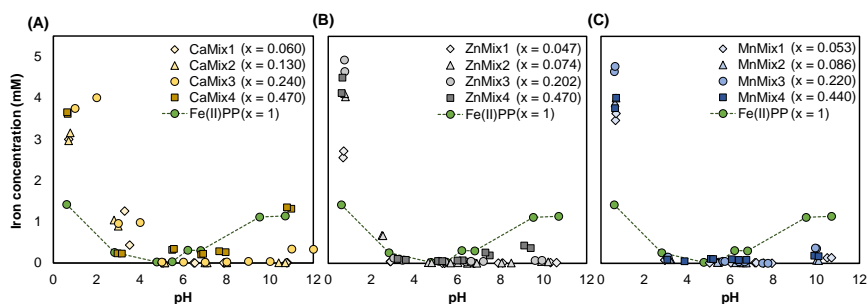


Figure 6.2 Dissolution behavior of iron from the mixed divalent metals Fe(II)-containing pyrophosphate salts in comparison to Fe(II)PP. Concentration of soluble iron from the mixed $M_{2(1-x)}Fe_{2x}P_2O_7$ salts where (A) $M = Ca$, (B) $M = Zn$, and (C) $M = Mn$, after 2 h incubation at 23 °C. The dissolution profile of iron from Fe(II)PP is shown for comparison (dashed lines).

In the case of Ca as the second divalent metal (i.e., $M = Ca$ in the mixed salts with the general formula $M_{2(1-x)}Fe_{2x}P_2O_7$, the dissolved iron concentration from all mixed salts decreased at $pH > 4.5$, compared to Fe(II)PP, Figure 6.2 A. One exception for this was the CaMix₄ salt with $x = 0.470$ at $pH 5.5$ and > 10 . At $pH 5.5$, the iron concentration from this salt (CaMix₄) was approximately 11 times higher than Fe(II)PP (i.e., 0.34 vs. 0.03 mM, respectively).

In the pH range 4.5–7, the mixed salts CaMix_{1–3} showed lower soluble iron concentration with up to ≈ 90 -fold decrease in the case of CaMix₁ salt with $x = 0.060$ at $pH 6.5$, compared to Fe(II)PP. Moreover, in this pH range the salt CaMix₄ with $x = 0.470$ had the highest iron dissolution among the mixed salts. Additionally, the dissolved iron concentration from the mixed salts with $M = Ca$ enhanced at $pH \leq 4$ with a rough maximum of 16-fold increase in the case of CaMix₃ with $x = 0.240$ at $pH 2$, compared to Fe(II)PP. Therefore, it is expected that the salts CaMix_{1–3} show lower iron-mediated reactivity at food pH, while exhibiting higher bio-accessibility at $pH 1$ –3, relative to Fe(II)PP (this is further discussed in section 6.3.3). These findings propose that the mixed $M_{2(1-x)}Fe_{2x}P_2O_7$ salts where $M = Ca$ with $x \leq 0.240$ are potential dual-fortificants for iron and calcium, particularly for the food vehicles in the pH range 5–7.

The results of dissolution behavior of iron from the mixed $M_{2(1-x)}Fe_{2x}P_2O_7$ salts where $M = Zn$ showed that in this case all mixed salts showed lower iron concentration in solution over the whole pH range 1–11, compared to Fe(II)PP (see Figure 6.2 B). The only exception to this was the salt ZnMix₄ with $x = 0.470$ with roughly similar iron dissolution at $pH 5$, compared to Fe(II)PP. This was in line with the fact that the dissolved iron concentration from this salt was similar to Fe(II)PP in a black tea so-

lution at the same pH, see chapter 5. Nevertheless, this salt was practically insoluble with a maximum soluble iron concentration of 0.05 mM (3.2 mg/l)¹⁴.

In the food-relevant pH (3-7), inclusion of Zn along Fe(II) in the pyrophosphate matrix decreased the soluble iron concentration from the mixed salts with respect to the pure Fe(II)PP. The lowest dissolved iron was measured for the salt ZnMix1 with $x = 0.047$ which was 12 and 120 times lower at pH 5.5 and 6.5, respectively, with respect to the iron dissolution from Fe(II)PP in this range. Furthermore, at $\text{pH} < 3$ iron dissolution from the mixed salts with $M = \text{Zn}$ was enhanced up to roughly 5 mM in the case of the salt ZnMix3 with $x = 0.202$ at $\text{pH} \approx 1$ which was 3.5 times higher than Fe(II)PP at this pH. It is worth noting here that this salt exhibited the highest dissolved iron concentration among all mixed divalent Fe(II)-containing salts at gastric-relevant pH range. According to what was discussed, the mixed Fe(II)-containing pyrophosphate salts with $x \leq 0.202$ in which Zn is included as the second mineral seem to be promising and potential candidates for the simultaneous fortification of foods with iron and zinc.

In the case of $M = \text{Mn}$ in the mixed $M_{2(1-x)}\text{Fe}_{2x}\text{P}_2\text{O}_7$ salts, the dissolution behavior of iron from the salts was very similar to the case in which $M = \text{Zn}$. Overall, the soluble iron concentration for all the mixed salts with $M = \text{Mn}$ was lower in comparison to Fe(II)PP at $\text{pH} > 3$ except for the salt MnMix4 with approximately 5 times higher iron concentration at pH 5, Figure 6.2 C. This salt, similar to the salt ZnMix4, was practically insoluble with 0.1 mM Fe concentration. At pH range 3-7, the salt MnMix1 with $x = 0.053$ showed decreased iron concentration in solution which was approximately 3-30 times lower than Fe(II)PP at pH 5-6.5, respectively.

In addition, the mixed salts with Mn as the second divalent metal showed enhanced iron dissolution at $\text{pH} < 3$, compared to the pure Fe(II)PP. Results indicated that the mixed salt MnMix3 with $x = 0.220$ had the maximum soluble iron concentration in this pH range (i.e., ≈ 4.8 mM) with an approximately 3.35-fold increase with respect to Fe(II)PP. These results suggest that the mixed $M_{2(1-x)}\text{Fe}_{2x}\text{P}_2\text{O}_7$ salts with $M = \text{Mn}$ and at least $x \leq 0.220$ are potential candidates for dual-fortification of foods with iron and manganese.

6.3.3 Dissolution behavior of the pure and the mixed divalent metal Fe(II)-containing pyrophosphate salts in gastric-mimicked conditions

Even though poorly water-soluble or water-insoluble iron sources are beneficial for food fortification, they have the drawback of low bio-availability of iron^{4,22}. It is worth noting here that bio-accessibility (i.e., the quantity of iron in solution and available for absorption in the gastrointestinal tract) is necessary but not the only requirement for iron bio-availability⁸. Therefore, it is of importance to ensure the bio-accessibility of iron by the condition that the solubility of iron source should be relatively high and fast at gastric and/or intestinal conditions. It has previously been

reported that higher quantities of total soluble iron at pH 1-3 can ensure adequate bio-accessibility of iron in the stomach^{20,23} and that *in vitro* solubility of Fe-containing salts at pH 1 is a good indicator for *in vivo* Fe uptake by rats⁷. Therefore, we explored soluble iron (II) and total iron concentrations from the pure and the mixed salts at gastric-like conditions (pH 2 and 37 °C) by UV-Vis spectroscopy using the ferrozine assay¹³. Accordingly, Fe(III) concentration can be obtained by the difference between total Fe and Fe(II) concentrations.

Quantification of the accuracy of total iron determination by the ferrozine assay was verified by comparison with the ICP-AES method, Figure 6.4 of Appendix 6.A. The iron concentrations measured by both methods were found to be in good agreement. The dissolution behavior of iron, second metal (M, i.e., Ca, Zn, or Mn), and phosphorus (P) from the pure and mixed salts $M_{2(1-x)}Fe_{2x}P_2O_7$ ($0 \leq x \leq 1$, when M = Ca, Zn, or Mn) based on the existing protocols reported in the literature^{24,25} were quantified after 75 min incubation at pH 2 and 37 °C to investigate the biological relevance of these salts, Figure 6.3.

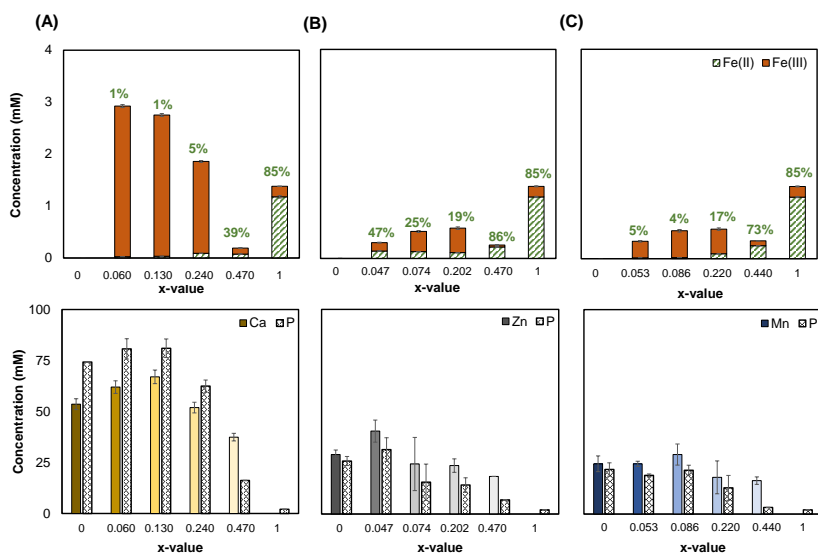


Figure 6.3 Dissolution behavior of iron from the salts in gastric-mimicked conditions. Quantification of the dissolved iron (II) (green, pattern) and iron (III) (orange, solid) concentrations (top, obtained from UV-Vis spectroscopy), as well as the second metal (M = Ca, Zn, or Mn, solid) and phosphorus concentrations (P, pattern) (bottom, obtained from ICP-AES) from the mixed $M_{2(1-x)}Fe_{2x}P_2O_7$ salts where (A) M = Ca, (B) M = Zn, and (C) M = Mn in gastric conditions. The percentage of Fe(II) with respect to the total iron in solution is written on each column (top).

The iron solubility from the Fe(II)PP was quantified, after incubation in gastric-mimicked conditions, see $x = 1$ in Figure 6.3 (top). Furthermore, under the same condition the dissolved iron from Fe(II)PP was compared to Fe(III)PP which is widely used in fortification of foods due to its poor solubility, Figure 6.5 in Appendix 6.A. The concentration of the dissolved iron from Fe(II)PP was measured to be approximately 1.38 mM, roughly 12 times higher than Fe(III)PP (~ 0.11 mM, which was in line with the soluble iron concentration from Fe(III)PP at pH 2 in our previously reported study¹⁵, see chapter 3). Accordingly, the results suggest that Fe(II)PP is more likely to be biologically accessible in gastric environment due to the higher total quantity of soluble iron from this salt, compared to Fe(III)PP. Additionally it has been previously shown that iron uptake is significantly higher when treating Caco-2 cells with Fe(II), compared to Fe(III)²⁶. Quantification of concentration of Fe(II) and total Fe showed that 85% of the total dissolved iron from Fe(II)PP remains in +2 oxidation state after 75 minutes incubation in gastric conditions, Figure 6.3. This, in combination with the results obtained from the reactivity assessment of the Fe(II)PP in black tea solution (see section 5.3.3 in chapter 5), indicates that the pure Fe(II)PP can be a better iron fortificant candidate for foods with moderate pH, compared to Fe(III)PP, owing to the fact that it has higher iron solubility in gastric conditions (with 85% Fe(II)) and causes less iron-mediated reactivity in a catechin model solution at pH ≈ 5 (i.e., less discoloration in the black tea solution in our study).

Incubating the mixed divalent metal Fe(II)-containing pyrophosphate salts at gastric relevant conditions (i.e., at pH 2 and 37 °C for 75 min) resulted in lower total soluble iron concentration from the mixed salts (with respect to Fe(II)PP), except for the salts in which $M = \text{Ca}$. This can be explained by higher final pH of the dispersions than the adjusted pH. The final pH of these dispersion was measured to be in the range of 2.1-3.3. In this pH range, in line with the results obtained from the pH-dependent dissolution behavior of iron from the mixed salts (see previous section), the total dissolved iron concentration from the salts with $M = \text{Zn}$ and Mn was lower and in the case of $M = \text{Ca}$ was higher, compared to Fe(II)PP.

The mixed salts $\text{M}_{2(1-x)}\text{Fe}_{2x}\text{P}_2\text{O}_7$, where $M = \text{Ca}$ (with measured $0.060 \leq x \leq 0.470$), showed increased total soluble iron concentration for all mixed salts except for the mixed salt with $x = 0.470$ (CaMix4), compared to Fe(II)PP ($x = 1$), Figure 6.3 A (top). The maximum soluble iron concentration was measured for the salt with $x = 0.060$ (CaMix1) which was $> 60\%$ of the total iron present in the salt with an approximately 2.1-fold increase with respect to Fe(II)PP. The enhanced dissolution of iron from the mixed salts upon increasing calcium content in their reaction mixture can be due to the pH-dependent dissolution behavior of CaPP, Figure 6.1 A. It has previously been shown as well that the high solubility of CaPP ($> 99\%$) at pH ≤ 3 ¹², enhanced the soluble iron concentration up to a fourfold increase at pH ≤ 3 (compared to pure Fe(III)PP) when mixing Ca with Fe(III) in a pyrophosphate matrix¹⁵,

see chapter 3. Furthermore, inclusion of Ca alongside Fe(II) in the pyrophosphate matrix resulted in oxidation of Fe(II) to Fe(III) in all mixed salts at pH 2. A maximum of 39% of the total dissolved iron remained as Fe(II) for the mixed salt with $x = 0.470$ (CaMix4). This can be explained to be a consequence of increased soluble iron concentration from these mixed salts that can undergo oxidation. Additionally, analysis of the data obtained from ICP-AES indicated that above 65% of the calcium present in all the salts dissolved at gastric conditions, Figure 6.3 A (bottom). The maximum soluble calcium concentration was measured to be approximately 67 mM for the mixed salt with $x = 0.130$ which was more than 99% of the total Ca present in the solid salt.

In the case of the mixed salts $M_{2(1-x)}Fe_{2x}P_2O_7$, where $M = Zn$ (with measured $0.047 \leq x \leq 0.470$), the total soluble iron concentration decreased up to 5.3-fold in the case of the mixed salt with $x = 0.470$, compared to Fe(II)PP ($x = 1$), Figure 6.3 B (top). The maximum measured iron concentration in the solution was 0.58 mM for the mixed salt with $x = 0.202$ (ZnMix3). Interestingly, neither the total soluble iron nor the percentage of the Fe(II) from the mixed salts was a monotonic function of their x -values in the case of zinc as the second divalent metal, Figure 6.3 B (top). Overall, inclusion of Zn alongside Fe(II) in the pyrophosphate matrix caused the least oxidation of Fe(II) among the divalent metals studied in this work, with the highest percentage of Fe(II) for the mixed salt with $x = 0.470$ (86% of the total dissolved iron) which was similar to Fe(II)PP. This can be explained by the fact that zinc has antioxidant activity^{27,28} and prevents the oxidation of Fe(II) to Fe(III) up to a certain extent at this pH range. Furthermore, quantification of the zinc concentration in the solution showed that for all the salts at least 40% of the initial zinc present in the salts dissolved, Figure 6.3 B (bottom). The soluble Zn concentration at gastric-mimicked conditions was the highest for the mixed ZnMix1 salt with $x = 0.047$ (roughly 40 mM) which was approximately 64% of the total zinc present in the solid salt.

In the case of the mixed salts with the general formula $M_{2(1-x)}Fe_{2x}P_2O_7$, where $M = Mn$ (with measured $0.053 \leq x \leq 0.440$), the concentration of iron in solution decreased up to 4.2-fold in the case of the mixed salt with $x = 0.053$ (MnMix1, 0.33 mM), compared to Fe(II)PP ($x = 1$), Figure 6.3 C (top). The maximum dissolved iron concentration was measured to be approximately 0.56 mM for the mixed salt with $x = 0.220$. Moreover, inclusion of Mn alongside Fe(II) in the pyrophosphate matrix exhibited the least oxidation of iron for the mixed salt with the highest iron content ($x = 0.44$) among the mixed pyrophosphate salts with 73% Fe(II) of the total dissolved iron. In addition, quantification of the soluble manganese concentration with ICP-AES indicated that at least 31% of the manganese present in the solid salt dissolved at gastric-mimicked conditions, Figure 6.3 C (bottom). The maximum measured soluble Mn concentration was approximately 29 mM in the case of the mixed salt with $x = 0.086$ which was 45% of the initial Mn present in the salt.

To summarize, the results obtained from our preliminary experiments on bio-accessibility of the minerals in the mixed salts $M_{2(1-x)}Fe_{2x}P_2O_7$ suggest that the mixed salt with $x = 0.060$ where $M = Ca$ shows the highest soluble iron concentration in gastric-mimicked conditions, with a 2.1-fold increase with respect to Fe(II)PP. Furthermore, the mixed salts with $x = 0.202$ and 0.220 , showed maximum and similar dissolved iron concentration (≈ 0.6 mM) where $M = Zn$ and Mn , respectively, in gastric pH and temperature.

In future experiments, pH-dependent dissolution behavior of iron from these mixed Fe(II)-containing pyrophosphate salts in the presence of the chemicals that are plentiful in the food products such as taste enhancers and phenolic compounds (more preferably poorly water-soluble or insoluble phenolics, based on the results of chapter 4) that are present in the food with pH 5-7 is suggested to be further investigated. Moreover, the *in vivo* bio-availability of the salts, chemical stability, and the required safety clearance of the studied mixed pyrophosphate salts, which can be product-specific, should be addressed in future but are beyond the scope of this work.

6.4 Conclusions

In the present study, we report the dissolution behavior of the pure as well the mixed divalent metal Fe(II)-containing pyrophosphate salts. We investigate for the first time the pH-dependent dissolution of iron (II) pyrophosphate (Fe(II)PP) after 2 h at room temperature (23 °C). Our results show that Fe(II)PP was very poorly soluble in the pH range of 3-7 ($< 0.5\%$), while it dissolved well in the pH < 3 up to 11 mM ($\approx 40\%$) at pH 1. In addition, the second divalent metal pyrophosphate salts (i.e., CaPP, ZnPP, and MnPP) showed low solubilities at food-relevant pH (4-7), but dissolved fast in the gastric pH range (1-3) with maximum 96% at pH ≈ 1 . Furthermore, our findings on the iron dissolution behavior from the mixed $M_{2(1-x)}Fe_{2x}P_2O_7$ salts ($0 < x < 1$) indicate that all the mixed salts ($M = Ca, Zn, \text{ and } Mn$) had very limited iron dissolution (< 0.5 mM) in the moderate pH range (5-7) while showing enhanced dissolved iron concentration in the gastric- and intestine-relevant pH up to 5 and 1.3 mM, respectively. Moreover, all the mixed salts with the lowest iron content showed the lowest iron dissolution at pH 6.5. These salts are CaMix1 ($x = 0.06$), ZnMix1 ($x = 0.047$), and MnMix1 ($x = 0.053$) with approximately 90-, 120-, and 30-fold decreased soluble iron concentrations, compared to Fe(II)PP at this pH.

Mimicking the gastric conditions (incubation at pH 2 and 37 °C for 75 min) showed that the soluble iron concentration from the Fe(II)PP was first approximately 12 times higher than Fe(III)PP, and second contained 85% Fe(II) with respect to the total iron in solution. Our results show that Fe(II)PP is more likely to be biologically accessible, compared to Fe(III)PP. Furthermore, quantifying the dissolved iron from the mixed

salts $M_{2(1-x)}Fe_{2x}P_2O_7$ at the gastric conditions indicated that among the studied second divalent metals (M), the soluble iron concentration increased only in the case of $M = Ca$ up to a 2.1-fold increase, compared to $Fe(II)PP$. Meanwhile the oxidation of the dissolved iron was the fastest in this case with a maximum of 39% $Fe(II)$ with respect to the total dissolved iron in for the mixed salt with $x = 0.47$. Moreover, at gastric-mimicked conditions the soluble iron decreased for the mixed salts where $M = Zn$ and Mn up to a 5.3- and 4.2-fold, respectively, compared to $Fe(II)PP$. However, in both cases of $M = Zn$ and Mn , for the mixed salts with the highest iron content ($x = 0.470$ and 0.440 , respectively), the oxidation of $Fe(II)$ to $Fe(III)$ was the lowest resulting in 86% and 73% $Fe(II)$ of the total iron in solution, respectively. Additionally, the second metals (Ca , Zn , or Mn) were soluble and therefore are expected to be biologically- accessible. Our results suggest that the mixed divalent metal $Fe(II)$ -containing pyrophosphate salts with $M_{2(1-x)}Fe_{2x}P_2O_7$ ($0 < x < 1$), are potential delivery systems for dual fortification of food products due to their poor solubility at food-relevant pH range and fast dissolution at gastric conditions.

6.5 Acknowledgments

The majority of the experiments of this work was performed in the Laboratory of Food Chemistry in Wageningen University and Reserach and for that we are thankful to Judith Bijlsma, Wouter J.C. de Bruijn, and Jean-Paul Vincken. We are grateful to Arjen Reichwein of Nouryon specialty chemicals B.V. for performing the ICP-AES measurements.

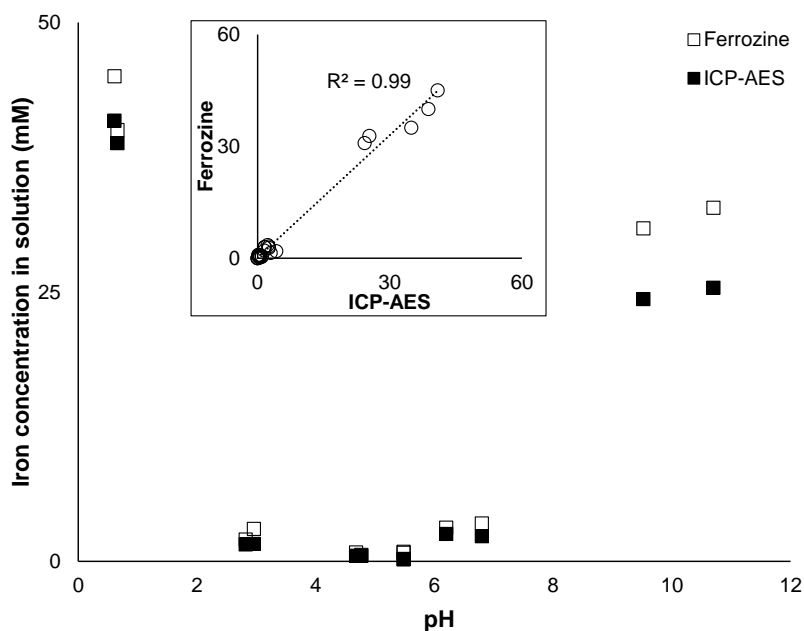


Figure 6.4 Verification of the ferrozine assay with ICP-AES method. Dissolution of iron from Fe(II)PP as a function of pH determined by ICP-AES (filled markers) and by the ferrozine (open markers) methods. The inset depicts the correlation between the iron concentration measured using both methods (including the experiments at gastric conditions). The iron concentrations in solution measured by the two different methods are found to be in good agreement ($R^2 = 0.99$).

6.A Appendix

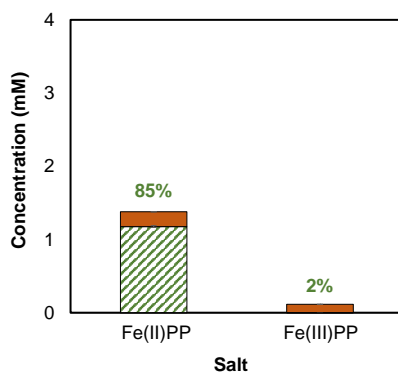


Figure 6.5 Dissolution behavior of iron from Fe(II)PP in gastric conditions. Quantification of the dissolved iron (II) (green, pattern) and iron (III) (orange, solid) concentrations (obtained from UV-Vis spectroscopy) from Fe(II)PP, compared to Fe(III)PP. The percentage of Fe(II) with respect to the total iron in solution is written on each column.

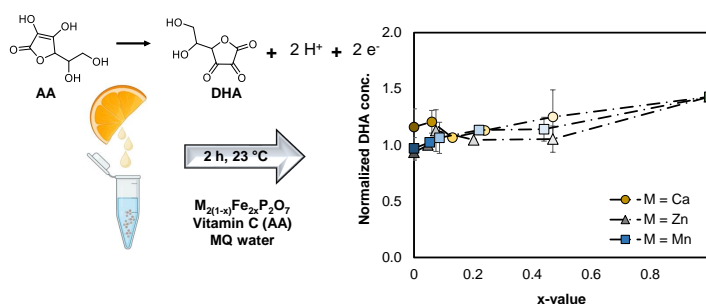
References

- 1 J. Bijlsma, W. J. de Bruijn, J. A. Hageman, P. Goos, K. P. Velikov, and J. P. Vincken, *Scientific Reports* **10**, 1 (2020).
- 2 E. Habeych, V. van Kogelenberg, L. Sagalowicz, M. Michel, and N. Galaffu, *Food Research International* **88**, 122 (2016).
- 3 R. F. Hurrell, *Nutrients* **14**, 1609 (2022).
- 4 C. M. Andre, D. Evers, J. Ziebel, C. Guignard, J. F. Hausman, M. Bonierbale, T. Zum Felde, and G. Burgos, *Journal of Agricultural and Food Chemistry* **63**, 9012 (2015).
- 5 V. Dueik, B. Chen, and L. Diosady, *Journal of Food Quality* **2017** (2017).
- 6 R. Hurrell, Nestel, Beard, and Freire, *Nutrition reviews* **60**, S7 (2002).
- 7 F. Rohner, F. O. Ernst, M. Arnold, M. Hilbe, R. Biebinge, F. Ehrensperger, S. E. Pratsinis, W. Langhans, R. F. Hurrell, and M. B. Zimmermann, *The Journal of Nutrition* **137**, 614 (2007).
- 8 K. J. Wienk, J. J. Marx, and A. C. Beynen, *European Journal of Nutrition* 1999 38:2 **38**, 51 (1999).
- 9 S. K. Bardal, J. E. Waechter, and D. S. Martin, *Applied pharmacology* (Elsevier Health Sciences, 2011).
- 10 A. Vatandoust and L. Diosady, *Current Opinion in Food Science* **43**, 232 (2022).
- 11 D. L. Perry, *Handbook of inorganic compounds* (CRC press, 2016).

- 12 Y. M. van Leeuwen, *Colloidal Metal Pyrophosphates Salts Preparation, Properties and Applications*, Ph.D. thesis (2013).
- 13 L. L. Stookey, *Analytical chemistry* **42**, 779 (1970).
- 14 A. Liangou, K. Florou, M. Psychoudaki, E. Kostenidou, E. Tsiligiannis, and S. N. Pandis, *Environmental Science and Technology* **56**, 3952 (2022).
- 15 N. Moslehi, J. Bijlsma, W. J. de Bruijn, K. P. Velikov, J.-P. Vincken, and W. K. Kegel, *Journal of Functional Foods* **92**, 105066 (2022).
- 16 J. I. Lee and L. M. Kwon, *Korean Journal of Chemical Engineering* 1989 6:1 **6**, 1 (1989).
- 17 C. M. Flynn Jr., *Chemical Reviews* **84**, 31 (2002).
- 18 C. L. Jiang, X. H. Wang, B. K. Parekh, and J. W. Leonard, *Mining, Metallurgy Exploration* **15**, 1 (1998).
- 19 D. R. Lide, *CRC handbook of chemistry and physics*, Vol. 85 (CRC press, 2004).
- 20 J. H. Swain, S. M. Newman, and J. R. Hunt, *The Journal of nutrition* **133**, 3546 (2003).
- 21 T. Tian, E. Blanco, S. K. Smoukov, O. D. Velev, and K. P. Velikov, *Food Chemistry* **208**, 97 (2016).
- 22 K. K. Khoja, M. F. Aslam, P. A. Sharp, and G. O. Latunde-Dada, *Food Chemistry* **335**, 127671 (2021).
- 23 F. M. Hilty, J. T. Knijnenburg, A. Teleki, F. Krumeich, R. F. Hurrell, S. E. Pratsinis, and M. B. Zimmermann, *Journal of Food Science* **76**, N2 (2011).
- 24 R. Blanco-Rojo and M. P. Vaquero, "Iron bioavailability from food fortification to precision nutrition. A review," (2019).
- 25 N. Sulaiman, D. I. Givens, and S. Anitha, *Frontiers in Sustainable Food Systems* **5**, 392 (2021).
- 26 W. L. He, Y. Feng, X. L. Li, Y. Y. Wei, and X. E. Yang, *Journal of Zhejiang University. Science. B* **9**, 707 (2008).
- 27 A. Primikyri, G. Mazzone, C. Lekka, A. G. Tzakos, N. Russo, and I. P. Gerothanassis, *Journal of Physical Chemistry B* **119**, 83 (2015).
- 28 Y. Song, S. W. Leonard, M. G. Traber, and E. Ho, *The Journal of Nutrition* **139**, 1626 (2009).

Mixed Fe(II)-containing: Redox interactions with vitamin C

Abstract



Addition of vitamin C (ascorbic acid) has proven to cause a significant increase in iron absorption from iron-fortified foods. However, it comes with the drawback of noticeable loss of vitamin C due to its oxidation in the presence of metals. In this work, we explore the oxidation of vitamin C in the presence of the pyrophosphate salts with the general formula $M_{2(1-x)}Fe_{2x}P_2O_7$ ($0 \leq x \leq 1$, where $M = Ca, Zn, \text{ or } Mn$) after 1 h, 2 h, and 48 h incubation at 23 °C. Results showed that although ferrous pyrophosphate (Fe(II)PP) enhanced the oxidation of vitamin C only up to 1.5 times (compared to the autooxidation of vitamin C) over 48 h, this was equivalent to only approximately 4% loss of vitamin C in the presence of this salt. Furthermore, over time the oxidation of vitamin C in the presence of the mixed Fe(II)-containing salts was reduced down to 1.4 times, compared to Fe(II)PP. Our findings showed that the potential dual-fortificants with $x = 0.06, 0.086, \text{ and } 0.053$ where $M = Ca, Zn, \text{ and } Mn$ respectively, do not enhance the oxidation of vitamin C over 48 h, compared to the autooxidation of vitamin C in pure water. These outcomes suggest that the pure Fe(II)PP and the mixed Fe(II)-containing pyrophosphate salts are expected to be suitable candidates for multi-mineral fortification of vitamin C-rich foods.

"Absence of understanding does not warrant absence of existence."

Avicenna – Persian polymath, 980-1037 AD

7.1 Introduction

One of the risk factors that increases the chance of developing iron deficiency is inadequate consumption of vitamin C from fresh fruits and vegetables¹. Vitamin C (or ascorbic acid) is a water-soluble vitamin and a well-known reducing agent for iron which enhances the amount of absorbed (non-heme *) iron from diet and most iron compounds substantially². Furthermore, recent works have reported a high prevalence of vitamin C deficiency (approximately 7-70% of the population in different countries) throughout the world³. The most common severe vitamin C deficiency is scurvy which is caused in the human body for insufficient intake of this micronutrient for three months. Addition of vitamin C to food products such as dry milk, infant formulas, cereal-based complementary foods, chocolate drink powders, beverages, fruit juices, fruit-flavored drinks, and juice-added soda water has been found to be successful in increasing intake of this nutrient^{1,4}. Therefore, addition of vitamin C to foods, particularly to the iron-fortified food products, has attracted a great deal of attention in food industry. Next to cocoa products as the suggested food vehicles for iron and vitamin C fortification, ascorbic acid is also added to oils, fats, soft drinks as iron absorption enhancer¹. Nevertheless, ascorbic acid is relatively unstable in the presence of oxygen, metals, humidity and/or high temperatures⁴. Thus foods that are appropriately packaged and not cooked are known to be the preferred vehicles for vitamin C fortification¹.

Vitamin C, which acts as scavenger of free radicals in biological systems, can oxidize to dehydroascorbic acid (DHA)^{1,5}. This oxidation reaction which is catalyzed in the presence of transition metals specially cupric (Cu(II)) and ferric (Fe(III)) is called Fenton reaction⁶ and is attributed to the loss of ascorbic acid in iron-rich food⁷, see Figure 7.1. Ascorbic acid can also accelerate formation of off-flavor and off-color in foods through these Fenton-like reactions⁸. This pro-oxidant effect occurs in the presence of the mentioned metal ions when the level of available ascorbic acid is relatively low and not sufficient to scavenge the radicals formed by Fenton-like reactions. In both food and physiological conditions, the key oxidative loss pathways for ascorbic acid are via reactive oxygen species (ROS) and transition metals, specially Fe(III) and Cu(II). However, to date the stoichiometric ratios, mechanisms, and rate constants for the transition metal reactions are unclear⁷.

*The iron that is found in plant foods such as nuts, seeds, and leafy greens.

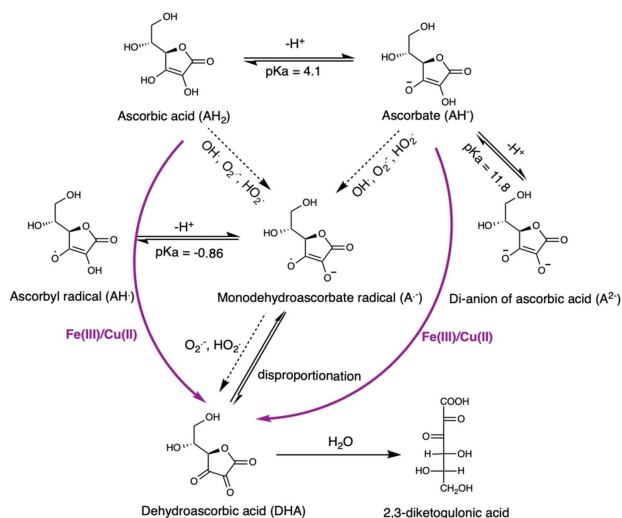


Figure 7.1 Pathways for oxidation of ascorbic acid. In this work, the concentration of dehydroascorbic acid (DHA) is evaluated as the oxidation product of ascorbic acid. Scheme is obtained with permission⁷.

In most studies, the addition of vitamin C and iron with 2:1 mole ratio (6:1 weight ratio) has shown to successfully increase the iron absorption from foods up to 2- to 3-fold in adults and children¹. However the main problem with using ascorbic acid as a food additive is that substantial amounts can be lost during food storage and preparation. In this work, we explore the potential application of Fe(II)PP and the mixed divalent metal Fe(II)-containing pyrophosphate salts $M_{2(1-x)}Fe_{2x}P_2O_7$ ($0 < x < 1$, where $M = Ca, Zn, \text{ or } Mn$) for being applied in food fortification in combination with vitamin C, intending for higher amounts of soluble iron and intact vitamin C accessible for absorption in the human body. To this aim, we investigate the iron-mediated oxidation of vitamin C (ascorbic acid) in water dispersions of these salts and compare its oxidation extent of in the presence of the salts to its autooxidation extent in pure water. Furthermore, in order to get more insight into the rate of the oxidation of vitamin C in the presence of these salts during storage, we investigate the effect of time on the oxidation of ascorbic acid in the presence of the salts up to 48 h.

7.2 Materials and methods

7.2.1 Materials

hydrochloric acid (HCl, 37 wt.%), 1,2 phenylenediamine (OPDA), 3-(2-pyridyl)-5,6-diphenyl-1,2,4-triazine-*p,p'*-disulfonic acid monosodium salt hydrate (i.e., ferrozine; ≥ 97 wt.%), and dehydroascorbic acid (DHA) were obtained from Sigma Aldrich (St. Louis, MO, USA). Iron (II) sulfate heptahydrate ($\text{FeSO}_4 \cdot 7\text{H}_2\text{O}$, ≥ 99 wt.%) was obtained from Alfa Aesar (Haverhill, MA, USA). Ethanol absolute (≥ 99 wt.%) and ascorbic acid (vitamin C, ≥ 99 wt.%) were obtained from VWR International (Radnor, PA, USA). The Milli-Q (MQ) water used was deionized by a Millipore Synergy water purification system (Merck Millipore, Billerica, MA, USA).

7.2.2 Autoxidation of iron from the pure Fe(II)PP and mixed divalent metal Fe(II)-containing pyrophosphates salts

In order to evaluate the autoxidation of the iron from the Fe(II)-containing pyrophosphate salts, their dried powders were re-dispersed in MQ water (final concentration: 10 mg/ml). Then, the dispersions were incubated at 1000 rpm using an Eppendorf Thermomixer® F1.5 (Eppendorf, Hamburg, Germany) at 23 °C for 1, 2, and 48 h. After the incubation, the final pH of the samples were measured, the samples were centrifuged at $15000 \times g$ for 10 minutes using an Eppendorf Centrifuge 5415R, and the supernatants were isolated to quantify the dissolved Fe(II) and Fe(III) concentrations by a ferrozine-based colorimetric assay⁹, as described in previous chapters. The absorbance at 565 nm was measured at room temperature by a CLARIOstar Plus Microplate Reader (BMG LABTECH, Ortenberg, Germany). All measurements were performed in duplicate and quantification of dissolved iron was performed based on intensity and with a calibration curve of FeSO_4 (0.0078–1 mM, $R^2 > 0.99$). Statistical analysis was carried out to evaluate the significance of differences in iron concentration (significant at $p < 0.05$).

7.2.3 Oxidation of vitamin C in the presence of the pure and mixed divalent metal Fe(II)-containing pyrophosphate salts

Re-dispersing the the dried salts were followed by addition of aqueous solution of vitamin C (ascorbic acid) to reach a final concentration of 10 mg/ml and 200 mM (at least 3 times in excess) for the salts and vitamin C, respectively. The dispersions then were incubated in the same condition as described in section 7.2.2, (i.e., under continuous stirring at 1000 rpm and 23 °C for 1, 2, and 48 h). Subsequently, the final pH of the samples were measured, and the samples were centrifuged at $15000 \times g$ for 10 minutes using an Eppendorf Centrifuge 5415R and the supernatants were

isolated to quantify the dissolved iron (i.e., Fe (II) and Fe(III)) and DHA concentrations, by the previously-described ferrozine-based colorimetric⁹ and an OPDA-based fluorometric⁵ assays, respectively.

Quantification of DHA concentration by an OPDA-based fluorometric assay

The concentration of the oxidation product of vitamin C (dehydroxy ascorbic acid, DHA) was monitored by an OPDA-based fluorometric assay⁵. Under acidic conditions, DHA reacts with 1,2 phenylenediamine (OPDA) and forms 3-(1,2-dihydroxyethyl)-fluoro[3,4-b]quinoxaline-1-one (DFQ), see Figure 7.2, which is a highly fluorescent compound and can be quantified by fluorescence spectroscopy with excitation and emission at approximately 365 and 430 nm, respectively^{5,10,11}. Since DHA and OPDA react with a 1:1 stoichiometry ratio, the change in DFQ concentration can be related to the change in DHA concentration and consequently the oxidation extent of vitamin C.

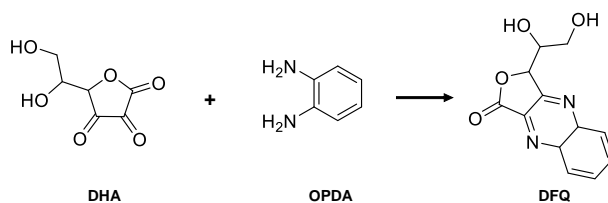


Figure 7.2 The reaction between DHA and OPDA. Dihydroxyascorbic acid (DHA) and 1,2 phenylenediamine (OPDA) react with 1:1 mole ratio and form 3-(1,2-dihydroxyethyl)-fluoro[3,4-b]quinoxaline-1-one (DFQ) which can be detected by fluorescence spectroscopy and related to the oxidation extent of ascorbic acid.

After isolation of the supernatants, a solution of OPDA in 0.1 M HCl (100 μ l, 200 mM) was added to 100 μ l sample. In order to ensure the complete reaction of DHA with OPDA, a 30 min reaction time was chosen⁵. The samples were then transferred to a 384-well black plate and the fluorescence at 425-435 nm was recorded at room temperature by a CLARIOstar Plus Microplate Reader (BMG LABTECH, Ortenberg, Germany). All measurements were performed in duplicate and quantification of total DHA was performed based on intensity with a calibration curve of DHA (0.001–1 mM, $R^2 > 0.99$). The concentration of DHA after exposure of vitamin C to the salts was normalized with respect to the concentration of DHA in the absence of the salts (i.e., the oxidation of vitamin C in pure water). Statistical analysis was carried out to evaluate the significance of differences in DFQ concentration which is equal to the differences in DHA concentration (significant at $p < 0.05$).

7.3 Results and discussion

7.3.1 Autoxidation of iron from the pure Fe(II)PP and mixed divalent metal Fe(II)-containing pyrophosphates salts

Dissolved iron ions in water are in equilibrium in two oxidation states; Fe(II) and Fe(III). Based on the autoxidation reaction: $2\text{Fe}^{2+} + \frac{1}{2}\text{O}_2(\text{g}) + 2\text{H}^+ \rightleftharpoons 2\text{Fe}^{3+} + \text{H}_2\text{O}$ (with the standard potential difference, $\Delta E^0 = 0.46\text{V}$), the ratio of Fe(III) to Fe(II) concentrations in equilibrium reads: $[\text{Fe}^{3+}]/[\text{Fe}^{2+}] = \sqrt{p_{\text{O}_2}^{1/2} 10^{-2pH} \exp(2F\Delta E^0/RT)}$, in which the p_{O_2} is the partial pressure of oxygen. Moreover, F , R , and T are the Faraday's constant, gas constant, and temperature, respectively. Although Considering $p_{\text{O}_2} = 0.2$ in water results in large values for $[\text{Fe}^{3+}]/[\text{Fe}^{2+}]$ ratios at $\text{pH} < 7$, the kinetics of this oxidation reaction can be slow depending on the pH. It has previously been reported that the oxidation rate of Fe(II) is a function of pH and is noticeably influenced by the counterions and complexes of the metals as well¹². For instance, while oxidation of about 95% of Fe(II) at pH 6 takes about a week, this reaction is up to 95% complete in a few minutes at pH 8¹³. Therefore, the oxidation reaction in the time span of the performed experiments in this work are expected to be incomplete which explains the obtained concentration ratios of Fe(III) to Fe(II) (or the percentage of Fe(II) with respect to the total dissolved iron in the solution). In the current work, in order to get more insight into the autoxidation of the dissolved iron from the pure and mixed Fe(II)-containing pyrophosphate salts (in the absence of vitamin C), the percentage of the dissolved Fe(II) from these salts with respect to the total dissolved iron was quantified by a ferrozine-based assay using UV-Vis spectroscopy after incubating them in water for 2 h at 23 °C, Figure 7.3.

Results showed that in the case of Fe(II)PP, the dissolved Fe(II) from this salt oxidized to a certain extent, $x = 1$ in Figure 7.3 A. The concentration of iron (II) from Fe(II)PP in water after 2 h was $\approx 60\%$ of the total soluble iron. Moreover, the total soluble iron from this salt was $< 0.1\text{ mM}$, $x = 1$ in Figure 7.3 B, which was in agreement with the results obtained from the dissolution behavior of this salt, see section 6.3.1 in chapter 6 (final pH = 4.5).

Incubating the mixed divalent metal Fe(II)-containing pyrophosphate salts with the general formula $\text{M}_{2(1-x)}\text{Fe}_{2x}\text{P}_2\text{O}_7$ ($0 < x < 1$, where $\text{M} = \text{Ca}$, Zn , or Mn) in water at 23 °C for 2 h resulted in final pH range of 5.4-7.3. The quantification of Fe(II)% from these mixed salts showed that the Fe(II)% was lower for all x -values, compared to Fe(II)PP. This means that the autoxidation of the dissolved iron from all mixed salts was faster, compared to Fe(II)PP ($x = 1$), Figure 7.3 A. In the case of $\text{M} = \text{Ca}$ and Zn , the retained Fe(II)% increased with decreasing the x -value, circles and triangles in Figure 7.3 A. Results indicated that the slowest autoxidation of iron from the salts

was observed in the case of $M = \text{Ca}$ and Zn for the mixed salts with the lowest iron content (i.e., 43.8% for $x = 0.060$ and 52.4% for $x = 0.047$, respectively).

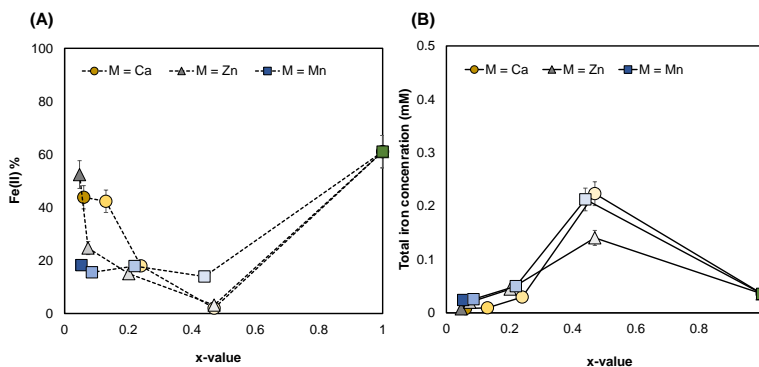


Figure 7.3 Autoxidation of iron from Fe(II)PP and the mixed divalent metal Fe(II)-containing salts. (A) Percentage of the dissolved iron (II) and (B) the total dissolved iron concentration from Fe(II)PP and the mixed salts $M_{2(1-x)}\text{Fe}_{2x}\text{P}_2\text{O}_7$ ($0 < x < 1$, where $M = \text{Ca}$, Zn , or Mn) after 2 h incubation in water (i.e., absence of vitamin C) at 23 °C.

Furthermore, in the case of $M = \text{Ca}$ and Zn , the percentage of Fe(II) decreased to roughly 2% and 3.1% in the case of the mixed salts with the highest iron content ($x = 0.470$ for both $M = \text{Ca}$ and Zn). Comparing the opposite trends in the results obtained from quantification of Fe(II)% and the total soluble iron concentration from the mixed salts confirms that in the case of calcium and zinc as the second divalent metal (M) in the pyrophosphate matrix, increasing the total iron concentration from the mixed salts in the solution results in autoxidation of iron and consequently lower Fe(II)% with respect to the total dissolved iron, Figure 7.3 B. Interestingly, the mixed salt with $M = \text{Zn}$ and the highest zinc content ($x = 0.047$) showed the minimum autoxidation of iron among all mixed salts with approximately 52% retained Fe(II) in the solution.

For the mixed salts in which $M = \text{Mn}$, the Fe(II)% remained approximately constant, squares in Figure 7.3 A. Interestingly, in this case, the autoxidation of iron from the mixed salts was independent of their x -values, and the Fe(II)% was measured to be fluctuating around $16.4 \pm 2\%$ for all the x -values (approximately 3.8 times lower, compared to Fe(II)PP), squares in Figure 7.3 B. However, the total dissolved iron from the salts increased versus their x -values. Moreover, 2 h incubating the mixed salt with the highest iron content (i.e., $x = 0.440$) showed the same soluble iron concen-

tration (≈ 0.2 mM) as the mixed salt with $M = \text{Ca}$ and $x = 0.470$, while the Fe(II)\% was almost 7-fold higher in the case of $M = \text{Mn}$.

7.3.2 Effect of time on the autoxidation of iron from the pure Fe(II)PP and mixed divalent metal Fe(II) -containing pyrophosphates salts

In order to effectively apply the mixed divalent metal Fe(II) -containing pyrophosphate salts in the fortified food products, autoxidation of the dissolved iron from them must be monitored during the storage time. Although the storage conditions could not be reached due to the time limitations of the experiments, we investigated the autoxidation of iron from these salts over time, i.e., after 1, 2, and 48 h incubation to get an insight into the rate of the autoxidation of iron from these salts, Figure 7.4.

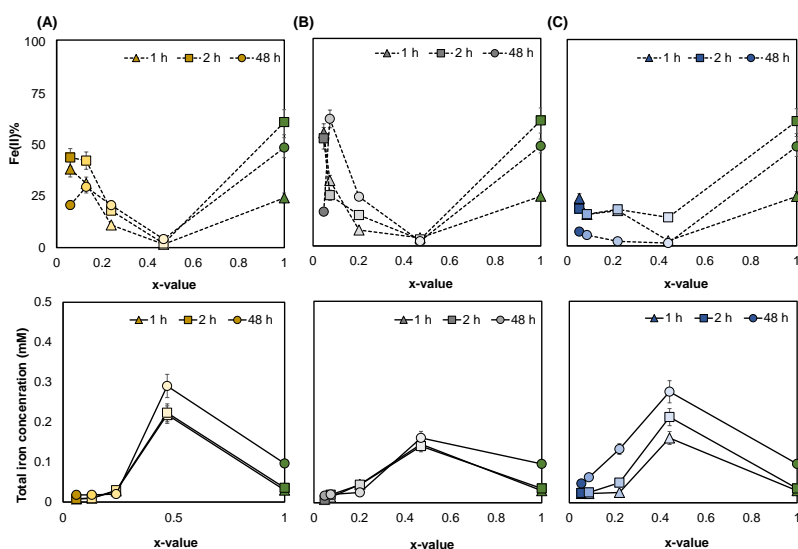


Figure 7.4 The effect of time on the autoxidation of the dissolved iron from Fe(II)PP and the mixed salts. The results of the quantification of the percentage of the dissolved iron (II) (dashed lines, top) and the total dissolved iron concentration (solid lines, bottom) from the mixed $M_{2(1-x)}\text{Fe}_{2x}\text{P}_2\text{O}_7$ salts where (A) $M = \text{Ca}$, (B) $M = \text{Zn}$, and (C) $M = \text{Mn}$ in pure water (i.e., absence of vitamin C) after 1 h, 2 h, and 48 h.

Monitoring the percentage of Fe(II) in solution by time in the case of Fe(II)PP ($x = 1$) indicated that the Fe(II)\% increased significantly ($p < 0.05$) to 2.5 times (61%) from 1 to 2 h incubation time. This is expected to be due to the increase in the total soluble iron (II) concentration from this salt by time. However, over 48 h incubation of the

Fe(II)PP, the Fe(II)% decreased to 48%. This can be explained by the slow autoxidation rate of iron from Fe(II)PP at this pH (≈ 4) which follows after its increased dissolution up to approximately 0.1 mM over 48 h, $x = 1$ in Figure 7.3 (bottom row). It was previously shown for Fe(III)PP that over 48 h incubation time, the total dissolved iron concentration from this salt increased in the pH range 5-8 as well¹⁴, see chapter 3.

Exploring the autoxidation of iron from the mixed $M_{2(1-x)}Fe_{2x}P_2O_7$ salts by time showed that in the case of $M = Ca$, the Fe(II)% increased from 1 to 2 h which is explained by the slow iron dissolution from these salts, Figure 7.3 A (top). However, the decreased percentage of Fe(II) in solution from 2 to 48 h is an indication of the slow autoxidation of the dissolved iron to Fe(III) over time.

In the case of $M = Zn$, no remarkable change was observed for the Fe(II)% in the solution between 1 h and 2 h, Figure 7.4 B (top). In this case, increasing the incubation time to 48 h resulted in enhanced Fe(II)% in the solution for the salts with $x < 0.470$ up to $\approx 62\%$ for the mixed salt with $x = 0.074$ which was similar to Fe(II)PP.

Furthermore for the mixed salts with $M = Mn$, increasing the incubation time from one to two hours resulted in an increase in Fe(II)% (from approximately 2.5 to 14%) for the salt with the highest iron content ($x = 0.440$), Figure 7.3 C (top). However, a significant decrease in Fe(II)% was observed over 48 h incubation of these salts with a maximum 7% for the mixed salt with $x = 0.053$. Comparison between the results for the mixed salts with $M = Mn$ revealed that although the total soluble iron from these mixed salts increased over time (48 h), the Fe(II)% reached its lowest values after 48 h for all x -values. Investigating the autoxidation behavior of the dissolved iron from the mixed salts over time suggests that when manganese is mixed along iron in the pyrophosphate salt matrix, the autoxidation of iron from the mixed salts is faster for all x -values, compared to Fe(II)PP and other mixed salts ($M = Ca$ and Zn). For future experiments, exploring the oxidation state of the dissolved manganese from these salts is of interest.

Our findings suggest that the dissolved iron concentration from Fe(II)PP and the mixed Fe(II)-containing undergoes oxidation in pure water. Therefore, it is expected that this iron (in +3 oxidation state) participates in the Fenton-like redox reaction in the presence of vitamin C. However, it is hypothesized that due to the low and/or slow dissolution of iron from these salts (which was explored and described previously in chapter 6), the oxidation of vitamin C in water dispersions of the salts occurs up to a limited extent.

7.3.3 Oxidation of vitamin C in the presence of the pure and mixed divalent metal Fe(II)-containing pyrophosphate salts

Vitamin C (or ascorbic acid) is well-known for undergoing redox interactions with iron (III) ions¹⁵. Under certain conditions, vitamin C can reduce iron (III) to iron (II) which results in formation of reactive oxygen species (ROS). It is known that

ascorbic acid is oxidized by Fe(III) and therefore initiates a series of redox reactions with dehydroascorbic acid (DHA) as the final oxidation product, see Figure 7.1^{5,15,16}. Therefore, we explored the oxidation of vitamin C in the presence of the pure as well as the mixed divalent metal Fe(II)-containing pyrophosphate salts. To this aim, the pure as well as the mixed salts were incubated in the presence of excess (at least 3 times) vitamin C for 2 h at 23 °C. The concentration of oxidation product of vitamin C (i.e., DHA) was quantified by an OPDA-based fluorometric assay, and normalized to the concentration of the produced DHA in the absence of the salts (i.e., the product of autoxidation of vitamin C in pure water). Furthermore, the percentage of Fe(II) with respect to the total iron concentration in the solution was measured with UV-Vis spectroscopy.

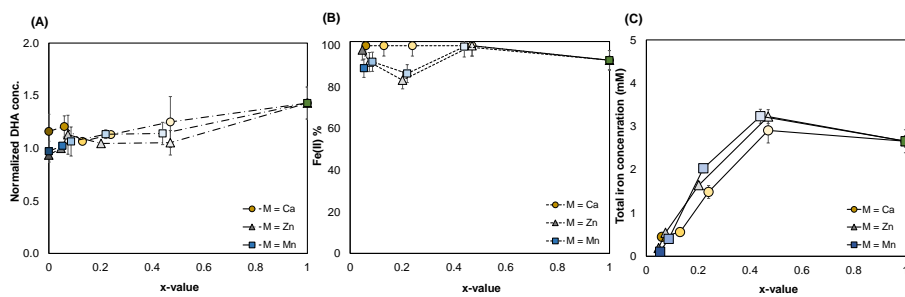


Figure 7.5 Oxidation of vitamin C in the presence of Fe(II)PP and the mixed divalent metal Fe(II)-containing salts. (A) Normalized DHA (i.e., the ratio of the produced DHA concentration in the presence of the salts to the absence of the salts), (B) percentage of the dissolved iron (II), and (C) the total dissolved iron concentration from Fe(II)PP and the mixed salts $M_{2(1-x)}Fe_{2x}P_2O_7$ ($0 < x < 1$, where $M = Ca, Zn, \text{ or } Mn$) after 2 h incubation at 23 °C. The oxidation extent of vitamin C in the presence of the salts increased up to maximum 1.5 times.

Results obtained from exposure of the pure as well as mixed pyrophosphate salts with the general formula $M_{2(1-x)}Fe_{2x}P_2O_7$ ($0 \leq x \leq 1$, where $M = Ca, Zn, \text{ or } Mn$) to vitamin C for 2 h at 23 °C are illustrated in Figure 7.5. It should be noted in this context that the final pH of the dispersions of the salts dropped to 2.4-3.6, which is within the pH range of vitamin C-rich foods.

Incubating Fe(II)PP in the presence of excess ascorbic acid in water for 2 h at room temperature (23 °C) resulted in formation of 3.8 mM DHA that was measured to be only 1.4 times higher than the DHA concentration resulting from autoxidation of vitamin C in pure water, $x = 1$ in Figure 7.5 A. This was only 2% of the initial concentration of vitamin C in the dispersion (considering 1:1 mole ratio of ascorbic acid to dehydroascorbic acid in the oxidation reaction) which means that a considerable amount of vitamin C in the presence of Fe(II)PP remained intact in solution. Furthermore, the Fe(II)% and the total soluble iron from this salt increased to $\approx 93\%$ and 2.6

mM, respectively, Figure 7.5 B and C. The increase in Fe(II)% is due to the presence of vitamin C which prevents the oxidation of the dissolved iron in the solution to Fe(III). Moreover, the increased soluble iron concentration in the presence of vitamin C, compared to its absence, is due to the lower pH of the dispersion in the presence of ascorbic acid. Our findings suggests that applying Fe(II)PP as an iron fortificant along vitamin C in a food vehicle (with $\text{pH} \approx 3$) is expected to enhance the available amount of iron(II) and still retain a considerable amount of vitamin C ($\approx 98\%$) for absorption.

Results showed that the oxidation of vitamin C in the presence of calcium pyrophosphate (CaPP, i.e., $x = 0$ where $M = \text{Ca}$), was slightly higher (≈ 1.2 times), compared to its oxidation in pure water. However, in the case of zinc pyrophosphate, ZnPP, and manganese pyrophosphate, MnPP (i.e., $x = 0$ where $M = \text{Zn}$ and Mn , respectively), the values of the normalized DHA were ≈ 1 , Figure 7.5 A. Therefore, it can be concluded that the presence of zinc and manganese pyrophosphate (ZnPP and MnPP, respectively) had no effect on the oxidation extent of vitamin C during the 2 h incubation.

In the case of the mixed $\text{M}_{2(1-x)}\text{Fe}_{2x}\text{P}_2\text{O}_7$ salts, the average concentration of DHA decreased significantly for all the mixed salts, compared to Fe(II)PP, up to roughly 1.43-fold in the case of the mixed salt with $M = \text{Zn}$ and $x = 0.047$ (except for the salt in which $M = \text{Ca}$ with $x = 0.470$), Figure 7.5 A. In addition, presence of the mixed salts with $M = \text{Zn}$ (all x -values) resulted in minimum oxidation of vitamin C among all mixed salts ($M = \text{Ca}$, Zn , and Mn). This minimum can be explained by the antioxidant activity of zinc, which can result in lower oxidation level of vitamin C in the presence of the mixed salt with the highest zinc content^{17,18}. Furthermore, our results showed that the oxidation of vitamin C in the presence of the mixed salts with $M = \text{Zn}$ was very similar to the salts in which $M = \text{Mn}$.

Quantification of Fe(II)% from the mixed salts showed that in the case of $M = \text{Ca}$, nearly 100% of the dissolved iron from all the salts was reduced to Fe(II). However, in the case of $M = \text{Zn}$ and Mn , the percentage of Fe(II) was measured to be lower, with a minimum of 83.4% for the salt with $x = 0.202$ and 86.6% for the mixed salt with $x = 0.220$, respectively. Nevertheless, these locally lower values of Fe(II)% can be due to the errors attributed to the ferrozine-based colorimetric assay as well.

Although the total iron concentrations from the mixed salts increased after mixing with vitamin C (due to lower final pH), the dissolved iron concentration from the mixed salts in a solution containing vitamin C was much lower than Fe(II)PP in the same condition which is beneficial for preventing Fe-mediated reactions with the food components that affect organoleptic properties of the food, Figure 7.5 C. Finally, the similarities in the total soluble iron from the mixed Fe(II)-containing salts at roughly same x -values are explained by their dissolution behavior at similar final

pH values of the dispersions when incubated in the presence of ascorbic acid, Figure 7.5 C.

7.3.4 Effect of time on the oxidation of vitamin C in the presence of the pure and mixed divalent metal Fe(II)-containing pyrophosphates salts

As mentioned previously, one of the main problems of adding vitamin C to the food products is that its content can decrease due to the redox reactions during storage. Therefore, it is important to explore the retention of vitamin C over time. In order to examine the oxidation of vitamin C in the presence of the pure and mixed divalent metal pyrophosphate salts in longer times, generation of DHA was studied (and normalized to the concentration of the generated DHA in the absence of any salts) as a function of time (1 h, 2 h, and 48 h incubation) at room temperature (23 °C).

Monitoring the normalized DHA concentration in the case of Fe(II)PP showed no significant difference and fluctuated in the range of 1.1 - 1.5 over time, $x = 1$ in Figure 7.6 (top row). Moreover, results indicated that although this value was noisy in the case of the mixed (vs. x -values) over time, the DHA concentration was always < 2 times higher for all the mixed salts, compared to their absence, Figure 7.6 A-C (top row). After 48 h incubation, the maximum value of DHA (among all mixed salts) was measured for the mixed salts with $x = 0.130$, 0.470 , and 0.440 when $M = \text{Ca}$, Zn , and Mn , respectively. This means that over the 48 h incubation, approximately 96% of the total vitamin C present in the solution remained intact.

Additionally, results indicated that presence of vitamin C in the dispersions caused the percentage of iron (II) in the solution to increase to almost 100% after 48 h incubation for Fe(II)PP and all the mixed Fe(II)-containing salts, Figure 7.6 A-C (middle row). Quantification of total dissolved iron from these salts showed enhanced iron concentration in solution for all the salts. Interestingly, the soluble iron concentration reached a plateau at the same value ($\approx 3.2 \text{ mM}$) as a function of x -value for each individual set of the mixed salts which refers to the solubility limit of iron from these salts over the time span of the experiments.

In summary, our findings show that the mixed salts $M_{2(1-x)}\text{Fe}_{2x}\text{P}_2\text{O}_7$ ($0 < x < 1$, where $M = \text{Ca}$, Zn , or Mn) are potential dual-fortificants suitable for addition to vitamin C-rich or fortified food products. Besides simultaneous delivery of two minerals, the main benefit of these salts is their minimal influence on the oxidation of vitamin C present in the food vehicle. The most preferred mixed salts for this purpose are $x \leq 0.240$ with $M = \text{Ca}$, $x \leq 0.202$ with $M = \text{Zn}$, and $x \leq 0.220$ with $M = \text{Mn}$. For future experiments, increasing the incubation temperature (up to 50 °C) can be applied to predict the oxidation extent of vitamin C after longer incubation times. Furthermore, investigating the oxidation of vitamin C in the presence of these salts in real food products and over real storage times, and its influence on the organoleptic properties of the food of interest.

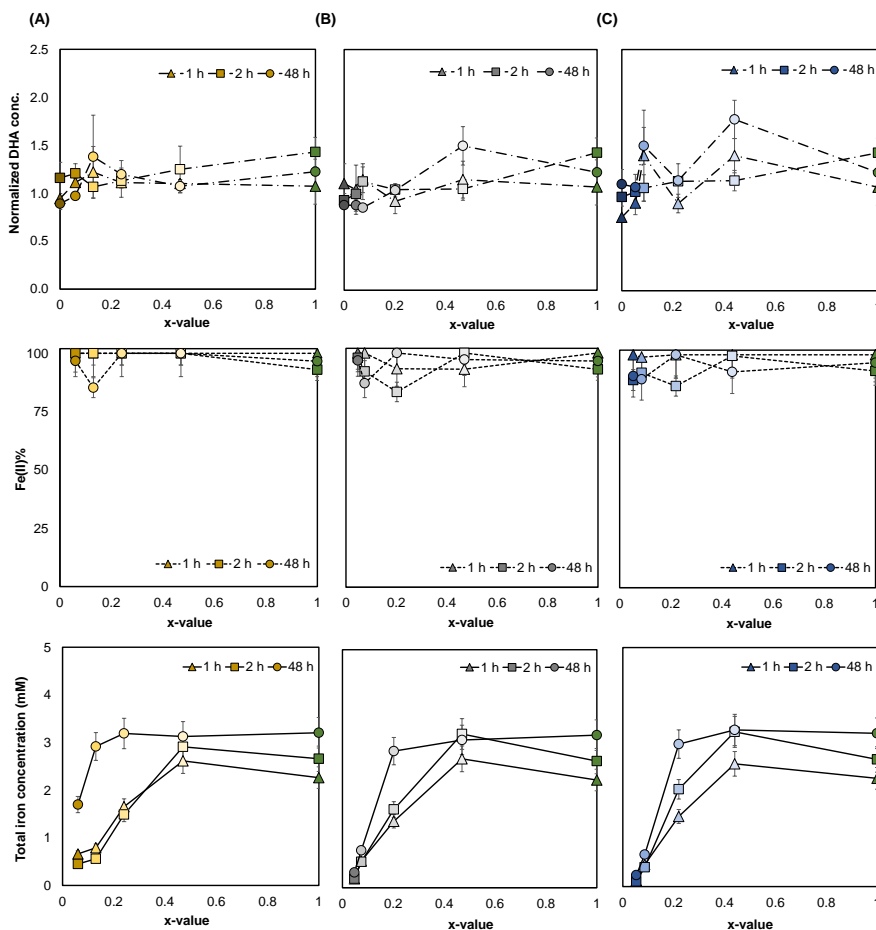


Figure 7.6 The effect of time on the oxidation of vitamin C in the presence of Fe(II)PP and the mixed salts. Normalized DHA concentration (dash dotted lines, top), the percentage of the dissolved iron (II) (dashed lines, middle) and the total dissolved iron concentration (solid lines, bottom) from the $M_{2(1-x)}Fe_{2x}P_2O_7$ ($0 \leq x \leq 1$) salts where **(A)** $M = Ca$, **(B)** $M = Zn$, and **(C)** $M = Mn$ after 1 h, 2 h, and 48 h at 23 °C. The results indicate that over time, the DHA concentration was always < 2 times higher, compared to their absence, which means 96% of the total vitamin C in the solution remained intact after 48 h.

7.4 Conclusions

In this work, we investigate the autoxidation of the dissolved iron from Fe(II)PP and the mixed divalent metal Fe(II)-containing pyrophosphate salts with the general formula $M_{2(1-x)}Fe_{2x}P_2O_7$ ($0 \leq x \leq 1$, where $M = Ca, Zn, \text{ or } Mn$). Furthermore, the oxidation of vitamin C in the presence of these are investigated in the same conditions (after 1 h, 2 h, and 48 h incubation at 23 °C). Results show that over time ferrous pyrophosphate (Fe(II)PP) enhanced the oxidation of vitamin C only up to 1.5 times over 48 h, which means only $\approx 4\%$ loss of vitamin C. Furthermore, over time the oxidation of vitamin C in the presence of the mixed Fe(II)-containing salts was lower up to 1.4 times, compared to Fe(II)PP. Our findings show that the mixed divalent metal Fe(II)-containing salts with the relatively lower iron contents, (i.e., $x = 0.06, 0.086$, and 0.053 where $M = Ca, Zn, \text{ and } Mn$ respectively) are potential dual-fortificants that do not increase the oxidation of vitamin C, compared to its autoxidation in water at these conditions. These outcomes suggest that the pure Fe(II)PP and the mixed Fe(II)-containing pyrophosphate salts are expected to be suitable candidates for multi-mineral fortification of vitamin C-rich foods with the main goal of higher amounts of soluble iron and intact vitamin C accessible for absorption in the human body. In future works, the dissolution behavior of these salts in gastric-mimicked conditions and/or their *in vitro* bio-availability after reacting with vitamin C in real storage timescales should be further explored.

7.5 Acknowledgments

Guus van Zadelhoff from Cellular Protein Chemistry group of Utrecht University is thanked for providing the thermomixer for performing the experiments. The author is grateful to Wouter J.C. de Bruijn from the Laboratory of Food Chemistry in Wageningen University and Research for the fruitful discussions. The graphical abstract was made with content from BioRender.com.

7.A Appendix

7.A.1 Autoxidation of iron from Fe(II)PP vs. Fe(III)PP

We made a comparison between the percentage of the Fe(II) in the solution with respect to the total dissolved iron concentration between Fe(II)PP and Fe(III)PP, see orange (solid) filled columns in Figure 7.7 A. This comparison showed that the total soluble iron concentrations were measured to be approximately the same for Fe(II)PP and Fe(III)PP and equal to 0.040 mM (final pH 4.5 and 3.7, respectively), Figure 7.7 B. Moreover, the concentration of iron (II) from Fe(II)PP in water after 2 h was still > 60% of the total soluble iron which was 2.2 times higher than the Fe(II)% from Fe(III)PP, Figure 7.7. It should be mentioned in this context that ferric ion in the solution can form a complex with ferrozine¹⁹. The ferric ion in this complex can further reduce to ferrous and absorb light in 562 nm and consequently it interferes with the quantification of Fe(II)^{20,21}. Therefore, it is expected that the quantified Fe% from Fe(III)PP is overestimated. In future works, colorimetric assays using other indicators that can preferably coordinate iron only in one oxidation state are of interest.

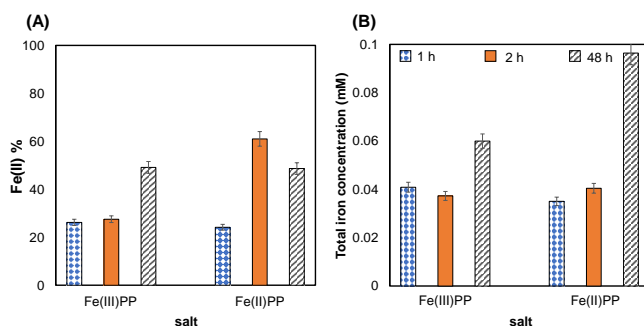


Figure 7.7 Autoxidation of dissolved iron from Fe(II)PP, compared to Fe(III)PP. (A) the percentage of the dissolved iron (II) and (B) the total dissolved iron concentration from Fe(II)PP and Fe(III)PP after 1h, 2 h, and 48 h incubation at 23 °C.

7.A.2 Oxidation of vitamin C in the presence of Fe(II)PP vs. Fe(III)PP

Incubation of Fe(II)PP and Fe(III)PP in the presence of excess amount of vitamin C for 2 h at 23 °C resulted in approximately the same oxidation extent of vitamin C, Figure 7.8. Furthermore, the Fe(II)% and total iron concentration in solution was same for these two salts, Figure 7.8 B, and C, respectively.

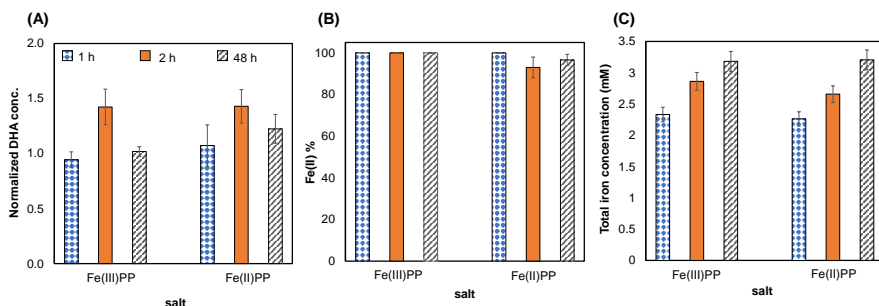


Figure 7.8 Oxidation of vitamin C in the presence of Fe(II)PP, compared to Fe(III)PP. (A) Normalized DHA, (B) the percentage of the dissolved iron (II), and (B) the total dissolved iron concentration from Fe(II)PP and Fe(III)PP after 1h, 2 h, and 48 h incubation at 23 °C.

References

- 1 L. Allen, B. de Benoist, O. Dary, and R. Hurrell, World Health Organization , 341 (2006).
- 2 A. Nilson and J. Piza, Food and Nutrition Bulletin 19, 49 (1998).
- 3 A. C. Carr and S. Rowe, Nutrients 2020, Vol. 12, Page 1963 12, 1963 (2020).
- 4 A. S.-M. M.-E. LEŠKOVÁ, Journal of food and nutrition research 45, 55 (2006).
- 5 S. J. Campbell, B. Utinger, D. M. Lienhard, S. E. Paulson, J. Shen, P. T. Griffiths, A. C. Stell, and M. Kalberer, Analytical chemistry 91, 13088 (2019).
- 6 M. C. Putchala, P. Ramani, H. J. Sherlin, P. Premkumar, and A. Natesan, Archives of Oral Biology 58, 563 (2013).
- 7 J. Shen, P. T. Griffiths, S. J. Campbell, B. Utinger, M. Kalberer, and S. E. Paulson, Scientific Reports 2021 11:1 11, 1 (2021).
- 8 M. L. Liao and P. A. Seib, Food Chemistry 30, 289 (1988).
- 9 L. L. Stookey, Analytical chemistry 42, 779 (1970).
- 10 G. Burini, Journal of Chromatography A 1154, 97 (2007).

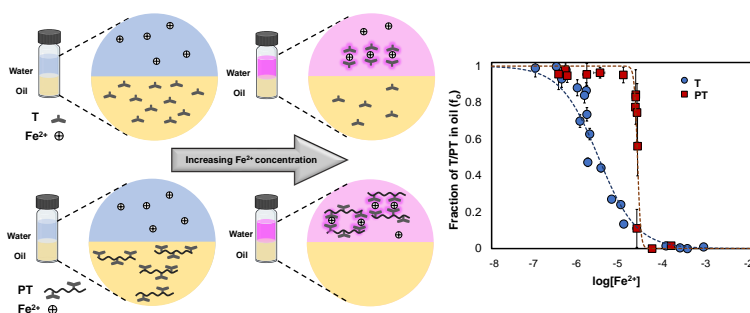
- 11 H. K. Chung and J. D. Ingle, *Analytica Chimica Acta* **243**, 89 (1991).
- 12 F. J. Millero, *Geochimica et Cosmochimica Acta* **49**, 547 (1985).
- 13 D. R. KESTER, R. H. BYRNE, and Y.-J. LIANG, , 56 (1975).
- 14 N. Moslehi, J. Bijlsma, W. J. de Bruijn, K. P. Velikov, J.-P. Vincken, and W. K. Kegel, *Journal of Functional Foods* **92**, 105066 (2022).
- 15 V. A. Timoshnikov, T. V. Kobzeva, N. E. Polyakov, and G. J. Kontoghiorghes, *International Journal of Molecular Sciences* 2020, Vol. 21, Page 3967 **21**, 3967 (2020).
- 16 A. Mlakar, A. Batna, A. Dudda, and G. Spiteller, *Free radical research* **4** **25**, 525 (2009).
- 17 A. Primikyri, G. Mazzone, C. Lekka, A. G. Tzacos, N. Russo, and I. P. Gerothanassis, *Journal of Physical Chemistry B* **119**, 83 (2015).
- 18 Y. Song, S. W. Leonard, M. G. Traber, and E. Ho, *The Journal of Nutrition* **139**, 1626 (2009).
- 19 E. Viollier, P. W. Inglett, K. Hunter, A. N. Roychoudhury, and P. Van Cappellen, *Applied Geochemistry* **15**, 785 (2000).
- 20 J. Im, J. Lee, and F. E. Löffler, *Journal of Microbiological Methods* **95**, 366 (2013).
- 21 A. S. Anastácio, B. Harris, H. I. Yoo, J. D. Fabris, and J. W. Stucki, *Geochimica et Cosmochimica Acta* **72**, 5001 (2008).

Part III

Cooperativity in binding of iron ions onto polymers

Cooperative binding of iron ions onto terpyridine-functionalized polymers

Abstract



A textbook example of allostery is the cooperative binding of oxygen to hemoglobin. This form of cooperativity occurs if a competition exists between at least two conformational states of the substrate: a ground state with low binding affinity for the ligand, and an excited state with higher binding affinity. We show that this phenomenon also occurs in much simpler macromolecules than hemoglobin. Cooperative binding occurs on an iron/terpyridine-functionalized polymer in a two-phase water/oil system. In the ground state, the polymer resides in the oil phase due to its hydrophobicity. We demonstrate that upon increasing the iron concentration in the water phase, a sharp cooperative transition occurs where the polymer moves from the oil to the water phase and iron binds to the terpyridine groups on the polymer backbone. This steep response to only a small change in the free iron concentration is explained and modeled by MWC theory which was initially introduced to describe the allosteric binding of oxygen on hemoglobin. This behavior can be explained by the competition between the hydrophobic energy of the polymer in oil, and binding of iron ions onto the terpyridine functional groups on the polymer in water.

This chapter is based on N. Moslehi, N. Dramountanis, J. L. Martin Robinson, B. G. P. van Ravensteijn, and W. K. Kegel, "Cooperative binding of iron onto terpyridine-functionalized polymers", *To be submitted*.

"Life is a balance of holding on and letting go."

"The art of knowing is knowing what to ignore."

Rumi – Persian poet, 1207-1273

8.1 Introduction

Cooperativity (of which allostery is a subclass), is typically introduced by the well-known example of binding oxygen molecules to heme groups on the hemoglobin molecule in biochemistry¹. Based on cooperative binding, under certain conditions binding several molecules becomes more favorable than binding one or a few. In the case of no cooperativity in the binding of oxygen to hemoglobin, the transition from no bound oxygen to saturation of the hemoglobin with oxygen (i.e., occupancy of all four binding sites on hemoglobin) would be expected to occur over a broad range of oxygen pressure². Here the hemoglobin is considered as a template with n_{max} subunits (i.e., the number of binding sites) of which n are occupied by oxygen molecules. By use of statistical thermodynamics, in the simple case where each oxygen molecule binds to the hemoglobin molecule with the binding (free) energy g_b and the fugacity $\lambda = \exp(\mu/k_B T)$ (i.e., related to partial pressure p by chemical potential, $\mu = \mu^0 + k_B T \ln(p/p^0)$), the grand partition function reads

$$\Xi = \sum_0^{n_{max}} \lambda^n Z(n, n_{max}, T) = \sum_0^{n_{max}} \lambda^n \binom{n_{max}}{n} \exp(-\beta n g_b) = (1 + \lambda \exp(-\beta g_b))^{n_{max}} \quad (8.1)$$

where β is the inverse thermal energy unit and equal to $1/k_B T$ in which k_B and T are the Boltzman constant and temperature, respectively. n is the number of bound species (oxygen molecules in this case) and n_{max} is the total number of binding sites (for the hemoglobin molecule $n_{max} = 4$). Furthermore, the canonical partition function for uncorrelated binding is $Z(n, n_{max}, T) = \binom{n_{max}}{n} \exp(-\beta n g_b)$. Consequently the fraction of occupied cites, θ , which is the ratio of the average number of bound species to the total number of binding sites (n_{max}) is given by:

$$\theta = \frac{\langle n \rangle}{n_{max}} = \frac{\lambda}{n_{max}} \frac{\partial \ln \Xi}{\partial \lambda} = \frac{\lambda \exp(-\beta g_b)}{1 + \lambda \exp(-\beta g_b)}. \quad (8.2)$$

Equation 8.2 is in fact the Langmuir adsorption equation. In reality the forementioned transition is observed to be much sharper than predicted by random adsorp-

tion behavior³. The sharp transition in the occupation of hemoglobin over a narrow range of oxygen pressure is explained and modeled by the well-known Monod, Wyman, and Changeux (MWC) theory⁴. Based on MWC theory, the hemoglobin molecule can be in (at least) two different conformational states with different free energies; ground/Tense state with low affinity and excited/Relaxed state with high affinity to oxygen. The Tense and Relaxed states are favorable and unfavorable states for the hemoglobin molecule in the absence of oxygen molecules, respectively. However, the Relaxed state can become favorable only if the concentration (or pressure) of oxygen is high enough. In this case the grand partition function is the summation of partition functions in the Tense and Relaxed states, Ξ_T and Ξ_R , which are given, respectively, by:

$$\Xi_T = \sum_0^4 \binom{4}{n} \lambda^n \exp(-\beta g_T n) = [1 + \lambda \exp(-\beta g_T)]^4 \quad (8.3)$$

$$\Xi_R = \exp(-\beta g) \sum_0^4 \binom{4}{n} \lambda^n \exp(-\beta g_R n) = \exp(-\beta g) [1 + \lambda \exp(-\beta g_R)]^4 \quad (8.4)$$

where g refers to the difference in free energy between the Relaxed and Tense states (Because the Relaxed state is unfavorable, $g > 0$). Furthermore, g_T and g_R are the binding energies of oxygen to hemoglobin in the Tense and Relaxed states, respectively. Accordingly, the fraction of occupied binding sites on hemoglobin will be:

$$\theta = \frac{\langle n \rangle}{4} = \frac{1}{4} \lambda \frac{\partial \Xi}{\partial \lambda} = \Xi^{-1} \{ \lambda \exp(-\beta g_T) [1 + \lambda \exp(-\beta g_T)]^3 + \exp(-\beta g) \lambda \exp(-\beta g_R) [1 + \lambda \exp(-\beta g_R)]^3 \}. \quad (8.5)$$

Even though the possibility that the occupied sites of the hemoglobin molecule somehow interact is not ruled out, this is not a necessary assumption by the original MWC model⁴. The only necessary requirement is that there should be two conformational states, one of which is unfavorable for the hemoglobin molecule but it can be stabilized once its binding sites are occupied by oxygen molecules, Figure 8.1.

According to what is discussed above, it is expected that the allosteric (cooperative) transitions are not limited to complex systems such as proteins like hemoglobin, but can be mimicked in much simpler systems. It has previously been shown that the cooperative transitions which occur in hydrophobic polyelectrolytes such as solubilization of bilayer membranes, formation of micelles, and reversible aggregation as a function of pH can be explained by a competition between two or more conformational states within the framework of MWC theory⁵.

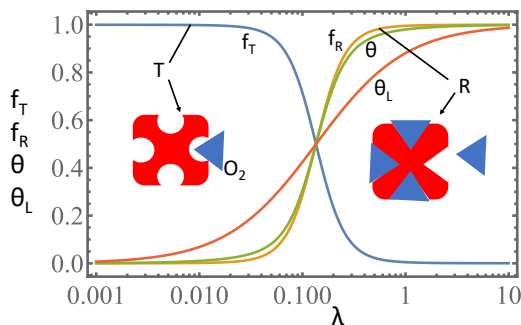


Figure 8.1 The cooperative binding of oxygen to hemoglobin, compared to the Langmuir behavior (random adsorption). The fraction of hemoglobin in the Relaxed (f_R) and Tense (f_T) states, and the fraction of bound oxygen on hemoglobin, Equation 8.5, as a function of λ . λ is proportional to the partial oxygen pressure. The Langmuir isotherm θ_L is Equation 8.2. The illustrations show the hemoglobin molecule in the Relaxed (R) and Tense (T) states.

In this work we aim to demonstrate cooperative binding of iron onto a terpyridine-functionalized polymer. Terpyridine is an extensively-used tridentate ligand, well-known for its high affinity towards complexation with many transition metals including iron ions^{6,7}. Furthermore, we design a two-phase water/oil experimental set-up in which solubilization of the terpyridine-functionalized polymer in oil or water is analogous to the Tense or Relaxed state, respectively. The experiments are performed at a fixed concentration of terpyridine functional groups and over a range of iron concentrations. In order to evaluate the binding behavior of iron onto terpyridine, we make a comparison between binding of iron onto terpyridine as monomers (T) and as functional groups on a polymer backbone with full terpyridine coverage (poly(terpyridine), PT). Subsequently, the water and oil phases are isolated and analyzed for the free iron and polymer (or terpyridine functional groups) concentrations with ICP-AES and UV-Vis spectroscopy, respectively. We hypothesize that upon increasing iron concentration in the water phase, the binding energy of iron onto terpyridine overcomes the hydrophobic energy of the polymer in the oil phase (the Tense or favorable state). As a consequence, it is expected that the polymer chains are stabilized in the water phase (the Relaxed or unfavorable state) and show a sharp transition from oil to water over a small range of free iron concentration.

8.2 Materials and methods

8.2.1 Designing terpyridine-functionalized polymers

Terpyridine-functionalized polymers with different terpyridine coverage along the polymer backbone were designed, synthesized, and characterized as described in the materials and methods in the Appendix 8.A. Figure 8.2 shows the chemical structures of terpyridine (as a monomer, abbreviated as T), and the three synthesized polymers for this work with different mole fractions of terpyridine as binding sites for iron. The degree of polymerization for all the polymers was on average 16 with a low polydispersity index ($PDI \approx 1.04$). The polymer with 100% terpyridine coverage is abbreviated as PT16, Figure 8.2. In addition, we designed random copolymers of acrylic acid or n-butyl acrylate along the terpyridine-functionalized repeating unit with 50% coverage of each, abbreviated as P(T8AA8) or P(T8nBA8), respectively, see Figure 8.2.

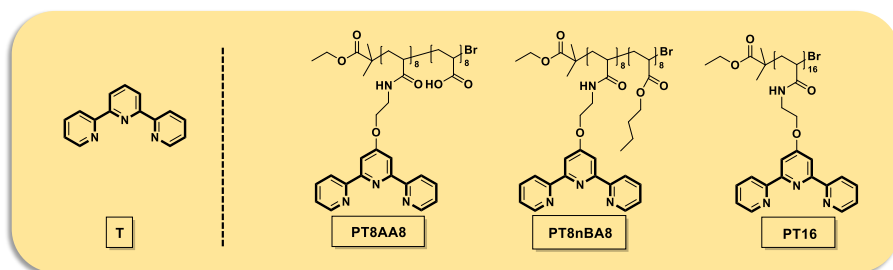


Figure 8.2 The chemical structures of different forms of terpyridine used in this study. Terpyridine (T) as monomers, polymers with 100% terpyridine coverage (PT16), 50% terpyridine and 50% acrylic acid (PT8AA8), and 50% terpyridine and 50% n-butyl acrylate (PT8nBA8).

8.2.2 Monitoring the binding behavior of iron onto terpyridine in a two-phase water and oil set-up

In order to monitor the binding behavior of the iron ions onto terpyridine monomer and the terpyridine-functionalized polymers, a two-phase water/oil set-up was designed, Figure 8.3. The oil phase was chosen to be dichloromethane (DCM) due to its immiscibility with water. Solutions of terpyridine monomer or terpyridine-functionalized polymers in DCM with the same concentration of terpyridine group ($200 \mu\text{M}$) were prepared. In addition, the aqueous phase contained various concentrations of FeCl_2 ranging between 10 and $200 \mu\text{M}$. To ensure the reduction of the iron ions to Fe^{2+} , an excess amount of ascorbic acid (AA) was added to the water solutions.

The described water and oil solutions were then exposed to each other in sealed vials and kept for 10 days after which the color of the aqueous phase in the vials turned pink. In the case of terpyridine-functionalized polymers, gel-like polymer networks were observed in the aqueous phase which is explained by the formation of bis (terpyridine) iron (II) complexes and therefore formation of crosslinked polymer chains with iron bridges, Figure 8.3 B. Finally, the water and oil phases were isolated and analyzed for iron and terpyridine concentrations, respectively.

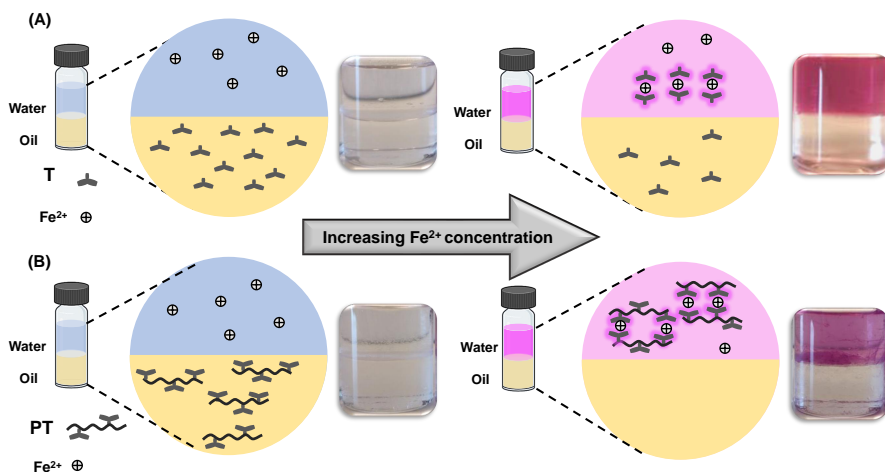


Figure 8.3 The schematics and images of the two-phase water/oil set-ups, for monitoring the binding behavior of iron ions onto (A) terpyridine (T) and (B) the terpyridine-functionalized polymer (PT). At low iron concentrations T or PT reside in the oil due to their hydrophobicity. However, beyond a certain concentration of iron T or PT moves to the water phase to gain the free energy of binding iron onto terpyridine. Here the oil phase is the bottom phase due to the higher density DCM than water.

Quantification of the free iron concentration in the water phase by inductively coupled plasma - atomic Emission spectroscopy (ICP-AES) and ultraviolet-visible light spectroscopy (UV-Vis)

The free iron (i.e., not coordinated by terpyridine) concentration in the water phase was measured by the difference between the measured iron concentration with ICP-AES and UV-Vis spectroscopies. In other words, the free iron concentration is equal to the total iron in the water phase (i.e., bound + free iron ions) minus the iron in coordinate complexes with terpyridine groups (i.e., bound iron ions). ICP-AES was performed on the solutions using an Optima 8300 instrument (PerkinElmer, Waltham, MA, USA) to obtain the total iron concentration in the water phase. Samples were dissolved in 10 ml of a 2% HNO_3 solution to achieve optimal measurement concen-

tration ranges. The measurements were performed in triplicate and the results were reported by an average and a standard deviation from duplicate measurements.

UV-Vis measurements were done on the solutions at $\lambda_{max} = 552$ nm at room temperature by a Lambda-35 spectrophotometer (PerkinElmer, Waltham, MA, USA), using quartz cuvettes. All measurements were performed in separate duplicates.

Quantification of terpyridine/terpyridine-functionalized polymers in the oil phase by ultraviolet-visible light (UV-Vis) spectroscopy

The concentration of terpyridine groups (i.e., also indicative of the concentration of the polymers) in the oil phase was quantified by UV-Vis with $\lambda_{max} = 279$ nm at room temperature. The oil solutions were mixed with acetonitrile (ACN) (1:1 volume ratio) prior to measurement^{8,9}. UV-Vis spectra of the solutions were then recorded on a Lambda-35 spectrophotometer (PerkinElmer, Waltham, MA, USA), using quartz cuvettes. All the measurements were done in separate duplicates.

8.2.3 Magnetic properties of the iron/terpyridine complexes

After the transition of the terpyridine-functionalized polymers from the oil to the aqueous state, the pink-colored gels were dried and weighed in a plastic cup for magnetic measurements. Magnetization curves were obtained via a MicroSense EZ-9 vibrating sample magnetometer (VSM). Hysteresis measurements were performed at room temperature (273 K, up to 1.5 Tesla) and in cryo mode (77 K, up to 2.2 Tesla) by using liquid nitrogen. All measurements were normalized by the weight of the samples. These measurements were done on pure terpyridine and FeCl_2 as well for comparison purposes.

8.3 Theory

8.3.1 Chemical equilibrium

Based on the experimental set-up described in section 8.2.2, we consider two coexisting phases of oil and aqueous that are in contact via an interface. Initially terpyridine molecules dissolve in oil (a hydrophobic liquid). However, in the presence of iron (II) ions (beyond a certain concentration of iron ions) in the water phase, terpyridine molecules partition in the aqueous (aq) phase:

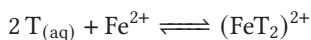


in which the terpyridine molecule is abbreviated as T. Since the concentration of terpyridine in the oil phase is more preferred as a variable due to its low solubility

in water, we define the partition coefficient of terpyridine between water and oil (in the absence of iron or any other metal ions) as:

$$K_p = \frac{[T_{(aq)}]}{[T_{(oil)}]} = \exp(-\beta g_H). \quad (8.6)$$

Here g_H is the free energy difference between terpyridine in water and terpyridine in oil (more specifically: the difference in standard chemical potential of terpyridine in oil and in water based on 1 M reference concentrations). The subscript H stands for 'hydrophobic'. Equation 8.6 is expected to be correct up to the water-solubility of terpyridine which is reported to be approximately 6 mM¹⁰. Additionally, bis (terpyridine) iron (II) complexes, $(FeT_2)^{2+}$, are formed in the aqueous phase via the following reaction:



It should be noted that the formation of mono (terpyridine) iron(II) complex, $(FeT)^{2+}$, is neglected based on the equilibrium constants reported previously¹¹. The equilibrium constant for formation of a bis (terpyridine) iron(II) complex in the aqueous phase is given by:

$$K = \frac{[(FeT_2)^{2+}]}{[T_{(aq)}]^2 [Fe^{2+}]} = \exp(-\beta g_{2w}). \quad (8.7)$$

Here g_{2w} is the reversible work of formation of a bis (terpyridine) iron(II) complex, $(FeT_2)^{2+}$, in water. Under standard conditions with 1 M reference concentrations of the components in Equation 8.7, $\beta g_{2w} \approx -48^{11}$. Thus, we write the equilibrium concentration of $(FeT_2)^{2+}$ as

$$[(FeT_2)^{2+}] = K K_p^2 [T_{(oil)}]^2 [Fe^{2+}]. \quad (8.8)$$

Equation 8.8 shows that in order to form $(FeT_2)^{2+}$ in water, there is an unfavorable step of transferring terpyridine from oil to water ($K_p < 1$), and a favorable step of binding iron to terpyridine ($K > 1$). We find the fraction of terpyridine in oil as a function of (free) iron concentration in water through the mass balance $[T_{(tot)}] = [T_{(oil)}](1 + K_p) + 2[(FeT_2)^{2+}]$ (based on equal volumes). Substitution of Equation 8.8 and solving for $[T_{(oil)}]$ leads to:

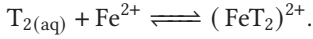
$$f_o = \frac{[T_{(oil)}]}{[T_{(tot)}]} = \frac{-1 + \sqrt{1 + 8KK_p^2 [T_{(tot)}] [Fe^{2+}]}}{4KK_p^2 [T_{(tot)}] [Fe^{2+}]}, \quad (8.9)$$

where we assumed that $K_p < 1$.

Anticipating the experimental results (which point to a significantly steeper dependence of the terpyridine fraction in the oil phase on the free iron (II) ions concentration), we consider the situation that terpyridine is in the form of dimers in the oil phase. In this case the equilibrium follows:



with the partition coefficient defined as $K'_p = [T_{2(aq)}]/[T_{2(oil)}] = \exp(-2\beta g_H) = K_p^2$. The bis (terpyridine) iron (II) complex will then form based on the reaction:



Thus, the equilibrium concentration of $(FeT_2)^{2+}$ is given by

$$[(FeT_2)^{2+}] = KK_p^2 [T_{2(oil)}] [Fe^{2+}]. \quad (8.10)$$

Now the fraction of terpyridine in oil becomes

$$f_o = \frac{[T_{2(oil)}]}{[T_{2(tot)}]} = \frac{1}{1 + KK_p^2 [Fe^{2+}]}. \quad (8.11)$$

Here we have used the mass balance $[T_{2(tot)}] = [T_{2(oil)}] + [(FeT_2)^{2+}]$ where $[T_{2(tot)}] = [T_{2(oil)}]/2$.

It will become clear in the results and discussion section that Equation 8.11 describes the experimental data much better than Equation 8.9. Furthermore, Equation 8.11 is analogous to the Langmuir adsorption equation as can be seen by writing the fraction of occupied sites (θ) of terpyridine dimers (T_2) by iron ions:

$$\theta = \frac{[(FeT_2)^{2+}]}{[T_{2(tot)}]} = \frac{KK_p^2 [Fe^{2+}]}{1 + KK_p^2 [Fe^{2+}]} = 1 - f_o. \quad (8.12)$$

8.3.2 Statistical thermodynamics

Terpyridine monomer

Here we apply the grand canonical ensemble to obtain the same results as discussed in the previous section (8.3.1). The terpyridine molecule can be in two states; dissolved in oil (with subscript oil) which is an energetically favorable state for the terpyridine molecule, and an aqueous state (with subscript aq) which is an unfavorable state for the terpyridine molecule in the absence of iron ions. However, the aqueous state can be stabilized due to the higher affinity of the terpyridine molecule in this state to iron ions. It is assumed that terpyridine is in thermodynamic equilibrium between the oil and aqueous phases (states) and that iron ions can be exchanged between terpyridine and the reservoir. Therefore, by using the grand canonical ensemble, the grand partition function of the terpyridine dimers is the summation over

all states and occupancy numbers (occupancy with iron). Therefore, the grand partition function reads

$$\Xi = \sum_{state\ i} \Xi_i = \Xi_{aq} + \Xi_{oil}. \quad (8.13)$$

Terpyridine in the aqueous state can be either occupied or unoccupied by iron ions. Thus,

$$\begin{aligned} \Xi_{aq} &= \exp(-\beta G_H) \sum_{N=0}^1 \lambda_F^N z(T, N) = \exp(-2\beta g_H) \sum_{N=0}^1 \lambda_F^N \exp(-N\beta g_{2w}) \\ &= \exp(-2\beta g_H) (1 + [Fe^{2+}] \exp(-\beta g_{2w})) \end{aligned} \quad (8.14)$$

in which $G_H (= 2g_H)$ is the free energy difference between terpyridine dimers in water and in oil phases (states). Here the fugacity of iron (with subscript F) is $\lambda_F = \exp(\beta\mu_F)$ and μ_F is the chemical potential of iron ions. $z(T, N) = \exp(-N\beta g_{2w})$ is the relevant part of the molecular partition function of terpyridine with N bound iron ions ($N = [0,1]$). In the second step in Equation 8.14, we wrote λ_F as the iron concentration, and at the same time we applied the appropriate standard states for terpyridine and iron ions, consistent with the chemical equilibrium approach. We assume that terpyridine in the oil state does not bind iron and thus $\Xi_{oil} = 1$. From that the fraction of terpyridine in oil is given by

$$f_o = \frac{\Xi_{oil}}{\Xi} = \frac{1}{1 + [Fe^{2+}] \exp(-2\beta g_H) \exp(-\beta g_{2w})} \quad (8.15)$$

and the average fraction of terpyridine occupied by iron (in the aqueous state) reads

$$\theta = \langle N \rangle = \frac{\lambda_F}{\Xi} \frac{\partial \Xi}{\partial \lambda_F} = \frac{[Fe^{2+}] \exp(-2\beta g_H) \exp(-\beta g_{2w})}{1 + [Fe^{2+}] \exp(-2\beta g_H) \exp(-\beta g_{2w})}. \quad (8.16)$$

Under the assumption of $\exp(-\beta g_H) = K_p \ll 1$, it is easily verified that Equations 8.15 and 8.16 are equal to Equations 8.11 and 8.12.

Terpyridine-functionalized polymers: Poly(terpyridine)

In this case the polymer can initially be in the form of single chains or in (small) clusters in oil: analogous to terpyridine monomer, it is expected that the poly(terpyridine) chains may also cluster in oil. We take the statistical thermodynamics approach here, although the results obtained can also be found by multi chemical equilibrium. In particular for the situation with copolymers of terpyridine and a second monomer (i.e., acrylic acid or n-butyl acrylate, see the next section for the random copolymers), the statistical thermodynamic approach is more straightforward. We write the (coarse-grained) partition function of a terpyridine-functionalized polymer chain in

the aqueous gel as

$$\Xi_{aq} = \exp(-\beta G_H) \sum_{N=0}^M \lambda_F^N Z(N, T, M), \quad (8.17)$$

where G_H is the hydrophobic free energy (> 0) penalty to transfer a polymer with M binding sites (number of terpyridine functional groups) from its hydrophobic reference state (dissolved in the oil phase) to the situation where the polymer is in contact with water. For a polymer with M terpyridine groups we expect that $G_H \approx M g_H$ and therefore in Equation 8.17, $\exp(-\beta G_H) \approx K_p^M$. However, deviations due to the interactions of terpyridine functional groups with the polymer backbone may occur. It is worth noting that the hydrophobic free energy penalty encloses other free energy changes due to the environmental change, such as differences in conformational entropy.

The coarse-grained canonical partition function for $M/2$ statistically independent binding sites of which N are occupied by iron ions with g_{2w} as the free energy gain in the formation of a bis (terpyridine) iron (II) complex, $(\text{FeT}_2)^{2+}$ reads $Z(N, T, M) = \binom{M/2}{N} \exp(-\beta N g_{2w})$. We estimate the number of ways that N coordination bonds can be distributed over $M/2$ sites as $\binom{M/2}{N} = (M/2)! / N! ((M/2) - N)!$. This is likely a reasonable approximation in terms of the number of available conformations per chain in the polymer gel. The total number of terpyridine pairs will be larger than $\binom{M/2}{N}$, but it is expected that many pairs are unavailable due to topological/geometrical constraints. Using that with Equation 8.17 and making use of the binomial theorem leads to:

$$\Xi_{aq} = \exp(-\beta G_H) \sum_{N=0}^{M/2} \binom{M/2}{N} \lambda_F^N \exp(-\beta N g_{2w}) = \exp(-\beta G_H) (1 + [\text{Fe}^{2+}] K)^{M/2} \quad (8.18)$$

in which we took $\lambda_F \exp(-\beta g_{2w}) = [\text{Fe}^{2+}] K$.

Equation 8.18 is revealing that for a terpyridine-functionalized polymer chain to be occupied by iron ions, there needs to be a competition between the two energy states it can be in; the favorable state of residing in the oil phase and the unfavorable aqueous state. In fact based on MWC theory, the transition of the poly(terpyridine) from the oil to the water phase comes with the hydrophobic free energy penalty of $\exp(-\beta G_H)$ and the gain of binding free energy (of formation of $(\text{FeT}_2)^{2+}$ complex) which is $\exp(-\beta g_{2w})$ and included in the term $[\text{Fe}^{2+}] K$.

As in the situation with terpyridine monomers, we assume that terpyridine in the oil state does not bind iron and thus, $\Xi_{oil} = 1$. Taking $\Xi = \Xi_{aq} + \Xi_{oil}$, we find for

the occupied fraction of terpyridine pairs:

$$\theta = \frac{\langle N \rangle}{M/2} = \frac{1}{M/2} \frac{\lambda_F}{\Xi} \frac{\partial \Xi}{\partial \lambda_F} = \frac{K[\text{Fe}^{2+}]K_p^M (1 + K[\text{Fe}^{2+}])^{(M/2)-1}}{1 + K_p^M (1 + K[\text{Fe}^{2+}])^{M/2}}. \quad (8.19)$$

Similarly, we find the fraction of poly (terpyridine) in the oil phase as $f_o = \Xi_{oil}/\Xi$:

$$f_o = \frac{1}{1 + \exp(-\beta G_H)(1 + [\text{Fe}^{2+}]K)^{M/2}}, \quad (8.20)$$

Combining Equations 8.19 and 8.20 leads to

$$\theta = \frac{K[\text{Fe}^{2+}]}{1 + K[\text{Fe}^{2+}]} (1 - f_o). \quad (8.21)$$

So, as long as $[\text{Fe}^{2+}] \gg K^{-1}$ (in our case $K^{-1} \approx \exp(-48)$, with concentrations in M) we have $\theta = 1 - f_o$, even at very low iron concentrations. In the language of MWC, the partitioning of the terpyridine-functionalized polymer molecules between the aqueous and oil phases is coupled to the conformational switch. Furthermore, based on MWC model f_o is the fraction of poly(terpyridine) in its 'hydrophobic' (i.e., ground) state or conformation.

Terpyridine-functionalized polymers: Random copolymers

The cooperative binding behavior of iron ions onto the terpyridine-functionalized polymers can be controlled by tuning the hydrophobicity of the polymer chains. To do so, one way is to randomly copolymerize a second (or substitute) monomer along the terpyridine-functionalized repeating unit in the polymer backbone. In general we expect that the compositional heterogeneity in the polymer chains does not affect the binding strength (and therefore the value of the equilibrium constant, K for formation of a $(\text{FeT}_2)^{2+}$ complex), and only influences the hydrophobic free energy difference for the polymers for moving from the oil to aqueous state. In this case, the hydrophobic free energy of the polymer can be written as the linear combination of hydrophobic contributions of the monomers. For a random copolymer with a mole fraction x of terpyridine-functionalized repeating unit (or monomer) and $(1 - x)$ of substitute monomer we expect:

$$g_H \approx xg_T + (1 - x)g_S, \quad (8.22)$$

where g_S and g_T are the hydrophobic contribution for substitute and the terpyridine-functionalized repeating units, respectively. The total hydrophobic free energy of the polymer chain then reads as $G_H = M_t g_H$ with M_t the total number of (both) repeating units per chain.

In the current work, we chose acrylic acid or n-butyl acrylate as the substitute monomers. Copolymers of 1:1 terpyridine and acrylic acid or n-butyl acrylate were

synthesized by random radical copolymerization with a fairly low polydispersity index of 1.04, see PT8AA8 and PT8nBA8, respectively, in Figure 8.2 and Appendix 8.A. As a result of random copolymerization, the copolymers are assumed to have normal distributions of the size (length) and chemical composition. We average over the compositions by taking the (Gaussian) weight $W(x, N, M_t) = \frac{1}{\sqrt{2\pi\sigma_c^2}} \exp\left(\frac{-(N-xM_t)^2}{2\sigma_c^2}\right)$ for N terpyridine functional groups with different fractions in the oil state. Here $\sigma_c^2 = M_t x(1-x)$ in which is the mole fraction of terpyridine-functionalized monomer units in the random copolymer. Moreover, we average over the size (or length) by assigning Gaussian weights of the lengths M_t : $W(M_t, \langle M_t \rangle) = \frac{1}{\sqrt{2\pi\sigma_L^2}} \exp\left(\frac{-(M_t - \langle M_t \rangle)^2}{2\sigma_L^2}\right)$. Here $\langle M_t \rangle$ is the average total number of monomers per chain and σ_L is the size polydispersity which is related to the polydispersity index (PDI) via $\sigma_L^2 = \langle M_t \rangle^2 (PDI - 1)$.

8.4 Results and discussion

The binding behavior of iron ions onto terpyridine monomer and the terpyridine-functionalized polymers was investigated using the quantification of free iron and terpyridine concentrations in the water and oil phases, respectively. The quantification of the fraction of terpyridine/terpyridine functional groups on the polymer chains (remained) in the oil phase vs. the free iron concentration are shown in Figure 8.4 (markers). Furthermore, the description of the data by the theoretical model is shown with the lines in Figure 8.4. Here, we first make a comparison between binding of iron onto terpyridine and poly(terpyridine) to show the cooperativity in this system. Next, we discuss the effect of a substitute monomer along terpyridine-functionalized repeating unit and the hydrophobicity of the second monomer on the cooperative behavior of binding onto the copolymers.

8.4.1 Terpyridine monomer vs. poly(terpyridine)

The experimental results showed a gradual decrease in fraction of terpyridine in the oil phase (f_o) from 1 to 0 upon increasing and over a broad range of iron concentration, see the blue circles in Figure 8.4 A. As it was mentioned in the section 8.3.1, the obtained fraction of terpyridine in the oil phase experimentally showed clear deviation from Equation 8.9. The blue dashed line in Figure 8.4 A is Equation 8.9 with $[T_{tot}] = 2 \times 10^{-4} M$ (based on the experiments). The best fit based on Equation 8.9 results in linear combination of binding and hydrophobic energies for each bis(terpyridine) iron (II) complex, $\alpha = -\beta(g_{2w} + 2g_H) = 21.8$. However, our results of binding iron ions onto terpyridine pointed to a significantly steeper dependence of the terpyridine fraction in the oil phase on the free iron (II) concentration. To resolve the mentioned discrepancy, we assumed that terpyridine in the oil state is not in monomeric form, but in the form of pairs. The blue solid line in Figure 8.4 A is

the best fit of Equation 8.11 to the experimental data of terpyridine (blue circles) with $\alpha = 12.8$ and gives a better match for the experiment results, compared to Equation 8.9.

There is evidence in the literature that shows the $\pi - \pi$ interactions between terpyridine molecules can cause the stacking of the pyridine rings in the solid state crystals^{12–14}. However, it is not clear to us why the experimental data are best described by taking the assumption of formation of terpyridine dimers in the solution in the presented model. Furthermore, it should be noted as well that the partitioning of terpyridine monomer in water in the presence of the oil (DCM) was not measurable due to the detection limit of the UV-Vis spectroscopy.

Poly(terpyridine) (or 'oligomers' which is a better qualification for chains with approximately 16 repeating units, abbreviated as PT16) undergo a remarkably sharp transition from being dissolved in oil to the aqueous state (phase) upon a very small change in the free iron concentration in water, see red squares in Figure 8.4 A. Additionally, the formation of the more energetically favorable $(\text{FeT}_2)^{2+}$ complexes (compared to $(\text{FeT})^{2+}$) leads to the formation of a polymer gel phase. The mentioned gel is a network of polymer chains which are crosslinked by iron ions that are in coordination bonds with terpyridine functional groups on the polymer backbone.

Monitoring the fraction of poly(terpyridine) in the oil phase shows that in the case that terpyridine is a functional group on a polymer backbone, the transition of the polymer from "dissolved in oil" state to "aqueous" state was much sharper and initiated at a higher free iron concentration, compared to the transition observed for the terpyridine monomer, Figure 8.4 A (red squares compared to blue circles, respectively). Equation 8.20 gives the best description of the effective cooperativity of the poly(terpyridine) with $M_{eff} = 32 \pm \Delta M$, with ($\Delta M \approx 10$), which leads to $\alpha = 10.8$, red dash dotted line in Figure 8.4 A. It should be noted that the uncertainty in the value of M_{eff} is due to the combinatorial factor in the model. In fact Equation 8.20 with $M = 16$ is also in good agreement with the experimental data. However, it seems that the transition is slightly sharper with a better fit with the estimation $M \approx 32$. This could be explained by the formation of crosslinks between polymer chains by iron ion bridges. Consequently, clustering of the polymer chains which was also visually observed in the experiments, (see the sample picture in Figure 8.3 B) results in an effective sharper cooperativity. In the situation of pre-existing clusters in oil of n polymers we will take an effective polymer length of $M_{eff}/2 = nM/2$ in Equations 8.18 and 8.20. However, it can be proven that the statistical weight of n polymer chains that form aggregates of size n in the aqueous phase, that is via $n\text{P}_{(oil)} + N\text{Fe}^{2+} \rightarrow \text{P}_n(\text{Fe})_N$ averaged over all possible N is overwhelmingly dominated by $n = 1$. Therefore, the M_{eff} is not significantly higher than the real M .

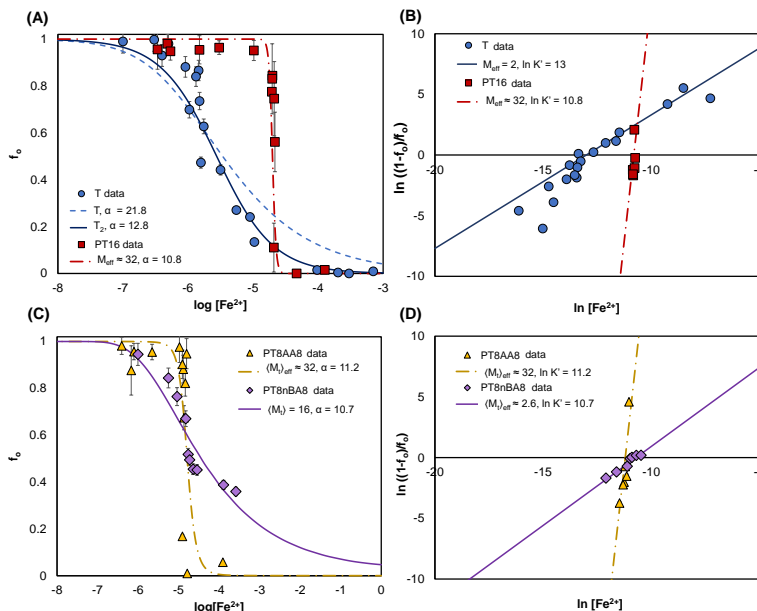


Figure 8.4 Comparison between experiments and theory for terpyridine monomer and the terpyridine-functionalized polymers. (A) Fraction of terpyridine (blue circles, T data) and poly(terpyridine) (red squares, PT16 data) in the oil phase (f_o) as a function of the free iron (II) concentration in the aqueous phase. Blue dashed line is Equation 8.9 which gives the best fit with $\alpha = 21.8$. The blue solid line which gives a better description of the data on terpyridine is Equation 8.11 with $\alpha = 12.8$. The red dash dotted line is Equation 8.20, which gives the best description of the experimental data on poly(terpyridine) with $\alpha = 10.8$ and $M_{eff} \approx 32$. (B) The corresponding Hill plots for terpyridine monomer (T) and poly(terpyridine) (PT16) with Hill coefficients $M_{eff}/2$ equal to 1 and 16, respectively. (C) Average fraction of 1:1 random copolymers of terpyridine and acrylic acid (yellow triangles, PT8AA8), and terpyridine and n-butyl acrylate (purple diamonds, PT8nBAA8) with $\langle M_t \rangle = 16$ in the oil (state) as a function of the free iron ion concentration in the aqueous phase. The yellow dash dotted line is the best fit based on the Equations 8.20 and 8.22 with $\alpha = 11.2$ and $\langle M \rangle_{eff} = 32$. Purple solid line is the best fit based on the Equations 8.20 and 8.22 averaged over the composition and size with $\alpha = 10.7$ and $\langle M \rangle_{eff} = 32$. (D) The corresponding Hill plots for the copolymers PT8AA8 and PT8nBAA8 with Hill coefficients (i.e., $M_{eff}/2$) equal to 16 and 1.3, respectively. In the case of PT8nBAA8, the smaller slope of the Hill plot is the indication of negative influence of the compositional polydispersity of the copolymers on the cooperativity and therefore broadening of the transition with respect to the free iron concentration.

Additionally, in the situation that $\exp(-2\beta g_H) \ll 1$, the Equations 8.19 and 8.20 can be rewritten in the following forms, respectively:

$$\theta = \frac{(K'[\text{Fe}^{2+}])^{M/2}}{1 + (K'[\text{Fe}^{2+}])^{M/2}} \quad (8.23)$$

$$f_o = \frac{1}{1 + (K'[\text{Fe}^{2+}])^{M/2}} \quad (8.24)$$

where $K' = \exp(-2\beta g_H)K = \exp(-\beta(g_{2w} + 2g_H))$ and therefore $\ln K' = \alpha$. The expression for θ in Equation 8.23 is in fact the Hill equation¹⁵ with Hill coefficient = $M/2$ which is consistent with the idea that to a good approximation, only two states of the polymer contribute: (i) polymers without occupied terpyridine groups in the oil state, and (ii) all the $M/2$ groups occupied in the aqueous state. The Hill plots for terpyridine and poly(terpyridine) in the form of $\ln((1 - f_o)/f_o)$ vs. $\ln[\text{Fe}^{2+}]$ with slope and intercept equal to $M/2$ and $(M/2) \ln K'$, respectively, are shown in Figure 8.4 B. The experimental data clearly shows a hill coefficient close to 1 (i.e., $M/2 \approx 1.3$) for terpyridine monomer, which is in good agreement with the assumption of formation of bis(terpyridine) iron(II) complexes, see blue circles in Figure 8.4 B. Furthermore, from the intercept of the line with $M_{eff} \approx 2$ it can be obtained that $\ln K' = 13$, which is similar to the value that was obtained for α from the fits (i.e., 12.8). Nevertheless, the same plot for the polymer (PT16) clearly shows a larger slope pointing to the formation of polymer networks and cooperativity of the system with $M_{eff} \approx 32$ and $\ln K' = 10.8$, see red squares in Figure 8.4 B.

Our findings show that exposing the same concentration of terpyridine in the form of monomers or functional groups on polymer chains to aqueous solutions of iron ions (a concentration series) results in different behavior of binding iron. In the case of terpyridine monomer, the aforementioned transition happens over a broad range of free iron concentration (i.e., 0.1 to 1000 μM) being indicative of random binding of iron onto terpyridine monomers. However, when the same experiment was performed with poly(terpyridine), the transition from oil to the water phase first initiated at a higher free iron concentration ($\sim 10 \mu\text{M}$) and second was observed to be much sharper than predicted by MWC model, compared to terpyridine monomer. Therefore, we have successfully mimicked the cooperative binding of iron ions onto terpyridine by following the transition of terpyridine from oil to the aqueous phase for a relatively simple system of terpyridine-functionalized polymers. Our results based on a model system suggest that the aforementioned cooperativity is not limited to complex biological systems such as proteins. In the next section we investigate the effect of hydrophobicity and compositional polydispersity of the terpyridine-functionalized polymers on the cooperative binding of iron.

8.4.2 Random copolymers of terpyridine-functionalized repeating units and a substitute monomer

The fractions of copolymers of terpyridine and acrylic acid (PT8AA8) and of terpyridine and n-butyl acrylate (PT8nBA8) as a function of free iron concentration are shown in Figure 8.4 C. PT8AA8 copolymer shows a sharp transition from the oil to the aqueous state over a narrow range of free iron concentration, see yellow triangles in Figure 8.4 C. Combining Equations 8.20 and 8.22 gives the best fit for the data of PT8AA8 with $x = 0.5$ leading to $\alpha = 11.2$ and $\langle M_t \rangle_{eff} \approx 32$, see the yellow dash dotted line in Figure 8.4 C. It was expected that the random copolymerization would lead to broadening of the transition with respect to the free iron concentration. However, in the case of PT8AA8 this is not the case. The sharp decrease in the fraction of PT8AA8 copolymer in the oil phase can be explained by first the relatively narrow molecular weight (or size) distribution and second low contribution of the repeating units containing acrylic acid groups in the hydrophobic free energy difference of the polymer chains. Moreover, similar to the PT16 the effective cooperativity for PT8AA8 is described by a slightly higher value of average number of monomer units on polymer chains, $\langle M_t \rangle_{eff} = 32$, which once again points to the formation of polymer networks by iron bridges between the copolymer chains.

In the case of PT8nBA8, the transition of the copolymer from the oil to the aqueous state is much broader than that of PT8AA8, see purple diamonds in Figure 8.4 C. In this case, the data are not well explained by random adsorption behavior either (the fit not shown), whereas the binding behavior of the iron ions onto terpyridine sites of the copolymer over a broad range of free iron ions concentration is well accounted for by the theory. The purple solid line in Figure 8.4 C is the best fit for PT8nBA8 with $\alpha = 10.7$ and $\langle M_t \rangle_{eff} = 32$ (from the fit). The drop in the fraction of PT8nBA8 in the oil phase over a broad range of free iron concentration can be explained by first the hydrophobic contribution of the second monomer and second by the large compositional polydispersity of the copolymer chains. As a result, each composition of the copolymer will have a separate sharp transition and therefore, it broadens the overall transition of the copolymer from the oil to the water phase vs. free iron concentration in the water phase.

In addition, the Hill plots for the studied copolymers clearly point to their different behavior, Figure 8.4 D. The smaller slope of the line $\ln((1 - f_o)/f_o)$ vs. $\ln[\text{Fe}^{2+}]$ in the case of PT8nBA8 shows the broadening of the transition in this case (compared to PT8AA8). Results suggest that in the case of PT8nBA8, the effective cooperativity of binding iron ions to the terpyridine functional groups on the copolymer decreases with $\langle M_t \rangle_{eff} = 2.6$ (from the Hill plot). In other words, the compositional polydispersity in the copolymers of the terpyridine-functionalized repeating unit and a substitute monomer with a hydrophobic contribution can effectively lead to a negative influence on the cooperativity.

Comparison between the results obtained for the PT8AA8 and PT8nBA8 copolymers clearly suggests that when the substitute monomer (in this case n-butyl acrylate in the PT8nBA8 copolymer) actively contributes to the hydrophobic free energy of the copolymer (to switch from the oil to the aqueous phase), the compositional polydispersity can influence the sharpness of the transition of the copolymer. Therefore, it can be concluded that the compositional polydispersity influences the range of the free iron concentration over which the transition occurs only on the condition that the substitute monomer is hydrophobic.

8.4.3 Verification of occupancy of the terpyridine monomer or terpyridine-functionalized polymers

The quantification of the occupancy i.e., the fraction of occupied terpyridine functional groups per chain in the water phase or $(1 - f_o)$ was verified using an independent calculation of the occupied fraction of terpyridine groups (i.e., θ). By using the mass balance of iron ions: $[\text{Fe}_{(tot)}^{2+}] = [\text{Fe}_{(free)}^{2+}] + [\text{Fe}_{(bound)}^{2+}]$, we define the fraction of occupied sites in the water phase, θ , as

$$\theta = \frac{[\text{Fe}_{(bound)}^{2+}]}{[\text{T}_{(tot)}]/2} \quad (8.25)$$

in which $[\text{Fe}_{(bound)}^{2+}]$ and $[\text{T}_{(tot)}]$ are the bound iron and initial terpyridine (functional group) concentrations, respectively. It is important to note that θ is calculated based on the assumption that the bis (terpyridine) iron (II) complex, $(\text{FeT}_2)^{2+}$, is the most favored complex¹¹. The comparison between $1 - f_o$ and θ for terpyridine monomer and terpyridine-functionalized polymers studied in this work is shown with filled and patterned markers, respectively, in Figure 8.5.

The results suggest that overall the two sets of data regarding the occupancy of terpyridine ($1 - f_o$ and θ) are in good agreement in all cases, particularly around the transition regions. Interestingly, the independent calculation of θ , based on Equation 8.25, leads to $\theta < 1$ for all cases at high free iron concentrations. Considering formation of polymer gels, this can be explained by the formation of topological defects such as dangling ends (or binding sites i.e., terpyridine functional groups) in the polymer network¹⁶, see the schematic in Figure 8.5 E. It is expected that a fraction of terpyridine groups remains unoccupied due to internal constraints such as spacial hindrance and electrostatic repulsion between the bound iron ions. In the case of PT16, the fraction of occupied terpyridine groups in the water phase remained noticeably low (≈ 0.8) due to the disordered nature of a dense (and most probably impenetrable at high iron concentrations) gel¹⁷. In the case of PT8AA8 and PT8nBA88 (see Figure 8.5 C and D), this effect is less significantly observed due to the less number of terpyridine functional groups per polymer chain which leads to the formation

of a gel with a lower crosslink density¹⁸. Other inconsistencies, particularly in low iron concentrations, are expected to be due to the low quantities of iron leading to noticeable errors in further calculations.

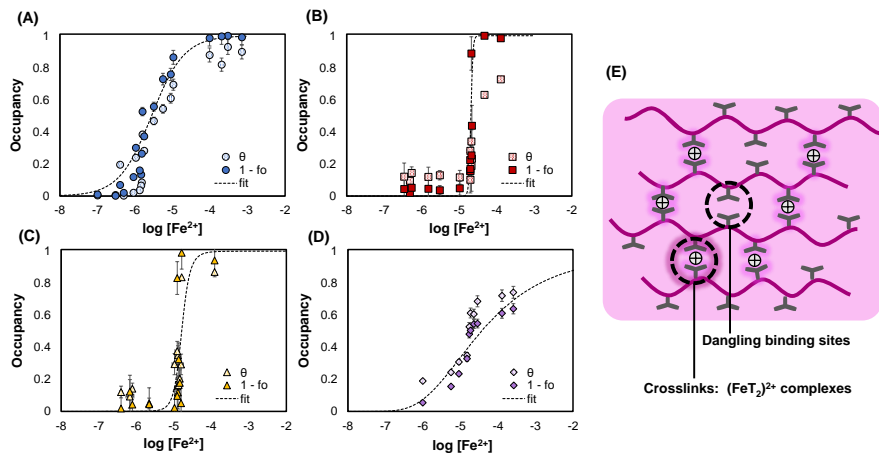


Figure 8.5 Verification of occupancy of the terpyridine groups ($1 - f_0$) with independent calculation of fraction of occupied sites in the water phase (θ). The comparison shows that in the case of (A) terpyridine monomer, the terpyridine-functionalized polymers with (B) full coverage of terpyridine (PT16), and copolymers of 1:1 terpyridine-functionalized repeating unit and (C) acrylic acid (PT8AA8), and (D) n-butyl acrylate (PT8nBA8), $1 - f_0$: open and θ : filled markers are in good agreement. (E) Schematic illustration of dangling binding sites and crosslinks in the polymer gel.

8.4.4 Interpretation of binding and hydrophobic free energies

The values for the linear combination of binding and hydrophobic free energies (i.e., $\alpha = -\beta(g_{2w} + 2g_H)$) for terpyridine and terpyridine-functionalized polymers are reported in Table 8.1. As expected from the discrepancy in the case of incorporating terpyridine as a monomer in the model ($M = 1$ and based on Equation 8.9), the value of α in this case is not close to the other cases. Among other cases (i.e., terpyridine dimers and terpyridine-functionalized polymers), the maximum difference of $\approx 2k_B T$ seems reasonable. Considering the previously reported value for binding free energy, $\beta g_{2w} = -48$ ¹¹, the best fits for terpyridine monomer and dimer based on Equations 8.9 and 8.11, lead to $\alpha = 21.8$ and 12.8 , which result in hydrophobic free energies $\beta g_H = 13.6$ and 17.6 , respectively.

Comparison between α for poly(terpyridine) and for terpyridine dimer indicates a decrease in the absolute value from 12.8 for the monomer (T_2) to 10.8 for the polymer (PT16), see Table 8.1. In general, the lower value for α can be interpreted in two ways; lower binding and/or higher hydrophobic free energies of the system. In the case of

Table 8.1 The values obtained from fitting the data on binding iron onto terpyridine in different forms. Terpyridine monomer (T), dimer (T_2), and terpyridine-functionalized polymers PT16, PT8AA8, and PT8nBA8. α and $\ln K'$ are the linear combination of the binding and hydrophobic free energies obtained from the f_0 and the Hill plots, respectively. M_{eff} or $\langle M_t \rangle_{eff}$ are the effect number of (average) monomer units indicative for the effective cooperativity of binding.

Parameter	T	T_2	PT16	PT8AA8	PT8nBA8
$\alpha = \ln K'$	21.8	12.8	10.8	11.2	10.7
M_{eff} or $\langle M_t \rangle_{eff}$	1	2	≈ 32	≈ 32	≈ 2.6

the polymer PT16, this behavior can be explained by the possible lower absolute value of binding free energy in the case of poly(terpyridine) ($\approx 5k_B T$) than for terpyridine to be due to the electrostatic repulsion between iron ions present in the $(FeT_2)^{2+}$ complexes in the polymer gel. Here, we chose the value of $\beta g_{2w} = -43$ which leads to slightly less hydrophobicity of PT16 (i.e., $\beta g_H = 16.1$), compared to terpyridine (dimer). This slightly lower obtained value of the hydrophobic free energy for PT16 can be explained by the presence of the ester group in the polymer backbone or the secondary amide in the side branches which result in slightly more hydrophilic nature of the polymer chains. Furthermore, formation of mono (terpyridine) iron (II) complexes $(FeT)^{2+}$, which are inevitable in reality, can lower the average binding free energy of the system as a whole. Therefore, the combination of these reasons can result in a lower α value for PT16.

In the case of the random copolymers, PT8AA8 and PT8nBA8, the best fits result in $\alpha = 11.2$ and 10.7 , respectively (see Table 8.1). For PT8AA8, the slightly higher value of α , compared to PT16, shows that the transition for this copolymer occurs at slightly lower free iron concentration (the transition point, yellow triangles compared to red squares in Figure 8.4 C and A, respectively). However, this effect is minor due to the high binding affinity of terpyridine functional groups to iron ions. In this case, the best fit for the data was based on the linear contribution of hydrophobic energies for terpyridine and acrylic acid groups (i.e., $\beta g_T = 18.8$ and $\beta g_S = 1$) and $\beta g_{2w} = -31$. It should also be noted that the pH of the aqueous phase was below 4 in all samples due to the addition of reducing agent (i.e., ascorbic acid). Therefore, it is expected that the acrylic acid groups are still protonated (pK_a for acrylic acid ≈ 4.2) and thus the value of hydrophobic contribution $\beta g_S = 1.0$ for acrylic acid groups seems reasonable. On the other hand, $\beta g_T = 18.8$ is higher than expected because the presence of acrylic acid groups results in slightly more hydrophilic nature of the polymer chains in general.

For the copolymer PT8nBA8, the chosen values for the best fits were $\beta g_T = 18$, $\beta g_S = 8.3$, and $\beta g_{2w} = -37$. In this case the best fit results in $\alpha = 10.7$ meaning a

transition point close to PT16 (10.8). However the hydrophobic contribution of the substitute monomer (i.e., n-butyl acrylate) and the compositional (or chemical) polydispersity of the random copolymer leads to a much broader transition, compared to PT16.

It should be mentioned in this context that lower values of binding free energy for both random copolymers does not seem justified due to the more distant terpyridine functional groups along the copolymer chains and therefore negligible influence of the electrostatic repulsion potential energy on the binding strength. However, the value of free energy of formation of bis (terpyridine) iron (II) complexes that are reported in the literature¹¹ are not able to describe the data of the random copolymers. Moreover, the values for hydrophobic free energies of these model compounds from the oil to the aqueous states seem higher than physical. In future works, independent determination of binding free energy and hydrophobic free energy penalty (by measuring the partitioning of terpyridine in a two-phase system of water and DCM and/or the solubility limit of terpyridine in DCM) is necessary.

In summary, we have successfully predicted and proven the cooperative binding behavior of a ligand (iron ions) onto a substrate (terpyridine functional groups) on a polymeric backbone using a two phase water/oil system. Our results suggest that this behavior is not limited to the system's components. In fact, the main condition for cooperative binding is having a substrate in at least two different energy states with different binding affinities towards a ligand. Furthermore, we have shown that the cooperativity in such systems can be manipulated by the competition between binding and self (in this case hydrophobic) free energies of the system at the different energy states. The prediction model that we present in this work is applicable in similar systems and promising for designing stimuli-responsive materials for which a narrow and/or adaptive range of conditions is required.

8.4.5 Magnetic properties of the iron/terpyridine complexes

Organometallic complexes which contain transition metals such as iron, have been widely studied for their various properties including magnetic properties¹⁹. In this work, we explored the magnetic properties of the obtained gels from the terpyridine-functionalized polymers (PT16, PT8AA8, and PT8nBA8) after their transition from the oil to the aqueous state. The results of the magnetization of the polymers up to 1.5 T at room temperature (273 K) and up to 2.2 T in cryo mode (77 K) are shown in Figure 8.6 A and B, respectively.

Comparison between the magnetization curves at room temperature shows that the slope of the magnetization vs. applied magnetic field was negative in all cases, except for FeCl₂ which is an indication of the latter being very weakly paramagnetic, Figure 8.6 A. All other compounds (with and without iron) were diamagnetic and the (absolute value) of the slope of magnetization vs. magnetic field increased for terpyri-

dine (T) and all terpyridine-functionalized polymers when in complexation with iron, filled markers compared to open markers in Figure 8.6 A. These results indicate that binding iron onto the terpyridine or terpyridine-functionalized polymers (in other words formation of FeT_2^{2+} complexes) induces a stronger diamagnetic response to the external field in the system at room temperature.

Furthermore, the magnetization of the compounds was investigated at low temperature which makes their thermal energy less influential. The results showed that at low temperature all compounds had a paramagnetic response to the external field, Figure 8.6 B. Additionally, the slope of the magnetization curves (i.e., indicative of the magnetic susceptibility) increased with decreasing temperature. Finally, the magnetization of the copolymer PT8nBA8 had an S-shape with respect to the applied magnetic field, filled purple diamonds in Figure 8.6 B.

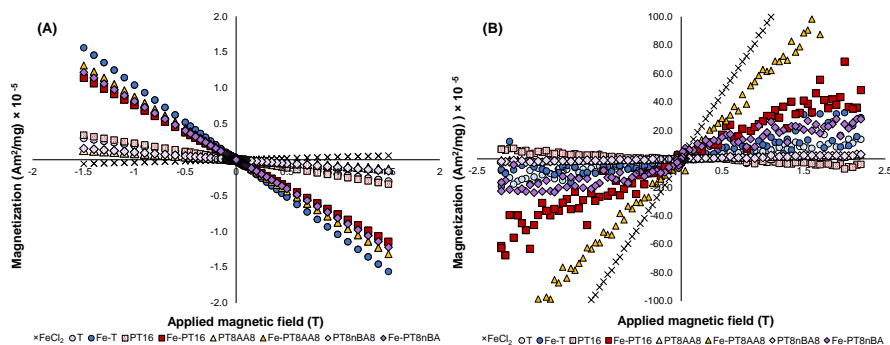


Figure 8.6 Magnetic properties of the iron/terpyridine complexes in different forms. Magnetization vs. the applied magnetic field for iron (II) ions (FeCl_2), terpyridine (T), iron/terpyridine complex (Fe-T), the terpyridine-functionalized polymers (PT16, PT8AA8, PT8nBA8), and their gel after complexation with iron (Fe-PT16, Fe-PT8AA8, Fe-PT8nBA8) at (A) Room Temperature (273 K, up to 1.5 T) and (B) in cryo mode (77 K, up to 2.2 T).

8.5 Conclusions

In the present study, we show that cooperative adsorption can be mimicked in a simpler model system, compared to proteins. For our model system, we designed terpyridine-functionalized polymers with tunable hydrophobicities, and then monitored the binding behavior of iron ions onto the terpyridine functional groups in a two-phase water/oil system. To this end, the solutions of the terpyridine monomer or terpyridine-functionalized polymers in oil were exposed to a series of solutions of iron in water with different concentrations. In the ground state, the terpyridine and terpyridine-functionalized polymers dissolve in oil due to their hydropho-

bicity. Upon increasing iron concentration in the water phase, the terpyridine or terpyridine-functionalized polymers move to the water phase which is followed by binding iron onto the terpyridine groups. In the case of terpyridine monomer, binding iron onto it follows random adsorption. However, in the case of the terpyridine-functionalized polymers a sharp decrease in the concentration of the polymer in the oil phase over a small range of free iron concentration is observed. Additionally, in the case of poly(terpyridine) (i.e., 100% terpyridine coverage of the polymer backbone), the effective cooperativity of binding iron onto terpyridine functional groups was slightly higher due to the formation of crosslinks by iron bridges between the polymer chains. Furthermore, binding behavior of iron onto copolymers of terpyridine-functionalized repeating units and a second (or substitute) monomer was investigated. Our observations suggest that in the case that the second monomer does not contribute to the hydrophobicity of the polymer chain, the transition remains sharp regardless of the length and compositional polydispersity of the copolymers. In other words, compositional polydispersity of the copolymers can broaden the transition only if the substitute monomer actively contributes to the hydrophobicity of the copolymer. In future works, the effect of pH on the transition of the copolymers (containing acrylic acid) and the influence of addition of a competing metal ion will be of interest for further investigation.

8.6 Acknowledgments

Bas G. P. van Ravensteijn and Kanvaly Lacina are thanked for their help with synthesizing the polymers. The author is grateful to James L. Martin Robinson and Jan Groenewold for fruitful discussions as well.

8.A Appendix

8.A.1 Materials

Copper (II) bromide (CuBr_2 , 99%), tris[2-(dimethylamino)ethyl] amine (Me_6TREN , 97%), ethyl α -bromoisobutyrate (EBiB, 98%), silica gel (high-purity grade (Davisil grade 633), pore size 60 Å, 200-425 mesh particle size), 2,2':6',2"-terpyridine (T, 98%), 4'-chloro-2,2':6',2"-terpyridine (Cl-T, 99%), methanol- d_4 (99.8%), dimethyl sulfoxide (DMSO, anhydrous 99.9%), iron (II) chloride tetrahydrate (FeCl_2 , 99%), L-ascorbic acid (L-AA), dimethyl sulfoxide- d_6 (DMSO- d_6 , 99.9%), ethanolamine (99.5%), N-(3-dimethylaminopropyl)-N'-ethylcarbodi-imide hydrochloride (EDC-HCl, 98%), N,N-dimethyl- formamide (DMF, 99.8%), and N-hydroxysuccinimide (NHS, 98%) were purchased from Sigma Aldrich (St. Louis, MO, USA). 2,2,2-trifluoroethanol (TFE, 99%), potassium hydroxide powder (KOH, ~ 85%), sodium chloride (NaCl) and sodium hydroxide pellets (99%) were purchased from Merck (Burlington, MA, USA).

Dichloromethane (DCM, 99%), methanol absolute HPLC (MeOH, 99.9%), tetrahydrofuran (THF, 99.8%), diethyl ether (Et₂O, anhydrous 99.5%), chloroform HPLC (99.9%) and acetonitrile (ACN, HPLC-R) were purchased from Biosolve B.V. (Valkenswaard, The Netherlands). Copper wire (Cu(o), d = 0.25mm, 99.99%) was purchased from Alfa Aesar (Haverhill, MA, USA). Hydrochloric acid (HCl, 37%) was purchased from Acros Organics (Geel, Belgium). Ethanol absolute (100%), acetone (100%), n-hexane (99%) and triethylamine (TEA, high purity grade) were purchased from VWR International (Radnor, PA, USA). *tert*-butyl acrylate (*t*BA) and *n*-butyl acrylate (*n*BA) were purified (using a 1:1 Al₂O₃:Silica column) and stored at 4 °C. Trifluoroacetic acid (TFA, 99%), aluminum oxide (98%) and sodium sulfate (Na₂SO₄, 99%) were purchased from Honeywell (Charlotte, NC, USA). Chloroform-d₁ (99%) was purchased from Carl Roth (Karlsruhe, Germany). Dimethyl sulfoxide (DMSO, 99.7%) was purchased from Thermo Fisher Scientific (Waltham, MA, USA). The Milli-Q (MQ) water used was deionized by a Millipore Synergy water purification system (Merck Millipore, Billerica, MA, USA).

8.A.2 Synthesis of the terpyridine-functionalized polymers

The synthesis of the terpyridine-functionalized polymers was done in multiple steps. As an overview, illustrated in Figure 8.7, the synthesis starts with synthesizing poly(*tert* - butyl acrylate) and deprotecting it into poly(acrylic acid) (PAA).

Subsequently, EDC/NHS activation was done on the carboxylic acid groups of PAA in order to synthesize poly (N-hydroxysuccinimide) (PNHS). To functionalize (PNHS) with terpyridine, Cl-T was synthesized with ethanolamine to yield an amine functionalized terpyridine, 2-(2,2':6',2"-terpyridine-4'-yloxy) ethylamine (ET), which was necessary in order to substitute the NHS groups on the polymer via nucleophilic substitution. Eventually, three terpyridine-functionalized polymers were synthesized and coded as: PT16, PT88AA8, and PT8nBA8 with structures (5), (7) and (11) in Figure 8.7, respectively. Numbers in the subscripts show the number of monomer units in each copolymer. After each synthesis step, the product was characterized with Infrared (IR) and nuclear magnetic resonance (¹H-NMR) spectroscopies.

Synthesis of 2-(2,2':6',2"-terpyridine-4'-yloxy) ethylamine (ET) (1)

Cl-T (267.71 mg, 1 mmol) and ethanolamine (67.17 μl, 1.1 mmol) were added to a suspension of powdered KOH (280.55 mg, 5 mmol) in DMSO (5 ml) and stirred at 40 °C for 2 h. The reaction mixture was then added to 40 ml of DCM and washed with MQ water (3 40 ml) by liquid-liquid extraction. The DCM solution was dried over Na₂SO₄ and the solvent was removed. 2-(2,2':6',2"- terpyridine-4'-yloxy) ethylamine (ET) was obtained as a light yellow solid and used subsequently without further purification

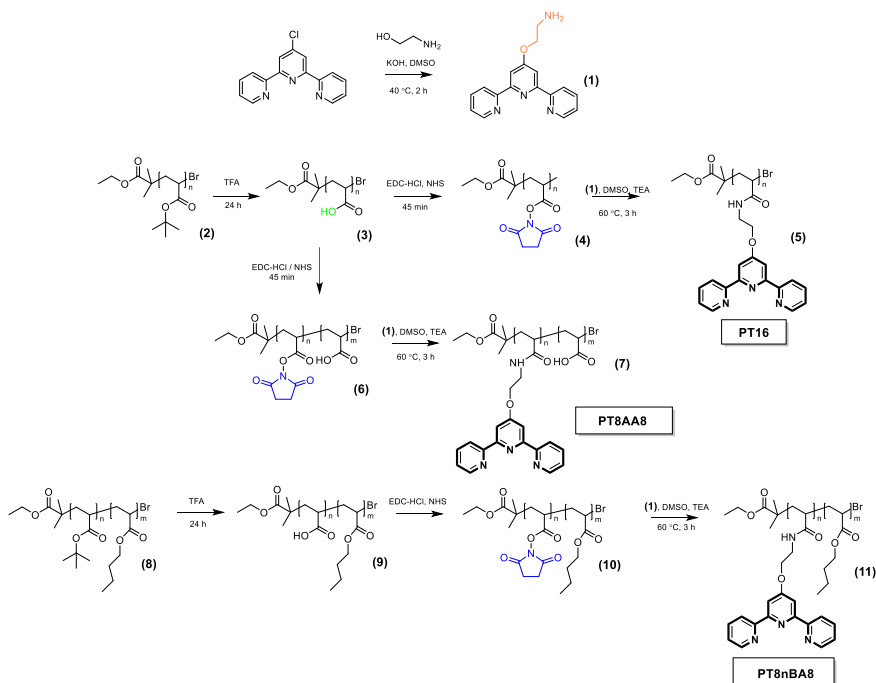


Figure 8.7 Overview of the steps of synthesizing the terpyridine-functionalized polymers. PT16: the polymer with 100% terpyridine coverage (compound 5), PT8AA8: the polymer with 50% terpyridine-functionalized and 50% acrylic acid (compound 7), and PT8nBA8: 50% terpyridine-functionalized and 50% n-butyl acrylate (compound 11).

(252.60 mg, 86.5% yield). $^1\text{H-NMR}$: 400 MHz (Chloroform- d_1) δ : 8.75-7 aromatic rings region (10H, m); 4.2 (2H, t); 3.1 (4H, t). IR: ν_{max} cm^{-1} : 1204s, 1027s.

Synthesis of poly(*tert*-butyl acrylate) (PtBA) (2)

CuBr_2 (7.59 mg, 0.034 mmol, 0.05 equiv. per initiating sites), TFE (1 ml) and Me_6TREN (33 μl , 0.123 mmol, 0.18 equiv. per initiating sites) were added in a 4-ml vial and the resulting solution was treated with ultrasonication for 30 minutes using a CPX8800H ultrasonic cleaning bath (Branson UltrasonicsTM, Brookfield, CT, USA). For Cu(o) source, 5cm of 0.25 mm thick Cu copper wire was cut and etched in HCl for 30-45 minutes. Afterwards, the wire was washed with acetone and dried with dust-free paper (three times). *t*BA (2ml, 13.7mmol, 20 equiv.) was added, together with the initiator, EBiB (101 μl , 0.685 mmol, 1 equiv.) to the mixture and the reaction was activated by adding a magnetic stir bar wrapped by the copper wire. The reaction was degassed under N_2 flow for the first 20 min was left for 4 hours (in total). The product

was then diluted with Et₂O, and purified by passing through a 1:1 Al₂O₃:Silica column. Consequently, the product was dissolved in minimal amount of DCM and washed 4 times by a 4:1 MeOH:water solution by centrifugation at $3273 \times g$ for 15 minutes using an Allegra X-12R Centrifuge (Beckman Coulter, Brea, CA, USA). Finally, the product was dried under N₂ flow and vacuum. The resulting material was a sticky viscous gel (DP_n \approx 16). ¹H-NMR: 400 MHz (Chloroform-d₁) δ : 4.1 (2H, m); 2.2 (1H, s); 2-1.5 (2H, m); 1.4 (9H, s); 1.2 (3H, m); 1.1 (6H, m). IR: ν_{\max} cm⁻¹: 2978m, 2934m, 1723s, 1141s.

Deprotection of (2) into poly(acrylic acid) (PAA) (3)

In a 4-ml vial, compound (2) (256.64 mg), TFA (2.6 ml) and a magnetic stir bar were added and left under stirring for 24 hours. Next, the mixture was diluted with minimal amount of DCM, added to an excess amount of Et₂O and centrifuged at $3273 \times g$ for 15 minutes. This was repeated three times. After centrifugation, the product was dried overnight and a white powder was obtained (\approx 80% yield). ¹H-NMR: 400 MHz (methanol-d₄) δ : 9.24 (2H, m); 8.43 (4H, m); 7.90 (2H, t); 7.70 (1H, t); 7.56 (2H, m); 6.78 (2H, t); 5.74 (4H, m); 5.50 (2H, m). IR: ν_{\max} cm⁻¹: 1604s, 1539s, 1470s, 1443s, 1375s, 1274s, 1009s, 965w, 845m, 762m, 738m.

EDC/NHS Activation of (3) into PNHS (4)

Compound (3) (47.55 mg, 0.057 mmol) was added together with EDC-HCl (164.24 mg, 0.857 mmol, 1.5 equiv. per carboxylic acid groups) and NHS (98.60 mg, 0.857 mmol, 1.5 equiv. per carboxylic acid groups) in a 20-ml vial. Afterwards, 8.57 ml MQ water was added to have 0.1 M EDC-HCl / NHS in water. The mixture was stirred at room temperature for 45 minutes. Consequently, the mixture was added to 35ml MQ water, vortexed vigorously and centrifuged at $3273 \times g$ for 20 minutes. This was repeated 3 times. The precipitate was dried overnight under a flow of N₂. The outcome was a white powder (51.73 mg, 49.5% yield). ¹H-NMR: 400 MHz (acetone-d₆) δ : 9.24 (2H, m); 8.43 (4H, m); 7.90 (2H, t); 7.70 (1H, t); 7.56 (2H, m); 6.78 (2H, t); 5.74 (4H, m); 5.50 (2H, m). IR: ν_{\max} cm⁻¹: 1604s, 1539s, 1470s, 1443s, 1375s, 1274s, 1009s, 965w, 845m, 762m, 738m.

Functionalization of PNHS (4) with ET (1) to get PT16 (5)

In a 4-ml vial, compound (4) (30 mg, 0.010 mmol) and compound (1) (72.51 mg, 0.25 mmol, 1.5 equiv. per NHS group) were added, following by addition of a magnetic stir bar. The vial was sealed and degassed under N₂ flow. Next, anhydrous DMSO (0.3 ml) was added, and the mixture was stirred until it became homogeneous. Afterwards, 1 drop of TEA was added and the vial was kept in an oil bath for 3 hours at 60 °C. During the reaction the solution became red. Consequently, the product was precipitated in 20 ml ice cold acetone, and then centrifuged at $3273 \times g$ for 30 minutes. The

precipitate red gel was left overnight under N_2 . The final product was a red gel-like solid (17.3 mg, $\approx 30\%$ yield). 1H -NMR: 400 MHz (acetone- d_6) δ : 9.24 (2H, m); 8.43 (4H, m); 7.90 (2H, t); 7.70 (1H, t); 7.56 (2H, m); 6.78 (2H, t); 5.74 (4H, m); 5.50 (2H, m). IR: ν_{max} cm^{-1} : 1604s, 1539s, 1470s, 1443s, 1375s, 1274s, 1009s, 965w, 845m, 762m, 738m.

EDC/NHS Activation of PAA (3) into PNHSAA copolymer (6)

The method was similar to the method described in section 8.A.2. Compound (3) (43.70 mg, 0.033 mmol) was added together with EDC-HCl (75.47 mg, 0.39 mmol, 0.75 equiv. per carboxylic acid groups) and NHS (45.31 mg, 0.39 mmol, 0.75 equiv. per carboxylic acid groups) in a 20-ml vial. Afterwards, 3.94 ml MQ water was added to result in 0.1 M EDC-HCl / NHS in water. The mixture was stirred at room temperature for 45 minutes. Consequently, the reaction mixture was added to 35 ml MQ water, vortexed vigorously and centrifuged at $3273 \times g$ for 20 minutes. This procedure was repeated 3 times. The precipitate was dried overnight under a flow of N_2 . The outcome was a white powder (44.97 mg, 50.8% yield). 1H -NMR: 400 MHz (acetone- d_6) δ : 9.24 (2H, m); 8.43 (4H, m); 7.90 (2H, t); 7.70 (1H, t); 7.56 (2H, m); 6.78 (2H, t); 5.74 (4H, m); 5.50 (2H, m). IR: ν_{max} cm^{-1} : 1604s, 1539s, 1470s, 1443s, 1375s, 1274s, 1009s, 965w, 845m, 762m, 738m.

Functionalization of PNHSAA (6) with Cl-T (1) to get PT8AA8 (7)

In a 4-ml vial, compound (6) (30 mg, 0.019 mmol) and compound (1) (67.99 mg, 0.228 mmol, 0.75 equiv. per NHS group) were added, following by addition of a magnetic stir bar. The vial was sealed and degassed under N_2 flow. Next, anhydrous DMSO (0.3 ml) was added, and the mixture was stirred until it became homogeneous. Afterwards, 1 drop of TEA was added and the vial was kept in an oil bath for 3 hours at 60 °C. During the reaction the solution became red. Consequently, the product was precipitated in 20 ml ice cold acetone, and then centrifuged at $3273 \times g$ for 30 minutes. The precipitated red gel was left overnight under N_2 flow. The final product was a red gel-like solid (45.3 mg, 80% yield). 1H -NMR: 400 MHz (acetone- d_6) δ : 9.24 (2H, m); 8.43 (4H, m); 7.90 (2H, t); 7.70 (1H, t); 7.56 (2H, m); 6.78 (2H, t); 5.74 (4H, m); 5.50 (2H, m). IR: ν_{max} cm^{-1} : 1604s, 1539s, 1470s, 1443s, 1375s, 1274s, 1009s, 965w, 845m, 762m, 738m.

Synthesis of copolymer of *tert*butyl acrylate and *n*-butyl acrylate (8)

The same procedure for synthesizing and purifying compound (1) was repeated. The only difference was that *t*BA (1 ml, 6.85 mmol, 10 equiv. per initiating sites) and *n*BA (1ml, 6.85 mmol, 10 equiv. per initiating sites) were added in the reaction vial as monomers. The resulting material was a sticky viscous gel ($\approx 80\%$ yield). 1H -NMR: 400 MHz (Chloroform- d_1) δ : 4.1 (2H, m); 2.3 (1H, m); 1.3 (3H, t); 1.1 (6H, m); 0.9 (3H, t);

6.78 (2H, t); 5.74 (4H, m); 5.50 (2H, m). IR: ν_{\max} cm^{-1} : 1604s, 1539s, 1470s, 1443s, 1375s, 1274s, 1009s, 965w, 845m, 762m, 738m.

Deprotection of (8) to get (9)

The method was similar to the deprotonation of (2) into (3), see section 8.A.2. In a 4-ml vial, compound (8) (493.2 mg), TFA (6 ml) and a magnetic stir bar were added and left under stirring for 24 hours. Next, the mixture was diluted with large amount of DCM and the solvent was completely removed under N_2 flow/vacuum (twice). Next, the product was diluted in minimal amount of THF, added to an excess amount of cold n-hexane and centrifuged at 3273 g for 15 minutes. This was repeated three times. After centrifugation, the product was dried overnight and a viscous gel was obtained ($\approx 70\%$ yield). $^1\text{H-NMR}$: 400 MHz (acetone- d_6) δ : 9.24 (2H, m); 8.43 (4H, m); 7.90 (2H, t); 7.70 (1H, t); 7.56 (2H, m); 6.78 (2H, t); 5.74 (4H, m); 5.50 (2H, m). IR: ν_{\max} cm^{-1} : 1604s, 1539s, 1470s, 1443s, 1375s, 1274s, 1009s, 965w, 845m, 762m, 738m.

EDC/NHS Activation of (9) into (10)

Compound (9) (80 mg, 0.04 mmol) was dissolved in 3 ml DMF until mixture was homogeneous. Simultaneously, EDC-HCl (92.016 mg, 0.48 mmol, 1.5 equiv. per carboxylic acid groups) and NHS (55.243 mg, 0.48 mmol, 1.5 equiv. per carboxylic acid groups) were dissolved in 2 ml DMF to get a homogeneous mixture. Subsequently, the mixtures were added together and were stirred for 90 minutes. Finally, the mixture was precipitated in 50% aqueous MeOH and centrifuged at 3273 g for 30 minutes. The resulting product was a viscous gel (71.32 mg, 65% yield). $^1\text{H-NMR}$: 400 MHz (acetone- d_6) δ : 9.24 (2H, m); 8.43 (4H, m); 7.90 (2H, t); 7.70 (1H, t); 7.56 (2H, m); 6.78 (2H, t); 5.74 (4H, m); 5.50 (2H, m). IR: ν_{\max} cm^{-1} : 1604s, 1539s, 1470s, 1443s, 1375s, 1274s, 1009s, 965w, 845m, 762m, 738m.

Functionalization of (10) with (1) to get PT8nBA8 (11)

In a 4-ml vial, compound (10) (71.32 mg, 0.026 mmol) and compound (1) (91.16 mg, 0.312 mmol, 1.5 equiv. per NHS group) were added, following by addition of a magnetic stir bar. The vial was sealed and degassed under N_2 flow. Next, anhydrous DMSO (0.3 ml) was added, and the mixture was stirred until it became homogeneous. Afterwards, 1 drop of TEA was added and the vial was kept in an oil bath for 3 hours at 60 °C. During the reaction the solution became red. Consequently, the product was precipitated in 20 ml ice cold acetone, and then centrifuged at 3273 g for 30 minutes. The white precipitate was a by-product. The supernatant was evaporated and a red gel was left. The gel was re-dissolved in DCM and precipitated in water two times. The resulting gel was left overnight under N_2 flow. The final product was a red gel-like solid (65.2 mg, 58.9% yield). $^1\text{H-NMR}$: 400 MHz (acetone- d_6) δ : 9.24

(2H, m); 8.43 (4H, m); 7.90 (2H, t); 7.70 (1H, t); 7.56 (2H, m); 6.78 (2H, t); 5.74 (4H, m); 5.50 (2H, m). IR: ν_{max} cm^{-1} : 1604s, 1539s, 1470s, 1443s, 1375s, 1274s, 1009s, 965w, 845m, 762m, 738m.

8.A.3 Characterization of the terpyridine-functionalized polymers

Infrared (IR) Spectroscopy

IR measurements were performed in attenuated total reflectance (ATR) mode on dried powders of the samples by an IR spectrometer (PerkinElmer, Waltham, MA, USA). The interferograms were accumulated over the spectral range of $1600 - 400 \text{ cm}^{-1}$ using a resolution of 4 cm^{-1} , with a background spectrum recorded before each measurement. The measurements were done from independent duplicates.

Nuclear Magnetic Resonance (NMR)

NMR spectra were recorded on an MRF 400 spectrometer (Agilent Scientific Instruments, Santa Clara, CA, USA). Deuterated chloroform- d_1 , DMSO- d_6 or methanol- d_4 were used as solvents, depending on the products.

Gel Permeation Chromatography (GPC)

The molecular weights and polydispersity index of the polymers were determined via GPC analysis. The instrument comprised an Alliance HPLC e2695 separation module (Waters, Milford, MA, USA) in combination with a PL-gel $5 \mu\text{m}$ mixed-D column fitted with a guard column (M_w range of 0.2–400kDa) coupled to a Waters 2414 refractive index detector. Polystyrene standards of known molecular weights were used as standards using HPLC grade THF, eluting at $1 \text{ mL} \cdot \text{min}^{-1}$ flow rate at 30°C .

References

- 1 A. Whitty, *Nature Chemical Biology* 2008 4:8 4, 435 (2008).
- 2 F. Yuan, S. S. Shen, H. M. Hu, R. An, X. Wang, Z. Chang, and G. Xue, *Inorganica Chimica Acta* 430, 17 (2015).
- 3 J. P. Changeux, *Annual Review of Biophysics* 41, 103 (2012).
- 4 J. Monod, J. Wyman, and J. P. Changeux, *Journal of Molecular Biology* 12, 88 (1965).
- 5 J. L. Martin Robinson and W. K. Kegel, *Proceedings of the National Academy of Sciences* 120, e2211088120 (2023).
- 6 N. Hannewald, M. Enke, I. Nischang, S. Zechel, M. D. Hager, and U. S. Schubert, *Journal of Inorganic and Organometallic Polymers and Materials* 30, 230 (2020).

- 7 K. Schöller, C. Toncelli, J. Experton, S. Widmer, D. Rentsch, A. Vetushka, C. J. Martin, M. Heuberger, C. E. Housecroft, E. C. Constable, L. F. Boesel, and L. J. Scherer, *RSC Advances* **6**, 97921 (2016).
- 8 L. Hu, W. Liu, C. H. Li, X. H. Zhou, and J. L. Zuo, *European Journal of Inorganic Chemistry*, 6037 (2013).
- 9 E. Belhadj, A. El-Ghayoury, E. Ripaud, L. Zorina, M. Allain, P. Batail, M. Mazari, and M. Sallé, *New Journal of Chemistry* **37**, 1427 (2013).
- 10 “ChemicalBook 2,2':6',2"-terpyridine,” Modified: 2022-08-15.
- 11 B. R. H. Holyer, C. D. Hubbard, S. F. A Kettle, and R. G. Wilkins, .
- 12 D. Rocco, A. Prescimone, E. C. Constable, and C. E. Housecroft, *Molecules* **2020**, Vol. 25, Page 3162 25, 3162 (2020).
- 13 W. Lu, M. C. Chan, N. Zhu, C. M. Che, C. Li, and Z. Hui, *Journal of the American Chemical Society* **126**, 7639 (2004).
- 14 A. M. Bünzli, E. C. Constable, C. E. Housecroft, A. Prescimone, J. A. Zampese, G. Longo, L. Gil-Escrig, A. Pertegás, E. Ortí, and H. J. Bolink, *Chemical Science* **6**, 2843 (2015).
- 15 A. V. Hill, *Proceedings of the Physiological Society* **40**, iv (1910).
- 16 F. Di Lorenzo and S. Seiffert, *Polymer Chemistry* **6**, 5515 (2015).
- 17 S. Biswas, V. V. Yashin, and A. C. Balazs, *Soft Matter* **16**, 5120 (2020).
- 18 M. Yamaguchi, S. Ono, and K. Okamoto, *Materials Science and Engineering: B* **162**, 189 (2009).
- 19 W. Wu, R. Tang, Q. Li, and Z. Li, *Chemical Society Reviews* **44**, 3997 (2015).

Summary

"When I want to understand what is happening today or try to decide what will happen tomorrow, I look back."

Omar Khayyam – Persian polymath, 1048-1131

IRON deficiency is one of the most prevalent nutritional problems in the world. However, iron is a challenging mineral to add to food products. Iron-containing compounds can react with the (phyto)chemicals present in foods and as a result cause severe changes in the organoleptic properties, for instance off-flavor and off-color. To date, iron fortification of foods has proven to be an efficient and cost-effective approach to overcome iron deficiency. Iron-containing compounds that are applied as iron fortificants are divided into three main categories; water-soluble, poorly water-soluble (but soluble in dilute acid), and water-insoluble (and poorly soluble in dilute acid). Although water-soluble compounds have the advantage of high iron bio-availability, the other categories are more in the center of attention because of their minimum influence on the organoleptic properties of the foods which is a consequence of their limited solubilities.

Among the poorly water-soluble or water-insoluble iron compounds, ferric pyrophosphate (Fe(III)PP) has attracted a great deal of attention. Fe(III)PP is a white/off-white solid that prevents addition of unwanted colors to foods. It has previously been shown that Fe(III)PP is very poorly soluble in the food relevant pH (3-7) which is the reason for the limited reactivity of this salt with the fortified food vehicle. Furthermore, Fe(III)PP has low solubility at low pH (<5% at pH 3) and enhanced dissolution at high pH (up to >99% at pH 7-8) which is advantageous for ensuring the sufficient iron bio-accessibility. However, it has previously been shown that addition of iron in the form of Fe(III)PP cannot fully prevent the discoloration of the phenolic-rich foods. Therefore, improving the function of Fe(III)PP as an iron fortificant (i.e., decreasing the iron-mediated reactivity while ensuring the iron bio-accessibility) still remains of interest. On the other hand, it has been shown before that the pyrophosphate salts of divalent metals have the opposite (reverse) dissolution behavior. For instance, calcium pyrophosphate (CaPP) dissolves well (>99%) at pH 3 but is poorly soluble (<5%) at pH 7-8.

In this work, we seek the strategies by which we can design iron-containing compounds with minimum solubility in the food-relevant pH (3-7), and high and/or fast dissolution in gastric and intestinal pH (1-3 and 6-8, respectively). Interestingly, mother nature can help us find the answer. Inspired by naturally-occurring miner-

als such as anapaite (i.e., a mixed calcium–iron phosphate mineral with the formula $\text{Ca}_2\text{Fe}^{\text{II}}(\text{PO}_4)_2 \cdot 4\text{H}_2\text{O}$), we intend to embed iron in the matrix of a second (divalent) metal (or mineral) salt, which is less chemically reactive, aiming for: (i) decreasing the iron-mediated reactivity to preserve the organoleptic properties of the food vehicle, and (ii) increasing iron dissolution from the designed multi-mineral salt in the gastric conditions to ensure bio-accessibility of iron (and the other mineral). Another benefit of using these multi-mineral salts is the possibility of simultaneous delivery of at least two minerals by the fortified food vehicle.

In **Part I** of this thesis, we explore the possibilities of improving the function of Fe(III)PP as an iron fortificant by mixing Ca along Fe in one salt matrix. In **chapter 2** we use a cheap, fast, and facile co-precipitation method to prepare the mixed Ca-Fe(III) pyrophosphate salts with the general formula $\text{Ca}_{2(1-x)}\text{Fe}_{4x}(\text{P}_2\text{O}_7)_{(1+2x)}$ ($0 \leq x \leq 1$). After characterization of these salts, we find out that the mixed salts with $0.14 \leq x \leq 0.35$ which are atomically homogeneous and amorphous, can be potential dual-fortificants with tunable iron composition.

In **chapter 3**, we investigate the dissolution behavior of iron from these mixed salts as a function of pH. In this chapter we show that besides having an off-white color and the possibility to simultaneously deliver two minerals, the main benefit of these salts is the decreased solubility of iron from them in food pH range (3-7) up to 8 times, with respect to Fe(III)PP. Moreover, these mixed salts with $x \leq 0.18$ show enhanced dissolution in gastric pH range up to a 4-fold increase, compared to pure Fe(III)PP.

In order to explore iron-mediated reactivity of the mixed $\text{Ca}_{2(1-x)}\text{Fe}_{4x}(\text{P}_2\text{O}_7)_{(1+2x)}$ salts next to their solubility, in **chapter 4** we focus on discoloration of these salts in the presence of a set of selected phenolic compounds (which are plentiful in fruits and vegetables) with different water-solubilities. Our findings show that the mixed Ca-Fe(III) pyrophosphate salts with $x \leq 0.18$ can potentially be used as dual-fortificants with limited iron-mediated discoloration and oxidation in foods containing slightly water-soluble or water-insoluble phenolics.

Part II of the present thesis is dedicated to iron (II)-containing pyrophosphate salts that are potential iron fortificants. In this part we explore the possibility of applying ferrous pyrophosphate (Fe(II)PP) in food fortification. Similar to the first part of the current book, the focus of **chapter 5**, is on the synthesis and characterization of the pure as well as mixed Fe(II)-containing pyrophosphate salts with the general formula $\text{M}_{2(1-x)}\text{Fe}_{2x}\text{P}_2\text{O}_7$ ($0 \leq x \leq 1$, where $\text{M} = \text{Ca}, \text{Zn}, \text{or Mn}$). Furthermore, we use black tea as a model solution representative for catechins and explore the discoloration of the black tea solution in the presence of these salts. We show that Fe(II)PP has the potential to be applied in iron fortification of foods as it readily causes acceptable discoloration in a black tea solution (this discoloration was to a lower extent, compared to Fe(III)PP). Moreover, our results suggest that in the case of $\text{M} = \text{Zn}$ and

Mn, the salt with $x = 0.470$ and $x \leq 0.220$, respectively, are the preferred salts for foods containing catechins.

In **chapter 6**, we demonstrate the pH-dependent dissolution profile of the pure and mixed divalent metal Fe(II)-containing pyrophosphate salts with the general formula $M_{2(1-x)}Fe_{2x}P_2O_7$ ($0 \leq x \leq 1$, where $M = Ca, Zn, \text{ or } Mn$) for the first time. We find that the pure pyrophosphate salts: Fe(II)PP, CaPP, ZnPP, and MnPP are very poorly soluble in the pH 4-7, while they dissolve well in pH 1-3. Additionally, the iron dissolution behavior from the mixed Fe(II)-containing pyrophosphate salts showed that all the mixed salts ($M = Ca, Zn, \text{ and } Mn$) had very limited iron dissolution ($< 0.5 \text{ mM}$) in the moderate pH range (5-7) while showing enhanced dissolved iron concentration in the gastric-relevant pH. Furthermore, our findings suggest that the pure Fe(II)PP and the mixed Fe(II)-containing pyrophosphate salts are expected to be biologically accessible.

Chapter 7 shows the possibility of applying Fe(II)PP and the mixed $M_{2(1-x)}Fe_{2x}P_2O_7$ ($0 < x < 1$, where $M = Ca, Zn, \text{ or } Mn$) salts for fortification of foods that contain vitamin C. In this chapter, we investigate the oxidation of vitamin C in the presence of these salts and compare it to the autooxidation of this vitamin in pure water. Our findings indicate that the oxidation of vitamin C in the presence of these salts occurs up to a limited extent (with $\approx 96\%$ intact vitamin C) due to the oxidation state of iron (+2) and its low/slow dissolution. We find that the mixed divalent metal Fe(II)-containing salts with relatively lower iron contents (i.e., $x = 0.06, 0.086, \text{ and } 0.053$ where $M = Ca, Zn, \text{ and } Mn$ respectively) are potential dual-fortificants that do not increase the oxidation of vitamin C over 48 h, compared to its autooxidation in water.

In **Part III** of this thesis, we challenge the notion that cooperative binding only happens in complicated biological systems like hemoglobin. In **chapter 8**, we address cooperative binding in a model system of iron/terpyridine-functionalized polymers by coupling with conformational states. To do so, the cooperative binding behavior of iron onto terpyridine functional groups on the polymer backbone is investigated and compared to terpyridine in its monomer form. We show for the first time that cooperativity occurs in such systems in a two-phase set-up of water and oil. At low iron concentrations, the polymer dissolves in the oil phase (its ground state) due to its hydrophobicity. However, by increasing the iron concentration in the water phase, a sharp transition of the polymer occurs from the oil to the water phase with a sudden full occupancy of the binding sites (terpyridine groups) with iron. We find that this considerable steep response, compared to terpyridine as an individual molecule, is resulted by a competition between the hydrophobic free energy of the polymer and binding of iron ions onto the terpyridine functional groups on the polymer in the water phase. Furthermore, we explain and model this type of cooperative binding by a modified formulation of MWC theory by which the allosteric binding of oxygen on hemoglobin molecule was originally described.

Summary

Samenvatting in het Nederlands

IJZER tekort is een van de meest voorkomende voedingsproblemen ter wereld. IJzer is echter een lastig mineraal om toe te voegen aan voedingsproducten. IJzerhoudende verbindingen kunnen reageren met (plantaardige) stoffen in voedsel, waarbij organo-leptische eigenschappen, zoals smaak of kleur, kunnen veranderen. Verrijking van voedsel met ijzer heeft zich bewezen als efficiënte en kosteneffectieve methode voor het voorkomen van ijzertekort. IJzer bevattende verbindingen die gebruikt worden voor verrijking van voedsel kunnen worden onderverdeeld in drie categorieën; wateroplosbaar, slecht wateroplosbaar (maar oplosbaar in verdund zuur), en niet wateroplosbaar (en slecht oplosbaar in verdund zuur). Hoewel wateroplosbare verbindingen het voordeel hebben van hoge biologische beschikbaarheid, worden de andere categorieën meer bestudeerd vanwege de minimale invloed die deze verbindingen, door hun beperkte oplosbaarheid, hebben op de organoleptische eigenschappen van voedsel.

Onder de slecht wateroplosbare of niet wateroplosbare verbindingen, is ijzerpyrofosfaat (Fe(III)PP) een veel bestudeerde verbinding. Fe(III)PP is een witte/gebroken witte stof, waardoor de toevoeging ervan geen ongewenste kleuren aan het voedsel geeft. Het is aangetoond dat Fe(III)PP erg slecht wateroplosbaar is in het pH gebied dat voor voedsel relevant is (3-7), wat ook de reden is van de beperkte reactiviteit van het zout met het verrijkte voedsel. Bovendien heeft Fe(III)PP een lage oplosbaarheid bij lage pH (< 5% bij pH 3) en een verhoogde oplosbaarheid bij hogere pH (tot >99% bij pH 7-8), wat de biologische beschikbaarheid ten goede komt. Het is echter ook aangetoond dat bij toevoeging van ijzer in de vorm van Fe(III)PP de verkleuring van fenolrijk voedsel niet volledig voorkomen kan worden. Daarom blijft het verbeteren van de functie van Fe(III)PP als voedselverrijking (dat wil zeggen: het verminderen van de ijzer-gefaciliteerde reactiviteit zonder vermindering van de biologische beschikbaarheid) een interessant onderwerp. Aan de andere kant is het ook aangetoond dat pyrofosfaat-zouten van divalente metalen een omgekeerd oplosbaarheidsgedrag vertonen. Zo is bijvoorbeeld calcium pyrofosfaat (CaPP) goed oplosbaar (> 99%) bij pH 3, maar is het slecht oplosbaar (< 5%) bij pH 7-8.

In dit werk onderzoeken we manieren waarop ijzer bevattende verbindingen kunnen ontwerpen met minimale oplosbaarheid in het pH gebied dat voor voedsel relevant is (3-7), en goede en snelle oplosbaarheid in het pH gebied van de maag en darmen (1-3 en 6-8, respectievelijk). Geïnspireerd door natuurlijke mineralen zoals anapaite (d.w.z. een calcium-ijzer fosfaat mineraal: $\text{Ca}_2\text{Fe}^{\text{II}}(\text{PO}_4)_2 \cdot 4\text{H}_2\text{O}$), zijn wij van plan om ijzer te integreren in een matrix van een tweede (divalent) metaal (of mineraal) zout dat minder chemisch reactief is, waarbij we mikken op (i) het verminderen van de ijzer-gefaciliteerde reactiviteit voor het bewaren van de organolep-

tische eigenschappen van het voedsel, en (ii) het verhogen van de oplosbaarheid van het ijzer uit het multi-mineraal zout in maagomgeving om de biologische beschikbaarheid te verzekeren. Een bijkomend voordeel van het gebruik van deze multi-minerale zouten is de mogelijkheid om meerdere mineralen gelijktijdig aan voedsel toe te voegen.

In **deel I** van dit proefschrift verkennen we de mogelijkheden om de functie van Fe(III)PP als ijzertoevoeging te verbeteren door naast Fe ook Ca toe te voegen in een zoutmatrix. In **hoofdstuk 2** gebruiken we een goedkope, snelle, en gemakkelijke co-precipitatiemethode om gemengde Ca-Fe(III) pyrofosfaat-zouten met de algemene formule $\text{Ca}_{2(1-x)}\text{Fe}_{4x}(\text{P}_2\text{O}_7)_{(1+2x)}$ ($0 \leq x \leq 1$) te maken. Na karakterisatie van deze zouten, vinden we dat gemengde zouten met $0.14 \leq x \leq 0.35$, die atomair homogeen en amorf zijn, gebruikt kunnen worden als duale toevoegingen met een aanpasbaar ijzergehalte.

In **hoofdstuk 3** onderzoeken we pH-afhankelijkheid van de oplosbaarheid van ijzer uit deze gemengde zouten. In dit hoofdstuk laten we zien dat, naast de gebroken witte kleur en de mogelijkheid om twee mineralen gelijktijdig toe te voegen, het grootste voordeel van deze gemengde zouten het tot wel 8 maal verminderen van de oplosbaarheid van ijzer in het pH gebied van voedsel (3-7) is, vergeleken met Fe(III)PP. Bovendien vertonen deze gemengde zouten met $x \leq 0.18$ een tot 4-voudig verhoogde oplosbaarheid in maagomstandigheden, vergeleken met Fe(III)PP.

Om naast de oplosbaarheid ook de ijzergefaciliteerde reactiviteit van de gemengde $\text{Ca}_{2(1-x)}\text{Fe}_{4x}(\text{P}_2\text{O}_7)_{(1+2x)}$ zouten te verkennen, richten we ons in **hoofdstuk 4** op de verkleuring van deze zouten in de aanwezigheid van een set fenolische verbindingen met verschillende wateroplosbaarheden, die veel voorkomen in groente en fruit. Uit onze bevindingen blijkt dat deze gemengde zouten met $x \leq 0.18$ potentieel gebruikt kunnen worden als dubbele toevoegingen met beperkte verkleuring in voedsel dat slecht wateroplosbare of niet wateroplosbare fenolen bevat.

Deel II van dit proefschrift is gewijd aan ijzer(II)houdende pyrofosfaat-zouten als potentiële ijzertoevoeging. In dit deel verkennen we de mogelijkheid om ijzerpyrofosfaat (Fe(II)PP) als voedseltoevoeging te gebruiken. Zoals het eerste deel van dit proefschrift, ligt de focus van **hoofdstuk 5** op de synthese en karakterisatie van zowel de pure als de gemengde Fe(II)houdende pyrofosfaat zouten met de algemene formule $\text{M}_{2(1-x)}\text{Fe}_{2x}\text{P}_2\text{O}_7$ ($0 \leq x \leq 1$, waar $\text{M} = \text{Ca}, \text{Zn}, \text{of Mn}$). Verder gebruiken we zwarte thee als modeloplossing voor catechines om de verkleuring van de oplossing door deze zouten te bestuderen. We tonen aan dat Fe(II)PP de potentie heeft om toegepast te worden als ijzertoevoeging in voedsel omdat het een acceptabele verandering in kleur veroorzaakt in zwarte thee (deze verkleuring was in mindere mate dan Fe(III)PP). Bovendien suggereren onze resultaten dat in het geval van $\text{M} = \text{Zn}$ en $\text{M} = \text{Mn}$, het zout met $x=0.470$ en $x \leq 0.220$, respectievelijk, de voorkeur hebben voor voedsel dat catechines bevat.

In **hoofdstuk 6** demonstreren we voor het eerst het pH-afhankelijke oplosbaarheidsprofiel van het pure en gemengde divalent metaal Fe(II)-bevattende pyrofosfaat-zouten met de algemene formule $M_{2(1-x)}Fe_{2x}P_2O_7$ ($0 \leq x \leq 1$, waar $M = Ca, Zn$, of Mn). We vinden dat de pure pyrofosfaat-zouten Fe(II)PP, CaPP, ZnPP, en MnPP erg slecht oplosbaar zijn in pH 4-7, terwijl ze goed oplosbaar zijn bij pH 1-3. Ook bleek uit de oplosbaarheid van ijzer uit de gemengde Fe(II)-bevattende pyrofosfaat-zouten dat alle gemengde zouten ($M = Ca, Zn$, of Mn) een beperkte oplosbaarheid van ijzer (< 0.5 mM) hebben bij gematigde pH (5-7), terwijl ze een verhoogde ijzeroplosbaarheid hebben in maagomstandigheden. Bovendien suggereren onze bevindingen dat de pure Fe(II)PP en de gemengde Fe(II)-bevattende pyrofosfaat zouten een hoge biologische beschikbaarheid hebben.

Hoofdstuk 7 beschrijft de mogelijkheid de gemengde $M_{2(1-x)}Fe_{2x}P_2O_7$ ($0 \leq x \leq 1$, waar $M = Ca, Zn$, of Mn) zouten en Fe(II)PP te gebruiken voor het toevoegen van ijzer aan voedsel dat vitamine C bevat. In dit hoofdstuk onderzoeken we de oxidatie van vitamine C in de aanwezigheid van deze zouten en vergelijken het met de auto oxidatie van de vitamine in puur water. Onze bevindingen geven aan dat de oxidatie van vitamine C in aanwezigheid van deze zouten in beperkte mate (met $\approx 96\%$ intact vitamine C) plaatsvindt door de oxidatietoestand van ijzer (+2) en diens lage en langzame oplosbaarheid. We vinden dat gemengde divalent metaal Fe(II)-bevattende zouten met relatief laag ijzergehalte (d.w.z. $x = 0.06, 0.086$, en 0.053 waar $M = Ca, Zn$, en Mn respectievelijk) potentiële voedseltoevoegingen zijn die de oxidatie van vitamine C niet versnellen voor 48 uur, vergeleken met de auto oxidatie van vitamine C in puur water.

In **deel III** van dit proefschrift dagen we het idee uit dat coöperatieve binding alleen gebeurt in complexe biologische systemen zoals hemoglobine. In **hoofdstuk 8** behandelen we coöperatieve binding in een modelsysteem van ijzer/terpyridine-gefunctionaliseerde polymeren door koppeling met staten van conformatie. Om dit te doen, onderzoeken we het coöperatieve bindingsgedrag van ijzer aan terpyridine functionele groepen op een polymeer en vergelijken we het met het bindingsgedrag met terpyridine in monomeervorm. We tonen voor het eerst aan dat coöperativiteit voorkomt in zulke systemen in een tweefasen-opstelling met water en olie. Bij lage ijzerconcentraties lost het polymeer op in de oliefase (zijn grondtoestand) vanwege zijn hydrofobiciteit. Daarentegen vindt een scherpe transitie plaats bij het verhogen van het ijzergehalte in de waterfase, waarbij het polymeer verplaatst naar de waterfase met een volledige bezetting van de bindingsplaatsen (terpyridine groepen) door ijzer. We vinden dat deze scherpe respons, vergeleken met terpyridine als los molecuul, het resultaat is van een competitie tussen de hydrofobe vrije energie van het polymeer en de binding van ijzerionen aan de terpyridinegroepen op het polymeer in de waterfase. Bovendien modelleren en leggen we dit soort coöperatieve

Samenvatting in het Nederlands

binding uit met behulp van een aangepaste formulering van MWC theorie, waarmee de allosterische binding van zuurstof met hemoglobine origineel werd omschreven.

Acknowledgments

"With a life as short as a half-taken breath,
don't plant anything but love."

Rumi – Persian poet, 1207-1273

"Love is how you stay alive, even after you are
gone."

*Morrie Schwartz – Tuesdays with Morrie (1997,
Mitch Albom)*

The PhD journey was a unique adventure for me. Besides the opportunity to pursue my education in depth and broaden the horizons of my knowledge, I had the privilege of having academic experience in a whole new world. Additionally, what makes these four years of work once-in-a-lifetime experience and even more special to me is getting to work with an amazing group of people. Needless to say, the presented work would not have been even close to possible without their help and support. I am grateful to not only those who helped, motivated, and inspired me, but also to those who created a pleasant working environment.

First and foremost, I would like to express my sincere gratitude to my promoters, **Willem Kegel** (Utrecht University) and **Krassimir Velikov** (Unilever Foods Innovation Centre - Hive), for their enthusiasm, great scientific vision, and guidance. I want to thank Willem in particular for always being patient, willing to take risks, and giving me freedom along the way to chase new ideas, give them a try, and learn from them, regardless of the results. Willem, words cannot express how honored I am to have worked with you and how much I appreciate your scientific feedback in our discussions as well as your mental support and level of understanding. I am also thankful to my second promoter, Krassimir for his excellent insights on the experimental procedures and analyzing the results. Krassimir, this work is accomplished only by your input as an expert in the field. You cannot imagine how much I have learned from the discussions we had in our monthly update meetings.

Next, I would like to appreciate the time and effort of both the reading and defense committee for reading and evaluating this thesis as well as providing me with their positive and kind words on this work. I am also very thankful to my paranymphs, **James** and **Judith**, whose support I had, not only for the big day but also for the whole PhD journey. I wish both of you best of luck with finishing and defending your PhD research projects.

Acknowledgments

Besides my supervisors, there is an excellent group of people who I had the pleasure to collaborate with in the Laboratory of Food Chemistry at Wageningen University and Research where a significant part of the experimental work described in this book was performed. I want to thank **Jean-Paul Vincken** and **Wouter de Bruijn** for being such pleasant supervisors. Thank you so much for arranging my visit in your group. I am forever thankful for the experience I gained and everything I have learned about food chemistry because of working with you. Moreover, I deeply appreciate all the time you took to give scientific feedback in our fruitful collaboration. I truly value your opinions on color shades as well. Honestly, making color-blind friendly figures has stuck in my mind as an important factor in the science visualization ever since. At last, but not least I want to thank **Judith Bijlsma** for being one-of-a-kind and a truly unique friend to me. Oh my dear Judith! How lucky am I?! Is there anything you have not supported me with?! I still remember when we first met in the Iron-Tech kick-off meeting. I had absolutely no clue that it was just the beginning of a beautiful friendship. I remember all our meetings, phone calls, planned experiments, home-made deadlines, and being each other's (iron) buddies! If I were to do a PhD a thousand more times, I would still want you to be one of my collaborators!

Furthermore, I am sincerely grateful to the industrial partners involved in the Iron-Tech consortium, **Arjen Reichwein** and **Alexey Zaitsev** (Nouryon), and **Bart Zwijnenburg** (Nobian) for their support with the measurements and their valuable insights in our semiannual meetings. Working in a collaborative manner on a valuable project in which science and application meet was most certainly a unique experience for me.

Next to Iron-Tech consortium, I got the chance to work with **Mariette Wolthers** from the Geochemistry group (Department of Earth Sciences) at Utrecht University. Dear Mariette, although our work together was very short and is not included in this thesis, I have to admit I learned from you more than you can imagine. Thanks for introducing me to the fascinating world of minerals and crystals. In fact, the idea behind the cover of this book was an inspiration I got from one of our very recent meetings. I appreciate the time you patiently spent with me, despite having a tight schedule, and the effort you made to answer all my (naïve) questions.

As an experimentalist, I spent most of my time either in the lab or doing measurements, and of course I had the luxury of having an amazing technical support staff around. I am thankful to the (former) technicians of the FCC group. Dear **Dominique**, thanks a lot for your assistance in the lab. Not only you are the technical "mom" of the group, you are always supportive of every single one of us in FCC too. I'll miss all the teasing and jokes we made during the coffee breaks, and all the times *moesten wij proberen Nederlands te praten!* Dear **Alex**, believe it or not, I am actually very happy you didn't leave FCC after your defense! Thanks a lot for answering all my

questions and always offering to help in the lab as well as in daily life. Dear (young!) **Kanvaly**, you are the one who introduced me to the lab and walked me towards my first steps. I missed you so much in the lab after you left but never lost your help with the synthesis even afterwards. Dear **Bonny**, I appreciate your patience and help with DLS, and how you kept notes of every single experiment throughout the years which came in handy afterwards! I am wholeheartedly grateful to the support staff at the electron microscopy department, **Chris Schneijdenberg** and **Hans Meeldijk** as well. Dear Hans and Chris, I promise not to bother you anymore with my endless questions and problems with the microscopes. I want to particularly thank Hans for his assistance with the TEM-EDX, elemental mapping by HAADF-STEM, and simultaneously sharing his valuable feedback on the results. Dear Hans, thank you for spending hours and hours on the measurements with me, and for teaching me "*tjonge jonge!*". It's actually very useful!

Many thanks to all my amazing (former) colleagues at FCC, first for being amazing gossip partners (!) and second for creating a perfect, healthy, and relaxed atmosphere to work in. Dear **Jasper**, your L^AT_EX template is obviously a piece of art. I am grateful for the time you spent to help me with the adjustments I asked for. Dear **Bas**, I'm truly thankful for having the opportunity to collaborate with you and to benefit from your valuable insight and expertise on the polymer chemistry. I want to acknowledge you for always being open to both scientific and decision-making discussions, as well as your never-ending supportive and welcoming manner! Dear **Pepijn**, could I *BE* any more grateful to you?! I still remember how you helped me break the ice and feel at home with your warm presence in the group. You are definitely one of my best friends for life! Dear **Riande**, I am always inspired by your kindness and hard work. During our time together at FCC you, you patiently listened to me nagging about the ups and downs in my project, and always told me "you'll be fine!". And that was indeed true! Dear **Frans**, you were an amazing colleague and lab-mate. I am thankful for all the help you offered me even after you left FCC. Dear **Alvaro**, thank you for always willing to discuss the possible hidden theories behind my results. I want to show my gratitude to **Mikal** as well. Although I never actually met him, I got inspired by his PhD work. Dear **Fara**, I enjoyed our Friday afternoon conversations a lot! Dear **Katherine**, in our time together at FCC, you were a true inspiration for me. I deeply appreciate the meaningful conversations we had at the coffee breaks! Dear **Alessio**, thanks for sharing the Popeye idea with me. I was lucky to have a creative colleague like you! Dear **Mariska**, my roomie in Greece with all the memories specially the pistachio ice cream! I want to appreciate your effort for doing SEM on my samples and finding the artistic sad scientist guy, despite being busy with having a "*thing*"! Dear **Azeem**, all the fun I had with you while sharing culture, cuisine, *khoraki*, and talking about future! Your warm presence in the group is indeed a great vibe if you *listen Linda!* I am also sorry for walking

Acknowledgments

into your office a million times! Dear **Amanda**, honestly I am so happy you ended up spending more time at FCC than the other group. I appreciate your great pieces of advice whenever I was struggling with something. Dear **Jesse**, thanks for all the funny stories, specially the *must-watch anime*! Dear **Henrik**, you are the one always reminding me of being *productive*! Dear **Matthijs**, I want to thank you specifically for patiently helping me with my Excel and KLM problems! Dear **Geert**, I wish we had longer over lap time at FCC, I wish you best of luck! Dear **Joren**, it might sound weird, but I am actually grateful to you as well! You are a package of random jokes, help and always-being-there for everyone! I appreciate all your effort for photography at different gatherings and the time you spent on editing the pictures. I am thankful to you particularly for photography at my defense and for the cover of my thesis as well. Dear office-mate and lab-mate, dear **James**! Where do I start? *It's such a mess*! Should I say you are my best (and only) office-mate? You were the one who actually brought me out of my loneliness in the office. When I look back, our friendship evolved over the years and recently reached the point where you made me feel the sweetness and craziness of having a younger brother. Thanks for always helping me with my questions about \LaTeX , Python, Mathematica, NMR, English language, and this list continues! I am also grateful to you for being patient with me specially when singing in the office. I know I was not the easiest office-mate (*jokes!*).

I am very grateful to the secretaries of the FCC group, **Marina** and **Sylvia** as well. Special thanks to Sylvia whom I spent more time with. Dear Sylvia, I appreciate you taking care of us with all the administrative work. You were a great help and listener to me and I am looking forward to the future of our friendship. I want to mention **Regina** as well, whose laughter is like the radiation of positive energy in the corridor! And finally, **Marianne**, whom I met through FCC and is one of the most supportive people I have ever met. Dear Marianne, the joy I feel with you being around is other-worldly!

I would like to show my sincere gratitude to other scientific staff members of the FCC group as well. Dear **Jan** (Groenewold), thanks a lot not only for your great comments in our brainstorm sessions, but also because of your concerns about me settling down in The Netherlands. I remember the very first day I stepped foot in FCC. I was waiting in the corridor for the brainstorm session to end when you came out. You were actually the first person from FCC whom I ever met! Dear **Hans** (Tromp), **Ben** (Ernè), and **Albert** (Philipse), I greatly appreciate you sharing your experience with me regarding job opportunities. Dear **Andrei** (Petoukhov), thank you very much for your feedback on my XRD results. Dear **Martin** (Haase), I appreciate the time you spent for our very short collaboration. At last but not least, I am so grateful to the sweet and energetic presence of **Marlous** (Kamp) who joined FCC recently. Dear Marlous, I loved our conversations and thanks for sharing your experience with me!

Furthermore, I had the chance of supervising students for their research projects. Dear **Wessel** (bachelor), **Karen**, **David**, **Martijn**, and **Bart** (second year Bachelor), **Ander** (Bachelor), **Nikos** (Master), **Isabelle** (Master), **Pascal**, **Koen**, and **Hanna** (U-Talent), **Thomas** (Internship), **Michiel** (Bachelor), and **Bo** (Master), if you learned half as much as I learned from you, I consider it a success. Not only your efforts gave me a better understanding of the projects, I enjoyed working with you as well. I am in particular grateful to Nikos and Michiel whose hard work had promising results and ended up in this thesis after further investigations.

To my family who is all I am, all I have, and all I ever want. I wish words could express how much I love you. Dear **Mom** and **Dad**, you are my beating heart on the other side of this planet! Thank you for your endless support and for always keeping me motivated. I want you to know that you and your sacrifices shaped me to the person I am now. I am grateful to you for all you gave up and the burdens you carried so that I can find my way and follow my dreams. To my dear sisters, **Negar** and **Nikoo**, who always cheer me up and have my back. I love you so much and miss all four of you. You are the family I am lucky to have, but don't deserve!

To my dearest and kindest, my other half, my mate, my fellow traveler for the journey of life, my husband, **Moslem**. All the sacrifices you made and all the moments you stood by me! I am grateful for your patience and tolerance, the resemblances you bear to **Maman Zamane**. I hope you know how much I owe this to you and that I couldn't have done it without you. You are my strength and the reason not to give up. With you in my life, I am not seeking happiness, I am living it!

And my final words to all my loved ones here, there, and everywhere:

I wish I could show you the astonishing light
of your own being(s).

Hafez – Persian poet, 1325-1390

*Love, Neshat
March 2023*

-

Acknowledgments

List of publications

This thesis is based on the following publications:

- N. Moslehi, J. Bijlsma, W.K. Kegel, and K.P. Velikov, “Iron-fortified food product”, WO2022048952A1 (2022). (chapters 2 and 5)
- N. Moslehi*, J. Bijlsma*, W. J.C. de Bruijn, K.P. Velikov, J-P. Vincken, and W.K. Kegel, “Design and characterization of Ca-Fe(III) pyrophosphate salts with tunable pH-dependent solubility for dual-fortification of foods”, *Journal of Functional Foods* 92 (2022): 105066. (chapters 2 and 3)
- N. Moslehi*, J. Bijlsma*, K.P. Velikov, W.K. Kegel, J-P. Vincken, and W. J.C. de Bruijn, “Reactivity of Fe(III)-containing pyrophosphate salts with phenolics: complexation, oxidation, and surface interaction.”, *Journal of Food Chemistry* 407 (2023): 135156. (chapter 4)

Manuscripts in preparation or submitted:

- N. Moslehi, M. van Eekelen, K.P. Velikov, and W.K. Kegel, “Mixed divalent pyrophosphate salts for simultaneous delivery of iron and calcium, zinc, or manganese in foods.”, (chapters 6 and 7)
- N. Moslehi, N. Dramountanis, J. L. Martin Robinson, B. G. P. van Ravensteijn, and W.K. Kegel, “Cooperative binding of iron onto terpyridine-functionalized polymers.”, (chapter 8)

*Equal contribution of the authors.

List of publications

About the author

"You are not a drop in the ocean.
You are the entire ocean in a drop."

Rumi – Persian poet, 1207-1273

Neshat Moslehi was born on January 10th, 1991 in Tehran, Iran. After finishing high school in 2009, she started her undergraduate studies at Amirkabir University of Technology (Tehran Polytechnique) in Tehran. By completing the second year, she was granted a double bachelor program in Polymer Engineering (Polymer Industries) and Biomedical Engineering (Biomaterials). Following her graduation in 2013, as one of the distinguished students, she was granted to follow a master program without taking The Iranian University Entrance Exam (Konkour). She pursued her education in Polymer Science with a focus on Nanomaterials at Tehran Polytechnique. In 2016, she accomplished her master diploma with a thesis project titled "The internal structure effects of methacrylate-butadiene-styrene core-shell nanoparticles on the interaction with styrene-acrylonitrile copolymer and mechanical strength of nano-blend" in the group of Physical Chemistry under supervision of Prof. Naser Mohammadi. Immediately after finishing her master studies, Neshat joined a spin-off innovation center and gained research experience in industrially-relevant projects with a focus on the structure-property connection of polymers for two years. In 2018, Neshat moved to The Netherlands to perform a PhD in the Van 't Hoff Laboratory for Physical and Colloid Chemistry (Debye Institute for Nanomaterials Science, Department of Chemistry) at Utrecht University, with Prof. Willem Kegel and Prof. Krassimir Velikov (Unilever Foods Innovation Centre - Hive) as her promoters. In a close collaboration with academic partners (Wageningen University and Research, and University of Amsterdam) and industrial partners (Nouryon and Nobian), Neshat worked on designing novel iron-fortificants for fortification of food products. In addition, she conducted a fundamental study on the cooperative binding behavior of iron onto terpyridine-functionalized polymers. Furthermore, Neshat attended the Han-sur-Lesse winter school for physical chemistry twice and supervised several students (for high school U-Talent, bachelor, master, and internship research projects) as well as giving teaching assistance in exercise classes. The majority of work done during her PhD research is described in this thesis. Part of the results of the current book has also been published in peer-reviewed journals and presented in Dutch conferences such as CHAINS (CHemistry As Inovating Science) and Dutch Soft Matter Meetings, as well as international conferences such as ESM (Edible Soft Matter), ECIS (European Colloid & Interface Society), and Brightlands Polymer Days.

